NORTHWESTERN UNIVERSITY

Microstructure and Creep Properties of Al-Sc Alloys Micro-alloyed with Lanthanides (Yb or Gd) and Transition Metals (Ti or Zr)

A DISSERTATION

SUBMITTED TO THE GRADUATE SCHOOL
IN PARTIAL FULFILLMENT OF THE REQUIREMENTS

for the degree

DOCTOR OF PHILOSOPHY

Field of Materials Science and Engineering

By

Marsha van Dalen

EVANSTON, IL

December, 2007

ABSTRACT

Microstructure and Creep Properties of Al-Sc Alloys Micro-alloyed with Lanthanides (Yb or Gd) and Transition Metals (Ti or Zr)

Marsha van Dalen

This thesis examines the effects of micro-alloying additions to Al-Sc alloys on the microstructure, coarsening resistance and creep properties. The overarching goal of this research is to develop castable, creep-resistant aluminum alloys which can be used at temperatures in excess of 300˚C. Successful high-temperature application of aluminum based alloys offers a lower cost and lower weight alternative to other materials commonly used at high temperatures, including titanium- and nickel-based alloys.

To this end, this aims to improve the properties of the Al alloys by adding various alloying elements in small quantities, on the order of several hundred atomic parts per million, to aluminum. The thesis begins by focusing on additions of Ti to Al-Sc. Ti is a slow diffuser in Al [1], and it will be shown that it improves the coarsening kinetics of the precipitate phase at 300˚C. Since these alloys are coarsening resistant, it is found that they can be aged and crept at temperatures of up to 425˚C. The properties displayed are similar to those of Al-Sc-Zr alloys studied previously [2, 3].

The examination of Ti additions is followed by a study of the additions of lanthanide elements. These elements are of interest since they are known to increase the lattice parameter of the precipitate phase [4-8], which could potentially lead to improved creep resistance [9]. Initially, binary Al-Yb alloys are studied to obtain some fundamental knowledge of the behavior of Yb in Al. Subsequent additions of Yb to Al-Sc result in improved creep resistance. A similar improved creep resistance is observed for additions of Gd to Al-Sc.

Finally, this dissertation concludes with the study of Al-Sc-Yb-Zr alloys. Since the goal of this research is to obtain a creep-resistant as well as coarsening resistant alloy, both a slow diffusing element (Zr) and an element which improves the creep resistance (Yb) are added. The quaternary alloys are found to maintain the creep resistance and coarsening resistance of the Al-Sc-Yb and Al-Sc-Zr alloys, respectively, which points to opportunities for future research in this area.

Acknowledgements

I would like to thank my advisors, Profs. David Dunand and David Seidman for providing me with the opportunity to study this subject and for providing me with guidance along the way. I would also like to thank my thesis committee members, Prof. Ian Robertson and Prof. Peter Voorhees for their input.

I would also like to thank Dieter Isheim, Richard Karnesky, Ketih Knipling, Marcus Young, Zugang Mao, Chantal Sudbrack and Stephan Gerstl for interesting technical discussions and providing me with significant help. I also acknowledge Thomas Gyger for the work he did on the Al-Sc-Yb-Zr alloys. I would also like to thank my former and current group members for making my time in the lab enjoyable.

Table of Contents

List of Figures

List of Symbols and Acronyms

A	Dorn constant
A_{KV}	Coarsening constant for evolution of number density (ternary alloy)
a	Lattice parameter
b	Matrix Burger's vector
C_i^j	Concentration of element i in phase j
ΔC_i^j	Supersaturation of element i in phase j
d_{max}	user-selected maximum-separation distance between solute atoms of interest
D	Diffusion coefficient
δ	Unconstrained lattice parameter mismatch
$\dot{\varepsilon}$	Strain rate
ε_s	Constrained lattice parameter mismatch
K_{KV}	Rate constant for coarsening for evolution of <R(t)> (ternary alloy)
K	Rate constant for coarsening for evolution of <R(t)> (binary alloy)
$\kappa_{i,KV}^{\alpha}$	Coarsening rate constant for evolution of matrix supersaturation (ternary alloy) of component i.
κ^{α}	Coarsening rate constant for evolution of matrix supersaturation (binary alloy)
$N_v(t)$	Number density of precipitates
N_{min}	Minimum number of solute atoms in a non-discarded cluster (envelope method)
n	Stress exponent for creep
n_{ap}	Apparent stress exponent
<R(t)>	Mean radius of precipitates
R_g	Ideal gas constant
T	Temperature
t	time
ν	Matrix Poisson's ratio
γ_{apb}	Anti-phase boundary energy
ϕ	Volume fraction of precipitates
ϕ_{eq}	Equilibrium volume fraction of precipitates
μ	Matrix shear modulus
λ	Interprecipitate distance
$\sigma^{\alpha/\beta}$	Interfacial energy between α-Al and β precipitate phase
σ	Applied stress
σ_{th}	Threshold stress
Q	Activation energy for creep
RE	Rare-earth Element
LSW	Lifshitz-Slyozov-Wagner model for coarsening
FIM	Field-ion microscopy
CTEM	Conventional transmission electron microscopy
HREM	High-resolution transmission electron microscopy
3DAP	3-dimensional atom probe microscopy
LEAP	Local-Electrode Atom-Probe Microscopy

1. Background Information

1.1 Introduction

This thesis examines the effects of micro-alloying additions to Al-Sc alloys on the microstructure, coarsening resistance and creep properties. The overarching goal of this research is to develop castable, creep-resistant aluminum alloys which can be used at temperatures in excess of 300˚C. Successful high-temperature application of aluminum based alloys offers a lower cost and lower weight alternative to other materials commonly used at high temperatures, including titanium- and nickel-based alloys.

To this end, this aims to improve the properties of the Al alloys by adding various alloying elements in small quantities, on the order of several hundred atomic parts per million, to aluminum. Each element was chosen for its different effects on the alloys, including elements which improve the coarsening resistance of the precipitate phase and elements which enhance the creep resistance.

The thesis begins by focusing on additions of Ti to Al-Sc. Ti is a slow diffuser in Al [1], and it will be shown that it improves the coarsening kinetics of the precipitate phase at 300˚C. Since these alloys are coarsening resistant, it is found that they can be aged and crept at temperatures of up to 425˚C. The properties displayed are similar to those of Al-Sc-Zr alloys studied previously [2, 3].

The examination of Ti additions is followed by a study of the additions of lanthanide elements. These elements are of interest since they are known to increase the lattice parameter of the precipitate phase [4-8], which could potentially lead to improved creep resistance [9]. Initially, binary Al-Yb alloys are studied to obtain some fundamental knowledge of the behavior of Yb in Al. Subsequent additions of Yb to Al-Sc result in improved creep resistance. A similar improved creep resistance is observed for additions of Gd to Al-Sc.

Finally, this dissertation concludes with the study of Al-Sc-Yb-Zr alloys. Since the goal of this research is to obtain a creep-resistant as well as coarsening resistant alloy, both a slow diffusing element (Zr) and an element which improves the creep resistance (Yb) are added. The interactions among the different alloying elements are examined. Fortunately, the quaternary alloys maintain the creep resistance and coarsening resistance of the Al-Sc-Yb and Al-Sc-Zr alloys, respectively, which points to opportunities for future research in this area. The relations among the different alloys examined in this thesis is shown below:

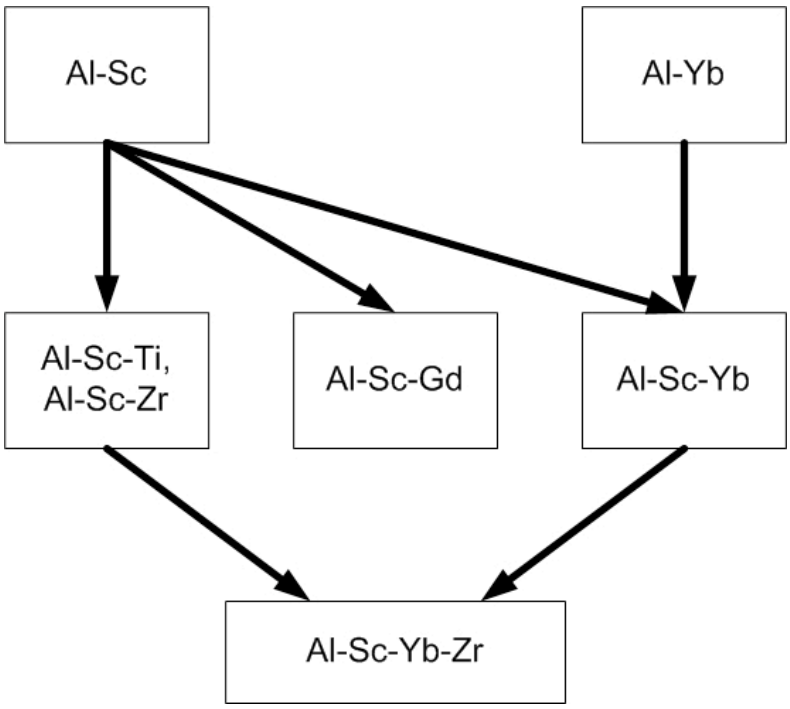

1.2 Benefits of Sc Additions

Aluminum alloys are of interest to various industries, including the aerospace industry, since they are less dense than typical structural alloys, such as steel or nickel-base alloys. Their lighter weight can result in substantial energy savings. However, most current Al alloys are limited to low temperature usage (less than 200°C) since above this temperature the precipitates coarsen rapidly or dissolve [10]. Development of aluminum alloys for higher temperature environments would allow additional replacement of heavier, more dense materials, particularly certain portions of the engine.

Aluminum-scandium alloys are of interest since they potentially have a higher use temperature than 200°C. The first publications on Al-Sc alloys are found in the Russian literature from the 1970's. While the solid solubility of Sc in Al is limited, Sc is a very potent strengthener. When normalized by solute concentration (at.%) Al-Sc alloys exhibit a much greater increase in

strength than Al alloys with various concentrations of other elements including, Zn, Cu, Mg, Li and Si [11]. Thus, on a per atom basis, Sc is the most potent strengthener compared to alloying elements common in Al alloys.

The use of Sc in Al alloys also has additional benefits, including that it can inhibit recrystallization [12], which, when combined with the addition of Zr leads to a much higher recrystallization resistance compared to Sc or Zr alone [13, 14]. Sc can also reduce the width of the precipitation free zones adjacent to grain boundaries, as demonstrated in an AA 7050 alloy [12]. Furthermore, it has been shown that Sc additions can increase the weldability of Al alloys [15]. An Al-Sc-Zr alloy prepared by powder metallurgy was shown to improve the corrosion resistance properties over an AA6061-T6 alloy [16]. Finally, increased grain refinement with additions of Sc have also been shown to lead to increased wear resistance [17].

As seen from the phase diagram (Fig. 1) there is limited solid-solubility of Sc in Al [18], with a maximum value of 0.23 at.% (0.38 wt.%) occurring at 660°C. Small additions of scandium to aluminum alloys produce nanoscale diameter Al_3Sc ($L1_2$) precipitates that precipitate homogeneously from a single-phase supersaturated solid-solution [18, 19]. Due to the lattice parameter misfit between the two phases, ($\Delta a/a$ = 1.05 % at 300°C [20]) and the resulting lattice strains, the precipitates remain coherent up to diameters of ca. 40 nm [21, 22]. Al-Sc alloys provide high strength at ambient temperature by precipitation and grain boundary strengthening [23], the later effect resulting from stabilization of a very fine grain structure by the precipitates for hypereutectic alloys [24]. At elevated temperature, the high stability and coarsening

resistance of the precipitates maintain this fine-grain structure, leading to superplastic behavior [25].

If, however, the alloy is homogenized at high homologous temperatures in the single-phase region, a coarse-grained matrix forms. Subsequent heat treatments in the two-phase region will create a fine dispersion of Al_3Sc precipitates within the coarse-grained structure. This structure is expected to lead to high creep resistance as a result of precipitation strengthening, as demonstrated in previous articles [20, 26-28]. Indeed, the coherent, nanosize Al_3Sc precipitates are found to be very efficient obstacles to dislocation climb, resulting in a threshold stress for creep at 300°C.

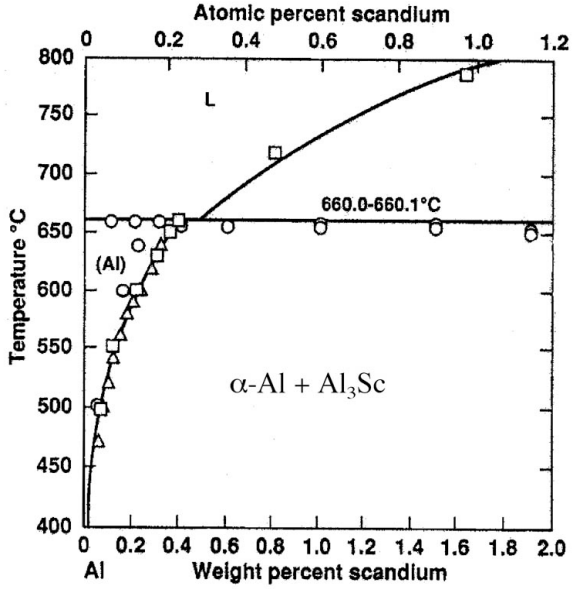

Figure 1.1: Al-Sc binary phase diagram on Al rich side [18].

1.3 Ternary and Quaternary additions to Al-Sc alloys

To further improve the coarsening and creep resistance properties of Al-Sc alloys, the effects of ternary additions on Al-Sc alloys have been investigated. Several methods can be used to further increase the strength of the binary alloys. Solid-solution strengthening can be exploited with elements such as Mg. For creep at high strain rates, solid-solution strengthening is additive to precipitation strengthening, since Mg does not affect significantly the precipitation kinetics of Al_3Sc [25]. Furthermore, Mg does not alter significantly the near-threshold creep behavior at low strain rates [26].

Zirconium additions to Al-Sc alloys have also been studied, as Zr partitions to the Al_3Sc precipitates, thus forming $Al_3(Sc_{1-x}Zr_x)$ precipitates [3]. In the intermetallic bulk, Zr can replace up to 50% of the Sc, while retaining the $L1_2$ structure [29]. Since Zr has a significantly lower cost than Sc (Table 1.1), the same precipitate volume fraction could be retained while employing a smaller amount of Sc. However, in the Al-Sc-Zr alloys, the Zr concentrations in the precipitates are found to be much lower than their solid-solubility, as a result of the low diffusivity of Zr in Al. Fuller et al. [2] studied Al-Sc-Zr alloys at an aging temperature of 300°C and found that the maximum concentration achieved in the precipitates was only ~1%. Even at higher aging temperatures, very little Zr is incorporated into the precipitates, as shown by a recent 3D atom-probe (3DAP) microscopy study [30]. When aged at 475°C, the concentration of Zr in the precipitates in an Al-0.09 at.% Sc-0.023 at.% Zr alloy was increased to 4.5 at.%. However, most of this Zr was at or near the interfacial region. Nevertheless, Al-Sc-Zr alloys exhibit improved precipitate stability and coarsening-resistance at 300°C as a result of Zr segregating to the α-

Al/Al_3Sc heterophase interface and acting as a barrier for the diffusion of Sc across the interface [3]. It was suggested by Deschamps et. al. [31] that there are two distinct regimes of growth. The first when the Sc precipitates and the second when the Zr precipitates out of the matrix. The core/shell structure has been observed by atom-probe [3, 30, 32, 33], TEM [34] and SAXS [31]. Recent kinetic monte carlo (KMC) simulations concluded that this core/shell structure was due to the differences in diffusion kinetics between Sc and Zr [32, 35]. Finally, Zr also reduces the lattice parameter of the $Al_3(Sc_{1-x}Zr_x)$ phase [29], thus decreasing the mismatch with the α-Al matrix. This could lead to a reduction in the driving force for coarsening [2].

Titanium is of interest as a ternary alloying element in creep-resistant Al-Sc alloys since Ti has the same high solubility in Al_3Sc ($L1_2$) as Zr (up to 50 at.% of the Sc can be replaced) and Ti reduces the lattice parameter of $Al_3(Sc_{1-x}Ti_x)$ to an even greater extent than Zr [29]. The concomitant reduction in interfacial and elastic strain energies may further improve the coarsening resistance of the $Al_3(Sc,Ti)$ precipitates [2], thus resulting in coarse-grained Al-Sc-Ti alloys, which are more creep resistant at higher temperatures than Al-Sc alloys. Additionally, the tracer diffusivity of Ti in Al is much smaller than that of Zr in Al (by a factor ca. 20 at 300ºC [1]), which may lead to precipitates that coarsen more slowly than in Al-Sc-Zr alloys. Indeed, in a recent study of the resistivity of hypereutectic Al-Sc-Ti alloys, it has been found that the addition of Ti stabilizes the precipitate structure at 300°C [36]. Furthermore, Ti is also significantly cheaper than Sc and would thus lower the cost of the alloy as it replaces Sc in the precipitates (Table 1.1). Finally, Ti has been shown to act as a grain refiner in Al-Sc alloys, especially for slow cooling rates from the melt [37]. It was suggested that Ti decreases the grain

size with respect to the binary alloys, since all of the primary precipitates nucleate grains (compared to only 2 % for the binary).

Table 1.1: Approximate Prices of the Elements [38].

Element	Price (USD/lb)
Al	0.5
Sc	4963
Zr	12
Ti	10
Y	33
Sm	33
Gd	40
Dy	46
Er	119
Yb	232

1.4 Properties of Al-Sc-RE alloys

Evidence that the rare earth (RE) elements have the potential to be compatible with the Al-Sc system is clear from the ternary phase diagrams (Fig. 2), which show that they are soluble in the Al3Sc phase. As the atomic number increases, the character of the Al3RE precipitate phase formed is more cubic [39-41]. For some rare earth elements, the solubilities are relatively modest, 12 and 15 at.% for Sm [4] and Gd [5] (expressed as a percentage of Sc in the precipitate), respectively. This relatively modest solubility is due to the differing crystal structures. For example, Al_3Sc is an fcc-based $L1_2$ structure, while Al_3Gd is hexagonal DO_{19} form [6]. For some of the heavier rare-earth elements (RE), such as Er [7] and Yb [8], the

solubility can reach 100%. Reference [6] discusses the difference among the lathanide elements, in particular they discuss Gd and Er. Er forms a continuous solid solution between Al_3Sc and Al_3Er, which both have the $L1_2$ structure [6]. An additional feature of the REs is that they increase the lattice parameter mismatch between the matrix and $Al_3(Sc_{1-x}RE_x)$ phase, which could lead to improved creep resistance. They also have a lower cost than Sc, which makes them attractive candidates for replacing Sc in the precipitate phase.

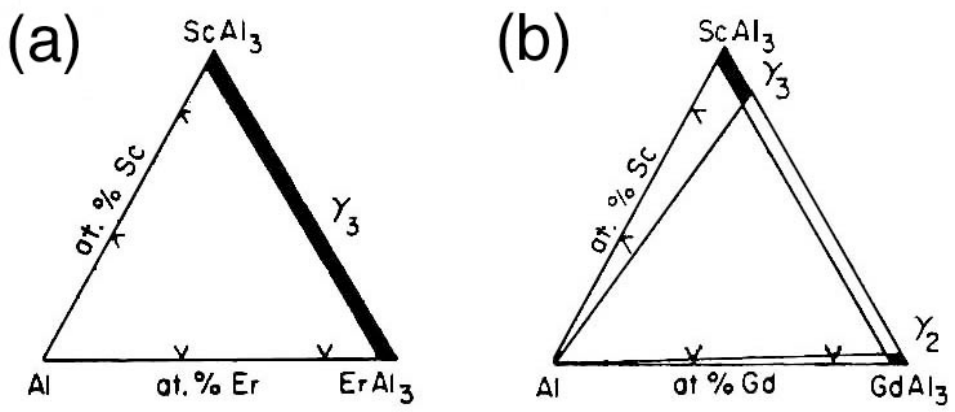

Figure 1.2: Ternary phase diagrams from Ref. [6] at 500ºC showing in (a) a continuous series of solid solutions of the Al_3X phase between Al_3Sc and Al_3Er. However, in (b) the Al_3Sc and Al_3Gd phases are not fully soluble and have different crystal structures.

Sawtell and Morris [42] studied Gd, Er and Y as ternary additions to Al-Sc alloys. Since the electronegativity of the RE's and Sc are similar, they should thus behave similarly chemically, and hence the rare-earth elements are expected to substitute for Sc in the Al_3Sc precipitates. To determine the effects of the RE substitution for Sc in the precipitates, the moderately rapidly solidified alloys studied contained 0.3 at.% of Sc and 0.3 at.% of an RE. The alloys were not

solutionized since they exceeded the solid-solubility and no primary precipitates were observed. The alloys were aged at temperatures ranging from 235-310°C.

The authors calculated that the lattice parameter of the $Al_3(Sc_{1-x}RE_x)$ phase should remain less than 0.176 nm in order for the $L1_2$ structure to remain stable, since the addition of RE into the precipitate will increase the lattice parameter. Upon aging, $L1_2$ was the only precipitate phase detected in the alloys. It was found that the ternary alloys had up to 25% higher tensile strengths than the highest strength obtained for the Al-0.3 at.%Sc binary alloy (251 MPa). The Al-0.3 at.% Sc-0.3 at.% Gd had the highest tensile strength of the ternary alloys involving RE at 309 MPa.

1.5 Properties of Al-RE Alloys

Much of the previous work involving lanthanide additions to Al involves binary rapidly solidified Al-RE. Al-RE alloys processed in this manner offer excellent potential for use at high temperatures. These alloys will have a relatively refined microstructure and will form hard and stable intermetallic compounds within the aluminum matrix. For example, Ruder and Eliezer [43] studied the Al-0.7at.%Er and Al-0.8at.%La systems and found that the microstructure after rapid solidification was relatively refined with grain sizes on the order of several microns. In the Al-Er alloy, nanosize, coherent Al_3Er formed near the melt spun contact surface and in the Al-La alloy, $Al_{11}La_3$ particles (~50 nm diameter) formed at the near contact surface with the cooled copper surface. Moreover, in more complex Al alloys, RE additions have also been found to refine the microstructure. Fu et al. [44] found that RE additions to commercial Al alloys containing Fe-rich precipitates reduces the size of the Fe-rich precipitates. Specifically, the

addition of Ce leads to the formation of small precipitates in spherical or short rod form. It was also commented by Nie et al. [45] that RE can increase the corrosion resistance and decrease the detrimental effects of hydrogen.

RE additions have significant effects on the mechanical properties of Al alloys. Some of the resulting high temperature properties of Al-RE alloys include good high-temperature tensile strength, reasonable thermal stability and moderate ductility. Nie et. al. [45, 46] studied binary Al-Er alloys (with additions of up to 0.1at.% Er) and found that Er additions increase the hardness and the yield strength over pure Al, in a similar manner to Sc. The grain size of the binary alloy is reduced and ductility is retained. When 0.02at.%Er is added to an Al-Zn-Mg or Al-Zn-Mg-Cu alloy, the strength is increased and additionally, the grain structure is refined and the dendrite structure "almost disappears" [47]. However, the ductility was somewhat reduced in these alloys. Nie et. al. also studied the effects of 0.04at.%Er on an Al-1.7at.%Cu alloy and found that the recrystallization temperature is increased and the dendrite structure is refined [47]. When added to Al-Li alloys, the strength is increased which is attributed to increased volume fraction and Al_3Li/Al_3Er composite precipitates [47]. When RE (La and Nd) are added to a rapidly solidified Al-Li-Cu-Mg alloy, the ductility is increased slightly, as evidenced by an increase in plastic elongation of up to 5% [48].

The creep properties of Al-RE alloys have also been investigated. In one study, however, it was found that Al-La and Al-Ce (with concentrations of 0.2-0.6at.%RE) alloys have a lower creep resistance than Al-1.3at.%Ni alloys [49]. It was noted, however, in this study that the coagulation of the intermetallic precipitates was limited due to the small diffusivities of rare earth elements in

Al. It is suggested in another study that rapidly solidified Al-RE alloys (RE = Ce, Er, Nd and Gd) would be good candidates for high temperature use due to the good corrosion resistance and high temperature stability of the precipitates up to 300°C [50].

1.6 High Temperature Properties

The creep properties of Al alloys have been studied for many different alloys. Pure Al has really low creep properties at 450˚C [51]. Studies have examined solid-solution strengthened alloys (eg. [52-54]), precipitation-strengthened alloys (e.g. [55-57]) and those which have additions of large ceramic particles [58-60].

The Al-Sc alloys in this thesis are coarse grained, with the average grain size on the order of several millimeters. According to the deformation mechanism maps, in the temperature and stress ranges examined in this thesis, the deformation will be controlled by dislocation climb [61]. Thus, a power-law equation for the steady state strain rate ($\dot{\varepsilon}$) is obtained, that is generally given by:

$$\dot{\varepsilon} = A_{ap}\sigma^{n_{ap}} \exp\left(\frac{-Q_{ap}}{RT}\right) \tag{1.1}$$

where A_{ap} is the Dorn constant, σ is the applied stress, n_{ap} is the apparent stress exponent, and Q_{ap} is the apparent matrix creep activation energy.

The presence of these precipitates leads to a threshold stress with very high values of n_{ap}, in excess of 10. The creep behavior of these precipitation-strengthened alloys can thus be described by the expression:

$$\dot{\varepsilon} = A(\sigma - \sigma_{th})^n \exp\left(-\frac{Q}{R_g T}\right); \quad (1.2)$$

where A is a constant, σ is the applied stress, σ_{th} is the threshold stress, n and Q are the matrix stress exponent and creep activation energy (usually equal to the activation energy for volume self-diffusion) and R_g is the universal gas constant.

A creep threshold stress in coarse-grained precipitation-strengthened alloys originates from the interaction of dislocations with precipitates, which are bypassed either by a shearing or a climb dislocation mechanism [62]. The operating mechanism can either be due to the stress required for detachment from the interface, or due to the increase of line length of the climbing dislocations. The first mechanism, the detachment stress, was used by Rösler and Arzt to explain the higher threshold stress values for completely incoherent particles, with and without an attractive interaction between the particle and the dislocation [63-66]. The latter mechanism is active in systems with coherent precipitates and was observed previously in Al-Zr-V alloys with $L1_2$ precipitates [67]. Similarly, climb-controlled threshold stresses were found in previous studies of Al-Sc [20, 27], Al-Mg-Sc [26] and Al-Sc-Zr [28] coarse-grained alloys.

Several models have been proposed which explain the presence of the threshold stress by the increase in line length. Brown and Shewfelt proposed a local climb mechanism, where the

dislocation line remains along the surface of the particle [68]. This model has been extended to general climb, where the dislocation line relaxes to a higher radius of curvature and thus does not follow the entire surface of the particle [69]. Furthermore, it has been extended to cooperative climb, where multiple particles are climbed over simultaneously by a given dislocation [70].

An alternate approach to the thermally activated detachment stress, is the threshold stress which arises from the creation of jogs. Without thermal activation, the climb step resulting from the jog can only occur if the work done during forward glide exceeds the energy of the jog pair (for climbing adjacent particles in opposite directions) creation [71]. The concept of jogs resulting in a threshold stress has also been examined by Mishra et al. [72], whose model was based on the climb and movement of grain boundary dislocations climb. At high temperatures where lattice diffusion dominates, the threshold stress is expected to be much lower and should be related to jog-jog interaction since the atoms from the jog core can then be removed directly into the lattice.

For the Al-Sc [20], Al-Sc-Zr [28] and Al-Mg-Sc [26] alloys, the threshold stress normalized by the Orowan stress was found to increase with precipitate size. This behavior is counter to that predicted by climb bypass models considering only the dislocation line length increase, where the normalized threshold stress is independent of precipitate radius. Marquis and Dunand modeled this effect by incorporating the elastic interactions between the climbing dislocations and the bypassed precipitate resulting from lattice parameter and stiffness mismatches between the precipitates and matrix [9]. This simplified model then predicts a normalized threshold stress increasing with precipitate radius, in semi-quantitative agreement with experimental data on Al-

Sc alloys [20, 28]. It is also predicted by this model that an increased mismatch between the coherent precipitates and the matrix will lead to an increase in the normalized threshold stress. This model was extended to an alloy with coherent precipitates and incoherent dispersoids to explain the increase in threshold stress due to the combination of these two populations [60].

2. Effects of Ti Additions on the Nanostructure and Creep Properties of Precipitation-Strengthened Al-Sc Alloys

2.1 Introduction

As discussed in the Introduction, Ti is of interest as a ternary alloying element since it has a low diffusivity in Al and hence could reduce the coarsening kinetics at high temperatures. In the present chapter, the temporal evolution of size and composition at elevated temperatures of nanosize $Al_3(Sc_{1-x}Ti_x)$ precipitates formed during aging of a dilute, hypoeutectic Al-Sc-Ti alloy is examined. The effect of these precipitates on hardness at ambient temperature and creep resistance at 300°C is measured, and compared with prior studies on coarse-grained, creep-resistant binary Al-Sc alloys [20, 21, 27], as well as ternary Al-Mg-Sc [26, 73] and Al-Sc-Zr alloys [2, 3, 28].

Three-dimensional atom-probe tomography, transmission electron microscopy and microhardness are used to investigate the temporal evolution of nanosize, coherent $Al_3(Sc_{1-x}Ti_x)$ precipitates ($L1_2$ structure) in a coarse-grained Al-0.06 at% Sc-0.06 at% Ti alloy aged between 300 and 450°C. The creep properties at 300°C are also examined.

2.2 Experimental Methods

An Al-0.060 at% Sc-0.059 at% Ti (Al-0.10 wt% Sc-0.10 wt% Ti) alloy was studied; referred to as Al-0.06Sc-0.06Ti in the remainder of this chapter. The composition was chosen to guarantee that this alloy was in the appropriate phase fields during homogenization and subsequent aging treatments, employing a calculated ternary phase diagram [74]. The alloy was produced by dilution casting, using Al-1.2 at% Sc (Ashurst Inc.) and Al-2.26 at% Ti (ALCOA) master alloys

with 99.99 at% pure Al (impurities: 22 ppm Fe and 38 ppm Si). The alloys were melted in an alumina crucible in a resistively-heated furnace at 750°C in air. After thoroughly stirring, the melt was cast into a graphite mold resting on a large copper platen. Homogenization was performed at 640°C for 24 h in air, after which the alloy was water-quenched to room temperature. Subsequent aging was performed in air at various temperatures between 300 and 450°C, and was terminated by water quenching.

Transmission electron microscope (TEM) foils were mechanically ground to a thickness of 200 μm and subsequently electropolished in a solution of 5 vol.% perchloric acid in methanol at -20°C, which was cooled in a bath of dry ice in methanol. Precipitate radii were determined from dark-field TEM micrographs. 3DAP tomograph sample blanks were produced by mechanically grinding material to a square cross-section of ca. 200x200 μm^2. The samples were then electropolished using a two-stage procedure. The initial polishing was performed using a solution of 10 vol.% perchloric acid in acetic acid. The final polishing was performed using a solution of 2 vol.% perchloric acid in butoxyethanol. Proximity histogram plots (proxigrams) [75] were calculated employing *ADAM* [76] using an isoconcentration surface of 9 at% Sc. This surface was chosen to correspond to the inflection point in the concentration curve. Three to four precipitates were analyzed for each aging time. The average precipitate and matrix concentrations were calculated by employing the fraction of total atoms in the relevant volume.

Vickers microhardness measurements were performed with a 200 g. weight at room temperature on samples ground to a 1 μm surface finish. Twenty measurements were recorded on each sample. Compression creep samples were machined into cylinders with an 8 mm diameter and a

16 mm length. Prior to testing, the samples were re-homogenized and aged to produce specimens with precipitates of specific radii, as measured by TEM, shown in Table 2.1. The samples were tested at 300°C after a soak at the test temperature for 2 h, to ensure a stable and uniform sample temperature. Tests were performed in a nickel-based superalloy compression cage with boron nitride lubricated platens to reduce the effects of friction. The platen displacement was measured using a linear variable differential transducer, which was connected to an extensometer. Increasing loads were applied to each sample and, for each load, sufficient time was allowed for a minimum strain rate to be established. Tests were terminated when the sample reached 5% strain.

2.3 Results

2.3.1 Microstructure and Hardness

Figure 2.1 shows the evolution of microhardness with aging time at 300°C for the Al-0.06 Sc-0.06 Ti alloy (all compositions are given in at% in what follows), which is typical of classical precipitation hardening behavior: (1) an incubation period; (2) under aging (precipitate formation stage); (3) peak aging; and (4) over-aging (due to coarsening). Comparison with data for the binary Al-0.06 Sc alloys (Fig. 2.2) demonstrates that the addition of 0.059 at% Ti produces only a relatively modest increase (~75 MPa) in the peak hardness at 300°C. By contrast, addition of 0.06 at% Sc (resulting in the binary Al-0.12 Sc alloy) increases the peak hardness by 300 MPa, demonstrating that Sc is significantly more effective than Ti at increasing strength, with the addition of a given atomic fraction, for the aging temperature of 300°C. Furthermore, it is

apparent that the addition of only 0.005 at% Zr increases the hardness by 220 MPa with respect to the binary Al-0.06 Sc alloy. Zirconium thus also appears to be a more efficient strengthener than Ti when aging at 300°C. Aging at slightly higher temperatures (310 and 320°C) reduces significantly, however, the peak hardness of Al-0.06 Sc-0.06 Ti (Fig. 2.1). Increasing the aging temperature even further to 330 and 350°C leads to a complete loss of hardening from the precipitates (Fig. 2.1), which is indicative of very rapid coarsening rates.

A high number density of $Al_3(Sc_{1-x}Ti_x)$ precipitates ($(3\pm2)\times10^{21}$ m^{-3}) is observed upon peak aging for 24 h at 300°C. The precipitates remain coherent in the temperature range 300-320°C, as ascertained by the presence, in two-beam bright-field TEM images, of Ashby-Brown strain contrast [77] typical of coherent precipitates, which is illustrated in Fig. 2.3 for a sample aged at 320°C for 24 h The coherency and nanometer scale of the precipitates is consistent with previous studies on Al-Sc binary alloys [19, 21, 22] and Al-Mg-Sc and Al-Sc-Zr ternary alloys [2]. Upon aging at 300°C for up to 64 days, the precipitates remain spheroidal, coherent and uniformly distributed in the matrix (Fig. 2.4a). The average radius of the precipitates, <R(t)>, increases slowly from a value of 5.1±0.4 nm after only 24 h to 7.9±0.7 nm after 64 days of aging, which is a 55% increase in <R(t)>.

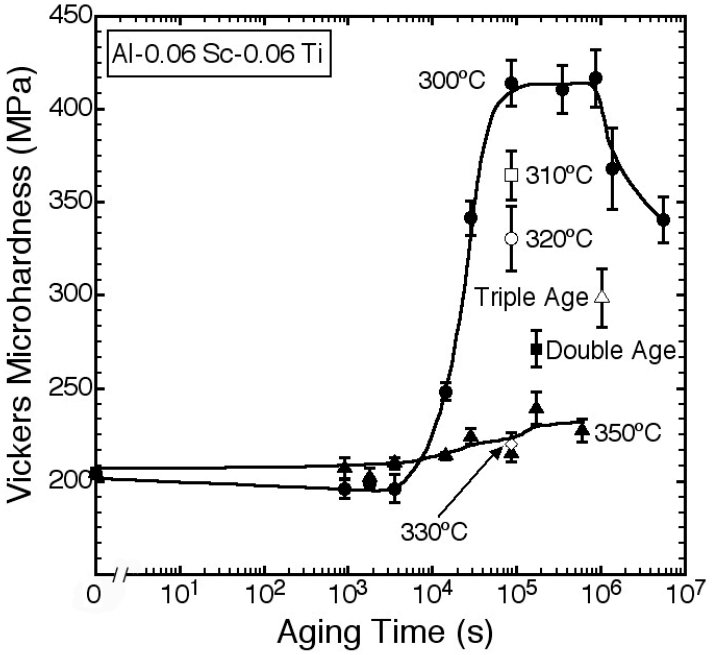

Figure 2.1: Microhardness of Al-0.06 Sc-0.06 Ti vs. aging time for temperatures between 300 and 450°C. The time for the samples aged at multiple temperatures is the sum of the aging times.

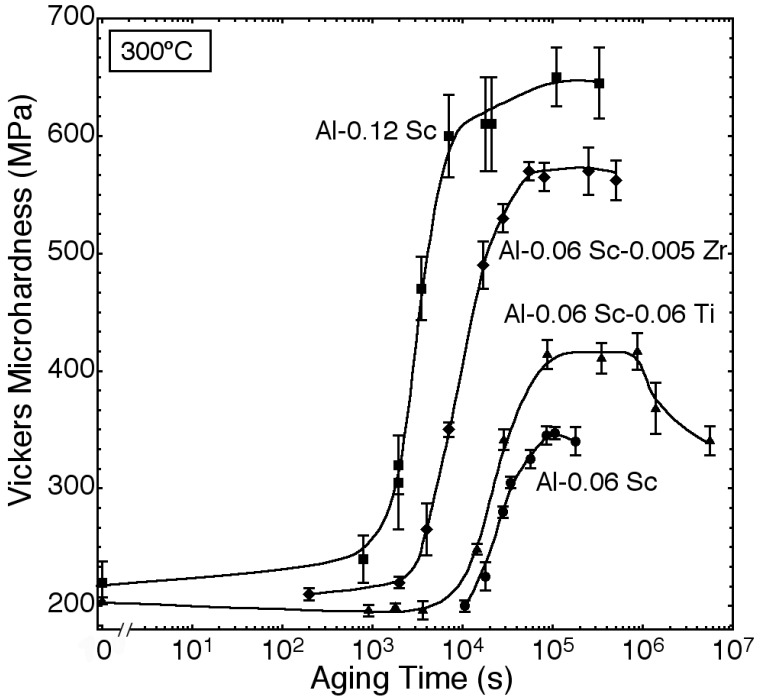

Figure 2.2: Microhardness *vs.* aging time at 300°C, comparing the present Al-Sc-Ti alloy with binary Al-Sc alloys [21, 26], and a ternary Al-Sc-Zr alloy [78].

The morphology of the precipitates changes significantly with small changes in aging temperature. When the aging temperature is raised by 20°C to 320°C, the precipitates are still distributed homogeneously in the matrix, but they are slightly non-spheroidal and exhibit lobes, which is a sign of growth instabilities (Fig. 2.4b) [79]. The approximate mean particle radius (calculated using an area equivalent radius) after a 24 h aging treatment at 320°C increases to 10.8±0.9 nm, more than double the value at 300°C. When the aging temperature is raised a mere 10°C, to 330°C, the precipitates nucleate predominately heterogeneously on dislocations (Fig. 2.4c) and exhibit highly non-spheroidal morphologies. The supersaturation decreases with increasing temperature and hence the thermodynamic driving force for nucleation decreases. Precipitation hardening is concomitantly reduced to near zero at and above this aging temperature (Fig. 2.1).

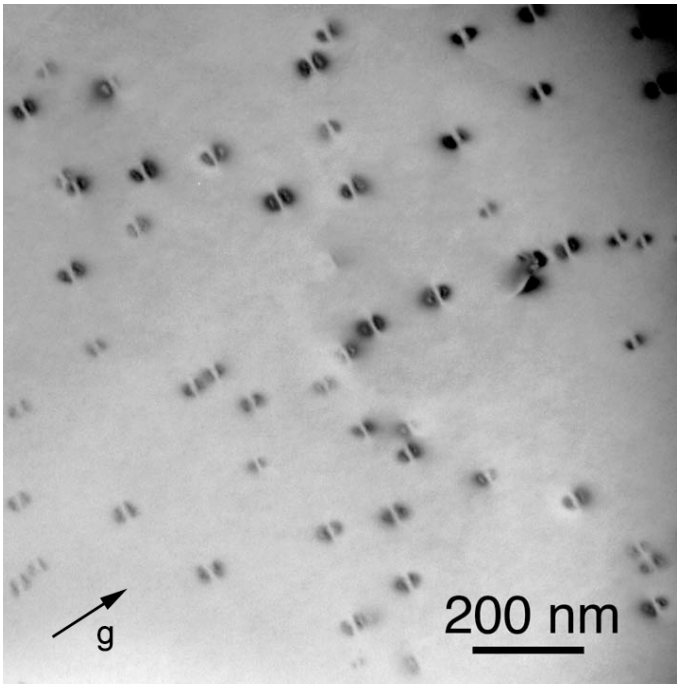

Figure 2.3: Two-beam bright-field TEM image showing coherent strain-field contrast around precipitates for Al-0.06 Sc-0.06 Ti aged at 320°C for 24 h., g = [200].

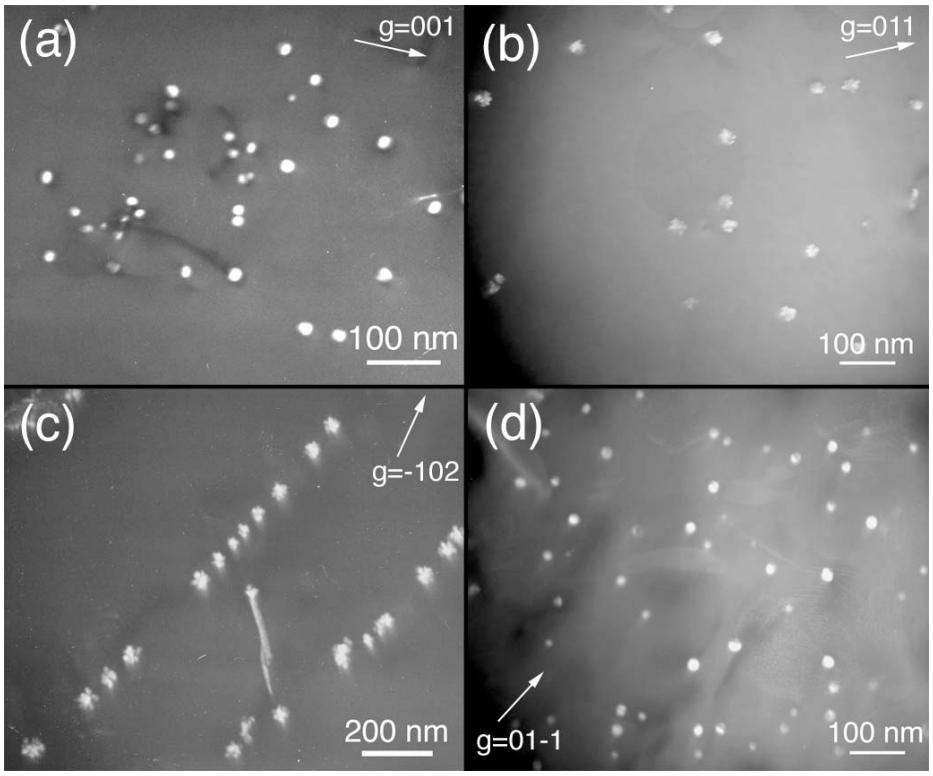

Figure 2.4: Dark-field TEM images of Al-0.06 Sc-0.06 Ti showing changes in precipitate radius, morphology, and distribution with aging treatment: (a) 300°C for 64 days, [110] projection; (b) 320°C for 1 day, [100] projection; (c) 330°C for 1 day, [211] projection; and (d) 300°C for 1 day, 400°C for 10 days, and 450°C for 2 days, [111] projection.

2.3.2 Coarsening Kinetics and Chemical Composition

Figure 2.5 displays the time dependence of the mean radius, <R(t)>, at 300°C for the present Al-0.06 Sc-0.06 Ti alloy and for a previously studied Al-0.06 Sc-0.005 Zr alloy [78]. The Lifshitz-Slyozov-Wagner (LSW) coarsening theory [80, 81] has been extended to multicomponent alloys by Umantsev and Olson [82], and analyzed in great detail for ternary alloys by Kuehmann and Voorhees, including capillary effects [83]. The time exponent for the evolution of <R(t)> of the

ternary alloys is predicted to be 1/3, the same as for the binary alloys, albeit with a different rate constant, K_{KV}, than the LSW model.

$$< R(t) >^3 - < R_0 >^3 = K_{KV}(t - t_o)\,; \tag{2.1}$$

where t is time.

The $Al_3(Sc_{1-x}Ti_x)$ precipitates were found to coarsen with time exponents smaller than predicted from Eq. (1), as shown in Fig. 2.5. Assuming the precipitates have reached the quasi-stationary-state coarsening regime after 24 h of aging, the time exponent is calculated, utilizing a multiple regression analysis to be 0.11. This is similar to the Al-0.06 Sc-0.005 Zr alloy, which also coarsens at a slower rate than predicted by the Kuehmann-Voorhees model. The ternary Al-Sc-Ti alloy coarsened at a slower rate than the binary Al-Sc alloy, which was demonstrated to coarsen with a time exponent of ca. 1/3 [21].

Coarsening resistance is even greater for samples having undergone double or triple aging treatments. Figure 2.4d exhibits the microstructure of a sample that was subjected to a triple aging treatment: first, aging was performed for 24 h at 300°C (peak hardness), with the goal of nucleating the precipitates homogeneously; second, aging was performed at 400°C for 10 days, and thirdly at 450°C for 48 h, in order to coarsen the precipitates. Despite these very high temperatures, <R(t)> remained relatively small at 10.0±0.8 nm (*i.e.*, similar to a single aging for 24 h at 320°C).

Samples aged for 1, 4, 16 or 64 days at 300°C were analyzed using 3DAP tomography. The three-dimensional reconstructions demonstrate that $Al_3(Sc_{1-x}Ti_x)$ precipitates with radii corresponding to those measured by TEM are present (Fig. 2.6). Proxigrams, displaying the concentration of each element as a function of radial distance from the 9 at% Sc iso-concentration surface, reveal that most of the Sc partitioned to the precipitates with little Sc remaining in the α-Al matrix. Figure 2.7 shows that compared to the matrix, there is an increase in Ti concentration in the precipitates, indicating that Ti also partitions to the precipitates during growth and coarsening and/or during the nucleation and growth stages. The average concentration of Ti in the precipitates continues to increase, albeit slowly, up to the longest aging time analyzed, 64 days.

The concentration of Ti in the precipitates varies with distance from the α-Al/$Al_3(Sc_{1-x}Ti_x)$ heterophase interface, Fig. 2.7. At the longer aging times (16 or 64 days), significant Ti segregation occurs at the α-Al/$Al_3(Sc_{1-x}Ti_x)$ heterophase interface, similar to results found for an Al-0.09 Sc-0.05 Zr alloy aged for 2,412 h at 300°C [3]**.** At the shorter aging times (24 or 96 h), no segregation of Ti to this interface is observed at 300°C, within experimental error.

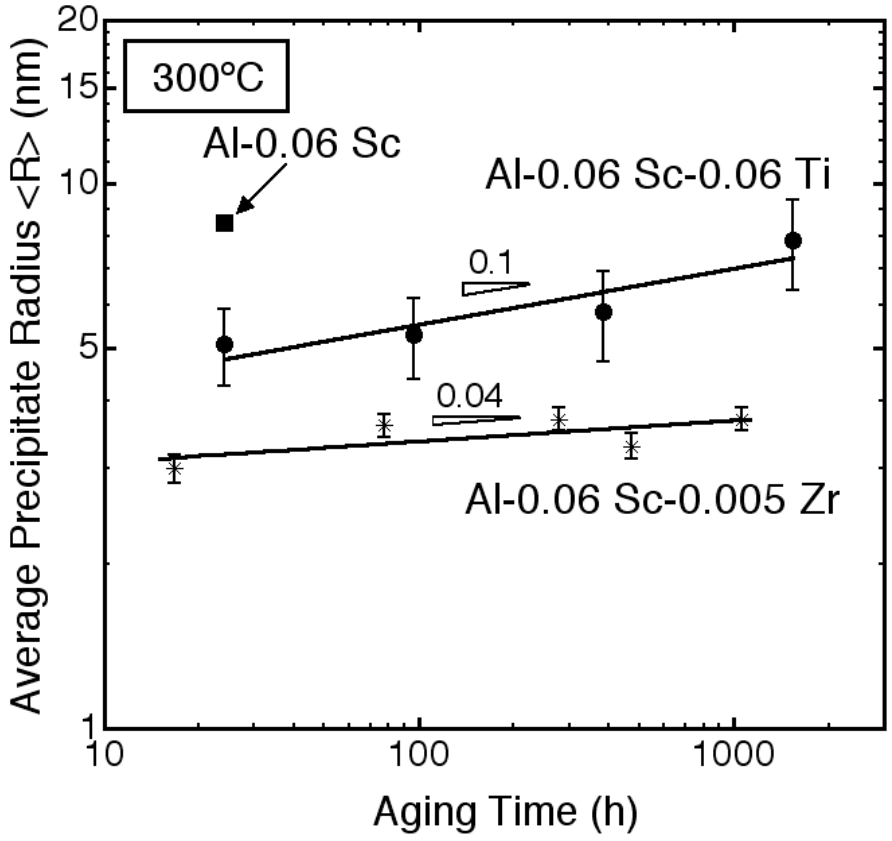

Figure 2.5: Double-logarithmic graph of mean precipitate radius, <R(t)>, for Al-0.06 Sc-0.06 Ti and Al-0.07 Sc-0.005 Zr [28] vs. aging time at 300°C. Both alloys coarsen at a lower rate than predicted by the Kuehmann-Voorhees model for ternary alloys, which predicts a slope of 1/3. One data point for Al-0.06 Sc [20] is also shown.

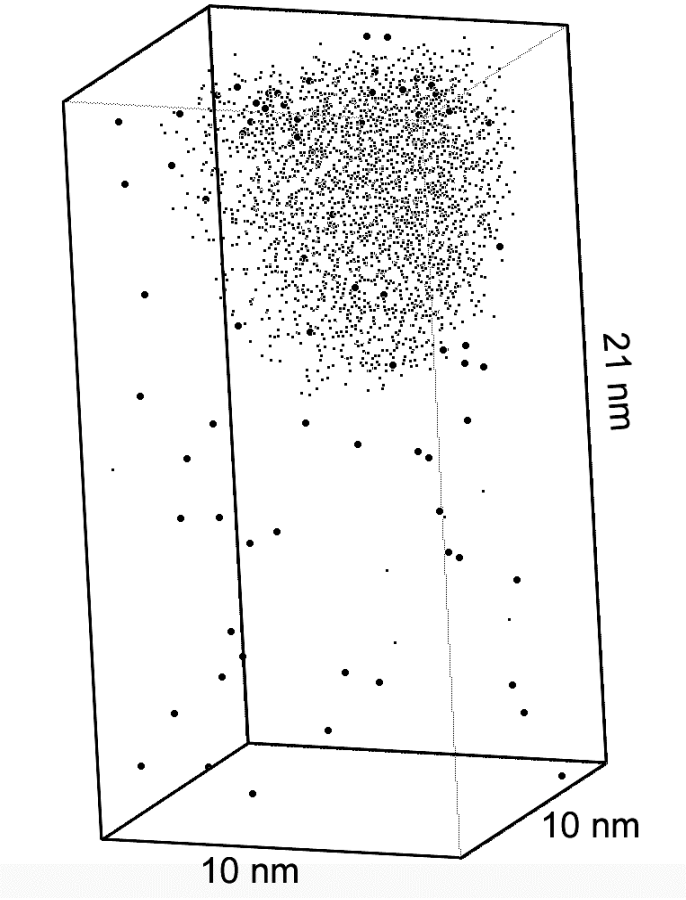

Figure 2.6: Three-dimensional reconstruction of a 10x10x21 nm box analyzed by 3DAP tomography in Al-0.06 Sc-0.06 Ti aged at 300°C for 96 h. The small dots represent Sc atoms (which are heavily partitioned to an $Al_3(Sc_{1-x}Ti_x)$ precipitate with $L1_2$ structure in the upper part of the volume) and the larger spheres represent Ti atoms. For the sake of clarity Al atoms are not included.

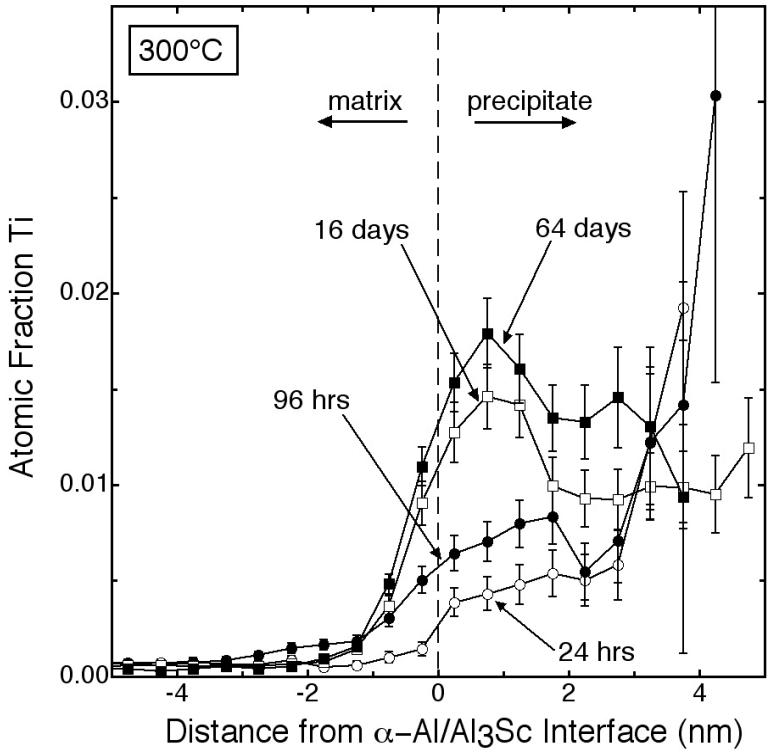

Figure 2.7: Proxigram showing the average concentration of Ti in Al-0.060 Sc-0.059 Ti for various aging times at 300°C vs. distance from the α-Al/Al_3Sc heterophase interface (x = 0), as defined by a 9 at.% Sc isoconcentration surface.

2.3.3 Creep Properties

Figure 2.8 shows the minimum creep rate at 300°C as a function of the applied compressive stress for four specimens with various precipitate radii (marked with asterisks in Table 2.1). It is apparent that the creep behavior at 300°C is characterized by high apparent stress exponents, 22-33, indicative of the presence of a threshold stress, σ_{th}, below which the creep rate, $\dot{\varepsilon}$, cannot be experimentally measured. The power-law creep equation is then modified as:

$$\dot{\varepsilon} = A(\sigma - \sigma_{th})^n \exp\left(-\frac{Q}{R_g T}\right); \qquad (2.2)$$

where A is the Dorn constant, σ is the applied stress, σ_{th} is the threshold stress, Q is the creep activation energy of Al, n is the stress exponent of Al, and R_g is the ideal gas constant.

Values for the threshold stresses were found according to Eq. 2, by plotting $\dot{\varepsilon}^{1/n}$ *vs.* σ [84] with n = 4.4, the stress exponent for pure Al [61]. For smaller precipitate radii, the threshold stresses, and thus the creep resistance, increase with increasing <R(t)> (from 16 MPa for the smallest <R(t)> of 5.8 nm to 19 MPa for <R(t)> equal to 10.8 nm). It then decreases to 16 MPa for the largest <R(t)> of 16.9 nm. Due to the high apparent stress exponent, a small relative increase of 3 MPa in threshold stress translates to a large difference in creep rate (in excess of a factor 10) at a given stress. A similar trend (increase followed by decrease of the threshold stresses with increasing <R(t)>) was also observed in binary Al-Sc [20], as well as in ternary Al-Mg-Sc [26], and Al-Sc-Zr alloys [28]. In these alloys, it is also noted that an increase in volume fraction increases the creep resistance.

Table 2.1: Effect of aging treatment (time and temperature) upon average precipitate radius <R(t)>, edge-to-edge inter-precipitate spacing, λ, calculated Orowan stress at 300°C, $\Delta\sigma_{or}$, and experimental threshold stress at 300°C, σ_{th}, for Al-0.06 Sc-0.06 Ti.

Aging Treatment	Radius (nm), <R(t)>	Edge-to-edge Inter-precipitate Spacing, λ (nm)	Orowan Stress $\Delta\sigma_{or}$ (MPa)	Threshold Stress (σ_{th}) (MPa)
24 h at 300°C	5.1±0.4	--	--	--
96 h at 300°C	5.3±0.4	--	--	--
16 day at 300°C	5.8±0.5*	141±12	74±5	16±0.2
64 day at 300°C	7.9±0.7	--	--	--
24 h at 310°C	7.4±0.7*	180±17	62±5	17±0.2
24 h at 320°C	10.8±0.9*	263±21	47±3	19±0.2
24 h at 300°C	16.9±0.8*	412±19	33±2	16±0.1
48 h at 425°C				
24 h at 300°C	10.0±0.8	--	--	--
10 day at 400°C				
48 h at 450°C				

* samples were creep-tested.

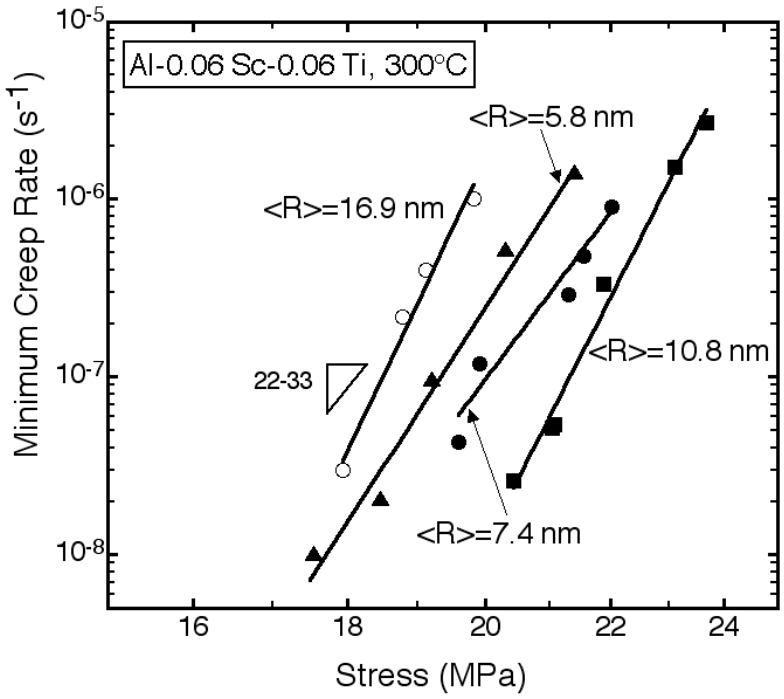

Figure 2.8: Double-logarithmic graph of minimum creep strain rate at 300°C vs. compressive stress for Al-0.06 Sc-0.06 Ti aged to produce various precipitate radii (given in graph). The stress exponent range is 22-33.

2.4 Discussion

2.4.1 Hardness at Ambient Temperature

The 3DAP tomographic results provide one explanation for the increased hardness of the present Al-0.06 Sc-0.06 Ti alloy, as compared to the binary Al-0.06 Sc alloy (Fig. 2.2). After peak aging (24 h), the average Ti concentration is much greater in the precipitates (0.50 at%) than in the matrix (0.069 at%) yielding a partitioning ratio of 7.2, defined as the concentration of Ti in the precipitates divided by the concentration of Ti in the matrix. At longer aging times, the concentration of Ti in the precipitates is even greater, with partitioning ratios of up to 40. The incorporation of Ti in the precipitates leads to an increased volume fraction of precipitates. The

volume fraction of precipitates is 0.24% after 64 days of aging if Sc but no Ti were to precipitate, as calculated from the matrix Sc concentration of 0.004 at% measured by 3DAP tomography. For this same aging treatment, the Ti concentration in the precipitates reaches 1.5 at%, which corresponds to a 6% relative increase in precipitate volume fraction, i.e. from 0.24 to .254 vol.%. For aging times longer than 250 hours, however, the alloy hardness decreases as precipitate coarsening more than compensates for the increase in volume fraction due to ongoing incorporation of Ti in the precipitates, Fig. 2.7.

The rapid decrease in peak-hardness with increasing aging temperature indicates that hardness is controlled by <R(t)> when all Sc has precipitated out of solution, rather than by a change of precipitate bypass mechanism from shearing to dislocation looping according to the Orowan mechanism, as in Al-Cu alloys. This hypothesis is tested by calculating the Orowan bypass stress σ_{or} from: [85]

$$\Delta\sigma_{or} = M\frac{0.4\mu b}{\pi\lambda}\frac{\ln(2\bar{r}/b)}{\sqrt{1-\nu}} \quad ; \tag{2.3}$$

where M = 3.06 is the orientation factor for aluminum [86], μ = 25.4 GPa is the shear modulus of aluminum, n = 0.345 is the Poisson ratio of aluminum, b = 0.286 nm is the magnitude of the Burgers vector in aluminum, and λ is the interprecipitate distance given by: [87]

$$\lambda = \left[\left(\frac{\pi}{\phi}\right)^{\frac{1}{2}} - 2\right]\bar{r} \quad ; \tag{2.4}$$

where ϕ is the volume fraction of precipitates, and $\bar{r} = \pi/4 < R(t) >$ [85].

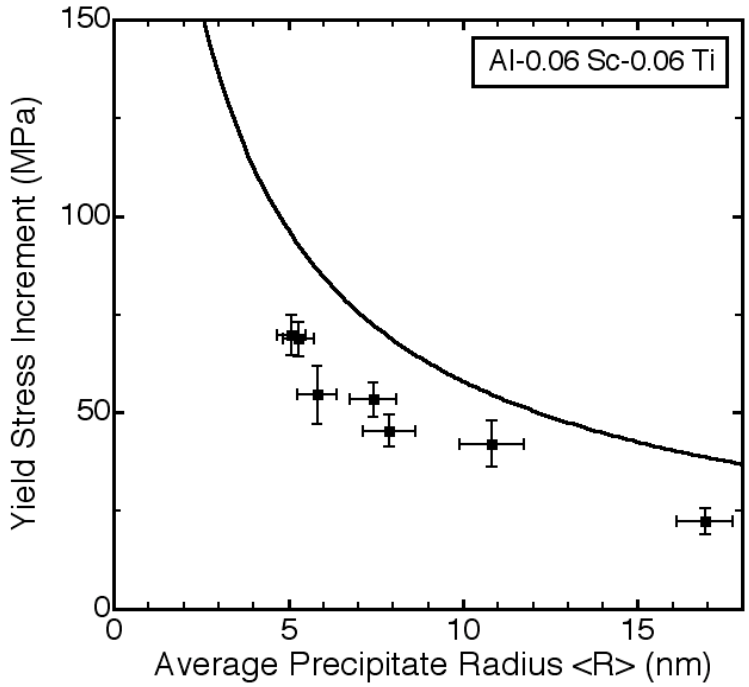

Figure 2.9: Yield stress increment (calculated from hardness measurements) vs. mean precipitate radius, <R(t)>, for Al-0.06 Sc-0.06 Ti. The solid line is calculated from Eq. 3 for the Orowan dislocation by-pass mechanism.

Figure 2.9 shows the effect of <R(t)> on the alloy yield stress increment (as compared to the value for the solutionized, unaged specimen), using a conversion factor of 3 between hardness and strength [88]. For the <R(t)> values measured for Al-0.06 Sc-0.06 Ti (<R(t)> equal to 5.1-16.9 nm), the experimental data are in general agreement with predictions from Eq. 2.3, assuming an Orowan dislocation looping mechanism. Calculations for the shearing mechanisms (using the same equations as in Ref. [28]) predict much higher stresses than those given by Eq. 2.3 over the <R(t)> range of interest, confirming that shearing is not operative. These conclusions are in agreement with prior results on Al-0.18 Sc [20] and several Al-Sc-Zr alloys [28], for which Orowan dislocation looping was the main strengthening mechanism for <R(t)> greater than ~2 nm. Furthermore, Miura [89] showed that for deformation at temperatures up to

250°C, the main mechanism was Orowan dislocation looping or dislocation climb in an Al-0.14 Sc alloy, for <R(t)> equal to 8 nm. Figure 2.9 thus demonstrates the importance of decreasing the coarsening rate of the precipitates by alloying with Ti or Zr, in order to maintain the highest possible strength at ambient temperature.

2.4.2 Precipitate Morphology

As the aging temperature is increased, the precipitate morphology changes from spheroidal at 300°C (Fig. 2.4a) to exhibiting lobes at 320°C (Fig. 2.4b), to being cauliflower-shaped at 330°C (Fig. 2.4c) and 350°C. A similar effect has been previously observed in Al-0.06 Sc alloys [21] aged at temperatures as low as 300°C, and in an Al-8.2 Li alloy aged between 285 and 305°C [90]. Doherty has described certain conditions under which small surface perturbations can become stable during bulk diffusion-controlled growth [79, 91]. One condition for dendritic growth is that the number density of precipitates must be sufficiently low that the precipitates can grow before their diffusion fields overlap. Thus, diffusion controls growth conditions rather than global equilibrium between the two phase fields. A second condition that promotes dendritic growth is the lack of rapid diffusion paths. Since the interfaces in both the Al-Li and Al-Sc-X alloys are coherent, rapid (short-circuit) diffusion along the interface is not anticipated. Also, since the precipitates are ordered, a more rapid diffusion in the precipitate, compared with the matrix is not expected, since in general diffusivities in ordered phases are smaller than in disordered solid-solutions [92]. Furthermore, the Al_3Sc phase exhibits a much higher melting temperature than the α-Al matrix (1320°C and 660°C, respectively), further increasing the diffusivity difference between these two phases with very different homologous temperatures.

2.4.3 Coarsening Kinetics

Equilibrium was not achieved in the present Al-Sc-Ti alloy, as illustrated by the fact that the concentration of Ti in the precipitates increases continuously to the longest aging time studied, 64 days (Fig 2.10). The average Sc/Ti (at%/at%) ratio in the precipitates decreases from 65 to 19 for the range of aging times studied, which is considerably greater than the achievable value of unity [29]. In the matrix, the Ti concentration decreases from 0.07 to 0.04 at% (Fig. 2.11) and has thus not yet reached the calculated equilibrium value of 0.01 at% [74].

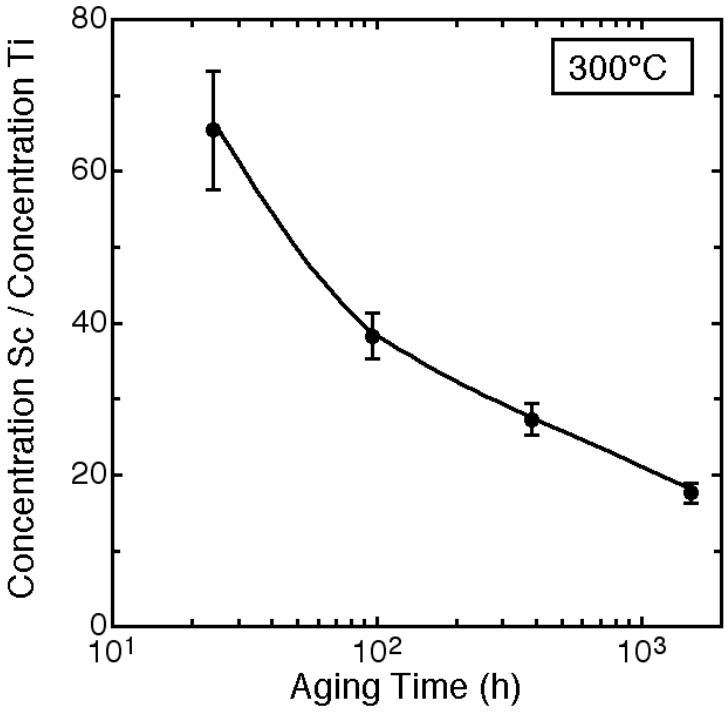

Figure 2.10: Ratio of the average concentration of Sc (at.%) to Ti (at.%) in precipitates in Al-0.06 Sc-0.06 Ti as measured by 3DAP tomography *vs.* aging time at 300°C.

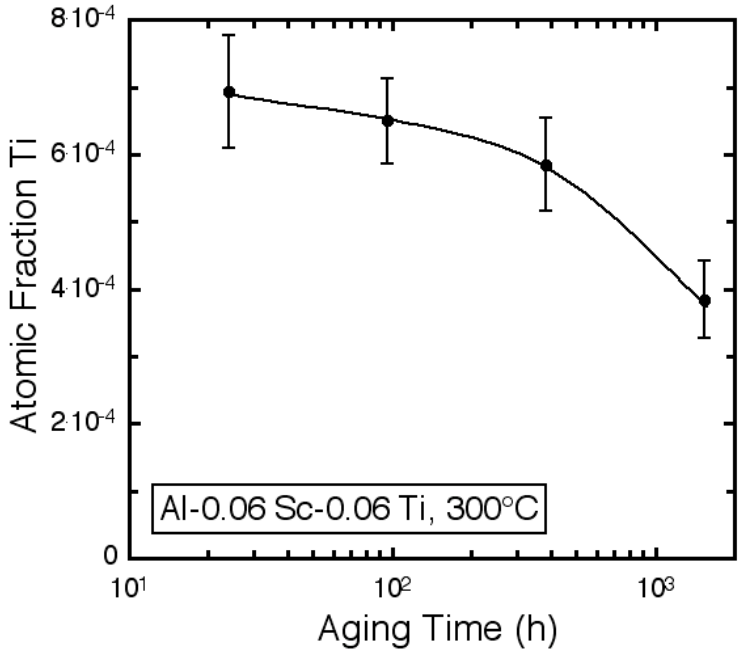

Figure 2.11: Ti matrix concentration in Al-0.06 Sc-0.06 Ti *vs*. aging time at 300°C.

It is apparent from Fig. 2.5 that Ti has the effect of retarding significantly the coarsening kinetics as compared to Al-0.06 Sc (e.g., the precipitates reach the same mean radius after aging for 1 day in the binary alloy and 64 days in the ternary alloy). This is in agreement with previous studies of Al-Sc-Zr alloys, where the addition of Zr also retards the coarsening kinetics [2], as illustrated in Fig. 2.5 for Al-0.06 Sc-0.005 Zr. As noted in Section 1, it was suggested by Fuller *et al.* [3] that Zr segregates at the heterophase interface, which may act as a barrier to diffusion. Titanium also reduces the coarsening kinetics, as indicated by the small values of the time exponents (0.11 for Ti and 0.04-0.05 for Zr, Fig. 2.5). One possible explanation for the lack of agreement with the Kuehmann-Voorhees coarsening model is that these systems have not yet entered the quasi-steady-state coarsening regime, since the compositions of both the matrix and precipitates are continuously changing significantly up to the longest aging times studied (Figs. 2.10 and 2.11). Thus, (dC/dt) is not approximately equal to zero, which is an assumption of the KV model for a

ternary alloy. Other possible reasons are that the KV model neglects the off-diagonal terms in the diffusion tensor and also assumes that the chemical potential of the vacancy is everywhere equal to zero.

The effect of the reduced coarsening rate is even more apparent in Al-0.06 Sc-0.06 Ti samples which have undergone double or triple aging, consisting of a first aging treatment at 300°C followed by one or two treatments at higher temperatures. In Fig. 2.4d, it can be seen that <R(t)> remains relatively small (10.0±1.6 nm), even after aging at a temperature of 450°C, resulting in the retention of hardness, Fig. 2.1. By contrast, aging for one day at 330°C leads to a complete loss of hardness, and thus much larger precipitate sizes, on the order of 50 nm across the non-spheroidal precipitates. It appears that once precipitates have nucleated, they are resistant to coarsening. It remains to be determined if the Ti concentration in the precipitates plays a significant role in this effect.

In the Al-Sc system the interface dominates the coarsening process since the parameter $L = \varepsilon^2 l C_{44}/\sigma^{\alpha/\beta}$ is *ca.* $5\text{x}10^{-2}$ (where $\varepsilon = 0.009$ is the constrained lattice parameter misfit, l = 5-10 nm is a characteristic length taken as the precipitate radius, C_{44} = 25.4 GPa [61] is an elastic constant of the matrix and $\sigma^{\alpha/\beta}$ = 160-185 mJ m^{-2} [93] is the interfacial energy), which is much less than the critical value of *ca.* 5, below which the coarsening rate is not significantly affected by the elastic stresses [94, 95]. Since the interfacial energy dominates, a change in the interfacial energy can have a considerable effect on decreasing the coarsening rate, as the coarsening rate constant contains the interfacial free energy in the numerator. The segregation of Ti to the interface thus

becomes important, as it can affect the heterophase interfacial energy. The Gibbsian excess of Ti relative to Al and Sc is [96]:

$$\Gamma_{Ti}^{Al,Sc} = \Gamma_{Ti} - \Gamma_{Sc}\left(\frac{C_{Al}^{\alpha}C_{Ti}^{\beta} - C_{Al}^{\beta}C_{Ti}^{\alpha}}{C_{Al}^{\alpha}C_{Sc}^{\beta} - C_{Al}^{\beta}C_{Sc}^{\alpha}}\right) - \Gamma_{Al}\left(\frac{C_{Ti}^{\alpha}C_{Sc}^{\beta} - C_{Ti}^{\beta}C_{Sc}^{\alpha}}{C_{Al}^{\alpha}C_{Sc}^{\beta} - C_{Al}^{\beta}C_{Sc}^{\alpha}}\right) \quad ; \qquad (2.5)$$

where Γ_m is the Gibbsian interfacial excess of element m and C_m^n is the equilibrium concentration of element m in phase n, where α and β are the matrix and precipitate phases, respectively (Γ_{Ti} is found to be much larger than the other two Γ_m terms in equation 5). Both Γ_m and C_m^n were obtained from the 3DAP tomography proxigrams.

Equation 5 yields a value of $\Gamma_{Ti}^{Al,Sc} = 0.60 \pm 0.38$ atoms nm^{-2} after aging for 1536 h. This is smaller than the Gibbsian excess of Zr relative to Al for an Al-0.09 Sc-0.05 Zr alloy, where $\Gamma_{Zr}^{Al,Sc}$ achieves a value of 1.23 ± 0.62 atoms nm^{-2} after aging for a shorter period (576 h) at the same temperature, 300°C [3]. This indicates that Ti segregates to a lesser degree than Zr, as expected since Ti is a slower diffuser, (D_{Zr}/D_{Ti}) = 23 at 300ºC [1, 97]). It could also indicate that more Zr is needed to produce a similar reduction in the lattice parameter misfit, since interfacial segregation could potentially lead to a reduction in the strain energy as the presence of additional Ti at the interface will reduce the lattice parameter mismatch.

At 300°C, the segregation of the Ti to the interface could result from the fact that Ti diffuses more slowly in the precipitate phase since it is an ordered intermetallic compound [92]. Hence, the coarsening of the precipitates may be interface-limited, since it diffuses to the precipitate through the matrix at a faster rate than it can be incorporated into the precipitate. Furthermore,

interfacial segregation is driven by the reduction in the heterophase interfacial free energy. According to the Gibbs adsorption isotherm for an ideal dilute solution (Eq. 6), after 64 days of aging the interfacial free energy is reduced by 3.0% for the {100} facets and by 2.6% for the facets, employing values of 160 mJ m^{-2} for {100} facets and 185 mJ m^{-2} for {111} facets [93]:

$$\Gamma_{Ti}^{Al,Sc} = -\frac{C_{Ti}}{kT}\left(\frac{\partial\sigma^{\alpha/\beta}}{\partial C_{Ti}}\right) \quad ; \tag{2.6}$$

where $\sigma^{\alpha/\beta}$ is the interfacial free energy, C_{Ti} is the concentration of Ti in the matrix and $\Gamma_{Ti}^{Al,Sc}$ is the relative Gibbsian interfacial excess of Ti with respect to Al and Sc.

Despite the similarly small values for the time exponent, the radii of the precipitates in the Al-0.06 Sc-0.06 Ti alloy are greater than the radii observed in the corresponding Zr-containing alloy, Al-0.06 Sc-0.005 Zr [2], for identical aging treatments, Fig. 2.5. One possible explanation for the differences in <R(t)> between the alloys is that the diffusivity of Ti in Al is even slower than that of Zr. Thus, the diffusivities of the Sc and Ti are so disparate (at 300°C, D_{Sc}/D_{Ti} = $3.3x10^5$ [1, 97]) that diffusion of Sc is unhindered by the presence of Ti, which remains mainly in solution until after the Al_3Sc precipitates have nucleated and commenced coarsening. In the case of Al-Sc-Zr, the ratio D_{Sc}/D_{Zr} (at 300°C, D_{Sc}/D_{Zr} = $1.4x10^4$ [97]) is smaller and thus the diffusivities of the Sc and Zr are perhaps close enough that Zr has an effect on the precipitates before they are able to grow to the radii observed in the Al-Sc-Ti system.

The presence of different radii in the two alloys can be used to explain the fact that Ti is not as effective a hardener (strengthener) at room temperature as Zr. Since Ti is not as effective at preventing the $Al_3(Sc_{1-x}Ti_x)$ precipitates from coarsening in the initial stages, the precipitates are

correspondingly larger for comparable alloy compositions and aging treatments, Fig. 2.5. Since the microhardness is dependent on radius and interprecipitate spacing of the precipitates, the Al-Sc-Zr alloy is correspondingly harder, as illustrated in Fig. 2.2.

2.4.4 Creep Properties

A threshold behavior was also found previously in similar coarse-grained Al-Sc [20, 27], Al-Mg-Sc [26] and Al-Sc-Zr [28] alloys with nanosize Al_3Sc ($L1_2$) precipitates. A similar behavior was also observed in Al-Zr-V alloys with $L1_2$ precipitates [67]. In these articles it is shown that the threshold stress originates from the interaction of dislocations with precipitates. The first possible mechanism, precipitate shearing, predicts threshold stress values much greater than measured experimentally, and can thus be discarded, similar to precipitate shearing at ambient temperature. The second possible mechanism, dislocation-bypass by climb of incoherent precipitates, predicts threshold values that are smaller than those measured and are independent of radius [63, 65]. This discrepancy was resolved by considering additional elastic interactions between the bypassing dislocations and the precipitates, whose origins are the lattice parameter and stiffness mismatches between coherent precipitates and matrix [9]. An important prediction of this modified climb model is that the threshold stress normalized by the Orowan stress should increase with increasing $<R(t)>$, whereas the original climb model predicts a small value (less than 0.05), which is independent of $<R(t)>$. Prior data on Al-Sc [20, 27], Al-Mg-Sc [26] and Al-Sc-Zr [28] alloys does indeed agree semi-quantitatively with these predictions.

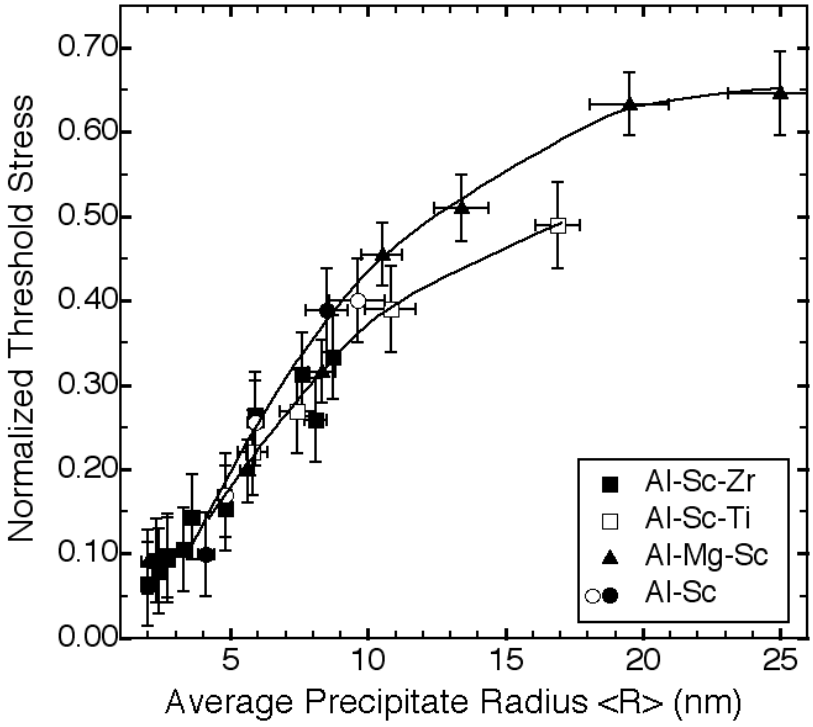

Figure 2.12: Measured creep threshold stress at 300°C normalized by calculated Orowan stress at 300°C vs. mean precipitate radius, <R(t)>, for Al-0.06 Sc-0.06 Ti and for binary Al-Sc alloys [20] and ternary Al-Sc-Zr alloys [28].

Plotting the threshold stress results for Al-0.06 Sc-0.06 Ti in a normalized threshold stress plot (Fig. 2.12), it is apparent that the general trend is very similar to that found for previously studied Al-Sc, Al-Mg-Sc and Al-Sc-Zr alloys, and in semi-quantitative agreement with model predictions [9]. The use of the normalized threshold stress removes the dependency on precipitate volume fraction, and thus allows for direct comparison of alloys with different volume fractions of precipitates. A slight decrease in normalized threshold stress is apparent for both Al-Sc-Zr and Al-Sc-Ti alloys, as compared to Al-Sc and Al-Mg-Sc alloys. This is expected qualitatively due to the reduced lattice parameters of $Al_3(Sc,Zr)$ and $Al_3(Sc,Ti)$ as compared to Al_3Sc, which leads to a reduction in lattice parameter mismatch between the precipitates and the

matrix. This effect results in a reduction of elastic interactions between lattice dislocations and the precipitates they bypass by climb, and a concomitant decrease in threshold stress. For a Ti precipitate concentration of 1.5 at% at 300°C, the lattice mismatch is reduced by a small amount, *i.e.,* from 1.10% to 1.08% [29, 98]. The difference between the binary and the ternary alloys is more apparent at larger radii since the elastic interaction volume of the precipitate scales with $<R(t)>^3$. The lack of a decrease in normalized threshold stress for the Al-Sc-Mg alloys may be due to the fact that Mg does not affect the near-threshold creep behavior.

In summary, the addition of Ti to binary Al-Sc alloys decreases slightly the creep resistance for given values of precipitate volume fraction and $<R(t)>$, as shown by the decreased normalized threshold stress values, Fig. 2.12. The coarsening resistance of the precipitates is, however, much improved, Fig. 2.5, so that the overall long-term creep resistance at 300°C is expected to be improved. The excellent coarsening resistance observed in the alloys subjected to triple coarsening may make long-term use of Al-Sc-Ti at ca. 350°C possible. At this temperature, binary Al-Sc alloys coarsen very rapidly [21] and are expected to exhibit almost no threshold stress. They therefore display very poor creep resistance at these temperatures. As compared to Al-Sc-Zr alloys, Al-Sc-Ti alloys have similar creep and coarsening properties. Although Ti is less expensive than Zr, the benefits of replacing Zr with Ti as a ternary alloying element in Al-Sc alloys are uncertain.

2.5 Conclusions

The nanostructure and mechanical properties of an Al-0.06 Sc-0.06 Ti alloy were examined at aging temperatures between 300 and 450°C for up to 64 days (1536 h), leading to the following conclusions:

- Spheroidal, coherent $Al_3(Sc_{1-x}Ti_x)$ precipitates with $L1_2$ structure are formed upon aging at 300°C, leading to peak hardness after 24 h, which is higher than for Al-0.6 Sc, but lower than for Al-0.12 Sc or Al-0.06 Sc-0.005 Zr. Increasing the aging temperature to 320°C reduces peak hardness and the precipitates exhibit lobes and cusps due to the smaller Ti supersaturation. At 330°C, precipitation occurs mostly heterogeneously on dislocations and precipitation hardening is lost.
- At 300°C, the precipitates coarsen at a significantly slower rate than observed in binary Al-Sc alloys or predicted by the Kuehmann-Voorhees coarsening model for a ternary alloy. This is due to incorporation of Ti in the precipitates, which also explains the increased hardness at ambient temperature as compared to the binary alloy. Titanium is, however, not as effective as Zr at reducing precipitate coarsening and hardening the Al-Sc alloy.
- At 300°C, Ti partitions to the $Al_3(Sc_{1-x}Ti_x)$ precipitates, although most of the Ti remains in solid-solution in the matrix ($x = 0.06$ for the longest aging time analyzed, 64 days). The concentration in the matrix and the precipitates continues to change up to the longest aging time analyzed, indicating that global thermodynamic equilibrium is not achieved. The much slower diffusion of Ti as compared to Sc most likely explains why precipitate coarsening occurs more slowly than in the binary Al-Sc alloy.

- For the specimens analyzed employing a 3DAP tomograph, after aging for longer periods at 300°C (16 or 64 days), Ti segregates to the α-Al/$Al_3(Sc_{1-x}Ti_x)$ heterophase interface, as reported previously for Zr in Al-Sc-Zr alloys. Segregation is not found for shorter aging times, 1 or 4 days.
- A creep threshold stress is found at 300°C, which when normalized by the Orowan stress, increases with increasing precipitate radius, <R(t)>, similarly to the previously studied alloys, Al-Sc, Al-Mg-Sc and Al-Sc-Zr. This is in semi-quantitative agreement with predictions from a model considering dislocation climb bypass including elastic interactions with the misfitting precipitates.

3. Precipitate Evolution and Creep Resistance of Al-0.06at.%Sc-0.06at.%Ti at Temperatures of 300-450˚C

3.1 Introduction

Prior studies on coarse-grained, creep-resistant binary Al-Sc alloys [20, 21, 27] as well as ternary Al-Mg-Sc [26, 73], Al-Sc-Zr [2, 3, 28] and Al-Sc-RE alloys [99-101] (RE = rare earth element) have shown that these alloys are creep resistant up to 300°C. The previous chapter showed that the coarsening resistance is significantly reduced with the addition of Ti. With Ti additions, the precipitates are expected to remain coarsening-resistant (thus imparting continued creep-resistance to the alloy) at temperatures significantly higher than 300°C [102]. The present chapter reports on the microstructure and creep properties of Al-0.06at.%Sc-0.06at.%Ti in the range of 300-450°C, corresponding to homologous temperatures of 0.61-0.77.

3.2 Experimental Procedures

The same Al-0.060at.%Sc-0.059at.%Ti (Al–0.10wt.%Sc–0.10wt.%Ti) alloy used in a previous creep study at 300°C [102] was used here (all compositions are in at.% in the remainder of this chapter unless otherwise noted). The micro-alloying composition was chosen to guarantee that each alloy was in the α-Al phase field during homogenization. Each alloy was produced by diluting small quantities of Al-1.2% Sc (Ashurst) and Al-2.26% Ti (Alcoa) master alloys in 99.99% pure Al. The alloy composition was verified by Luvak Inc. (Bolyston, MA) to be 0.060±0.003 %Sc and 0.059±0.003 %Ti. The alloy had an Fe impurity concentration of 0.0022±0.0001 %Fe and Si impurity concentration of 0.0038±0.0002 %Si. The alloys were

melted in an alumina crucible in a resistively-heated furnace at 750°C in air. After thorough stirring, the melt was cast into a graphite mold resting on a large copper platen to promote directional solidification. Homogenization was performed at 640°C for 72 h in air and terminated by water-quenching to room temperature. Aging was performed in air first at 300°C followed by water quenching and subsequent aging at 400°C and 450°C, on samples machined into cylinders with an 8 mm diameter and a 16 mm length. The samples to be creep tested at 300-400ºC were subjected to a double aging treatment consisting of 24 h at 300ºC followed by 120 h at 400ºC. Samples to be crept at the highest temperatures of 425-450ºC were triple-aged as follows: 24 h at 300ºC, 240 h at 400ºC and 48 h at 450ºC.

To ensure uniform temperature during creep testing, the samples were allowed to soak at the testing temperature for 2 h prior to loading. Tests were performed in a nickel-based superalloy compression cage and the sample ends were lubricated with boron nitride to reduce friction between the cage and the sample. The displacement was measured with a linear variable differential transducer connected to an extensometer. Sufficient time was allowed to reach a minimum strain-rate for each successively higher load applied to the sample. The creep experiments were terminated when a sample achieved a strain of 10 %. No sample was crept more than 10 days to ensure that the precipitates did not coarsen significantly during the test.

Vickers microhardness measurements were performed at room temperature using a 200 g load on aged samples that were mounted in acrylic and ground to a 1 μm surface finish. Ten measurements were performed on each sample.

Sample blanks for atomic probe tomography were produced by mechanically grinding material to a square cross-section of ca. 300x300 μm^2. An atomically sharp tip was then created by electropolishing. Initial polishing was performed using a solution of 10 vol.% perchloric acid in acetic acid. Final polishing was performed using a solution of 2 vol.% perchloric acid in butoxyethanol. Three dimensional local electrode atom probe (3-D LEAP) tomography was performed using a LEAP-3000 instrument (Imago Scientific Instruments, Madison, WI) [103] operated in voltage pulsing mode at a specimen temperature of 30 K, at a pulse frequency of 200 kHz, and a 20 % pulse fraction (pulse voltage divided by steady-state dc voltage). Proximity histogram plots (proxigrams [75]) were calculated employing the APEX [76] or IVAS (Imago Scientific Inst.) software programs, using an isoconcentration surface of 7 at.% Sc (corresponding to the inflection point in the concentration curve). The average precipitate composition was determined by counting the number of atoms in the precipitates with the interface set at the inflection point on the Sc concentration profile. A review of the development of the technique is given by Refs. [104, 105].

3.3 Experimental Results

3.3.1 Microstructure and Composition

The addition of Ti results in precipitates which are quite coarsening resistant and remain nano-size and spherical upon double and triple aging (Fig. 3.1). The samples are aged first at 300°C for 24 h to nucleate the precipitates at a temperature where there is a high supersaturation and hence a high number density of precipitates forms. Subsequently, they are aged at higher

temperatures (400°C for 120 h for the doubly aged sample and an additional 48 h at 450°C for the triply aged sample) to coarsen the precipitates at a temperature at least as high as the creep temperature. It was found previously that a single aging treatment performed above 330°C led to precipitates which were much larger and heterogeneously nucleated [102]. The doubly-aged samples, with a final aging treatment at 400ºC, exhibited an average precipitate radius of 8.3±2.9 nm, as measured by dark-field TEM. These precipitates were coherent with the matrix, as illustrated by the Ashby-Brown strain contrast visible in Fig. 3.2. The precipitate radius increased modestly to 10.0±0.8 nm for the triple-aging treatment, despite a much higher final aging treatment at 450ºC.

The concentration of Ti within the precipitates after double aging (24 h at 300ºC followed by 120 h at 400ºC) is measured to be 2.8±0.1 % Ti, with a clear segregation of Ti near the matrix interface (Fig. 3.1) where a maximum concentration of 5.8 % is found (Fig. 3.3). This corresponding to a relative Gibbsian interfacial excess of Ti atoms compared to Al and Sc atoms at the $Al/Al_3(Sc_{1-x},Ti_x)$ interface of 3.9 atoms/nm^3 (using the same procedure as in Ref. [102]). The matrix composition of Ti after the double aging treatment is 0.033±0.005 at.%, corresponding to about half of the original Ti content in the matrix (Fig. 3.4). By contrast, the Sc concentration in the matrix is only 0.0037±0.0005%, indicating that most of the Sc has partitioned to the precipitate phase.

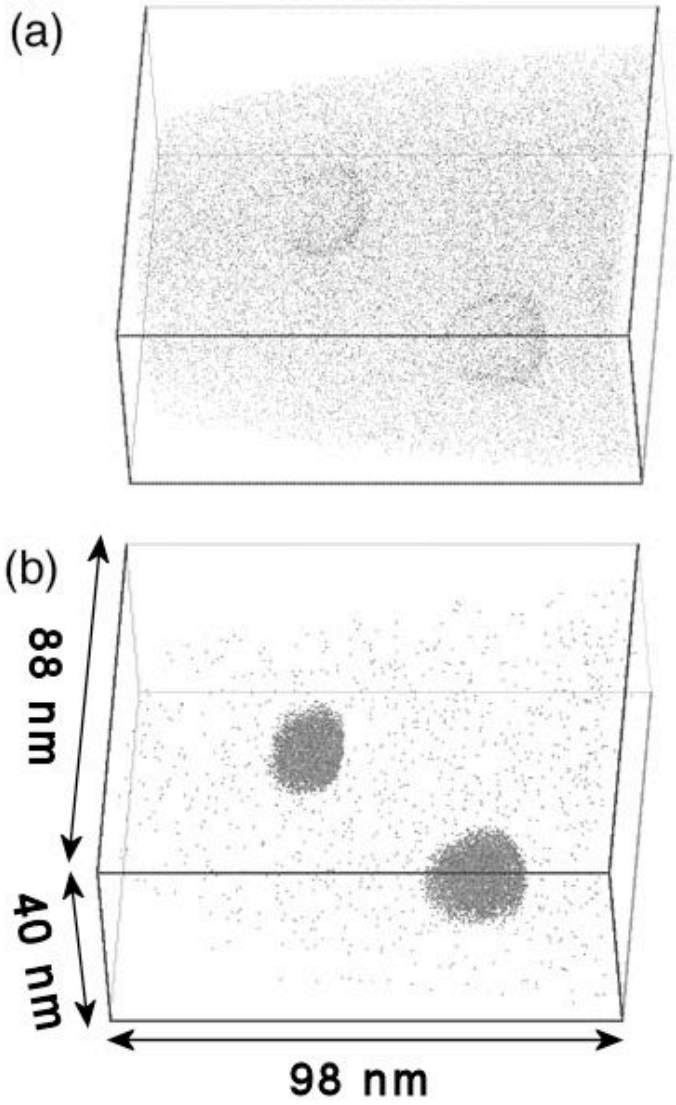

Figure 3.1: LEAP reconstruction showing two $Al_3(Sc_{1-x}Ti_x)$ precipitates in the α-Al matrix after double aging (24 h at 300˚C and 120 h at 400˚C). The data set contains 7.7 million atoms. (a) Ti atoms only shown, illustrating segregation to the interface. About half of Ti atoms are located in the matrix (matrix composition 0.033 at. %). (b) Sc atoms only shown, illustrating strong partitioning to the precipitate phase with very few Sc atoms in the matrix.

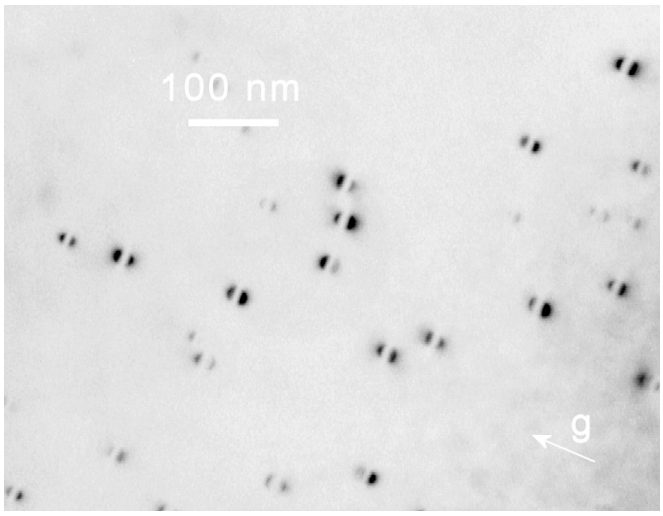

Figure 3.2: Two-beam bright field TEM image of Al-0.06Sc-0.06Ti after double aging (24 h at 300˚C and 120 h at 400˚C) showing $Al_3(Sc_{1-x}Ti_x)$ precipitates with Ashby-Brown strain contrast indicative of coherent precipitates.

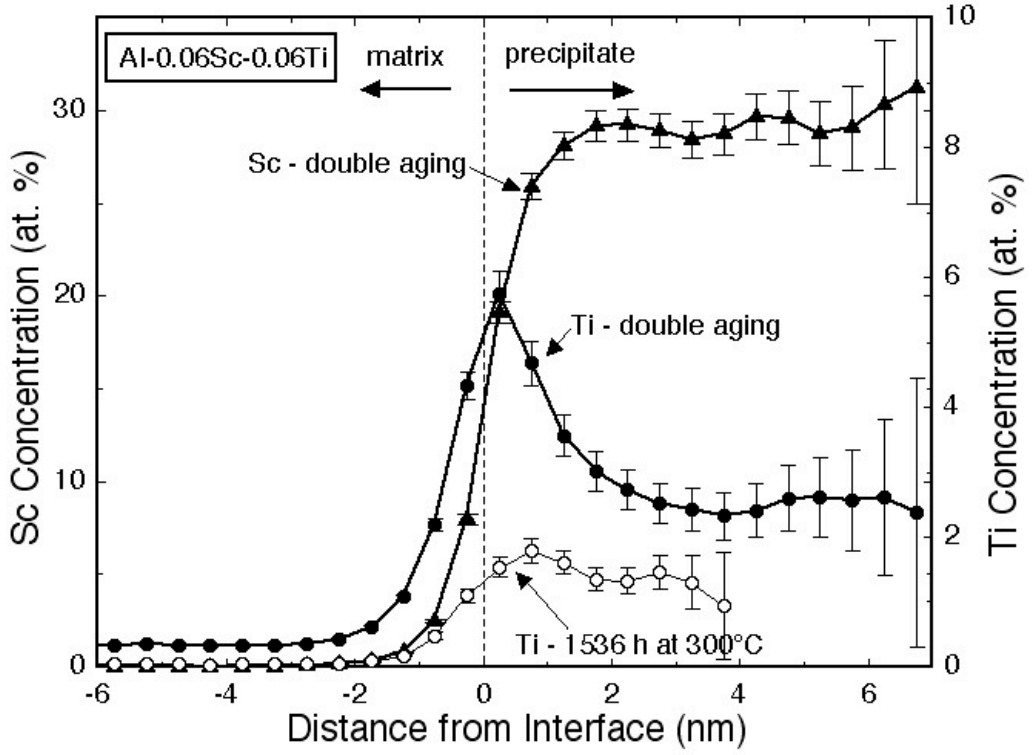

Figure 3.3: LEAP proxigram of $Al_3(Sc_{1-x}Ti_x)$ precipitates after double aging (24 h at 300˚C and 120 h at 400˚C). The dashed line indicates the interface between α-Al and $Al_3(Sc_{1-x}Ti_x)$ which shows a clear segregation of Ti to the interface. Also shown is a proxigram for the same alloy after single aging for 1536 h at 300ºC from Ref. [102], with a smaller Ti diffusion distance. Based on an isoconcentration surface of 9at.%Sc.

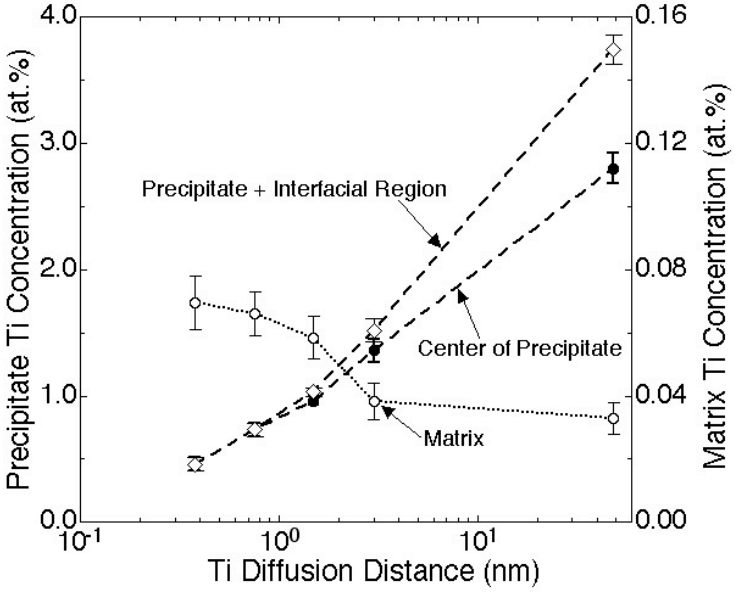

Figure 3.4: Ti concentration in $Al_3(Sc_{1-x}Ti_x)$ precipitates and the α-Al matrix as measured by LEAP vs. Ti diffusion distance. The data points with diffusion distances less than 4 nm are for samples aged at 300ºC for 24-1536 h (1-64 days) from Ref. [102]. The double aging (24 h at 300˚C and 120 h at 400˚C) used for the creep samples gives a much larger diffusion distance, due to the higher aging temperature of 400ºC.

3.3.2 Mechanical Properties at Room Temperature and Elevated Temperatures

The alloy microhardness measured previously for single-aging at 300ºC [102] and measured here for double and triple aging is plotted in Fig. 3.5 as a function of the total Ti diffusion distance $\Sigma(6D(T)\cdot t)^{1/2}$, where D(T) is the diffusion coefficient of Ti in Al at the aging temperature T (2.74×10^{-25} and 8.86×10^{-22} m^2s^{-1} at 300 and 400ºC [1]) and t is the corresponding aging time. It is apparent that the drop in microhardness between single aging at 300°C for 1536 h and the double aging at 300 and 400°C is only modest (about 20 MPa). Also, the precipitates in the double-aged specimens seem to remain stable after long-term creep at 300-400°C, even after doubling of the

Ti diffusion distance (creep at 400°C for 288 hours). Triple aging at 300, 400 and 450°C leads to a further small drop of 25 MPa in hardness as compared to the double aging treatment, and the specimen subsequently crept at 425ºC retains its microhardness within error, indicative of negligible precipitate coarsening at 425ºC (corresponding to a homologous temperature of $0.75T_m$). However, creep at 450ºC for 10 days leads to significant coarsening, as indicated by the complete loss of microhardness after the creep test (as homogenized hardness before precipitation is 210 MPa). Hence, creep results at 450ºC are not reported here.

The precipitate radii measured by LEAP for single aging at 300°C after 24 h (peak aging) and 1536 h, as well as after the double and triple aging treatments are shown in Fig. 3.6 are plotted as a function of microhardness stress increment (homogenized microhardness subtracted from microhardness value divided by 3). Also shown is the prediction from the theoretical Orowan stress increment, as given by:

$$\Delta\sigma_{or} = M\frac{0.4\mu b}{\pi\lambda}\frac{\ln\left(2\bar{r}/b\right)}{\sqrt{1-\nu}} \tag{3.1}$$

Where M=3.06 is the orientation factor for aluminum [86], μ=25.4 GPa [61] is the shear modulus of aluminum, ν = 0.345 is the Poisson ratio of aluminum, b=0.286 [61] is the magnitude of the Burgers vector, λ is the interprecipitate spacing and $\bar{r} = \pi/4 < R >$ is the mean planar radius [106]. Although there are slightly lower values for the microhardness stress increment, the general trend of decreasing values with increase in radius indicates that Orowan strengthening is the main operating mechanism at these radii at room temperature, in agreement with previous studies on several Al-Sc alloys [20], several Al-Sc-Zr alloys [28] and Al-0.06Sc-0.005RE (RE = Yb or Gd) [100].

Figure 3.7 presents the minimum creep strain rate as a function of applied compressive stress for double-aged samples tested in the range of 300 - 400°C and for a triple-aged sample tested at 425°C, which can be fitted to a power-law equation:

$$\dot{\varepsilon} = A_{ap}\sigma^{n_{ap}} \exp\left(\frac{-Q_{ap}}{RT}\right) \tag{3.2}$$

where Q_{ap} is the apparent activation energy, R is the universal gas constant, n_{ap} is the apparent stress exponent, and A_{ap} is a constant. The high value of the apparent stress exponent n_{ap} = 18-35 is indicative of the presence of a threshold stress, σ_{th}, below which creep is not measurable. The data can then be fitted to a modified power law exponent:

$$\dot{\varepsilon} = A(\sigma - \sigma_{th})^{n} \exp\left(-\frac{Q}{RT}\right) \tag{3.3}$$

where A, n= 4.4 [62] and Q are the Dorn constant, the stress exponent and activation energy for pure Al[61]. Values for the threshold stresses were found by plotting $\dot{\varepsilon}^{1/n}$ vs. σ and are marked in Figure 3.7 and listed in Table 3.1. Experimental uncertainties are calculated from the error in the fitting procedure.

Table 3.1: Threshold stress values with temperature for Al-0.06at.%Sc-0.06at.%Ti.

Temperature (˚C)	Threshold Stress (MPa)
300	16.6±2.4
350	15.0±3.7
375	11.4±2.4
400	10.2±2.8
425	6.7±1.7

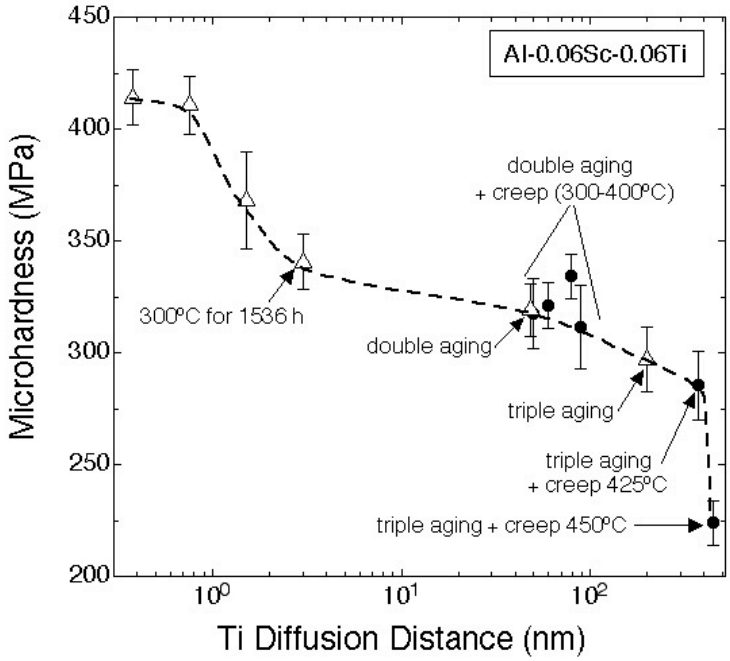

Figure 3.5: Vickers microhardness vs. Ti diffusion distance. Open symbols represent microhardness for samples before creep and after single aging at 300ºC [102], double aging (300+400°C) or triple aging (300+400+450°C). Solid symbols represent microhardness of aged samples after creep testing.

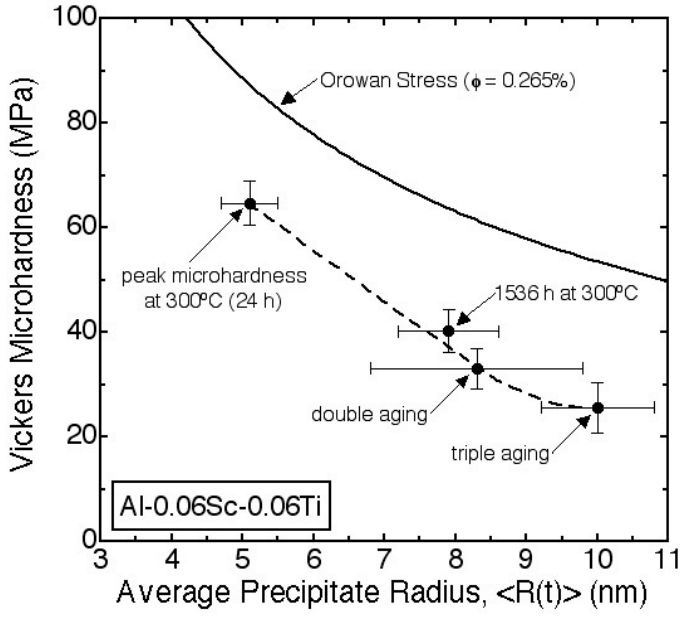

Figure 3.6: Vickers microhardness stress increment (homogenized microhardness subtracted from microhardness value divided by 3) *vs.* average $Al_3(Sc_{1-x}Ti_x)$ precipitate radius, <R(t)>, as determined by TEM for single aging at 300ºC [102], double aging (300+400°C) and triple aging (300+400+450°C).

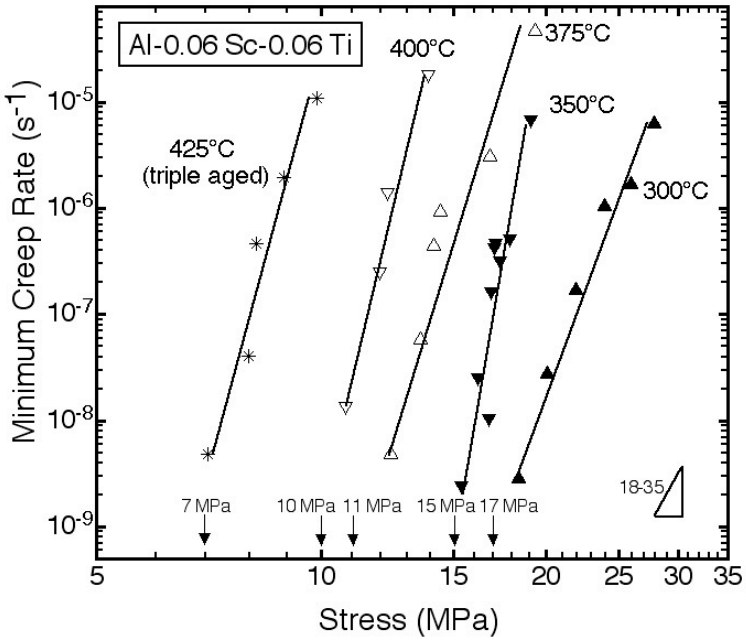

Figure 3.7: Minimum creep strain rate *vs.* compressive stress for double-aged (300+400ºC) samples tested at 300-400°C and a triple-aged (300+400+450 ºC) sample tested at 425°C.

3.4 Discussion

3.4.1 Microstructure and Composition

The low coarsening rates of the $Al_3(Sc_{1-x},Ti_x)$ precipitates shown in Figs. 3.5 and 3.6 at temperatures up to 450°C is linked to the very slow diffusion of Ti in the Al matrix [1]. The slow diffusion of Ti is also evidenced by the slow increase of Ti concentration in the precipitates with aging time and the concomitant slow decrease of Ti in the matrix (Fig. 3.4). Since diffusion is generally slower in the $L1_2$ precipitates as opposed to the FCC matrix, due to high correlation of diffusion, the Ti remains at the interface after it has diffused there.

With the creep temperatures approaching the aging temperatures, coarsening of the precipitates must be considered. In fact, it was recently observed in an Al-Mg-Li-Zr-Sc-Zn alloy that the Al_3(Sc,Zr) precipitates coarsen faster under stress [107]: there was still a $t^{1/3}$ dependence on the radius, but the coarsening constant was higher, when compared with specimens at the same temperature but under no load. Faster coarsening during creep was also found in a magnesium-based alloy [108].

In the present study of Al-Sc-Ti, the samples were found to retain their hardness after the creep experiment, up to temperatures of 425ºC, as shown in Fig. 3.5, indicating that coarsening was negligible and the creep tests valid, at least for the testing times used here. The exception is the sample crept at 450ºC which showed a large drop in microhardness indicative of a considerable increase in radius and/or loss of coherency.

The change in precipitate volume fraction with creep temperature must also be considered. The initial volume fraction for the samples undergoing the double aging treatment is 0.265±0.017%, The precipitate volume fraction can also be calculated from the overall composition by subtracting the solute content in the matrix after aging (found by LEAP tomographic measurements of the aged alloys) from the overall solute content in the as-homogenized state (also found by LEAP tomographic measurement), assuming that the amount of solute no longer in the matrix has formed the precipitate phase with the stoichiometric composition. Since the solubility of Sc in the matrix increases with temperature, the concentration of Sc in the matrix and hence the volume fraction could change during creep. There is, however, only a small increase in the Sc concentration in the matrix upon aging at higher temperatures. Upon aging at

400ºC for 120 h, the Sc concentration in the α-Al matrix is: 0.0037±0.0005%, as measured by LEAP tomography. In contrast, after extended (1536 h) aging at 300ºC, the Sc concentration in the matrix is 0.0016±0.0012%, corresponding to a volume fraction decrease of only 0.01%, upon aging at the higher temperature of 400ºC.

An additional factor affecting the volume fraction is that the Ti concentration in the precipitates has continued to increase slowly up to the double aging treatment. As shown in Fig. 3.4, beyond 1536 h of aging, the composition in the matrix continues to decrease, (0.04±0.006 at.% after 1536 h (64 days) of aging at 300ºC [102] compared with 0.033±0.005 at.% for the double aging treatment). The solubility of Ti, however, is not expected to be very low since Murray's calculation of the ternary phase diagram [74] gives 0.01% at 300ºC and 0.047% at 400ºC for the solubility of Ti in the matrix. Ab initio calculations by Liu and Asta [109, 110] of the binary Al-Ti system showed an even higher Ti solubility at 0.11at.% for metastable $L1_2$ Al_3Ti at 300ºC. These solubility values indicate that the volume fraction should not increase much further during creep since the Ti concentration in the matrix is not expected to decrease much further, due to the fact that the concentrations in the matrix are already below the calculated values. These solubility values also indicate that the presence of Sc reduces the Ti solubility in the matrix.

3.4.2 Creep Properties

3.4.2.1 Activation Energy for Creep

Equation 3.3 can be used to calculate the activation energy for creep, Q. By plotting $\dot{\varepsilon}$ vs. T^{-1} on a semi-logarithmic plot for constant effective applied stress (threshold stress subtracted from the

applied stress), Q is found to be 130±20 kJ/mol. Q was found to remain fairly constant (±1 kJ/mol) with effective applied stress. This activation energy can provide a clue as to the mechanism controlling the threshold stress. If dislocation climb over the precipitates were the operating mechanism, diffusion in the Al matrix would be the rate limiting mechanism. The activation energy for Al diffusion in the matrix is 142 kJ/mol [61], which is within the error range of the activation energy for creep measured presently. This suggests that climb of precipitates is the operating mechanism. Other mechanisms, such as precipitate shearing and the Orowan looping mechanism, can be excluded since the experimental threshold stresses are much lower than the ambient temperature yield stress determined from the hardness [102]. The activation energy found here is similar to that found for an Al-0.12at.%Sc alloy [20], and for higher temperatures in an Al-Cu-Mn-Cr-Zr-Fe alloy [57] where it was also concluded that dislocation climb was the operating mechanism.

3.4.2.2 Temperature Dependence of the Threshold Stress

The threshold stress decreases strongly with increasing temperature, as displayed in Table 3.1 and Figs. 3.7 and 3.8. Previous studies have also found a temperature dependence of the threshold stress [111, 112]. The temperature dependence of the threshold stress can be given by an equation of the form:

$$\frac{\sigma_0}{\mu} = B_0 \exp\left(\frac{Q_0}{RT}\right) \tag{3.4}$$

where Q_o is the activation energy associated with a precipitate overcoming an obstacle [57], although some authors remain uncertain as to its significance [113, 114]. In Eq. (3.4), the temperature dependent shear modulus is given as $\mu = \mu_o[(1-(T-300)/2)/T_m]$ where μ_o=25.4 GPa

and T_m=933 K [61]. The apparent activation energy, obtained from Eq. (3.4), is determined by plotting ln (σ_o/μ) vs. 1/T (Fig. 3.8). The value obtained is Q_0=20.4 kJ/mol. The threshold value at 425ºC was not used in this calculation, because it is much lower than the others and corresponds to a different pre-aging treatment.

Finally, the threshold stress is plotted in Fig. 3.9 normalized by the Orowan stress, which will account for differences in volume fraction. Data points with similar radii were chosen so that the data could be directly compared. The effect of the change in mismatch is clearly seen in Fig. 3.9.

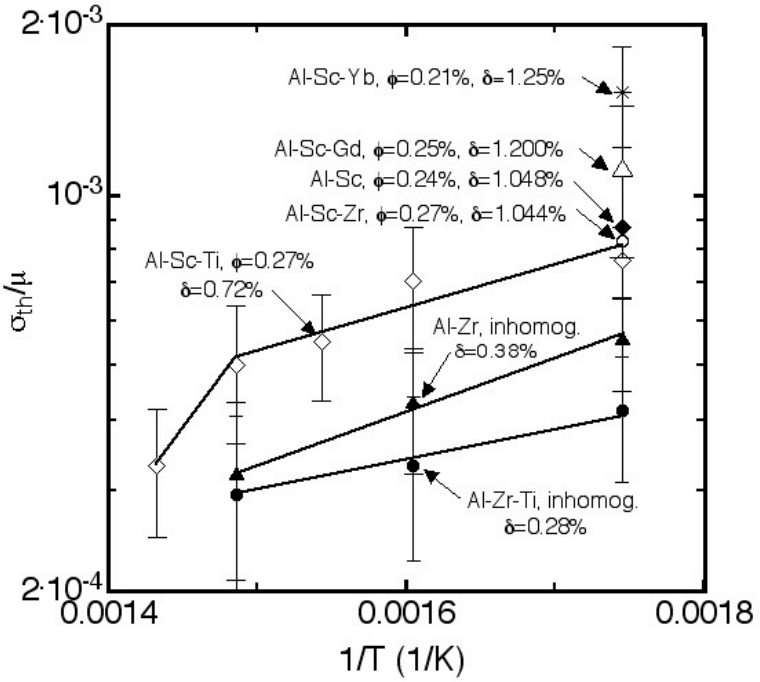

Figure 3.8: Arrhenius plot showing the threshold stress (normalized by the temperature-dependent shear modulus) vs. the inverse creep temperature for Al-0.06at.%Sc-0.06at.%Ti. Literature data for other coarse-grained, cast, precipitation-strengthened alloys are also shown: Al-0.06Sc [20], Al-0.1Zr and Al-0.1Zr-0.1Ti with inhomogenous precipitate distribution [115], Al-0.06Sc-0.005Zr [28], Al-0.06Sc-0.005Yb and Al-0.06Sc-0.005Gd [100]. Mismatch between precipitates and matrix, δ, are listed for 300˚C.

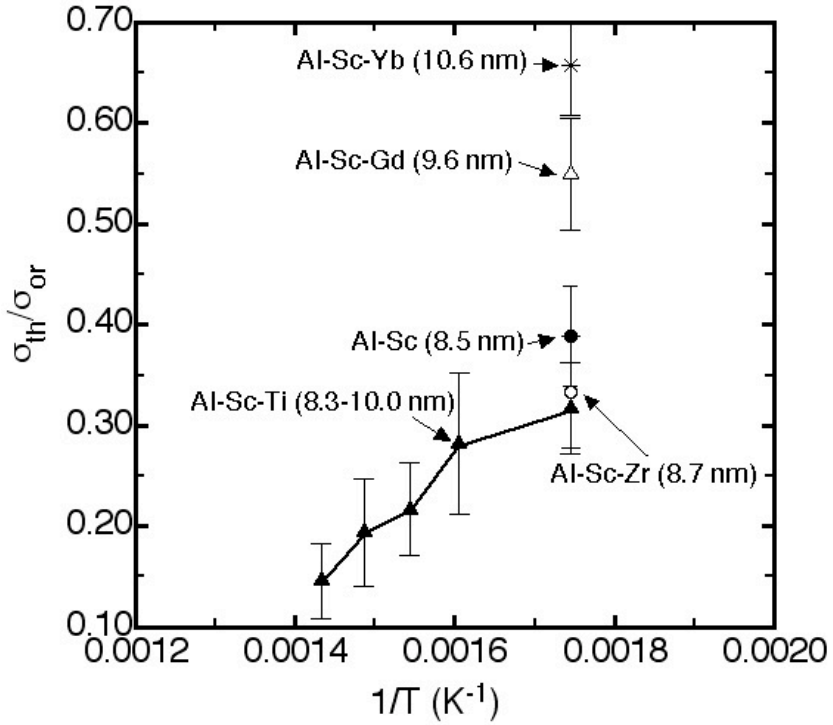

Figure 3.9: Threshold stress, σ_{th}, normalized by the Orowan stress, σ_{or}, vs. inverse creep temperature. The data points depicted all have similar radii, which allows for a direct comparison. Al-0.06Sc-0.06Ti is compared with Al-0.06Sc [20], Al-0.07Sc-0.02Zr [28], Al-0.06Sc-0.005Yb and Al-0.06Sc-0.005Gd [100].

Previous studies have found a similar dependence of the threshold stress on temperature. However, they described mechanisms involving incoherent processes including the detachment stress [55, 113, 116], impurities at the interface [117] or interfacial dislocations [118] – each of these mechanisms being sensitive to temperature. The above mechanisms apply to incoherent precipitates, unlike the coherent precipitates present in the Al-Sc-Ti alloy. Systems with coherent precipitates have also been examined, for example, a recent study examined the creep of an alloy with disordered, coherent precipitates in an intermetallic matrix [119]. The authors attributed the temperature dependence of the threshold stress to the stress needed to pull the dislocations through the precipitates or shear them. This mechanism is also not operable in the Al-Sc-Ti

alloy, since the precipitates are non-shearable. Thirdly, it was suggested by Kaibyshev [112] that the decrease in threshold stress with increasing temperature can be at least partially attributed to the decrease in volume fraction. However, in the Al-Sc-Ti system, there is only a small change in the volume fraction, as discussed in Section 4.1.

The mechanism for creep that is applicable in the present alloy is bypass of the impenetrable precipitates according to the general climb model [64, 69, 84, 120] which predicts a small threshold stress. If the precipitates exhibit a misfit with the matrix, as in the present case, the climb bypass mechanism can be made more difficult resulting in higher threshold stress values, as modeled in Ref. [9, 121]. Here, the stress field of the coherent mismatching precipitate interacts with that of the dislocation and it is predicted that precipitates with high mismatch lead to higher threshold stress values, and that the threshold stress increases with increasing precipitate radius. The effects of temperature were not directly addressed, but it is known that an increase in temperature should increase the kinetics of bypass as the diffusion of vacancies is increased. An increase in temperature will also reduce the mismatch which will also reduce the creep resistance: for example an increase in temperature from 300 to 425ºC changes the mismatch from δ=0.99% to δ=0.89% at 425ºC, due to the differences in coefficient of thermal expansion between the two phases.

For an Al-0.06at.%Sc (Al-Sc) alloy at 300˚C, the mismatch is 1.048% [122] ($\langle R(t)\rangle$=8.5±0.5nm, volume fraction 0.24% [20]). For the present Al-Sc-Ti alloy ($\langle R(t)\rangle$=8.3±2.9nm, volume fraction 0.254%), the mismatch at 300˚C is 0.99% [29]. Ignoring the small differences in precipitate volume fraction and radii, it is then predicted that the former alloy should have a

higher threshold stress than the latter one. This is indeed observed, with values of 19 MPa [29] and 16.6±2.4 MPa, respectively, as shown in Fig. 3.8. This figure also shows the threshold stress values for Al-0.06at.%Sc-0.005at.%Yb (Al-Sc-Yb) and Al-0.06at.%Sc-0.005at.%Gd (Al-Sc-Gd) alloys [100], are also higher that for the current Al-Sc-Ti, despite their smaller average precipitate radii (3.4 nm and 2.1 nm, respectively). The mismatches for these alloys were 1.25% and 1.20%, respectively, much higher than for the present Al-Sc-Ti (0.72%). The Al-Sc and Al-Sc-RE alloys, however, coarsen rapidly at 300˚C and higher temperatures, even upon double aging, rendering them ineffective for creep testing above that temperature.

Comparisons can, however, be made with several alloys with coarsening resistant precipitates. A recent study of Al-0.1at.%Zr (Al-Zr) and Al-0.1at.%Zr-0.1at.%Ti (Al-Zr-Ti) alloys [115] resulted in lower threshold stresses than the present Al-Sc-Ti alloy (Fig. 3.9). These Al-Zr and Al-Zr-Ti alloys, although they also have excellent resistance against coarsening of precipitates, exhibit even lower mismatches, (0.38% and 0.28% at 300˚C, respectively, assuming the same coefficient of thermal expansion as Al_3Sc), which is an important reason for their lower threshold stresses. Additionally, these Al-Zr and Al-Zr-Ti alloys show precipitate free-zones as a result of the peritectic solidification of the alloy [123]. More modeling is necessary to determine the effect of the precipitate free zones on the creep resistance.

Finally, a recent study on an Al-0.07 Sc-0.02 Zr alloy showed a higher normalized threshold stress than the Al-Sc-Ti alloy as expected from its higher mismatch (1.044 % at 300˚C) with $\langle R(t) \rangle$=7.5 nm [28]. All of the above mentioned alloys appear to validate the models for

threshold stress based on general climb bypass affected by the lattice parameter mismatch between matrix and particles.

3.5 Conclusions

Cast, coarse-grained aluminum micro-alloyed with 0.06 at.% of both Sc and Ti forms, upon multi-step aging treatments, $L1_2$ $Al_3(Sc_{1-x}Ti_x)$ precipitates which remain nanosize and coherent up to 450ºC. This exceptional stability and coarsening resistance is due to the very slow diffusivity of Ti in Al and to the replacement of Sc with Ti in the Al_3Sc precipitates, which increases with aging time and temperature, especially at the interface with the matrix where Ti segregates.

These coarsening-resistant, coherent $Al_3(Sc_{1-x}Ti_x)$ precipitates interact with matrix dislocations, thus providing creep resistance to this alloy in the temperature range of 300-425ºC as expressed by a threshold stress decreasing from 17 to 7 MPa over this temperature range. The slight reduction of mismatch between precipitates and matrix due to the substitution of Sc with Ti results in slight reduction of the threshold stresses as compared to binary Al-Sc alloy with the same precipitate fraction and radii. However, Ti-free precipitates in such binary alloys coarsen rapidly above 300°C, rendering the alloys unsuitable for creep applications, unlike the present ternary alloy whose slow-coarsening $Al_3(Sc_{1-x}Ti_x)$ provide creep resistance up to 425º (i.e., an homologous temperature of 0.75).

4. Microstructure and Diffusion Properties of Binary Al-Yb Alloys

4.1 Introduction

As discussed in the introduction chapter, the heaviest lanthanide elements (Er-Lu) are of interest since they form Al_3RE with stable $L1_2$ structures in Al [7, 8]. Hence, they can substitute 100% on the Sc sublattice in the $Al_3(Sc_{1-y}X_y)$ phase, presumably allowing for a higher volume fraction and replacement of the more expensive Sc with RE. It is known that these elements increase the lattice parameter of the $L1_2$ phase, with the mismatch with Al reaching a maximum of 4.1% (the Al_3Er phase has the highest mismatch) [4, 5, 8]. Due to the increased mismatch, it is thought that addition of these elements could improve the creep resistance of Al-Sc alloys [9]. Yb is chosen here as the element to study, in part because of the lower cost of Yb with respect to Tm and Lu. In a parallel study, Karnesky et. al. are examining Er additions to Al and Al-Sc [99].

In this chapter, the precipitation kinetics of a binary Al-0.03at.%Yb alloy, without the presence of Sc, is studied. The Al-Yb phase diagram, with a eutectic point at ~4at.%Yb, has not been precisely determined in the literature [124]. The maximum solid-solubility of Yb in Al is one quantity that remains unknown. Hence a measurement of the maximum solid-solubility by LEAP tomography is made. A calculation of the diffusivity of Yb in Al, based on the supersaturation of Yb in the matrix and the evolution of $\langle R(t) \rangle$, is also made. These properties are important to determine the effects Yb will have as an addition to Al-Sc alloys.

4.2 Experimental Procedures

The composition of the alloy examined is Al-0.027±0.005 at.%Yb (verified by ATI Wah Chang (Albany, OR)) (hereafter referred to as Al-0.03Yb). An alloy richer in Yb (Al-

0.060±0.001at.%Yb) was also examined. An Al-0.3at.% Yb master alloy was produced by arc-melting 99.9% pure Yb (Stanford Materials) with 99.999% pure Al (<1 ppm of Fe or Si). Casting was performed in air from the Al-0.3at.% Yb master alloy and 99.999% pure Al into a graphite mold. The cast alloys were homogenized for 72 h at 625˚C (the eutectic temperature of Al-Yb [124]) and water quenched to room temperature. The alloys were immediately aged isochronally in 25˚C increments for 1 h at each temperature in air, starting at room temperature (25˚C). Subsequent isothermal aging was performed at 300˚C. The TEM and LEAP procedures are identical to those described in Chapter 3. The precipitate radii were measured both by LEAP and TEM.

4.3 Results

4.3.1 Solid-solubility of Yb in Al

In order to determine the maximum solid-solubility of Yb in Al, a homogenized sample from an Al-0.06at.%Yb alloy was examined. The composition of this alloy had exceeded the maximum solid-solubility, since large Yb-rich precipitates (on the order of 1 μm) are visible in the SEM in the homogenized state. The Yb concentration remaining in the matrix upon homogenization in this sample was determined by LEAP tomography to be 248±7 at. ppm. The maximum solubility at 625°C of the alloy is thus quite low (assuming the quenching procedure maintains the maximum amount of Yb in the matrix.). It is an order of magnitude lower than the value of 0.2at.% suggested by [124].

Thus, a composition of Al-0.03at.%Yb (300 at. ppm Yb) was chosen for the subsequent microstructural evolution study so that the maximum volume fraction of Al_3Yb could be obtained and also because most of the solute in the alloy would remain in the matrix upon homogenization and quenching.

4.3.2 Microhardness and Conductivity

The microhardness and conductivity were examined for the Al-0.03Yb alloy. The motivation for isochronally aging from low to high temperature is to promote homogeneous nucleation. The supersaturation of Yb in the matrix is expected to decrease with temperature, hence the driving force for precipitation will be greater at lower temperatures. Aging at lower temperatures could thus promote homogeneous nucleation, since the nucleation barrier for homogeneous nucleation is higher than heterogeneous nucleation on a dislocation. This same effect is observed in the Al-Sc-Ti alloy discussed in this thesis: the alloy precipitates with no evidence of heterogeneous precipitation at 300˚C, however, when the temperature is raised to 330˚C, extensive heterogeneous nucleation is observed.

The microhardness was measured after aging at each 25˚C interval. The microhardness shows a maximum at 250˚C (Fig. 4.1). A decrease in microhardness at higher temperatures is observed, an indication that the precipitates have reached the growth and coarsening regime at temperatures higher than 250˚C. The microhardness was also measured upon aging in 50˚C increments for 2 h. A similar trend is observed, although there is consistently a slightly lower microhardness value. The maximum value occurs at a slightly lower temperature of 200˚C. These differences are not unexpected since after aging at a given temperature the total diffusion

distance for the 50˚C increment aging treatment is higher. Also shown in Fig. 4.1 is the Al-0.12 at.%Sc alloy aged isochronally in 25˚C increments for 1 h. Despite the much higher value of ϕ, this alloy shows no significant increase in microhardness until 250˚C.

Fig. 4.2 shows the percentage of Yb which has precipitated into the Al_3Yb precipitate phase for the isochronal aging of 25˚C increments for 1 h. This was determined from the conductivity measurements, assuming that the value 25˚C corresponded to 0% precipitation and the value at 375˚C corresponded to 100% of the precipitation. As the aging temperature is increased, the percentage of Yb precipitated continues to increase, and is approaching a plateau at 375˚C.

After aging isochronally up to 300˚C in 25˚C increments for 1 hr, the alloy was aged at 300˚C for various times to determine the coarsening kinetics at this temperature. Fig. 4.3 shows the microhardness as a function of aging time. A decrease in microhardness with aging at this temperature is observed.

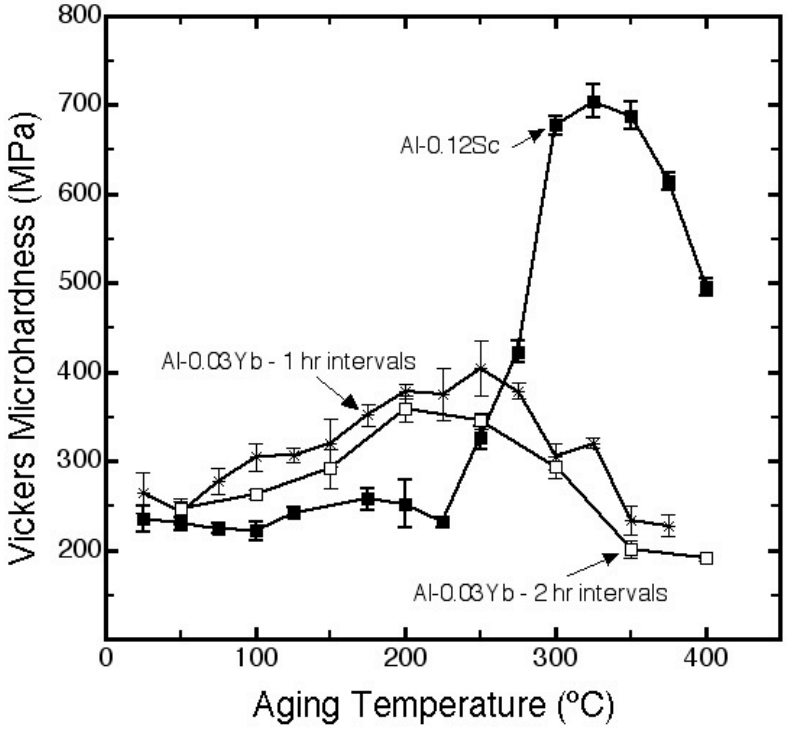

Figure 4.1: Isochronal microhardness vs. aging time at 300˚C for Al-0.03at.%Yb and Al-0.12at.%Sc. 1 h intervals were aged in 25˚C steps. 2 h intervals were aged in 50˚C steps.

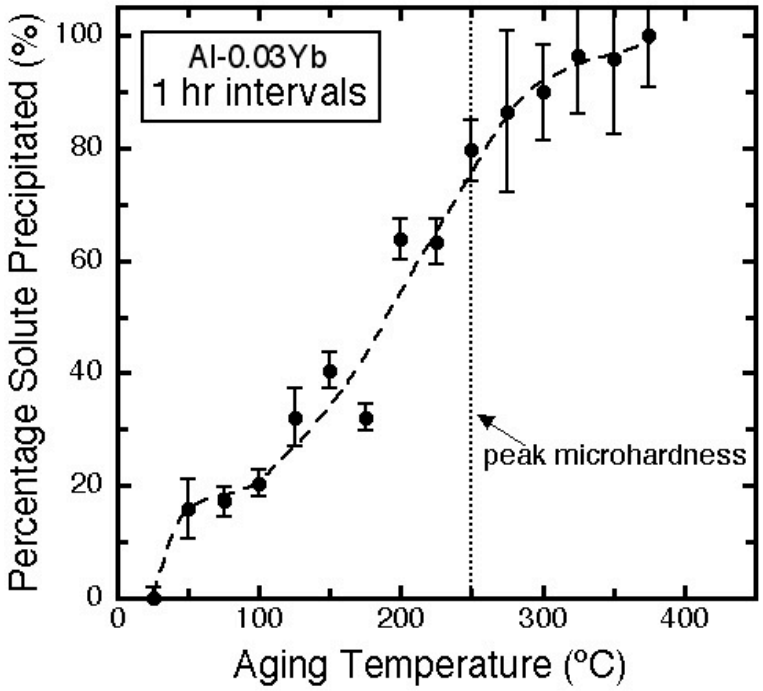

Figure 4.2: Percentage of Yb precipitated (based on conductivity data) vs. maximum aging temperature for isochronal aging in 25˚C increments for 1 h.

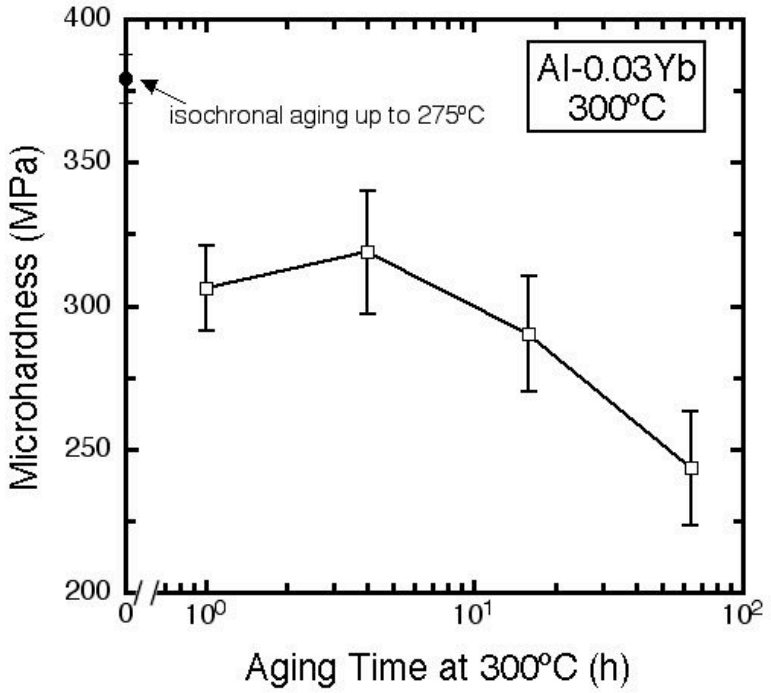

Figure 4.3: Vickers microhardness vs. aging time at 300˚C for Al-0.03Yb. Before the aging treatment at 300˚C, these samples had been isochronally aged up to 275˚C in 25˚C increments for 1 h at each temperature.

4.3.3 Heterogeneous Nucleation

It is seen in Fig. 4.4 that the precipitation is heterogeneous after the isochronal aging treatments and subsequent aging at 300˚C. After 1 h of aging at 300˚C, Al_3Yb precipitates can be observed which have heterogeneously nucleated along dislocations. These precipitates have larger radii than the precipitates away from the dislocations. Around the dislocation, precipitate-free zones are also visible. After 64 h of aging at 300˚C (Fig. 4.5), the precipitates along the dislocations have coarsened significantly. Furthermore, within the region which initially appeared homogeneous, there are now precipitates which appear to be coarsening along dislocations. This leaves few regions which contain entirely homogeneous precipitates.

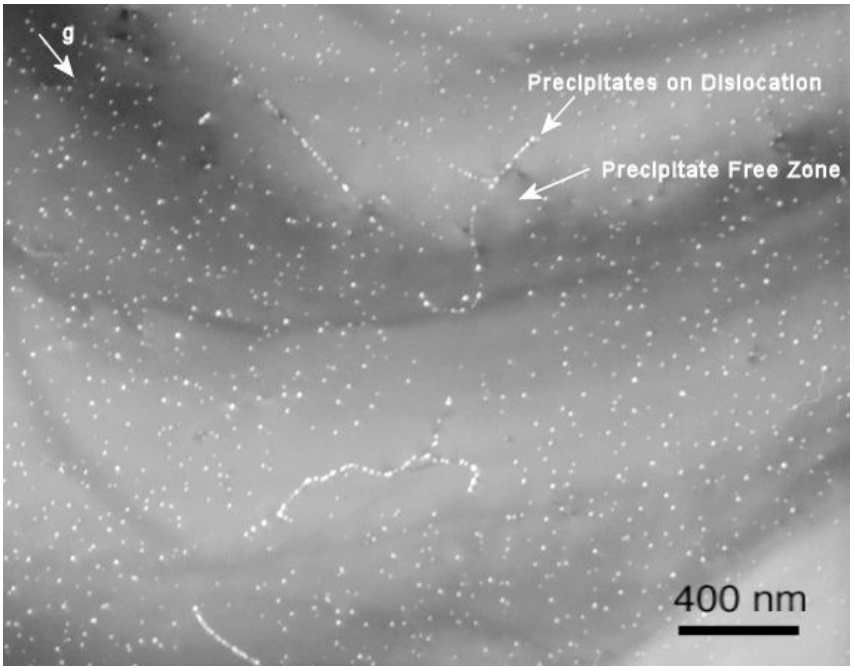

Figure 4.4: Dark-field TEM micrograph for Al-0.03Yb aged isochronally up to 300˚C in 25˚C increments for 1 h. [111] projection.

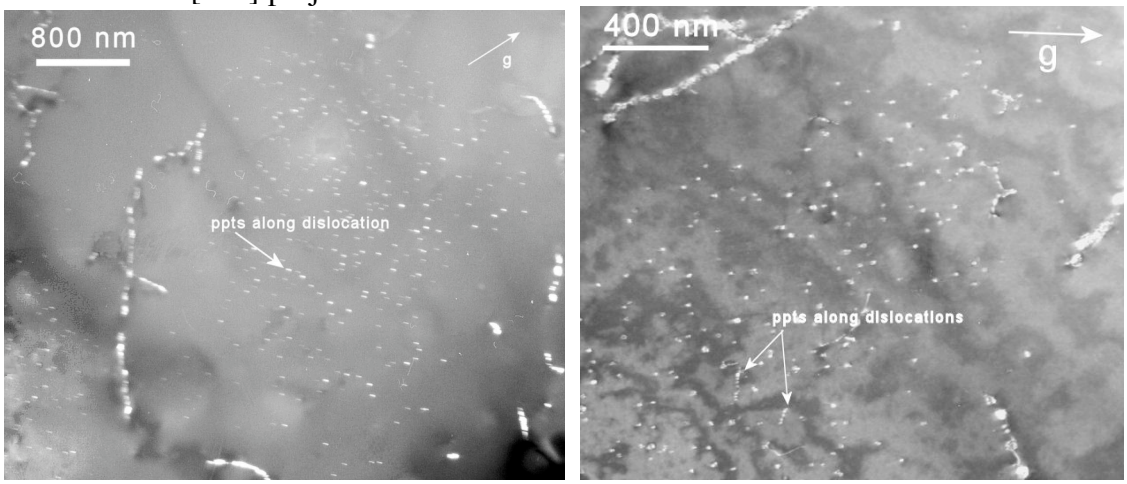

Figure 4.5: Dark-field TEM micrographs for Al-0.03Yb aged isochronally up to 300˚C in 25˚C increments for 1 h followed by aging for 64 h at 300˚C. [100] and [110] projection.

4.3.4 Average Precipitate Radius, <R(t)> and Yb Matrix Supersaturation, $\Delta C_{Yb}^{\alpha}(t)$ During Aging at 300˚C

The values of <R(t)> and $\Delta C_{Yb}^{\alpha}(t)$ for the 1, 4 and 64 h aging times at 300˚C are measured using TEM and LEAP tomography. Before aging at 300˚C these samples underwent an isochronal aging in 25˚C increments for 1 h intervals. $\Delta C_{Yb}^{\alpha}(t)$ is found by subtracting C_{Yb}^{α}(t) from the solubility at t_{∞}, where the solubility at t_{∞} is found from extrapolation of the experimental data. Data was gathered in the regions which appeared homogeneous, at least 100 nm from any precipitates heterogeneously nucleated on dislocations. As can be seen in Table 4.1 and Fig. 4.6, <R(t)> is increasing, while C_{Yb}^{α} and $\Delta C_{Yb}^{\alpha}(t)$ are decreasing.

Table 4.1: Average precipitate radius, <R(t)>, Yb matrix concentration and Yb matrix supersaturation, $\Delta C_{Yb}^{\alpha}(t)$, for Al-0.03Yb aged isochronally in 25˚C increments for 1 h up to 300˚C. Aging time shown is the aging time at 300˚C following the isochronal aging treatment.

Aging Time at 300˚C (h)	Radius <R(t)> (nm)	Yb matrix concentration C_{Yb}^{α} (at. ppm)	Yb supersaturation $\Delta C_{Yb}^{\alpha}(t)$ (at. ppm)
1	3.8±0.5	15.8±1.6	14.8±2.1
4	4.4±1.2	13.3±1.4	12.3±1.9
64	9.7±1.4	4.0±1.0	2.9±1.5

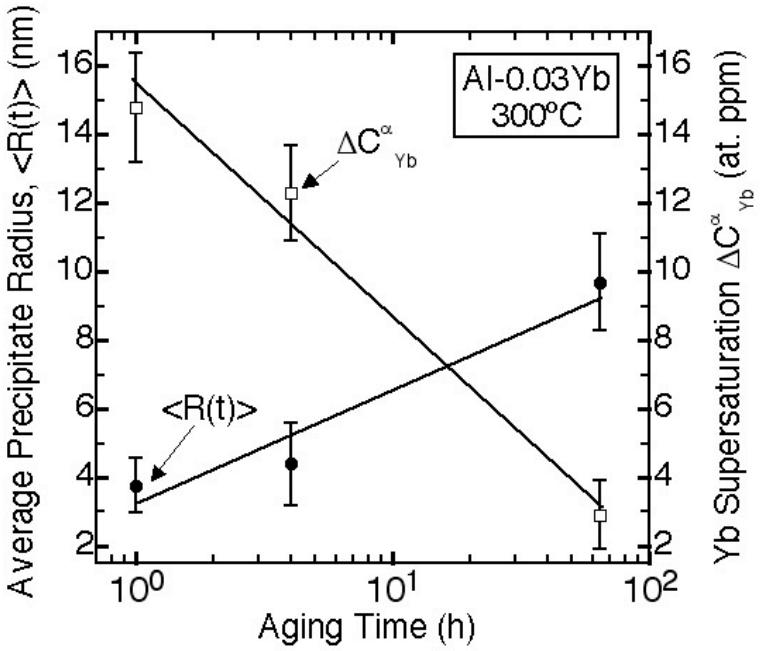

Figure 4.6: Average precipitate radius <R(t)> and the Yb supersaturation in the Al matrix, $\Delta C^{\alpha}_{Yb}(t)$ for Al-0.03at.%Yb aged at 300˚C after isochronal aging up to 300˚C in 25˚C increments for 1 h.

4.4 Discussion

4.4.1 Maximum Solid-Solubility and Precipitation Kinetics

A homogenized, conventionally cast sample of an Al-0.06at.%Yb alloy shows a Yb concentration in the matrix of 248±7 at. ppm. An attempt was made to increase the amount of solute in the matrix by means of increasing the cooling rate of the alloy. A wedge shaped mold was created with a 7˚ angle, resulting in a very thin region at the bottom of the mold. There are, however, large (~1μm) eutectic precipitates in the matrix following casting, indicating that a 600 ppm solute concentration in the matrix was still not achieved.

Since precipitation is occurring at lower temperatures in the Al-Yb alloy than in the Al-Sc alloy (Fig. 4.1), this indicates that the Yb is diffusing faster than the Sc in the Al-matrix. An interesting feature of Fig 4.1 is that the microhardness is higher at 25˚C than at 375˚C and 400˚C. This indicates that there is possibly some diffusion and precipitation upon quenching from the homogenization temperature down to 25˚C.

Fig. 4.2 shows that the precipitation of Yb is occurring up until relatively high temperatures. When examining percentage of the solute which has precipitated for the Al-0.03Yb alloy, about 40% of the solute has already precipitates by 150˚C. The percentage of Yb precipitated increases up to 300˚C when about 90% of the solute has precipitated out of the matrix. Since the diffusivity, and hence the diffusion distance, is expected to be much smaller at the lower temperatures, it is conceivable for the Yb to still be precipitating when isochronally aged up to 300˚C. The continued precipitation at high temperatures indicates that there is an opportunity for heterogeneous nucleation at higher temperatures, unless the alloy remains at low temperatures for long times.

4.4.2 Microstructure: Al_3Yb Precipitates and Heterogeneous Nucleation

Upon aging at 300˚C for 1 h after the isochronal aging treatment, Al_3Yb precipitates have formed (Fig. 4.4). An Al_3Yb precipitate imaged by LEAP tomography of a sample aged for 1 h at 300˚C after the isochronal aging treatment is shown in Fig. 4.7, as evidenced by the much higher concentration of Yb atoms as compared with the matrix (precipitate/matrix partitioning ratio = 14,000±2,000). The concentration of Yb in this precipitate (measured by LEAP tomography to be 25.8±0.7%) confirms the Al_3Yb structure. Further confirming the presence of Al_3Yb

precipitates is the diffraction pattern in the TEM. The faint superlattice reflections, which correspond to an $L1_2$ structure, can be seen in Fig. 4.8. These are so faint since the volume fraction of precipitates is so low, at 0.11 ± 0.02 %. The lattice parameter of the Al_3Yb phase can be measured from TEM. It is calculated to be 0.4186 ± 0.001 nm which is close to the value from the literature of 0.4201 nm [8].

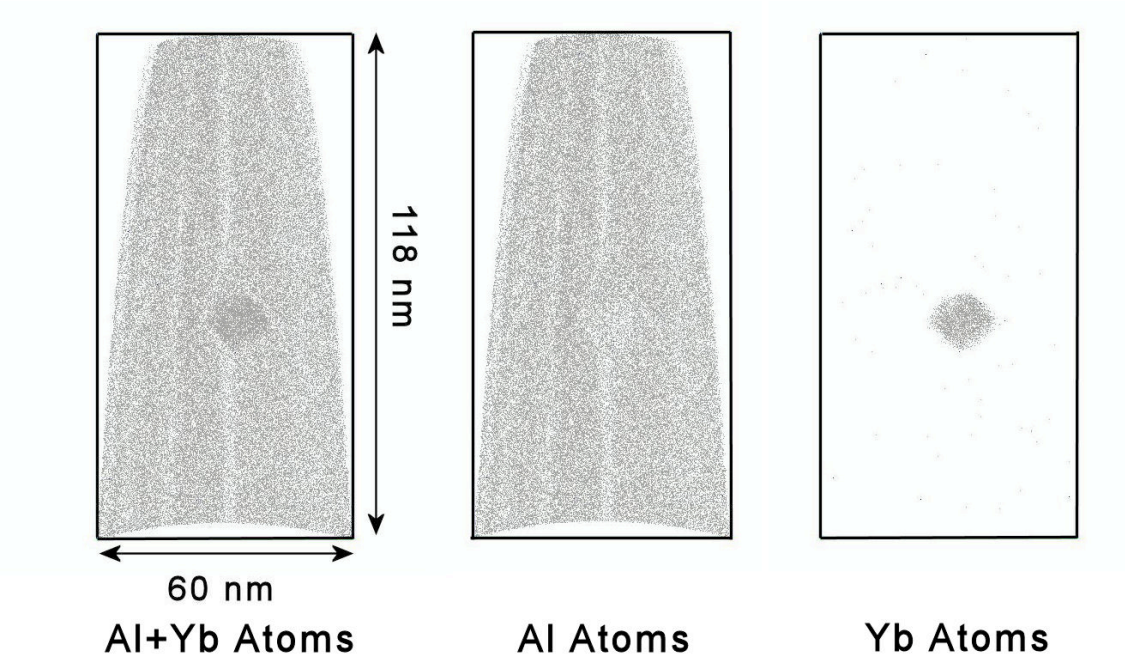

Figure 4.7: 6 nm thick slice through LEAP reconstruction (60 x 118 nm^2) showing the density of atoms in the Al matrix and an Al_3Yb precipitate aged isochronally up to 300˚C in 1 h increments.

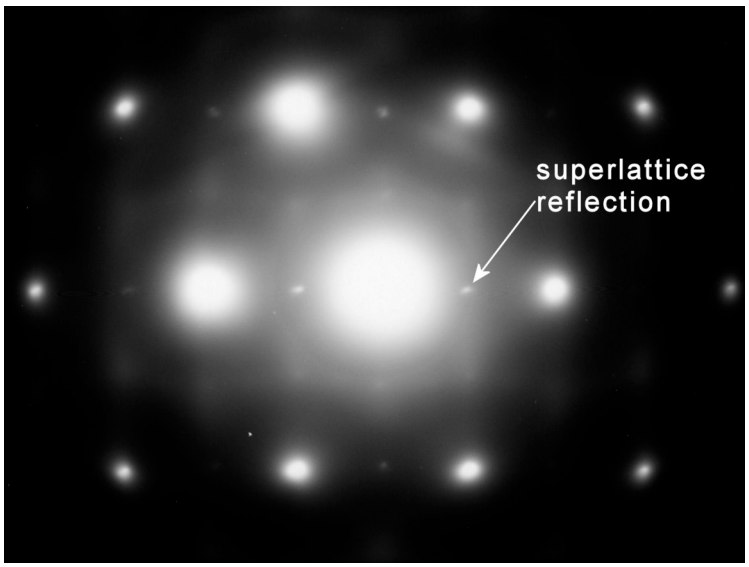

Figure 4.8: Diffraction Pattern from TEM for the Al-0.03at.%Yb alloy upon aging isochronally in 25˚C increments for 1 h up to and including 300˚C.

The process of aging at lower temperatures initially by isochronally increasing the temperature did not succeed in nucleating a homogeneous microstructure of $L1_2$ structured Al_3Yb precipitates. Many regions appear homogeneously nucleated after 1 h, but, there are also precipitates nucleated on dislocations (Fig. 4.4). After 64 h, it appears as if there is coarsening occurring of precipitates along dislocations within the regions of precipitates which initially appeared homogeneous (Fig. 4.5), thus resulting in a microstructure which is even more heterogeneous. This microstructural evolution is similar to that reported for an Al-0.1at.%Zr-0.1at.%Ti alloy [115], which also contained nanosize $L1_2$ $Al_3(Zr,Ti)$ precipitates. In that alloy there were initially precipitate-rich dendritic regions and interdendritic regions which contained a few large precipitates. These regions formed due to segregation during casting. The dendrite regions initially appeared homogeneous, however upon aging, there was preferential coarsening

along dislocations within the dendrites, leading to precipitate-free zones around these larger precipitates.

On the other hand, the heterogeneous precipitation of the Al-0.03at.%Yb alloy is in contrast to Al-Sc alloys containing solute concentrations below the maximum solid solubility (0.23 at.%) [18, 19, 21, 125-127]. These alloys contained a homogeneous distribution of coherent Al_3Sc precipitates upon aging at 300˚C. No evidence of precipitation on dislocations was found in those alloys. The Al-Sc-Ti alloy discussed in this thesis also precipitates with no evidence of heterogeneous precipitation at 300˚C. When the temperature is raised to 330˚C, however, extensive heterogeneous nucleation is observed.

4.4.4 Diffusivity of Yb in Al

$D_{Yb}(T)$ was calculated using the same approach as in Ref. [128]:

$$D_{Yb}(T) = \frac{9(C_e^{\beta} - C_e^{\alpha})}{4}(K^2 \kappa^{\alpha})^{1/3} \tag{4.1}$$

where C_e^{β} and C_e^{α} are the equilibrium concentrations of Yb in the matrix (α) and precipitate (β) phases. The coarsening constants K and κ^{α} are determined experimentally from the evolution of <R(t)> and $\Delta C_{Yb}^{\alpha}(t)$. According to the LSW equations for coarsening in a binary alloy [80, 81, 129]:

$$< R(t) >^3 - < R_o >^3 = K(t - t_0) \tag{4.2}$$

$$C^{\alpha}(t) - C_e^{\alpha} = \left(\kappa^{\alpha}(t - t_0)\right)^{-1/3} \tag{4.3}$$

From these three data points D_{Yb}(300°C) is estimated to be $(5.7\pm1.9)\times10^{-17}$ m^2s^{-1}, with errors being propagated from the error in the individual quantities. According to Akaiwa and Voorhees [130], the concept of the screening distance can be used to determine the distance at which the precipitates will have an effect on each other. This was estimated to be ~ 40 times the average radius. Thus, for a 4 nm radius, the screening distance would be 160 nm. For larger radii, this screening distance will increase. As can be seen in Fig. 4.5, at the longer aging time, there is no region remaining unaffected by the heterogeneous precipitates. It should be noted that the values for <R(t)> were measured in regions away from precipitates heterogeneously nucleated on the dislocations (at least 100 nm from the large heterogeneous precipitates). It was more difficult to ascertain the location within the microstructure of the LEAP measurement since the collected volume is on the order of 50x50x100 nm^3. Hence, the matrix composition is measured in regions where precipitates with the average <R(t)> are present.

In order to determine how homogeneous the microstructure is in the regions away from the heterogeneous precipitates, <R(t)> and $N_v(t)$ for regions of 100 nm thickness as a function of distance from the dislocation are examined. $N_v(t)$ within the initial 100 nm is much lower than beyond 100 nm (Fig. 4.9). After 100 nm, $N_v(t)$ remains constant within the experimentally determined error bars. There are no drastic changes for the values of <R(t)> – even within the first 100 nm. This is encouraging since <R(t)> is needed to determine the diffusivity.

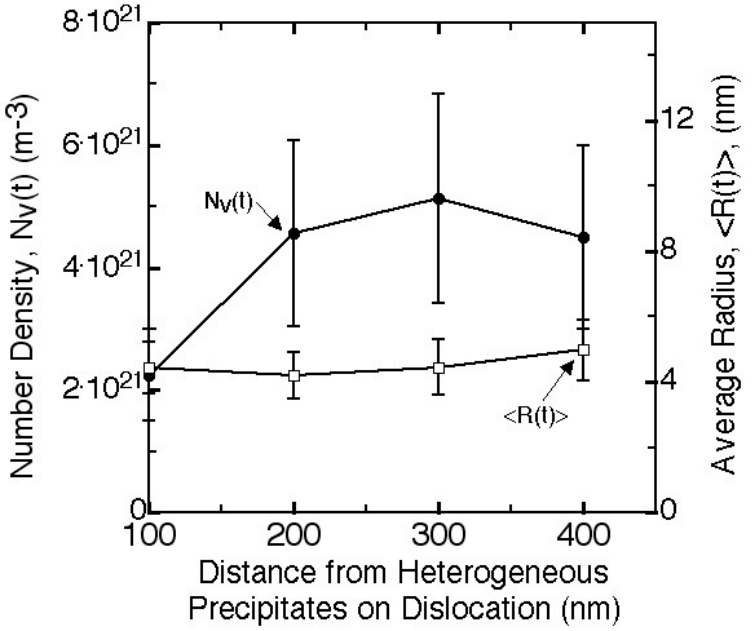

Figure 4.9: Average Precipitate Radius, <R(t)> and number density, $N_v(t)$ for Al_3Yb precipitates as a function of distance from precipitates nucleated heterogeneously on a dislocation. Regions of 100 nm thickness were sampled.

Since the diffusivity of Yb is calculated in Al-Yb to be 1500 times faster than that of Sc in Al-Sc [97] at 300˚C, Yb is not anticipated to decrease the coarsening kinetics of a ternary Al-Sc-Yb alloy. However, it could be the case that the Sc will slow down the diffusion of the Yb. For example, in a recent study on Al-Li-Sc alloys, it was shown that the coarsening occurred at a slower rate with the addition of Sc [131]. Li is known to diffuse faster than Sc in Al. The addition of Sc also led to a higher $N_v(t)$ of smaller precipitates.

4.4.5 Evaporation Characteristics

Finally, it is interesting to examine the experimental details of the LEAP tomography results. Fig. 4.7 shows a 6 nm thick slice through a LEAP reconstruction of the Al-0.03Yb alloy aged

isochronally in 25˚C increments for 1 h up to and including 300˚C with one Al_3Yb precipitate visible at the center. When the Al and Yb are both visualized simultaneously, the Al_3Yb precipitate appears much denser than the matrix. This indicates it must have a lower evaporation field than the matrix.

This is in contrast to the Al_3Sc and $Al_3(Sc_{1-y}X_y)$ phases which evaporate at a higher electric field and hence appear less dense than the matrix. The higher evaporation field for the $Al_3(Sc_{1-y}X_y)$ phase has been shown previously by a much brighter evaporation in the field-ion microscope in the Al-Sc-Ti [132] and Al-Sc-Zr [133] systems. It would be interesting to determine in the FIM if the Al_3Yb phase thus evaporated less brightly. The Al_3Yb does have a lower melting temperature (980˚C) than Al_3Sc (1320˚C).

4.5 Conclusions

An Al-0.03at.%Yb alloy is studied to determine the precipitation kinetics and several quantities of the system, including the solid-solubility and the diffusivity of Yb in Al. This information may help predict the behavior of Yb as a ternary addition to Al-Sc alloys.

- The maximum solid-solubility of Yb in Al is determined to be 248±7 at. ppm, which is about one order of magnitude lower than that of Sc (2300 at. ppm). Hence the volume fraction of Al_3Yb precipitates which can be obtained is limited.
- The evolution of the microhardness and conductivity of the Al-0.03at.%Yb alloy were measured upon isochronal aging in 25˚C increments for 1 h. Precipitation occurs at

temperatures as low as 50˚C and continues over a wide range of temperatures up to 325˚C.

- Despite the initial aging at lower temperatures, the microstructure of the alloy is not homogeneous. Some precipitates have heterogeneously nucleated on dislocations. These precipitates are larger than the surrounding precipitates and lead to precipitate-free regions in the surrounding matrix.
- The evolution of the average precipitate radius, <R(t)>, and the supersaturation of Yb in the matrix, $\Delta C_{Yb}^{\alpha}(t)$, were examined at 300˚C. <R(t)> increases from 3.8±0.5 to 9.7±1.4. $\Delta C_{Yb}^{\alpha}(t)$ is quite low during this range of aging times with values of less than 15 at. ppm.
- Despite the inhomogeneities of the microstructure, an estimate of the diffusivity of Yb in Al at 300˚C was determined to be $(5.7\pm1.9)\times10^{-17}$ m^2 s^{-1}, which is faster than Sc in Al.

5. Nanoscale Precipitation and Mechanical Properties of Al-0.06 at.% Sc Alloys Micro-alloyed with 50 ppm of Yb or Gd

5.1 Introduction

In this chapter, dilute Al-0.06 at.% Sc alloys are examined with micro-alloying additions of two RE (Yb or Gd), which have dissimilar solubilities in Al_3Sc. The pseudo-binary Al_3Sc-Al_3Yb system exhibits complete solubility between these two $L1_2$ intermetallics [8]. In contrast, only 15% of the Sc atoms in the Al_3Sc ($L1_2$) phase can be replaced by Gd, corresponding to a composition of $Al_3(Sc_{0.85}Gd_{0.15})$ [5]. As was discussed in the Introduction, Rare-earth (RE) elements are attractive ternary additions because: (i) many RE substitute for Sc in the Al_3Sc precipitates forming $Al_3(Sc_{1-x}RE_x)$ ($L1_2$ structure) with a high solubility, thereby replacing the more expensive Sc [5, 8]; (ii) the light RE have a smaller diffusivity in Al than Sc [134], improving the coarsening resistance of the precipitates; (iii) however, both the light RE and ytterbium (Yb) have a larger diffusivity in Al [134] than Zr or Ti [1], so that RE atoms are incorporated into the $L1_2$ precipitates more rapidly than Zr or Ti atoms; and (iv) unlike Ti or Zr [29], RE increase the lattice parameter mismatch between α-Al and $Al_3(Sc_{1-x},RE_x)$ [5, 8] , which could increase the creep resistance of the alloy [9].

In this chapter the results are presented of a study to determine the effects of micro-alloying concentrations (50 atomic ppm) of Yb or Gd on the microstructures of Al-0.06 at.% Sc alloys. The creep resistance at 300ºC is also examined and found to be much improved by the Yb or Gd micro-alloying additions.

5.2 Experimental Procedures

The nominal composition of the alloys studied is Al-0.06 at.% Sc-0.005 at. % RE, where RE = Gd or Yb. This composition was chosen to increase the probability that the Sc and RE atoms are fully dissolved in a single-phase solid-solution, α-Al, during the solutionizing treatment (the maximum solid-solubility of Sc in Al is 0.23 at.% [135], but that of Gd and Yb is imprecisely known [124, 136]). Each alloy was produced by dissolving in a melt of 99.99 at.% pure Al (impurities: 22 at. ppm Fe and 38 at. ppm Si) small quantities of two master alloys, Al-1.2 at.% Sc and Al-0.30 at.% RE (the latter was produced by arc melting the pure elements). The alloys were melted in a resistively-heated furnace at 750°C in air using an alumina crucible. After thoroughly stirring to ensure uniform composition, the melt was cast into a graphite mold positioned on a large copper plate to promote directional solidification and a large grain diameter. The solutionization treatment was performed at 640°C for 72 h in air, after which the alloy was water-quenched to room temperature. Aging was subsequently performed at 300°C in a salt bath (a mixture of sodium nitrite, sodium nitrate and potassium nitrate) for times less than 5 minutes and in air for longer times, which was also terminated by water quenching. After homogenization, the alloy composition was verified by three-dimensional local-electrode atom-probe (LEAP) tomography and by direct-coupled plasma mass-spectroscopy analysis (performed by ATI Wah Chang Laboratories, Albany, OR); the results are listed in Table 5.1. The Sc concentration is somewhat higher in the Al-Sc-Gd alloy than the Al-Sc-Yb alloy, but within single significant digit accuracy, the alloys have the same composition (Al-0.06 at.% Sc-0.005 at.% RE, hereafter abbreviated as Al-Sc-RE). Grain boundaries were revealed by etching for 30 sec in Poulton's etchant (2 mL HF, 3 mL HCl, 20 mL HNO_3, 175 mL water) and the grain

diameters were found to be greater than 1 mm. The LEAP tomography, TEM and creep experiments followed the same procedures as in Chapter 3.

5.3 Results

5.3.1 Hardness Measurements

After 4 h of aging at 300ºC, both alloys have achieved, within experimental error, their peak hardness values (Fig. 5.1). These values, when compared to the original quenched and unaged microhardness value, are higher by a factor of 2.2 for Al-Sc-Yb and 2.6 for Al-Sc-Gd. Figure 5.1 also demonstrates that Al-Sc-Yb hardens at a faster rate than Al-Sc-Gd: the incubation time for the increase in hardness for Al-Sc-Yb is less than the shortest measured aging time of 30 seconds, while Al-Sc-Gd has an incubation time of about 10 minutes. Finally, both Al-Sc-RE alloys exhibit a hardness decrease due to overaging at the longest aging time of 16 days (384 h).

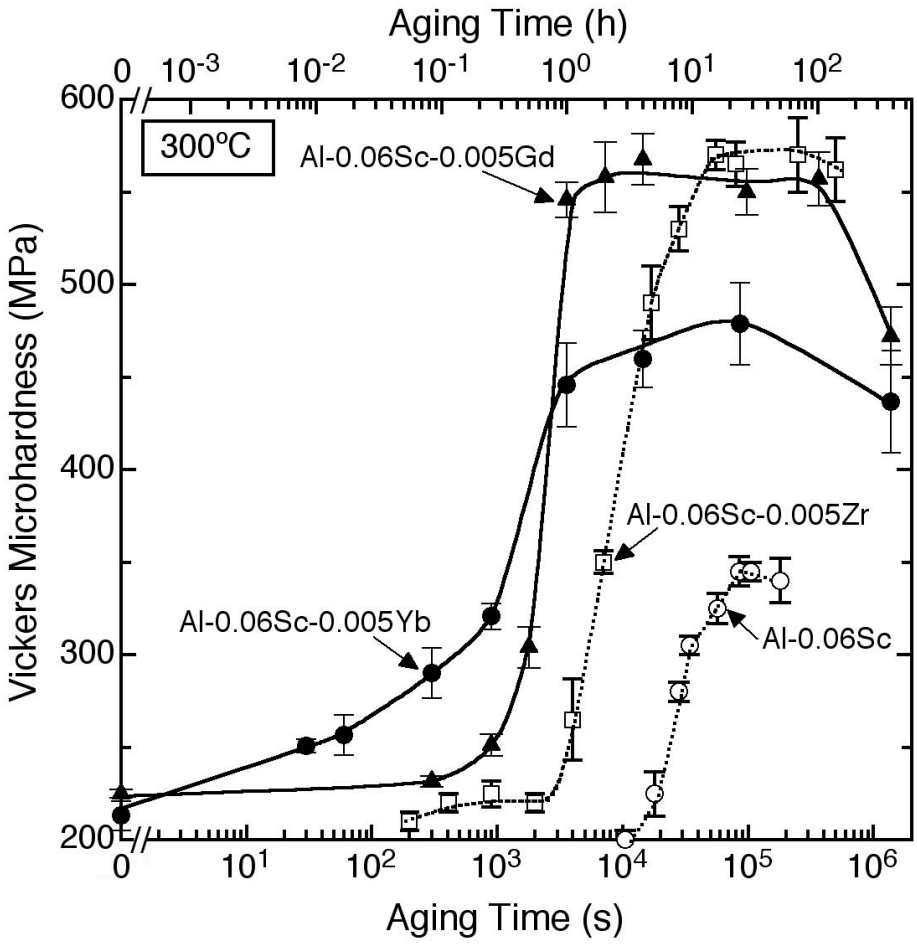

Figure 5.1: Vickers microhardness (MPa) vs. aging time (seconds) at 300ºC for the Al-0.06 at.% Sc-0.005 at.% Yb and Al-0.06 at.% Sc-0.005 at.% Gd alloys. Literature data for Al-0.06 at.% Sc [20] and Al-0.06 at%Sc-0.005 at.% Zr [28] alloys are also displayed for comparison.

5.3.2 3-D Local-Electrode Atom-Probe (LEAP) Tomographic Results

Three-dimensional reconstructions of LEAP tomographic data (Fig. 5.2) demonstrate that both Al-Sc-RE alloys achieve high number densities of nano-size precipitates at the peak aging time of 4 h. The precipitate number density for the Al-Sc-Gd alloy, $(8.6\pm0.9)\times10^{22}$ m^{-3}, is found to be about four times higher than for the Al-Sc-Yb alloy, $(2.3\pm0.9)\times10^{22}$ m^{-3} (Table 5.1). The average precipitate radius is somewhat smaller for the Al-Sc-Gd alloy as compared to the Al-Sc-Yb alloy (2.1±0.4 nm *vs*. 3.2±0.7 nm, respectively). A second factor contributing to the higher number

density in the Al-Sc-Gd alloy is that the volume fraction of precipitates is slightly lower for the Al-Sc-Yb alloy (ϕ = 0.21±0.01 %) than for the Al-Sc-Gd alloy (ϕ = 0.25±0.01 %). ϕ can also be calculated from the overall composition by subtracting the solute content in the matrix after aging (found by 3-D LEAP tomographic measurements of the aged alloys) from the overall solute content in the as-homogenized state (also found by 3-D LEAP tomographic measurement), assuming that the amount of solute no longer in the matrix has formed the precipitate phase with the stoichiometric composition. The actual concentration of Sc plus RE within the precipitates (27.0 % for Al-Sc-Yb and 26.8 % for Al-Sc-Gd) is found to be slightly greater than the stoichiometric composition, which is, however, most likely a field-evaporation effect that has been observed previously for Al_3Zr [115, 137] and Al_3Sc [138] precipitates in Al. When using the matrix compositions, similar values for ϕ are obtained (0.22±0.01 % for Al-Sc-Yb and 0.25±0.01 % for Al-Sc-Gd), confirming the accuracy of the direct 3-D LEAP tomographic measurement of volume fraction.

The proxigrams after peak-aging (4 h) are displayed in Figs. 5.3 and 5.4 and reveal additional differences between the two alloys. For the Al-Sc-Yb alloy (Fig. 5.3), the average Yb concentration in the precipitates is 3.3 at.%, corresponding to $Al_3(Sc_{0.87}Yb_{0.13})$. In the $L1_2$ precipitate cores, however, the Yb concentration achieves a concentration as high as 11 at.%. The proxigram for the Al-Sc-Gd alloy (Fig. 5.4) exhibits a lower average RE precipitate concentration of 1.4 at.% Gd, corresponding to $Al_3(Sc_{0.94}Gd_{0.06})$. The Gd atoms are also more uniformly distributed within the precipitates than the Yb atoms in the Al-Sc-Yb alloy. Upon further aging to 24 h, the average precipitate radius and number density remain almost constant within experimental error (Table 5.1). The average concentration, however, of Yb and Gd in the

precipitates increases to 3.7 % and 2.0 %, respectively (Figs. 5.3 and 5.4). This is a 12 % and 43 % increase, respectively, in RE concentration in the precipitates over the 4 h aging time.

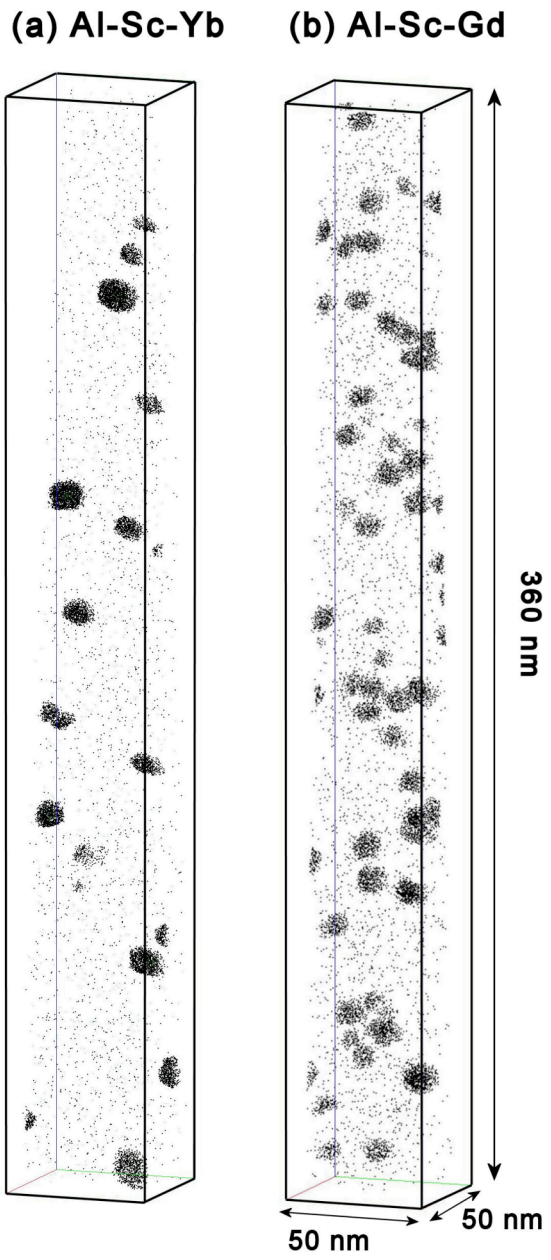

Figure 5.2: 3-D LEAP tomographic reconstructions for: (a) Al-Sc-Yb; and (b) Al-Sc-Gd. Each alloy was peak-aged for 4 h at 300ºC and each data set contains 15 million atoms. Only Sc atoms are displayed for the sake of clarity.

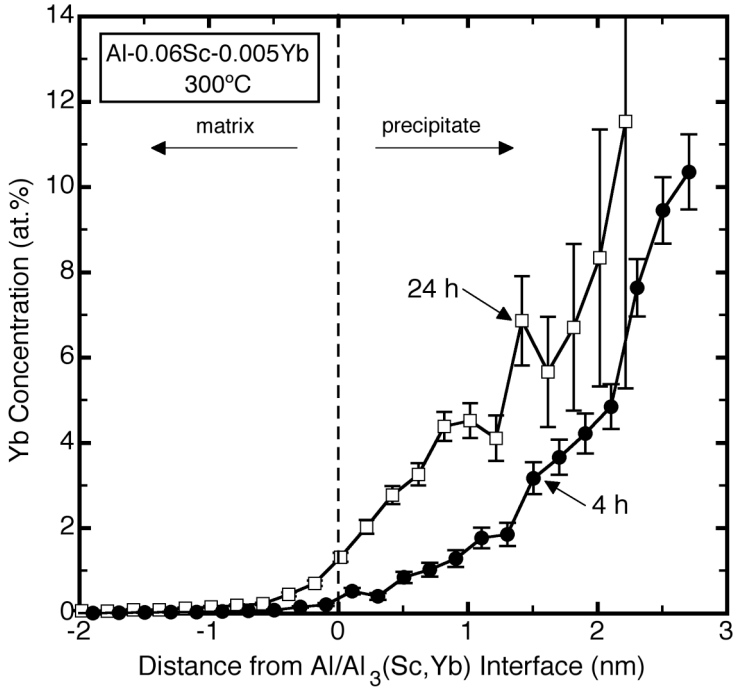

Figure 5.3: Proxigrams showing the Yb concentration (at.%) as a function of radial distance (nm) from the α-Al/Al_3(Sc,Yb) heterophase interface (x = 0) for Al-Sc-Yb aged for 4 and 24 h at 300ºC. The interface is based on an isoconcentration surface of 9at.%Sc.

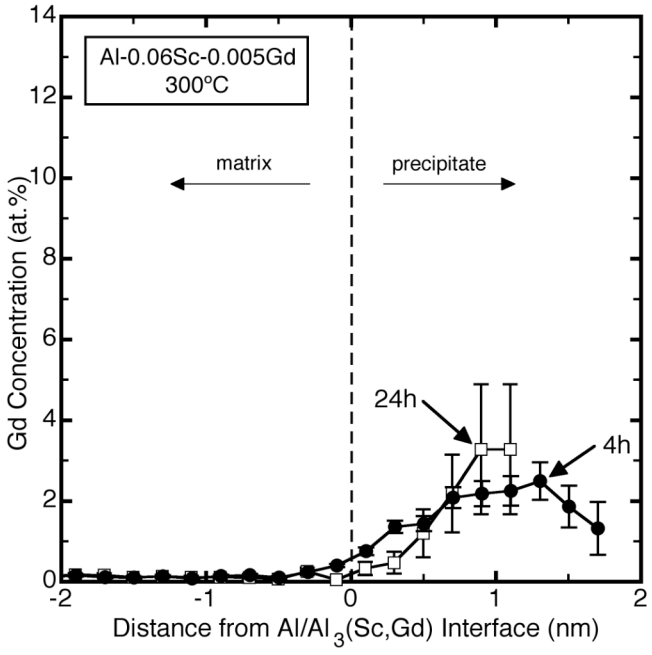

Figure 5.4: Proxigrams showing the Gd concentration (at.%) as a function of radial distance (nm) from the α-Al/Al_3(Sc,Gd) heterophase interface (x = 0) for Al-Sc-Gd aged for 4 and 24 h at 300ºC. The interface is based on an isoconcentration surface of 9at.%Sc.

5.3.3 Radial Distribution Functions (RDF)

The hardness of the Al-Sc-Yb alloy (Fig. 5.1) increases at an earlier aging time than it does for the Al-Sc, Al-Sc-Zr and Al-Sc-Gd alloys. This initial rapid increase in hardness indicates the presence of either short-range order clusters and/or some precipitation at these early aging times. In the three-dimensional reconstruction of the LEAP tomographic data there is no clear evidence of visible precipitates at an aging time of 15 minutes (Fig. 5.5). It is difficult to evaluate the state of clustering from Fig. 5.5 by the procedure used by Schmuck *et al.* [139-141]. Therefore to examine the early stages of precipitation in more detail, a radial distribution function (RDF) analysis [142, 143] was employed to evaluate the presence of solute clustering in the Al-Sc-Yb alloy in the homogenized state and after 15 minutes of aging. An important advantage of performing an RDF analysis using 3-D LEAP tomography is that the analysis is performed in direct space, whereas scattering (x-ray of neutron) experiments are performed in reciprocal space and this implies that the results need to be deconvolved to obtain direct space information. The standard definition of an RDF [144] at a given radial distance is defined as the average concentration of component i around a given solute species X, when summed over all of the atoms of type X, by:

$$RDF = \frac{< C_i^X(r) >}{C_i^o} = \frac{1}{C_i^o} \sum_{k=1}^{N_X} \frac{N_i^k(r)}{N_{tot}^k(r)}; \tag{5.1}$$

where C_i^o is the overall concentration of element i in the alloy, $C_i^X(r)$ is the concentration of component i at a distance r from component X, $N_{tot}^k(r)$ is the total number of atoms in the shell at a distance r from the k^{th} atom of type X, $N_i^k(r)$ is the number of atoms of type i in the shell at a distance of r from the k^{th} atom of type X. The RDF plot of the data for the 15 minute aging time (Fig. 5.6b) demonstrates that the partial RDF for Yb-Yb reaches a maximum of 32, indicating that, at a given distance from a Yb atom, there is 32 times the concentration expected from a random distribution of Yb atoms at the second nearest-neighbor position. The partial RDF for a perfectly random distribution of atoms corresponds to a value of unity and is given by the horizontal lines in Figs. 5.6a and 5.6b. For the initially homogenized state, Fig. 5.6a, the partial RDF for Yb-Yb is ca. 4.5 at the second nearest-neighbor position, which implies that it is a factor of ca. 7 smaller than after 15 minutes of aging. Figures 5.6a and 5.6b taken in concert indicates that much of the clustering of Yb atoms has occurred during this 15 minute aging period.

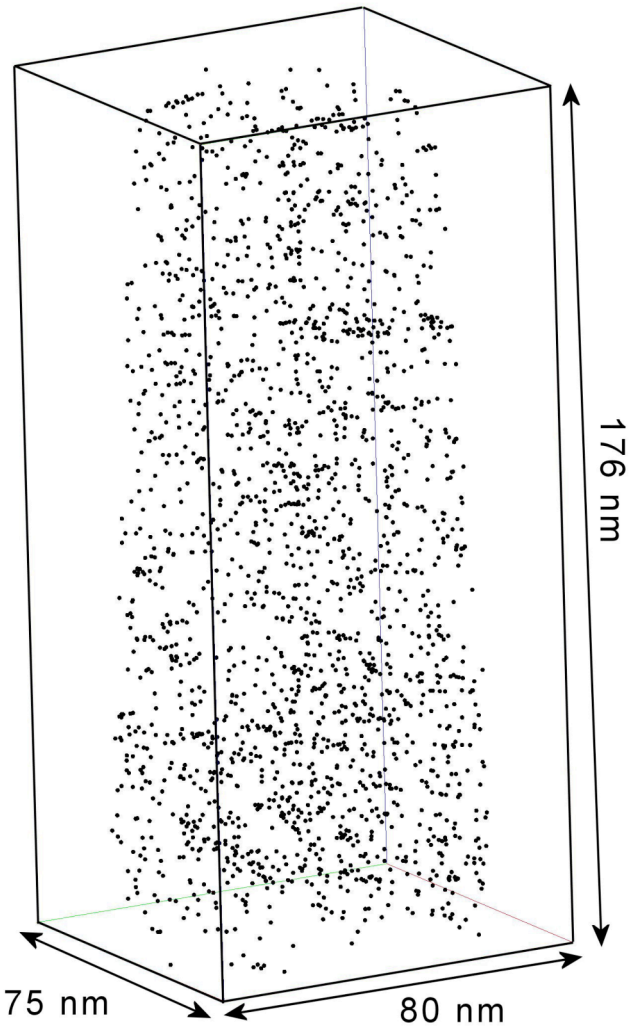

Figure 5.5: 3-D LEAP tomographic reconstruction for the Al-Sc-Yb alloy aged for 15 min. at 300ºC, where only the Yb atoms are shown for the sake of clarity. This data set contains 19 millions atoms.

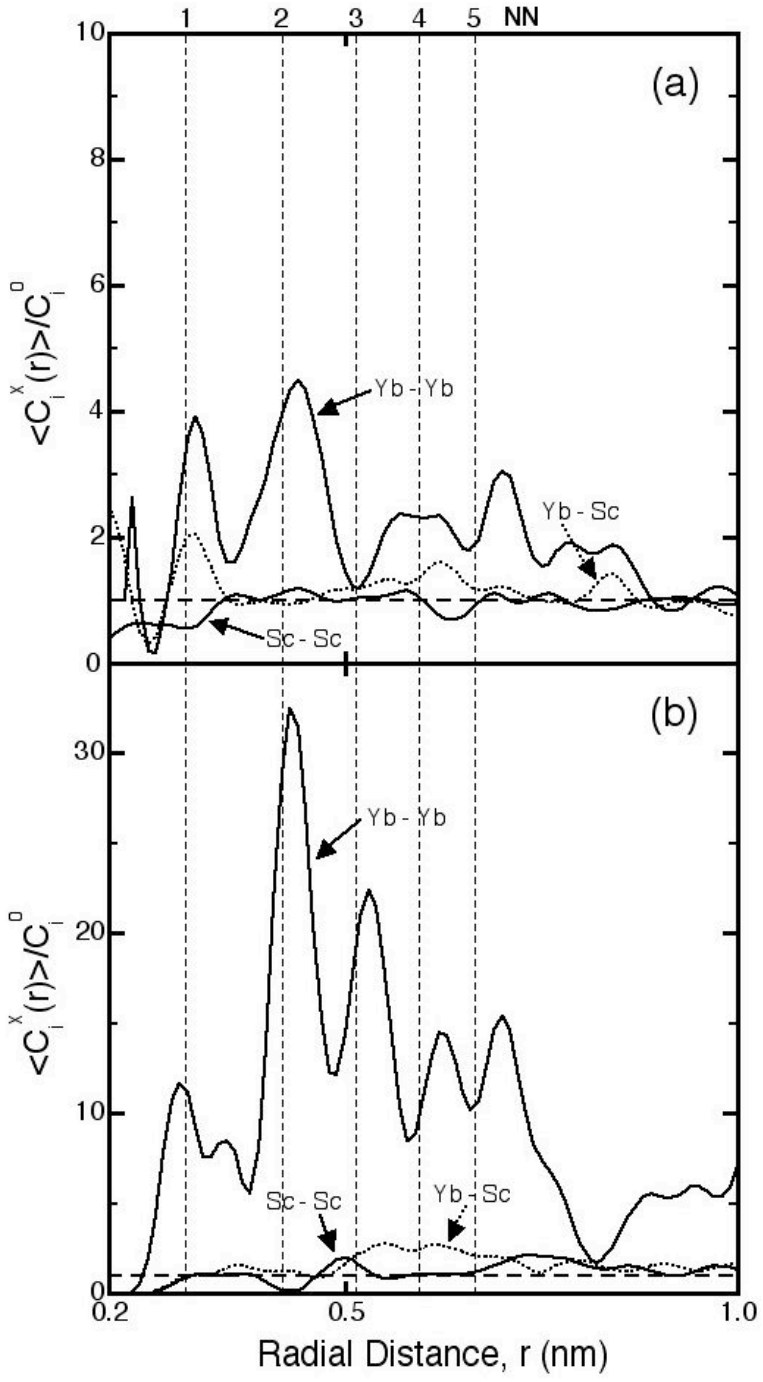

Figure 5.6: Experimental partial radial distribution functions (RDFs) for Al-Sc-Yb in: (a) the homogenized state; and (b) aged for 15 minutes at 300ºC, showing the radial distance (nm) of the second element with respect to the central first element. The dashed horizontal line at unity indicates the value expected for a completely random distribution of solute atoms. Vertical lines indicate the first to fifth nearest- neighbor (NN) distances for Al_3Yb.

5.3.4 High-Temperature Creep Experiments

Figure 5.7 demonstrates that both Al-Sc-RE alloys exhibit creep behavior at 300°C characterized by a high apparent stress exponent of 29-37, which is indicative of the presence of a threshold stress, σ_{th}, below which the creep rate, $\dot{\varepsilon}$, cannot be experimentally measured [62]. The power-law creep equation including a threshold stress is:

$$\dot{\varepsilon} = A(\sigma - \sigma_{th})^n \exp\left(-\frac{Q}{R_g T}\right); \tag{5.2}$$

where A is the Dorn constant, σ is the applied stress, Q is the activation energy of creep in pure Al, n = 4.4 is the stress exponent of pure Al [61], and R_g is the ideal gas constant. By plotting $\dot{\varepsilon}^{1/n}$ vs. σ [84], threshold stresses of 24 MPa for Al-Sc-Gd and 33 MPa for Al-Sc-Yb are calculated.

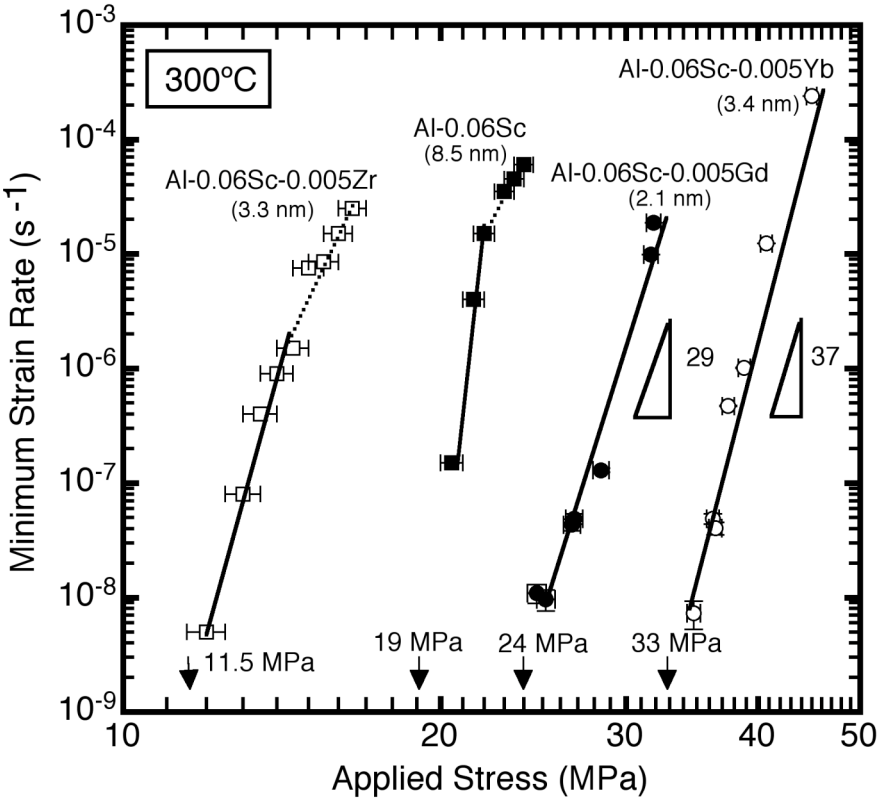

Figure 5.7: Double logarithmic plot of minimum strain rate (s^{-1}) vs. applied stress (MPa) for creep at 300ºC of Al-Sc-Yb and Al-Sc-Gd, as well as Al-Sc [20] and Al-Sc-Zr [28], with precipitate radius given in parentheses. Threshold stresses are marked as vertical arrows along the applied stress axis.

Table 5.1: Alloy compositions, precipitate number densities, and mean precipitate radii for Al-Sc-RE, Al-Sc-Zr [28], and Al-Sc [20] alloys for different aging times at 300ºC.

Alloy/ Aging treatment	Sc concentration (at. ppm)		RE concentration (at. ppm)		Precipitate number density (m^{-3})	Precipitate mean radius (nm)
	Bulk[a] Analysis	LEAP[b] Analysis	Bulk[a] Analysis	LEAP[b] Analysis		
Al-Sc-Yb 4 h - 300ºC	540	573	80	40	$(2.3\pm0.9)\times10^{22}$	3.2±0.7
Al-Sc-Yb 24 h - 300ºC	540	573	80	40	$(1.2\pm0.2)\times10^{22}$	3.4±0.7
Al-Sc-Gd 4 h - 300ºC	630	610	50	50	$(8.6\pm0.9)\times10^{22}$	2.1±0.4
Al-Sc-Gd 24 h – 300ºC	630	610	50	50	$(1.3\pm0.2)\times10^{23}$	1.8±0.4
Al-Sc 24 h - 300ºC	570	575	-	-	$(9\pm2)\times10^{20}$ [d]	8.5±0.6
Al-Sc 66 h – 275ºC	570	575	-	-	$(5\pm1)\times10^{22}$ [d]	4.1±0.3
Al-Sc-Zr 72 h - 300ºC	600[c]	-	50[c] (Zr)	-	$(9\pm1)\times10^{22}$ [d]	3.3±0.2
Al-Sc-Zr 5 h - 300ºC + 4.75 h - 400ºC	600[c]	-	50[c] (Zr)	-	$(2\pm1)\times10^{22}$ [d]	5.9±0.3

[a] Chemical analysis performed by ATI Wah Chang Laboratories. Error for Sc: 25 at. ppm and the error for RE is 10 at. ppm.
[b] Error for the 3D-LEAP analyses is ±5 at. ppm for Sc and ± 4 at. Ppm for the RE, although a much smaller volume is sampled.
[c] Chemical analysis performed by Luvak Inc.
[d] Calculated from radius and volume fraction.

5.4 Discussion

5.4.1 Hardness Measurements and Strength

In both Al-Sc-RE alloys, the large increase in hardness in the peak-aged condition as compared to the homogenized state (Fig. 5.1) is attributed to the formation of a high number-density of $Al_3(Sc_{1-x}RE_x)$ precipitates (Table 5.1 and Fig. 5.2). For the Al-Sc-Yb the peak number density is

$(2.3\pm0.9)x10^{22}$ m^{-3} at 4 h, and for Al-Sc-Gd, it is $(1.3\pm0.2)x10^{23}$ m^{-3} after aging for 24 h at 300°C. Figure 5.8 displays the yield stress increment for both alloys as a function of precipitate radius after aging for 4 and 24 h at 300°C, respectively. The yield stress increment is calculated by taking the increase in microhardness (aged value subtracted from homogenized value) and dividing by a factor 3 to convert from hardness to yield stress [88]. Calculated curves are shown for three strengthening mechanisms: (i) Orowan strengthening, where dislocations bypass the precipitates; (ii) order strengthening, where dislocations shear the precipitates; and (iii) coherency and modulus strengthening, where dislocations are repelled by the precipitates (before shearing occurs) due to the mismatch in elastic modulus and lattice parameter between the matrix and precipitate phases. The same analysis was previously performed for dilute Al-Sc alloys [20] and Al-Sc-Zr alloys [28], and we utilize the same equations as in Ref. [28] with the lattice parameter mismatch at ambient temperature given by 1.46 % for Al-Sc-Gd and 1.64 % for Al-Sc-Yb. Vegard's law was assumed and used to calculate the average lattice parameters of the precipitates after peak aging for 4 h, based on the composition-dependence of the lattice parameter of $Al_3(Sc_{1-x}RE_x)$ [5, 8] and assuming a spatially uniform distribution of a RE in the precipitates.

The dashed lines in Fig. 5.8 represent the three strengthening contributions calculated for the larger volume fraction of $\phi = 0.25$ % in the Al-Sc-Gd alloy, while the smaller volume fraction in the Al-Sc-Yb alloy of $\phi = 0.21$ % (solid lines) leads to somewhat smaller strength values. Mechanism (i) occurs in parallel with mechanisms (ii) and (iii), which are in series with each other. From Fig. 5.8, it is then predicted that order strengthening controls strength at the lowest precipitate radii (to 0.7 nm), followed by modulus/coherency strengthening (from 0.7 to 1.8 nm),

while Orowan strengthening is the controlling strengthening mechanism at larger precipitate radii.

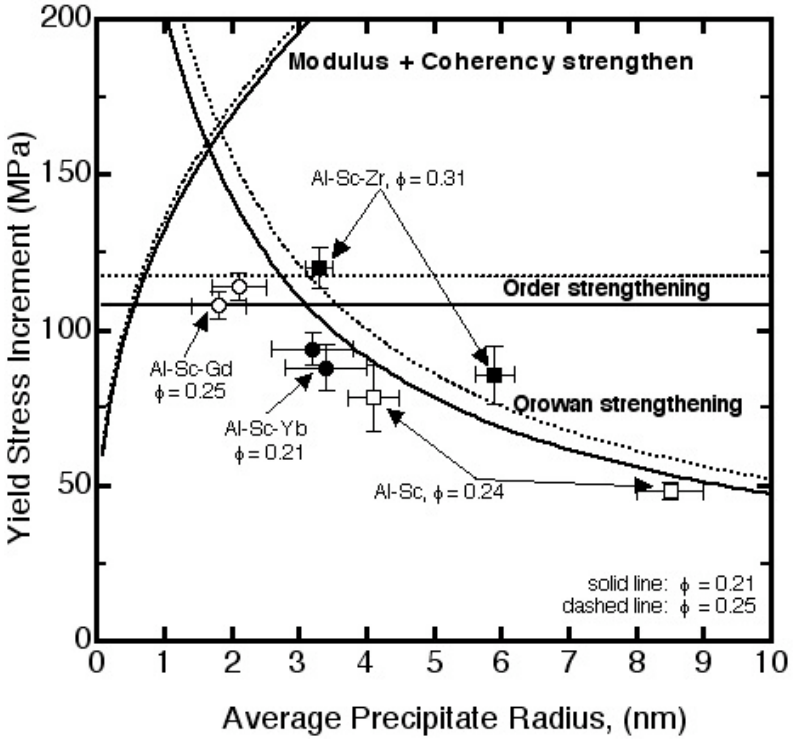

Figure 5.8: Yield stress increment (MPa) calculated from microhardness vs. average precipitate radius (nm) for Al-Sc-Yb and Al-Sc-Gd. Literature values for Al-Sc [20] and Al-Sc-Zr [28] are also displayed. The solid and dashed lines represent the theoretical strength increments for the three possible strengthening mechanisms calculated using the equations in Ref. [28] for the volume fractions, ϕ, of the Al-Sc-RE alloys at peak aging.

The 3.2-3.4 nm radius precipitates in the Al-Sc-Yb alloy fall in the regime where Orowan strengthening is predicted to be dominant, and there is good agreement between predicted and measured yield stress increment. The 1.8-2.1 nm radii precipitates in the Al-Sc-Gd alloy correspond to the regime where the modulus/coherency strengthening mechanism overlaps with the Orowan mechanism, and the experimental values are lower than the predicted values. This may be due to the non-uniform radius and spatial distribution of the precipitates. For an Al-0.06 at.% Sc-0.005 at.% Zr alloy (previously reported in Ref. [28] and hereafter referred to as Al-Sc-

Zr) with an average precipitate radius of 3.3 nm, Fig. 5.8 demonstrates that the Orowan mechanism is the strength-controlling mechanism. The same alloy with a larger precipitate radius of 5.9 nm exhibits a decreased strength value, which is consistent with the dominance of the Orowan mechanism. The relatively large average radii (4.1 and 8.5 nm) of the precipitates in an Al-0.06 at.% Sc alloy (previously reported in Ref. [20] and hereafter referred to as Al-Sc) leads to smaller strength increments. Again, hardness values for both Al-Sc and Al-Sc-Zr are in good agreement with predictions based on the Orowan strengthening mechanism.

5.4.2 Temporal Evolution of Precipitates

The earlier increase in hardness for the Al-Sc-Yb alloy, which is observed at aging times as short as 30 seconds (Fig. 5.1), is attributed to the formation of Yb clusters as demonstrated by the RDF analysis (Fig. 5.6). Clusters are difficult to detect in a 3D-reconstruction for the 15 minute aging time (Fig. 5.5) but are quantified by the RDF diagrams displayed in Fig. 5.6. Furthermore, the large positive oscillation at the second nearest-neighbor distance in the Yb-Yb partial RDF and the relatively small value at the first nearest-neighbor distance in these curves indicate the possibility of short-range order. Indeed, the Yb atoms are expected to be at the second nearest-neighbor distance in Al_3Yb ($L1_2$ structure), but not at the first nearest-neighbor distance. Partial RDFs for Yb-Sc and Sc-Sc pairs display values significantly closer to unity (no higher than 2.8 for Yb-Sc and 2.2 for Sc-Sc), indicating that the clustering of Sc is much less significant at 15 minutes of aging.

While no experimental data for the diffusivity of Yb in Al was found in the literature, Fig. 5.6 implies that Yb diffuses significantly faster than Sc in Al at 300°C, and that Yb-rich clusters form within minutes of aging at this temperature, thereby increasing markedly the hardness of the alloy (Fig. 5.1). After 4 h of aging (Figs. 5.2a and 5.3), the precipitates consist of a Yb-rich core surrounded by a Sc-rich spherical shell; such a cored structure was also observed in the Al-Sc-Ti [102], Al-Sc-Zr [3, 30, 32, 34, 78], Al-Li-Sc [145], Al-Li-Ti [146], Al-Li-Zr [48, 147] and Al-Li-Hf [148] systems. For Al-Sc-X alloys (where X=Ti, Zr or Li), Sc is located in the core while for Al-Sc-RE alloys Sc is found in the shell. This indicates that the slower-diffusing Sc subsequently diffuses toward the Yb-rich precipitates formed at early aging times. The Sc/Yb ratio of 7 measured in the precipitates for the 4 h peak-aged alloy is somewhat lower than the overall alloy elemental ratio measured by 3D-LEAP tomographic analyses in the homogenized and quenched alloy. However, the matrix concentration of Sc after 4 h of aging, as measured by 3D-LEAP tomography, is 100±3 at. ppm, higher than the equilibrium solubility of Sc in Al in the binary alloy, which is 20±6 at. ppm, as calculated from 3D-LEAP tomographic data at longer aging times.

The Yb-rich core obtained after 4 and 24 h of aging indicates that diffusion does not homogenize the precipitates for these aging times. This may be due to the small diffusivity of Yb and Sc in $Al_3(Sc,Yb)$, as expected from the high melting point of Al_3Sc (1320˚C) and the lower atomic mobility in ordered alloys as compared to disordered alloys because of correlation effects. The Yb enrichment towards the precipitate center may also be linked to the increase in lattice parameter of $Al_3(Sc,Yb)$ with increasing Yb concentration [8], which exacerbates the lattice parameter mismatch with the α-Al matrix and concomitantly the elastic strain energy. Similarly,

the slight Gd enrichment in the precipitate cores of the Al-Sc-Gd alloy (Fig. 5.4) may be also be due to an increase in lattice parameter mismatch with the substitution of Gd for Sc in Al_3Sc [5].

The Al-Sc-RE alloys contain smaller precipitates as compared to the binary Al-Sc alloy, which is in qualitative agreement with their more rapid precipitation kinetics at 300°C; peak hardness is achieved after ca. 4 h for the ternary Al-Sc-RE alloys, as compared to 24 h for the binary Al-Sc alloy. The precipitation kinetics of the Al-Sc-Zr alloy is somewhat slower than those of the Al-Sc-RE alloys, achieving peak hardness after 16 h at 300°C, most likely due to the smaller diffusivity of Zr in Al. The larger number density, smaller average precipitate radius, and more rapid precipitation kinetics in the Al-Sc-RE alloys compared with the Al-Sc alloy indicates that the RE, even for the microalloying concentrations investigated in this study, have a considerable effect on the nucleation and growth kinetics of the precipitates. The differences are explainable by the different nucleation currents in the two alloys, which are a result of the different heterophase interfacial free energies and supersaturations of solute species. The exact heterophase interfacial free energy values for these alloys are, however, unknown, and the Sc, Gd, or Yb supersaturations cannot be calculated because the ternary phase diagrams in the relevant regions are unknown. It is also possible that the increased number density of precipitates results from RE clusters serving as heterogeneous nucleation sites for precipitate formation.

5.4.3 Creep Properties

Figure 5.7 demonstrates that micro-alloying additions of Yb or Gd increase dramatically the creep resistance of the binary Al-Sc alloy. In a previous study, the threshold stress for an Al-Sc

alloy with 4.1 nm average precipitate radius was 8 MPa [20], or about one quarter of the value of 33 MPa for the Al-Sc-Yb alloy with a similar precipitate radius of 3.4 nm. When compared to Al-Sc-Gd with a threshold stress of 24 MPa, the value of the threshold stress for Al-Sc with 4.1 nm average precipitate radius is about one third. It is known that increasing the precipitate radius in Al-Sc alloys increases the threshold stress [9, 20, 26, 28]. Despite this fact, in Fig. 5.7 is displayed the creep data for the Al-Sc alloy with 8.5 nm radius precipitates [20] which, when compared to the Al-Sc-RE alloys with significantly smaller (2.1-3.4 nm radius) precipitates, still has threshold stresses 1.3-1.7 times lower. In comparison to an Al-Sc-Zr alloy with similar composition and precipitate radius [28], the Al-Sc-RE alloys display threshold stresses that are 2-3 times greater (Fig. 5.7).

The remarkable increase in threshold stress displayed by the Al-Sc-RE alloys may be due to the known increased lattice parameter mismatch between the α-Al matrix and the $Al_3(Sc_{1-x}RE_x)$ precipitates [8] as compared to Al_3Sc or $Al_3(Sc_{1-x}Zr_x)$ [29]. An increase in threshold stress with increasing lattice parameter mismatch was recently predicted by a model which considered the elastic effects on climb of dislocations over precipitates [9]. This model, as well as experimental results [20, 26, 28], indicate that increasing the mean precipitate radius increases the threshold stress normalized by the Orowan stress. Thus, it should be possible to achieve even higher values of the threshold stress for Al-Sc-RE alloys if precipitate radii are coarsened beyond the current values of 3.4 nm and remain coherent or semi-coherent with the matrix.

5.5 Conclusions

The nanostructure and mechanical properties of two Al-0.06 at.% Sc alloys microalloyed with 0.005 at.% (50 at. ppm) Yb or Gd are studied. Upon aging at 300°C, both alloys harden by formation of nanosize, coherent $Al_3(Sc_{1-x}RE_x)$ ($L1_2$) precipitates, but they exhibit dissimilar precipitation kinetics resulting in disparity in both microstructures and temporal evolution of the hardness.

- When compared to the binary Al-Sc alloy, the Al-Sc-RE alloys show an increase in peak microhardness values and decrease in aging times to reach peak hardness. This is due to a higher number density of precipitates, or equivalently, to a smaller precipitate radius at peak hardness.
- The Al-Sc-Gd alloy attains a higher peak hardness (90 MPa) compared to the Al-Sc-Yb alloy, due to a four-fold increase in precipitate number density.
- Both Gd and Yb segregate to the precipitate phase. At peak hardness, the average RE concentration in the precipitates is more than twice as large for Al-Sc-Yb as it is for Al-Sc-Gd, 3.3 vs. 1.4 at. %, respectively.
- The Al-Sc-Yb alloy exhibits an earlier onset of hardening than the Al-Sc-Gd alloy, due to the formation of Yb-rich clusters, which are originally free of Sc (as determined by 3-D LEAP tomography for an aging time of 15 min employing a radial distribution function analyses). This indicates that the diffusivity of Yb is greater than that of Sc in this alloy.
- In Al-Sc-Yb (and to a lesser extent in Al-Sc-Gd), the RE is more concentrated in the center of the precipitates than at the heterophase interface. For the Al-Sc-Yb alloy, this

can be interpreted as Yb first forming $Al_3(Yb_{1-x}Sc_x)$ precipitates, followed by subsequent Sc partitioning to the precipitates as they grow. For both Gd and Yb, a further possible cause for the RE enrichment in the center of the precipitates is the minimization of lattice parameter mismatch with the matrix, which is increased by the presence of RE in the precipitates.

- Both Al-Sc-RE alloys have much improved creep resistance when compared to binary Al-Sc or ternary Al-Sc-Zr alloys with the same composition and precipitate radius. The observed increase in threshold stress is thought to result from the increase in lattice parameter mismatch produced by the RE in the precipitates, which affects the dislocations bypassing the precipitates.

6. Clustering, Nucleation, and Growth in an Al-0.06at.%Sc-0.02at.%RE (RE = Yb or Gd) Alloys

6.1 Introduction

It was observed for Al-0.06Sc-0.005RE (at.%) alloys (RE = Yb or Gd) that the creep properties were improved with even a small addition (50 at. ppm) of Gd or Yb. Hence, in this chapter, the microstructure of Al-Sc-Yb and Al-Sc-Gd alloys richer in RE are examined Al-0.06 at.%Sc-0.02 at.%RE (Al-600 ppm Sc-200 ppm Yb) alloys (RE = Yb or Gd). Furthermore, it was observed in Chapter 5 that the Yb atoms form precipitates within minutes of aging at 300˚C. Thus this chapter will focus in particular on the details of precipitation at early aging times, from the unaged state to 6 h of aging at 300˚C.

The clustering in the early stages of aging has been studied in various other Al alloys, and the initial clustering and precipitation are found to significantly affect properties upon subsequent aging. In Al-Cu-Mg alloys, it was found that co-clustering of Cu and Mg atoms leads to significant hardening of the alloy [149]. The addition of Ag to the Al-Cu-Mg alloys leads to the formation of Mg-Ag clusters in addition to the Mg-Cu clusters, and as a result there is a shorter aging plateau because of the formation of a new phase, X' [150]. Cd additions to Al-Cu and Al-Cu-Mg alloys lead to enhanced precipitation of the θ' phase. Elemental clusters of Cd are present in the matrix or are attached to the θ' phase. In the Al-Cu-Mg alloy, nucleation of the σ phase is also enhanced [151]. In an aluminum 6111 alloy, the response of a pre-aged alloy is 60-85 MPa while 20-25 MPa in a sample aged at room temperature [152]. This was attributed to the change in the clustering which affects the later precipitation. The pre-precipitate clustering in Al-Si-Ge alloys has also been studied [153] and Al-Mi-Si [154]. Ringer et. al. suggest that interactions

among various solute atoms can produce an exaggerated from of precipitation hardening called "cluster hardening" [155].

In addition to the experiments, clustering processes have been modeled as well [156]. In order to model the precipitation kinetics, however, it is necessary to know the thermodynamic data as well as the diffusion properties, as was done for multicomponent alloys with multiple types of precipitates [157]. A recent study of Al alloys utilizing Kinetic Monte Carlo simulations showed that the addition of 0.12at.% Sc to Al-3.75at.%Ag retards the clustering of Ag since the Sc ties up the vacancies resulting in a finer dispersion of precipitates [158]. This was performed confirmed using TEM.

6.2 Experimental Procedures/Analysis Techniques

The composition of the alloy studied was Al-0.06 at.%Sc-0.02 at.%RE (RE = Yb or Gd) which was verified by ATI Wah Chang (Albany, OR) to be: Al-(0.058±0.003)Sc-(0.024±0.008)Yb, Al-(0.061±0.003)Sc-(0.018±0.009)Gd (at.%) (alloys hereafter referred to as Al-Sc-Yb and Al-Sc-Gd) (impurities: 0.0022±0.0001 % Fe and 0.0038±0.0002 Si). Details of the alloy processing are similar to those of Al-Sc-RE alloys containing 0.005at.% of Yb or Gd (Chapter 5). The microstructural analysis procedures are also similar to those performed on the Al-Sc-RE alloys with 0.005at.% of Yb or Gd and the Al-Sc-Ti alloy (Chapter 3).

6.3 Experimental Results

6.3.1 Room Temperature Mechanical Properties

In the unaged state, the Al-Sc-Yb alloy possesses a larger value of the Vickers microhardness than Al-Sc or Al-Sc-Gd alloys (Fig. 6.1). This is similar to that observed in the alloy containing 50 ppm of Yb [99]. For the Al-Sc-Yb alloy aged at 300°C, the hardness increases rapidly, within 10 seconds, in contrast to the Al-Sc and Al-Sc-Gd alloys, which both exhibit distinct incubation periods (5 h and 15 minutes, respectively) before an increase microhardness is measurable. Also, unlike Al-Sc [20], Al-Sc-Zr [28] and the presently studied Al-Sc-Gd alloy where there is a single rapid increase in the microhardness as the precipitates from, in the Al-Sc-Yb alloy, there appears to be an initial hardness increase followed by a plateau followed by a distinct second increase. The peak microhardness of Al-Sc-Yb is achieved after 6 h of aging at 300°C.

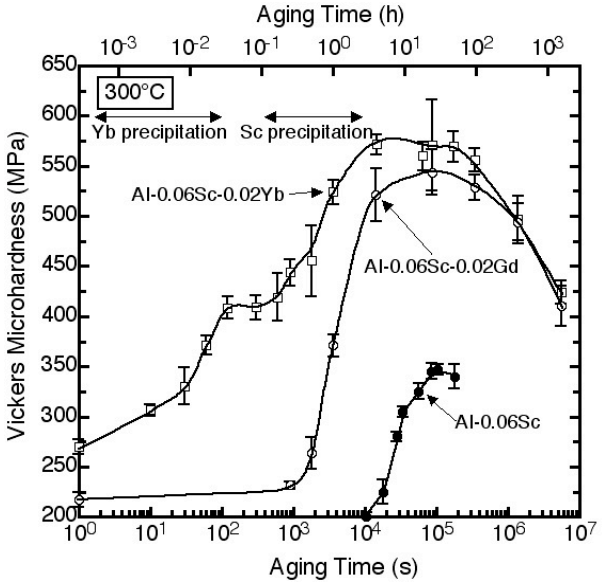

Figure 6.1: Vickers microhardness vs. aging time at 300˚C for Al-0.06Sc-0.02Yb (at.%), Al-0.06Sc-0.02Gd (at.%) and Al-0.06Sc (at.%) [21].

6.3.2 Microstructure

6.3.2.1 Unaged State

The 3-dimensional reconstruction of the LEAP tomography data in the unaged state for the Al-Sc-Yb alloy (Fig. 6.2) does not show evidence for precipitation. The envelope method (Described in Appendix A) also does not detect any precipitates with 5 or more atoms. LEAP tomography data in the homogenized state is used to calculate partial RDF plots. The maximum of the peaks in the Yb-Yb partial RDF shows values greater than one, up to 4, which indicates that at that particular distance the concentration is four times that of the overall composition in the alloy. This would indicate some clustering/ordering is occurring in the alloy during the quenching process prior to aging at 300°C (Fig. 6.3). The Yb-Sc and Sc-Sc partial RDFs exhibit values much closer to one. By contrast, for the Al-Sc-Gd alloy, the Gd-Gd, Gd-Sc and Sc-Sc partial RDFs do not exhibit values greater than 1.5 in the unaged condition. The errors associated with the partial RDFs will be discussed in detail in Appendix B.

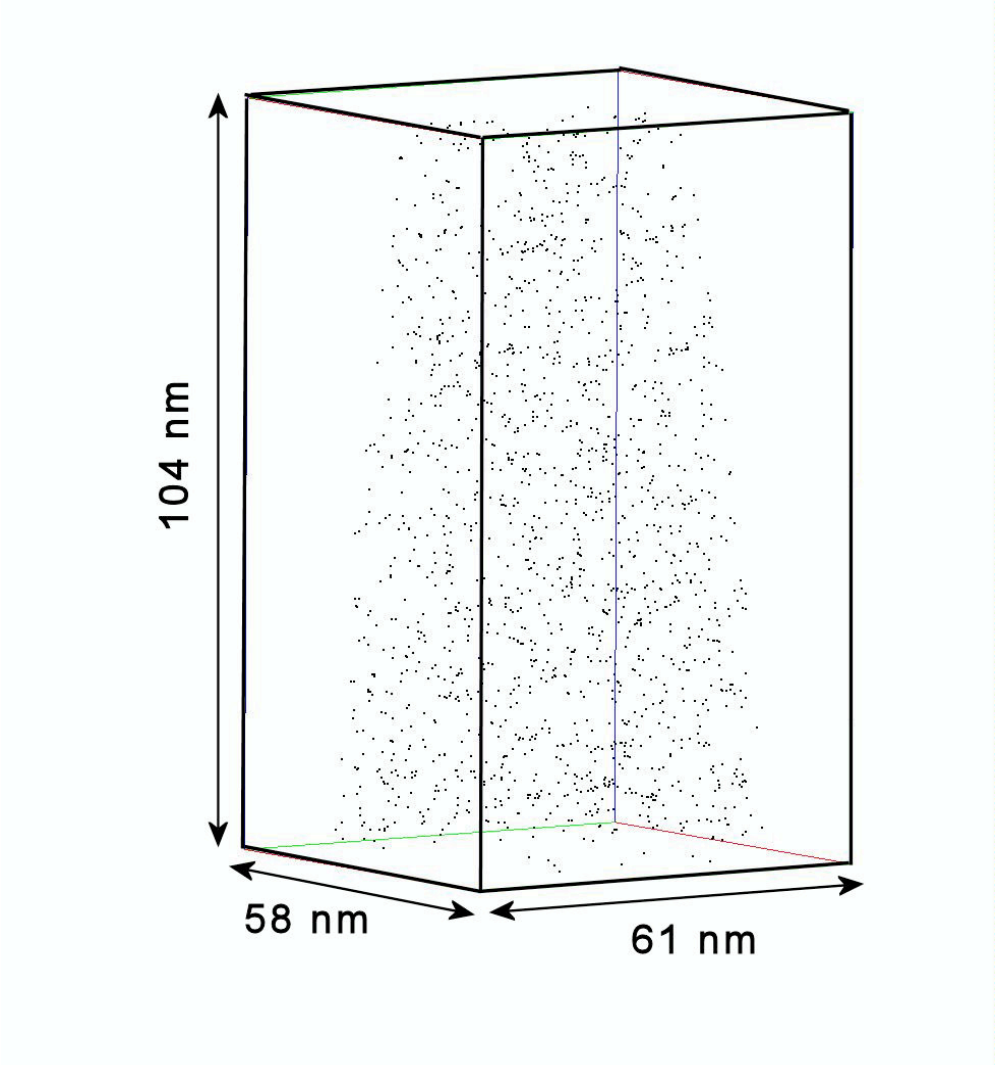

Figure 6.2: Three-dimensional reconstruction of LEAP tomography data of Al-0.06Sc-0.02Yb (at.%) in the unaged state. All of the Yb atoms are displayed in this 6.4 million atom data set. The Sc and Al atoms are not visualized for clarity.

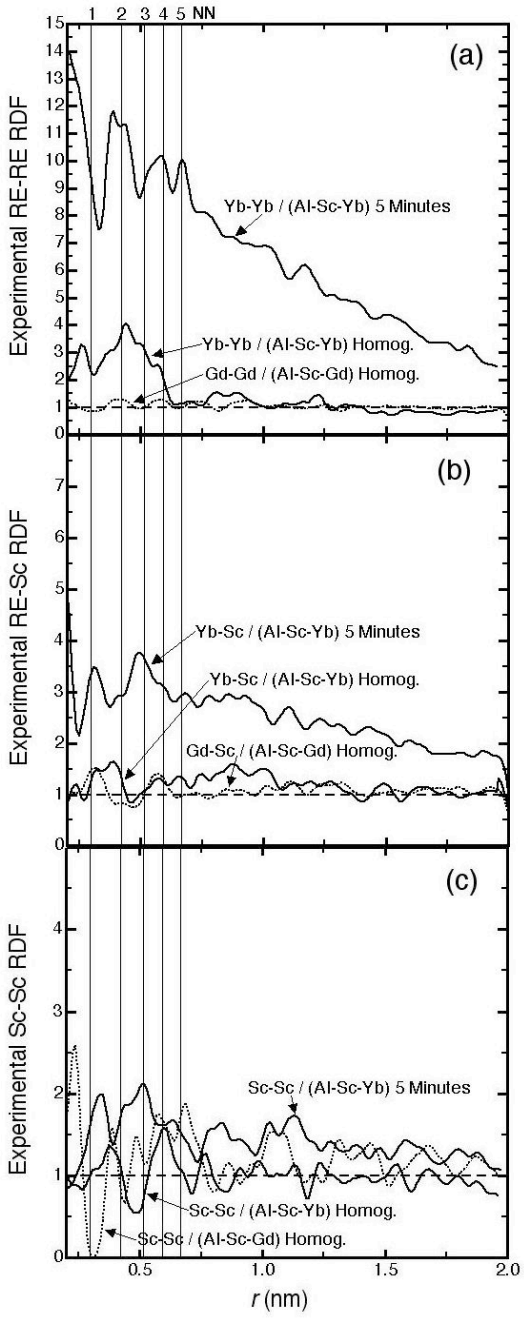

Figure 6.3: Partial radial distribution functions (RDF) vs. radial distance, r, for Al-0.06Sc-0.02Yb for the homogenized state and 5 minutes, and Al-0.06Sc-0.02Gd in the homogenized state. Vertical lines indicate the nearest neighbor distances for the $L1_2$ structure of Al_3Yb. Values of unity indicate a random solid-solution, while a value greater than unity indicates a preference for that type of atom to reside at that distance from the central atom. (a) RE-RE partial RDF; (b) RE-Sc partial RDF; and (c) Sc-Sc partial RDF.

6.3.2.2 Al-Sc-Yb Precipitation at 300˚C

After 10 s of aging, when the hardness is beginning to increase, precipitates are observed by LEAP tomography, using the envelope method to analyze the data [159, 160]. The largest precipitate detected in the data set contains 13 Yb atoms, uncorrected for the efficiency of the detector. After 120 s, the hardness continues to increase and there are some precipitates that have grown beyond the critical nucleus radius of R* = 1.2 nm, as estimated from the precipitate size distribution (PSD) (Fig. 6.4 a and b). The majority of the clusters at both aging times still contain less than 20 detected Yb atoms (uncorrected for detector efficiency), forming a bimodal distribution of precipitates. There are Sc atoms present in all of the precipitates larger than R* = 1.2 nm radius, but only a few of the smaller precipitates contain Sc. During this aging time (30 – 120 s), the volume fraction of precipitates, ϕ, remains constant within the experimentally determined error bars.

After 5 min of aging, the precipitates are clearly visible in the 3-dimensional reconstruction (Fig. 6.5). Fig. 6.6 displays the Sc/Yb concentration vs. cluster size (uncorrected for detector efficiency) after 5 min. Scandium atoms are present in most of the clusters, except for the smallest ones (< 400 detected atoms, uncorrected for detector efficiency). There is a wide range of compositions. There is, however, a slight trend for larger clusters to have a greater Sc content. Fig. 6.7 shows the Yb concentration in the matrix with aging time. Most of the Yb has precipitated out of solution by 5 minutes of aging, with only 27±5 ppm remaining in the matrix out of a total of 200 ppm in the alloy. The proximity histogram demonstrates that the precipitates are Yb rich (Fig. 6.8a) with some Sc having already diffused to the precipitates since, on

average, they contain 1.6 at.% Sc (Fig. 6.8b). Partial RDFs are also calculated for the 5 minute aging treatment, for comparison with the unaged state. After the 5 minute aging treatment, there is a clear positive value for the Yb-Yb partial RDF (Fig. 6.3), reaching values up to 14, indicating a concentration at that distance which is 14 times the average composition in the alloy. The Yb-Sc and Sc-Sc partial RDFs are also greater than unity (Fig. 6.3 b-c), confirming precipitation of $Al_3(Yb_{1-x}Sc_x)$, which is observed directly in the 3-dimensional reconstruction (Fig. 6.5).

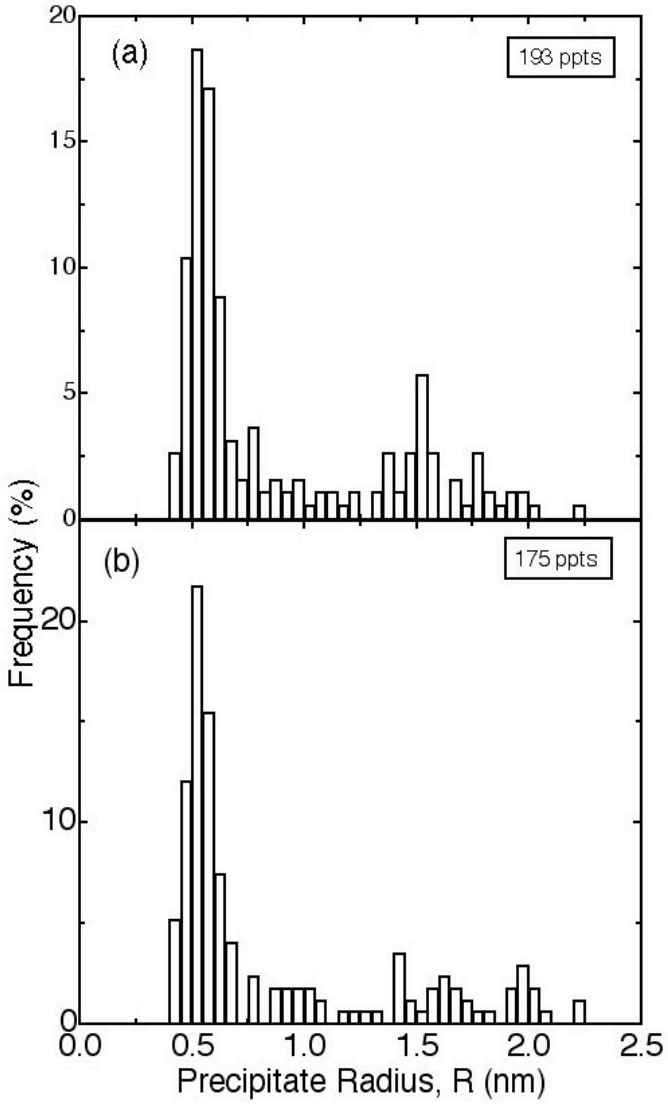

Figure 6.4: Precipitate size distributions (PSDs) for Al-0.06Sc-0.02Yb aged for: (a) 120 s and (b) 10 min of aging at 300°C.

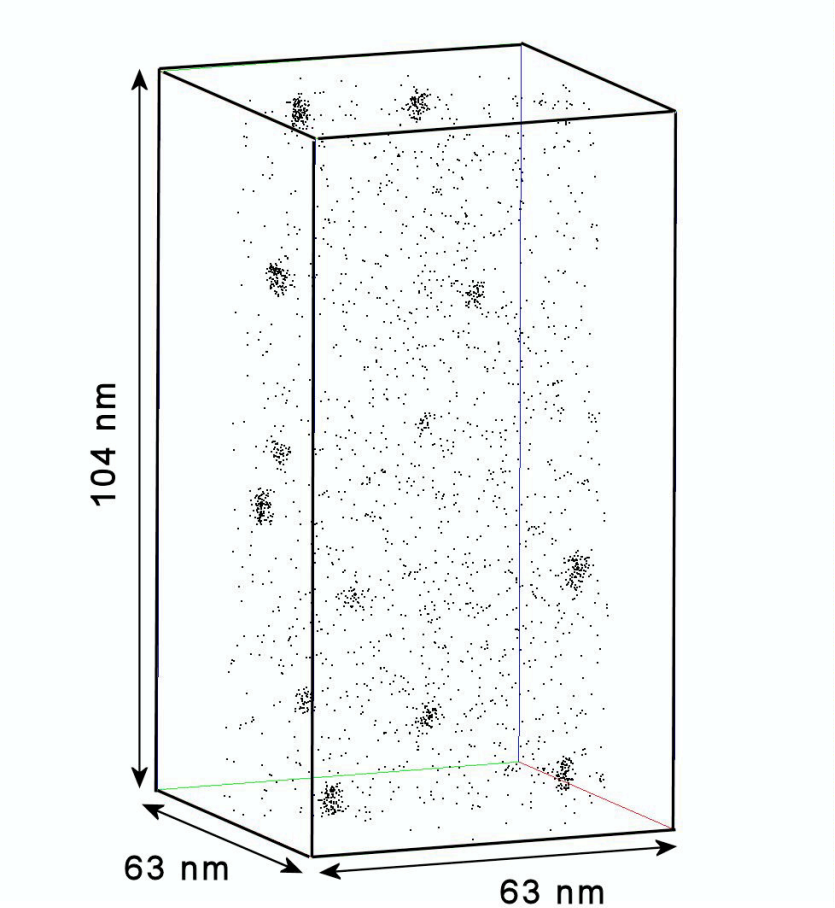

Figure 6.5: Three-dimensional LEAP tomography reconstruction of Al-0.06 Sc-0.02 Yb aged for 5 minutes at 300°C. Only Yb atoms are displayed. The Al and Sc atoms are not shown for the sake of clarity.

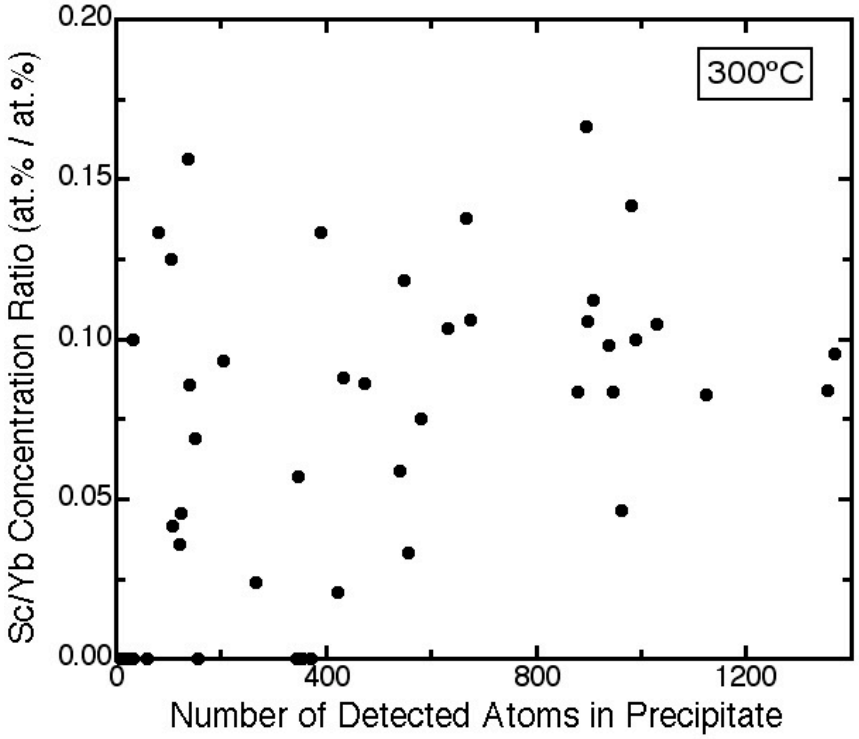

Figure 6.6: The Sc/Yb (at.%/at.%) concentration ratio vs. number of detected atoms in cluster at 5 min of aging. Number of detected atoms is uncorrected for the detector efficiency.

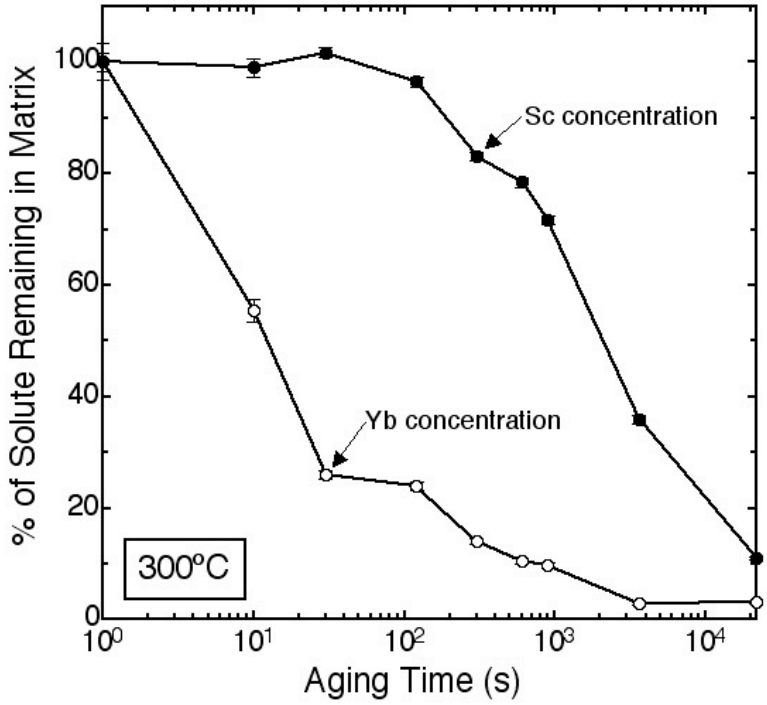

Figure 6.7: Percentage of Sc or Yb remaining in the Al matrix as a function of aging time at 300˚C for Al-0.06 Sc-0.02 Yb (at.%).

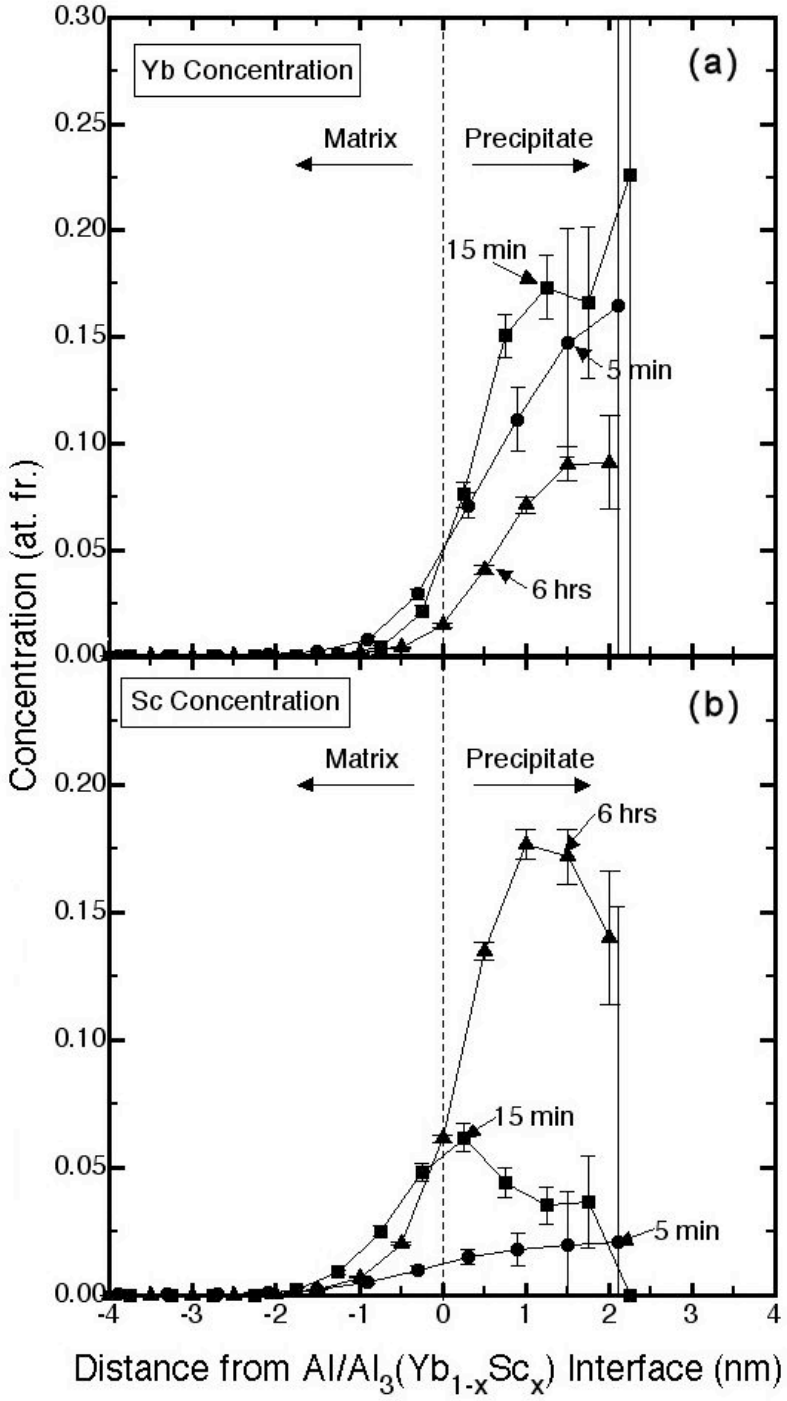

Figure 6.8: Proximity histograms showing: (a) Yb concentration and (b) Sc concentration as a function of radial distance from the α-Al/$Al_3(Yb_{1-x}Sc_x)$ heterophase interface. 5 and 15 minute aging times are based on Yb isoconcentration surfaces of 5%. 6 h aging time is based on a 9at.% Sc isoconcentration surface.

Between 120 s and 15 min of aging, the number density, $N_v(t)$, of precipitates decreases (Fig. 6.9). During this time, there is a plateau in the ϕ vs. aging time plot, with only a slight increase in ϕ from 0.046±0.02 % to 0.053±0.02 % (Fig. 6.10). The average Sc concentration in the precipitates increases during this time from 1.6±0.2% to 5.0±0.9% (Fig. 6.8b), as the slower diffusing Sc diffuses to the precipitates. There is also a decrease in the matrix concentration of Yb between 5 and 15 min, from 27±5 ppm to 13±6 ppm (Fig. 6.7). Finally, the distribution of elements also changes slightly during this aging period: at the shorter aging times, 5 and 10 min, there is a small concentration of Sc in the precipitates, which appears to be relatively homogeneously distributed. After 15 min of aging, however, segregation of Sc to the interface commences to be observed (Fig. 6.8b).

At a longer aging time of 6 h, precipitate nucleation and growth continues, as evidenced by a larger ϕ of 0.29±0.08% (Fig. 6.10). The concentration of Sc in the matrix continues to decrease up to 6 hrs (Fig. 6.7). After 6 h of aging, 91% of the Sc has precipitated from the super-saturated α-Al-matrix (Fig. 6.7). The value of $N_v(t)$ also increases between aging times of 15 min and 6 h (Fig. 6.9), indicating concomitant nucleation and growth. At this point, the Sc has become the majority species in the precipitates (Figs. 6.8a-b, 6.11). The larger precipitates are those that have the highest concentration of Yb with precipitates with 2000-6000 detected atoms (uncorrected for detector efficiency) have a Yb concentration > 1.5% (Fig. 6.11).

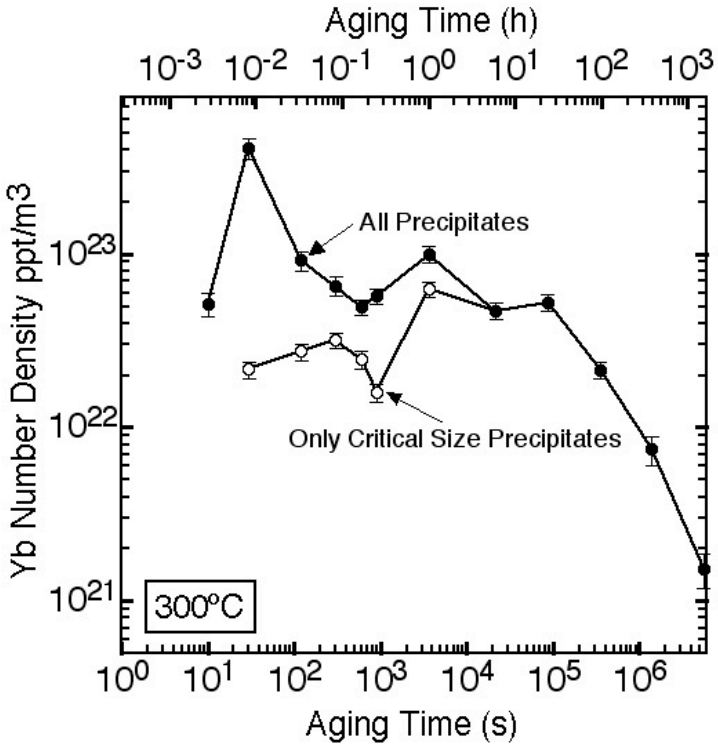

Figure 6.9: Precipitate number density ($N_v(t)$) vs. aging time at 300°C for Al-0.06Sc-0.02Yb showing all of the precipitates and those who have reached R*.

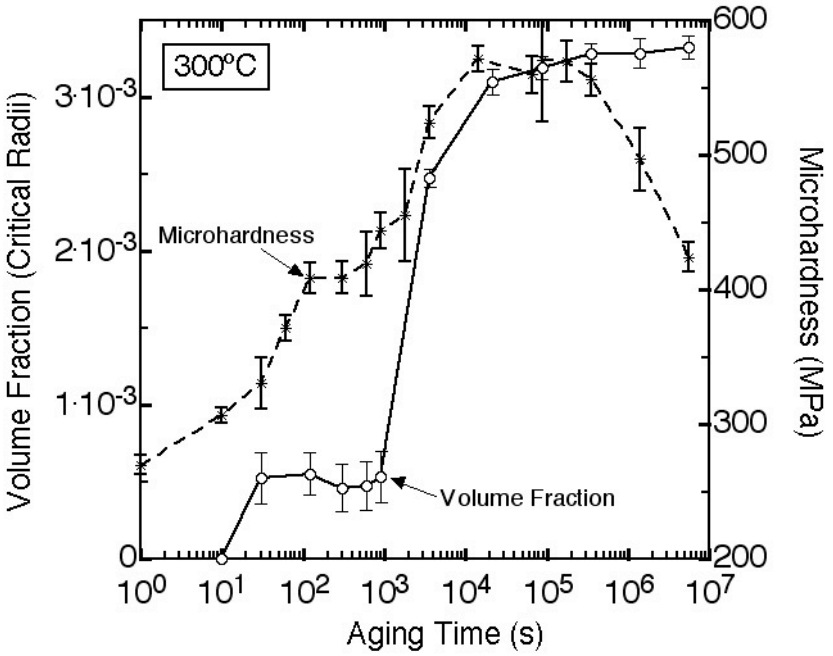

Figure 6.10: Volume fraction, ϕ, and Vickers microhardness of precipitates as a function of aging time at 300°C for Al-0.06 Sc-0.02 Yb (at.%).

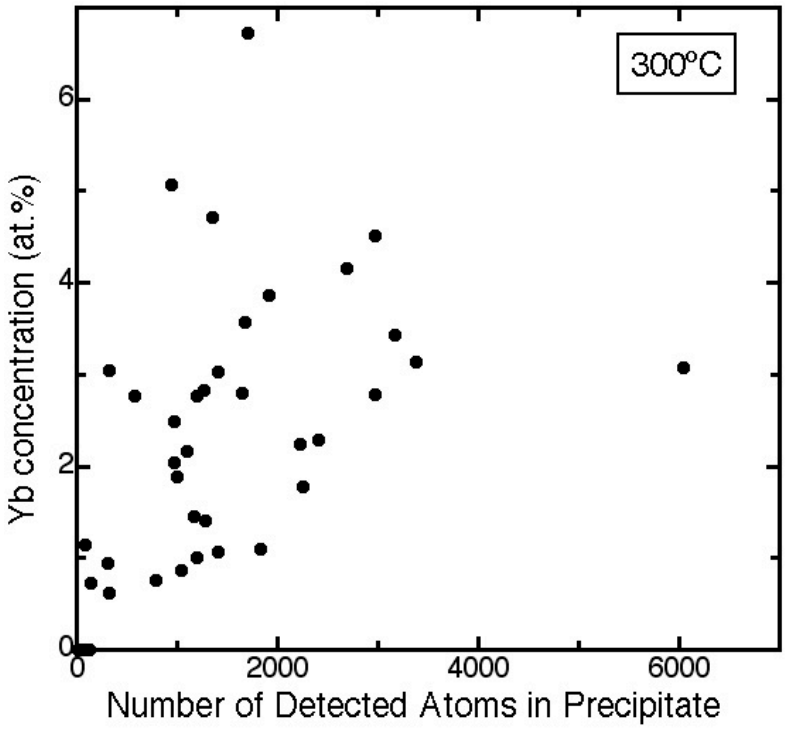

Figure 6.11: Yb concentration (at.%) vs. number of detected atoms (Yb + Sc + Al) the precipitates for the Al-0.06Sc-0.02Yb (at.%) alloy at 6 h of aging. Number of detected atoms is uncorrected for the detector efficiency.

6.4 Discussion

6.4.1 Mechanical Properties

Even in the unaged state, the hardness is greater for the Al-Sc-Yb alloy than for pure Al, Al-Sc-Gd and the other Al-Sc alloys [20, 28] (Fig. 6.1). Although there are no precipitates observed, there is some evidence for ordering/clustering at this aging time, as shown by the partial Yb-Yb RDF (Fig. 6.3). The greater hardness in the unaged state can be explained through the presence of clustering or short-range ordering (SRO) as SRO can increase the flow stress of a material [161]. It has also been suggested that there is an exaggerated or super form of solid-solution

strengthening for clusters, so perhaps this is the mechanism for the strengthening in the unaged state since we are not able to detect genuine precipitates [149, 150, 162].

Precipitation upon aging leads to a larger microhardness value. After only 120 s of aging, the hardness has increased with respect to the unaged state by 140 MPa. Based on the increase in microhardness of the alloy, the yield stress increase is estimated. The yield stress increment is taken as the microhardness increment (the value for an unaged Al-Sc sample subtracted from the aged hardness) divided by 3 [88]. The yield stress increment is plotted as a function of <R(t)> in Fig. 6.12 for 120 seconds of aging. This yield stress increment is then compared to the theoretical strengthening mechanisms, including Orowan looping, order strengthening, modulus strengthening and coherency strengthening (using the equations in Ref. [28]).

Recognizing that there are two populations of precipitates (Fig. 6.4b), the strengthening mechanisms for the volume fractions associated with each of the populations of precipitates is displayed separately. In Fig. 6.12a, the data for the sub-critical nuclei (R < 1.2 nm) is displayed (ϕ = 0.01%). For these precipitates, the dominating strengthening mechanism is the sum of the modulus and coherency strengthening. For the precipitates with R > 1.2 nm ((ϕ = 0.04%), the dominant mechanism is Orowan looping (Fig. 6.12b). Since the measured yield stress increment in both Fig. 6.12 a and b is above the theoretical strengthening curves, it is likely that both of the populations are contributing to the microhardness. Fig. 6.12c shows, however, the curves for the strengthening mechanisms associated with the total volume fraction at 120 s (ϕ = 0.05%) are all higher than the experimentally measured value.

Finally, although ϕ remains fairly constant at 0.05% from 30 s to 15 min, the hardness increases by about 100 MPa. Thus, the structure which forms at longer aging times, which contains larger precipitates, is more effective at strengthening.

6.4.2 Microstructure

6.4.2.1 Unaged State

For the Al-Sc-Yb alloy, the estimated cooling rate is 100-1000 K s^{-1}, thus, there is a possibility that ordering/clustering occurred during quenching. Several different methods have been used to evaluate the presence of clustering and ordering. A study by Wendt and Haasen using a 1-D atom probe plotted the concentration as a function of depth [163]. They pointed out that precipitates smaller than the probe hole diameter, or those that intersected the edge of the hole, would lead to lower concentration peaks that might not be greater than the statistical noise. The contingency table has also been used to determine correlations between elements [150, 154]. The χ^2 method was used by Schmuck et al. [139, 140], although this has proven insensitive to the presence of SRO for certain systems [141].

The method used here is the radial distribution function (RDF), also referred to as pair-correlation functions. Pair-correlation functions were used by de Gueser et al. for studying an Al-Mg-Si alloy to show the interactions between Mg-Mg and Si-Si atoms in the as-quenched state [143, 164]. De Gueser et al. concluded that there were two distinct populations of clusters since

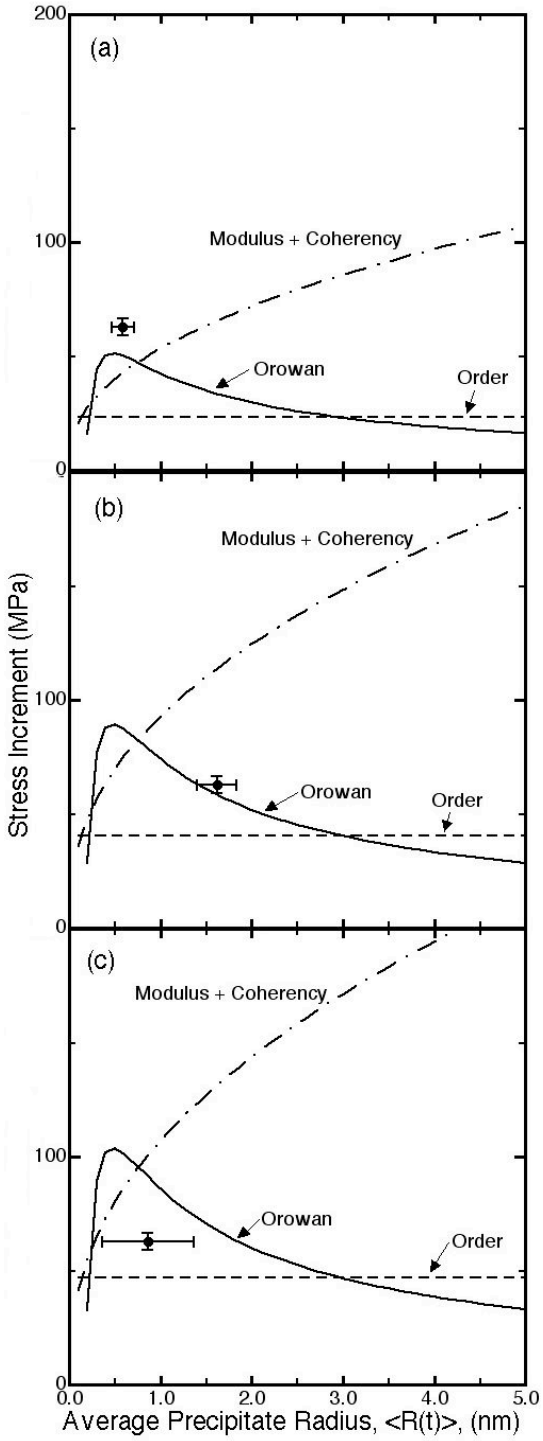

Figure 6.12: Stress increment (MPa) vs. average precipitate radius, <R(t)>, for Al-0.06Sc-0.02Yb (at.%) aged for 120 seconds. (a) sub-critical nuclei below R*; (b) only precipitates beyond the critical radius, R*; and (c) all precipitates.

there is no Si-Mg interaction in the unaged state. Upon aging at 363 K they did find some interaction between the Si and Mg atoms. During room temperature storage, the Mg-Mg clusters dissolve. Furthermore, Sudbrack et. al. utilized an RDF analysis to detect the presence of SRO in a concentrated Ni-Al-Cr alloy [142].

The partial RE-RE RDFs are shown in Fig. 6.3a. In an unaged sample for the Al-Sc-Gd alloy, the Gd-Gd partial RDF shows smaller values, within a range of 0.8 to 1.5, than does the Yb-Yb partial RDF for the Al-Sc-Yb alloy, indicating that there is a smaller interaction among the Gd atoms than among the Yb atoms in the unaged state. The Gd atoms have not had an opportunity to diffuse, since aging at 300˚C has yet to commence. This is consistent with the microhardness results, which show a larger hardness value prior to aging for Al-Sc-Yb compared with Al-Sc-Gd and Al-Sc alloys [99]. The RE-Sc partial RDFs for both alloys in Fig. 6.3b do not exceed values of 1.6, indicating that the correlations in the unaged state are not as strong as for the Yb-Yb interactions. The Sc-Sc partial RDFs (Fig. 6.3c) also exhibit weaker interactions than among the Yb atoms.

These results are not unexpected given that Yb is a faster diffuser in Al than Sc [97] and also the RE for which the diffusivity in Al is known [165]. The fact that Yb is a faster diffuser than the other light RE is not unexpected as Yb has some different chemical and thermodynamic properties than the other lanthanides [166-168], including a lower melting temperature.

6.4.2.2 Precipitation at 300˚C – Temporal Evolution of Composition, Volume Fraction, ϕ, and Microhardness

The temporal evolution of precipitation is displayed in Fig. 6.7, which shows the percentage of solute (Yb or Sc) remaining in the matrix as a function of aging time. The concentration of Yb in the matrix decreases rapidly initially, and on subsequent aging the Sc concentration in the matrix decreases. Ytterbium precipitates out of the matrix at a much faster rate than Sc: 91 % of the Yb precipitates in 15 minutes, while only 29 % of the Sc precipitates in that time. The majority of the Sc precipitates between 15 min and 6 h of aging. The decrease in solute concentration in the matrix is in agreement with the temporal evolution of the measured ϕ and microhardness values (Fig. 6.10). Both ϕ and microhardness exhibit a similar two stage aging behavior. The first increase resulting from the precipitation of Yb into $Al_3(Yb_{1-x}Sc_x)$ and the second increase in ϕ and microhardness is due to diffusion of the slower diffusing Sc to the precipitates.

After 5 minutes, the Sc/Yb ratio vs. number of detected atoms (Fig. 6.6) demonstrates that all of the precipitates have Yb in them, although 55% of the small clusters contain no Sc. Ytterbium clearly plays a role in nucleation since all of the precipitates contain Yb. Fig. 6.6 shows there is a slight trend for the larger clusters to have a higher Sc content, possibly indicating that the larger precipitates nucleated first giving Sc more time to diffuse to the precipitates.

The concentration of Yb in the matrix continues to decrease up to 6 hrs (Fig. 6.7). Despite coarsening of Yb-rich precipitates at earlier aging times, the Yb could be continuing to serve as a nucleation site for the Sc precipitation, since $N_v(t)$ increases during this time. After 6 h of aging,

the smallest precipitates are those that have the smallest concentration of Yb (Fig. 6.11). The reason for this could be that the smallest precipitates are those that formed last when there was less Yb in the matrix with which to nucleate and grow a precipitate.

Due to the sequence of first Yb precipitation and then Sc precipitation (Fig. 6.7 and 6.10), Sc is found close to the heterophase interface while the Yb concentration is greater toward the center of the precipitates (Fig. 6.8 a-b). After 15 min, the Sc has begun to diffuse to the precipitates resulting in segregation at the interface. After 6 h of aging, Sc is the majority species in the outer spherical shell region. Core/shell structures have been observed in the Al-Sc-Ti [102], Al-Sc-Zr [3, 30-32, 34, 78], Al-Li-Sc [145], Al-Li-Ti [146], Al-Li-Zr [48, 147] and Al-Li-Hf [148] systems, due to a two-stage precipitation process which occur due to differences in diffusivity or solubility in the Al matrix at different temperatures. For Al-Sc-X alloys (where X=Ti, Zr or Li), Sc is located in the core while for Al-Sc-RE alloys Sc is found in the shell. The diffusion within the ordered precipitates is anticipated to be slower than in the disordered matrix because it is highly correlated [92]. Deschamps et al. [31] showed that the free energy of formation of a vacancy inside an $L1_2$ precipitate is very large thereby decreasing diffusional transport. The slower diffusion in the precipitate compared with the matrix can result in a pile-up of Sc at the interface.

6.4.2.3 Density of Atoms: Cluster vs. Precipitate

As indicated by the partial RDFs for Yb-Yb and Yb-Sc (Fig. 6.3) and the 3-dimensional reconstructions (Fig. 6.5), the Yb atoms cluster and form precipitates within seconds of aging at 300˚C. To determine how the precipitates form from the clusters, the density of the detected Yb

atoms within the clusters is measured. The distance between each Yb atom to its nearest-neighbor Yb atom is measured. The average minimum distance is then taken for all atoms within a cluster.

The clusters were found using the envelope method, and is described in Appendix A. Clusters of five or more Yb detected atoms are used to generate Fig. 6.13. Aging times ranging from 10 s to 10 min are examined. The small clusters have a wide range of average minimum distances between the Yb atom and its nearest neighbor. For the 5 atom Yb clusters, the values range from 0.4-1.0 nm. This wide range of values at small cluster sizes persists with aging time up to 10 min. At 10 min there are very few Yb atoms left in the matrix (26±12 ppm), hence it does not seem likely that the less dense clusters are simply random concentration fluctuations. An example of a cluster containing 5 detected Yb atoms after 10 min of aging is shown in Fig. 6.14. At the concentration of 26±12 at. ppm, the average Yb atoms are expected to be 11 nm apart, assuming that they are on a regular square lattice array.

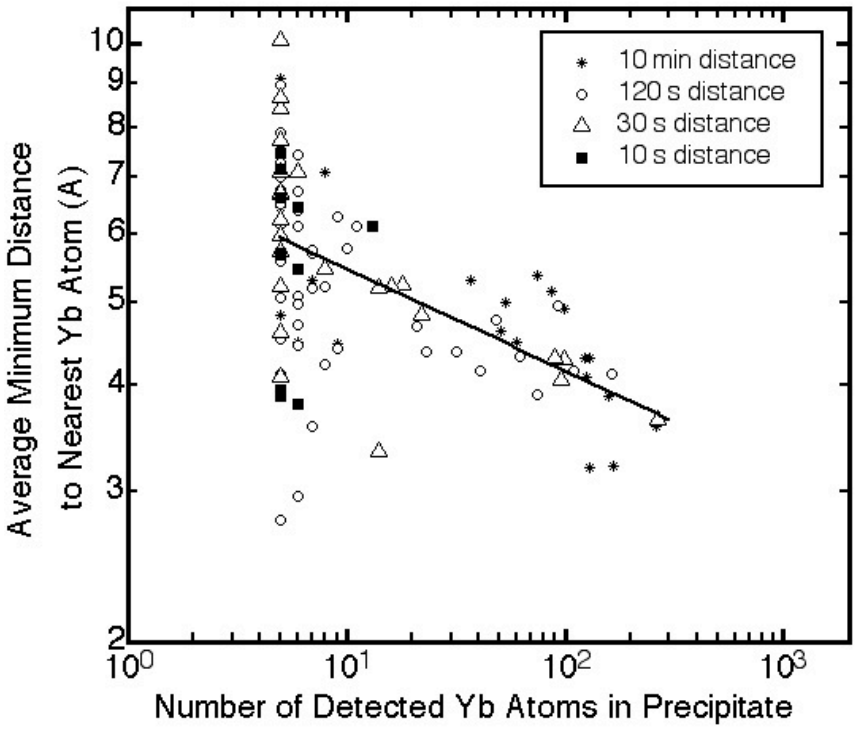

Figure 6.13: Average minimum distance from each Yb atom to the nearest Yb atom in the cluster vs. number of atoms in the cluster for aging times ranging from 10 seconds to 10 minutes at 300˚C.

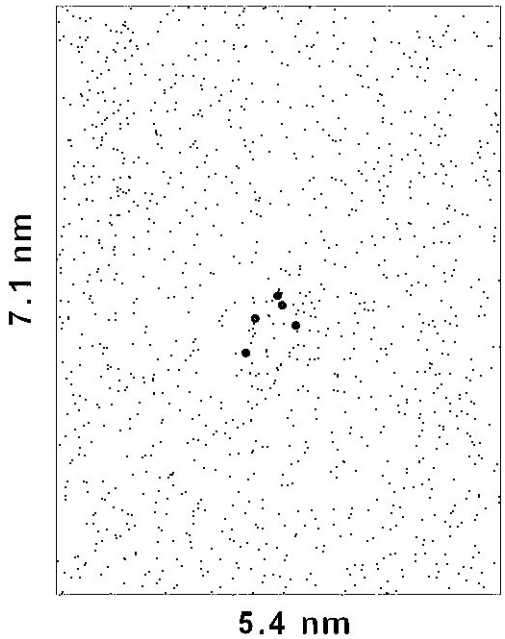

Figure 6.14: Three-dimensional reconstruction from LEAP tomography of a Yb cluster from Al-0.06Yb-0.02Yb (at.%) with a 10 min aging at 300˚C. The data is a 1 nm thick slice from the data set. The large atoms are Yb and the small atoms are Al.

For clusters containing 8 Yb atoms, the average minimum distance values range has shrunk to 0.4-0.7 nm. For clusters over 20 atoms, clusters all have values below 0.54 nm, for all of the aging times. As the clusters become larger the average distance between atoms decreases, with 0.4 nm appearing to be the minimum average atomic separation. The theoretical distance between Yb atoms in the Al_3Yb structure is the second nearest-neighbor distance, which is 0.4201 nm.

The larger clusters are clearly precipitates since they have a density approaching the theoretical value. For only the very smallest clusters (5 Yb atoms) is the average distance to the nearest neighbor over 0.8 nm, which is twice the expected distance. Hence, we argue that most of the smaller "clusters" are indeed Al_3Yb precipitates, with subcritical radii. Under this definition, there are precipitates beginning at 10 s of aging.

6.4.2.4 Precipitation at 300˚C – Nucleation Rate and Critical Precipitate Size

The PSDs (Fig. 6.4) show that there is a peak at small radii but there is also a distribution of precipitates at larger radii. Between the small and large precipitates, there appears to be a minimum frequency in the PSD at R ≈ 1.2 nm, depending on the aging time. According to Xiao and Hassen, the PSD can be used to estimate the value R* of the system [169]. These authors studied Ni-Al alloys and found a bimodal distribution in the PSDs. They also calculated the theoretical critical radius which coincided with the minimum frequency in the PSD. This same effect was also seen in Al-Li alloys [170]. At 120 seconds, R* is estimated to be 1.2 nm. After 10

minutes of aging, there are many more precipitates with larger radii, although there are still many small precipitates (Fig. 6.4b), and R* is still estimated to be 1.2 nm.

The chemical and elastic free energies can be calculated using the following equations [169, 171].

$$\Delta F_{ch} = \frac{RT}{V_m} \sum X_i^{\beta} \ln\left(\frac{X_i^o}{X_i^{\alpha}}\right); \tag{6.1}$$

$$\Delta F_{el} = \frac{2\mu^{\alpha} K^{\beta} \left(\nu^{\beta} - \nu^{\alpha}\right)^2}{\left(3K^{\beta} + 4\mu^{\alpha}\right)\nu^{\beta}}; \tag{6.2}$$

where ΔF_{ch} is the chemical driving force per unit volume, ΔF_{el} is the elastic free energy, R_g is the universal gas constant, T is temperature, X_i^j is the concentration of component i in the j phase, X_i^o is the composition of component i in the overall alloy, μ^{α} is the shear modulus of the matrix phase (25.4 MPa [61]), K^{β} is the bulk modulus of the precipitate phase (91.5 GPa [172]), ν^j is the Poisson ratio in phase j.

Using ideal solution theory, a value of ΔF_{ch} = -439 kJ/mol is obtained for Al-Sc-Yb. This compares to a value of ΔF_{ch} = -447 kJ/mol for a binary Al-0.06Sc solution. The ΔF_{el} values are much smaller than ΔF_{ch}, at ΔF_{el} = 1.1 kJ/mol for Yb precipitation and ΔF_{el} = 1.1 kJ/mol for Sc precipitation in the Al-Sc alloy. Thus, the chemical driving force term dominates.

The quasi-stationary state nucleation rate for precipitates is estimated from the 30 s and 120 s aging times to be 1.91×10^{20} $m^{-3}s^{-1}$. Hyland [18] found for an Al-0.11at.%Sc alloy the quasi-

stationary nucleation rate to be $9x10^{18}$ $m^{-3}s^{-1}$ at 288°C and $1.01x10^{19}$ $m^{-3}s^{-1}$ at 343°C, which are both smaller than the quasi-stationary nucleation rate for the Al-Sc-Yb alloy.

The larger nucleation current with the addition of Yb could be due to the following possible reasons: (i) clusters of RE in the as-quenched state serve as effective heterogeneous nucleation sites for precipitates; (ii) the chemical driving force is greater than in the Al-Sc alloys; or (iii) the interfacial Gibbs free energy between the $L1_2$ precipitate phase and α-matrix phase is smaller in the Al-Sc-Yb than in Al-Sc alloys. The less negative value of ΔF_{ch} for the Al-Sc-Yb alloy indicates that there is a smaller driving force for precipitation, which is contrary to the increased precipitation kinetics. Perhaps the ideal solution approximation, which is based entirely on the initial and final concentrations in the matrix (and the concentration in the precipitates), introduces some error.

6.4.2.5 Diffusivity of Yb in Al

The diffusivity of Yb in the Al-Sc-Yb alloy was calculated using the early aging time data employing an approach first developed by Marquis and Seidman for a ternary alloy [173]. The aging time range utilized is 5-15 minutes. During this time, there is a decrease in the number density of precipitates which have R>R* (R* is measured experimentally in the previous section) (Fig. 6.9). Additionally, there is only a slight increase in ϕ, (Fig. 6.10). Since $N_v(t)$ decreases for aging times between 5 and 15 min., this indicates that the system is in the growth and coarsening regime during this time. A criterion for a quasi-steady state is that the volume fraction is approaching the equilibrium value. Since there is a plateau in the value of ϕ (Fig. 6.10) this indicates that the Al_3Yb phase is approaching an equilibrium. The supersaturation must also be

approaching equilibrium for there to be a quasi-steady-state. This is plotted in Fig. 6.15 and there is a modest (14 %) decrease of ΔC_{Yb}^{α}. This quasi-steady state is only temporary as the Sc begins to precipitate at longer aging times. Using the Marquis-Seidman approach [173] leads to D_{Yb} = (1.5±0.7) x 10^{-18} m^2/s (Table 6.1).

A second method for calculating D_{Yb} is from the critical time required for the formation of a distribution of metastable nuclei, as in Ref. [169]. The incubation time is taken to be 5±4 s since there are no clear precipitates in the as-quenched state but there are precipitates after 10 s of aging. This leads to D_{Yb} = (1.4±1.7)x10^{-19} m^2 s^{-1} (Table 6.1).

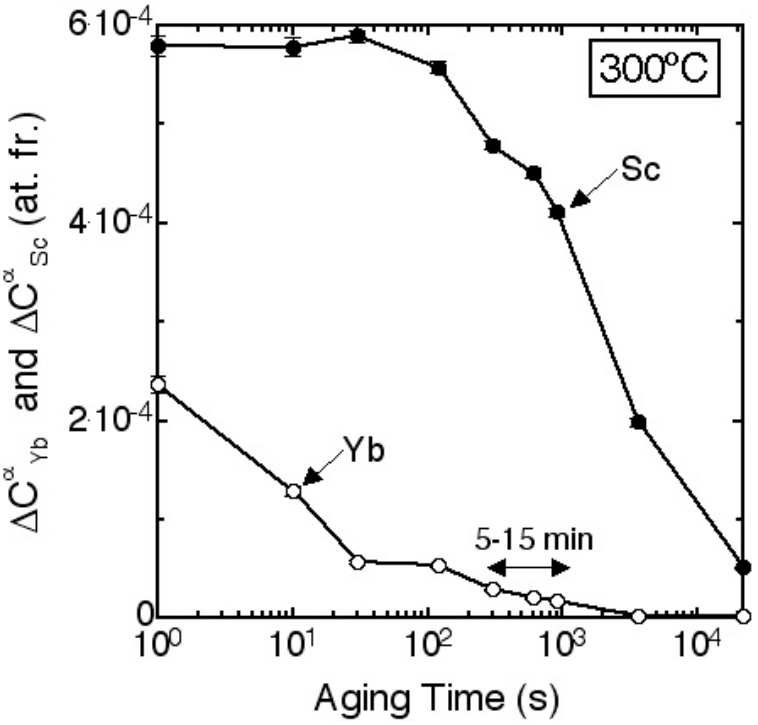

Figure 6.15: Supersaturation of Yb, ΔC_{Yb}^{α}, and Sc, ΔC_{Sc}^{α}, in the matrix vs. aging time at 300°C.

A third method utilized to calculate D_{Yb} is a diffusion distance measurement. Between the 10 s and 30 s aging times, the increase in the average number of atoms in a precipitate is calculated. Assuming an initial uniform distribution of atoms in the matrix, it is possible to determine the average distance from which the Yb atoms would have had to diffuse to reach the nearest cluster. Using the change in the average precipitate sizes between 10 and 30 s, this results in $D_{Yb} = (3.6\pm2.9)\times10^{-19}$ m^2 s^{-1} (Table 6.1).

The diffusivity of Sc in Al at 300°C is 9×10^{-20} m^2 s^{-1} [97]. Thus, the value of D_{Yb} that is calculated for each of the three methods above is greater than the diffusivity of Sc in aluminum, which is consistent with our experimental observations. This is physically reasonable given the faster precipitation kinetics of Yb compared with that of Sc. The three values obtained here are slower than the D_{Yb} value for the binary Al-Yb alloy, calculated to be $(5.7\pm1.9)\times10^{17}$ m^2 s^{-1}. It is possible that the presence of Sc is slowing down the diffusion of Yb.

Table 6.1: Different Methods Utilized to Calculate the Diffusivity of Yb in Al, D_{Yb} at 300°C.

Method	D_{Yb} (m^2 s^{-1})	Comments
Incubation time of metastable distribution of undercritical nuclei	$(1.4\pm1.7)\times10^{-19}$	Using approach from Ref. [169]
Coarsening data between 5 – 15 min	$(1.6\pm0.8)\times10^{-18}$	Some Sc is diffusing to the precipitates during this period.
Diffusion distance measurement	$(3.6\pm2.9)\times10^{-19}$	Distance atoms had to travel to form cluster.

6.5 Conclusions

The kinetic pathways for the evolution of the microstructures of the Al-0.06at.%Sc-0.02at.%Yb and Al-0.06at.%Sc-0.02at.%Gd alloys are studied at early aging times, from the unaged state to 6 h of aging at 300˚C.

- A two-stage precipitation sequence is found: an initial rise within 1 minute of aging due to the precipitation of Yb followed by a plateau in microhardness and volume fraction, ϕ, and a second increase in microhardness and ϕ due to the precipitation of Sc. In contrast, in the Al-Sc-Gd alloy, Sc-rich $Al_3(Sc_{1-x}Gd_x)$ precipitates are the first ones to form.
- Yb-rich precipitates are found within seconds of aging at 300˚C, yielding a $N_v(t)$ value of $(3.2\pm0.8)x10^{22}$ ppt/m^3 of $Al_3(Yb_{1-x}Sc_x)$ precipitates after 5 min., which contain a majority of the Yb atoms with ~1-2 % Sc atoms. With increasing aging time the concentration of Sc in the precipitates continues to increase as Sc diffuses to the precipitates.
- There is evidence of clustering/ordering in the unaged state for the Al-Sc-Yb alloy, since the partial Yb-Yb RDF reaches values of up to 4 in the unaged state. This is in contrast to the Al-Sc-Gd alloy in which the values for the Gd-Gd partial RDF do not exceed 1.5.
- In the Al-Sc-Yb alloy, it is determined that precipitates that have 5 or more detected Yb atoms contribute to the hardening.
- The diffusivity of Yb is calculated by several methods. It is found for each of the three methods utilized, a higher diffusivity is calculated than that of Sc in Al at 300˚C. However, the diffusivities calculated for the ternary are lower than that calculated for the binary Al-Yb alloy, indicating that Sc slows the diffusion of Yb.

7. Temporal Evolution of $Al_3(RE_{1-x}Sc_x)$ and $Al_3(Sc_{1-x}RE_x)$ Precipitation in Dilute Al-Sc-RE Alloys (RE = Yb or Gd)

7.1 Introduction

As shown in Chapters 5 and 6, the addition of small concentrations of Yb or Gd (50-200 at. ppm) to the Al-0.06at.%Sc alloy results in improved creep resistance and successful replacement of the Sc with the RE. The two-stage precipitation sequence of the Al-Sc-Yb additions was also examined. In this chapter, the coarsening kinetics of the $Al_3(Sc_{1-x}RE_x)$ precipitates for aging at 300˚C is examined for aging times ranging from 24 – 1536 h.

7.2 Experimental Methods

The composition of the alloy studied was the same as in the pervious chapter: Al-0.06 at.%Sc-0.02 at.%RE (RE = Yb or Gd) (all compositions are in at.% in the remainder of this chapter unless otherwise noted). The composition was verified by ATI Wah Chang (Albany, OR) to be: Al-(0.058±0.003)Sc-(0.024±0.008)Yb, Al-(0.061±0.003)Sc-(0.018±0.009)Gd (at.%) (alloys hereafter referred to as Al-Sc-Yb and Al-Sc-Gd). Details of the alloy processing are similar to those of Al-Sc-RE alloys containing 0.005at.% of Yb or Gd (Chapter 5). The microstructural analysis procedures are also similar to those performed on the Al-Sc-RE alloys with 0.005at.% of Yb or Gd and the Al-Sc-Ti alloy (Chapter 3).

7.3 Experimental Results

7.3.1 Microhardness

The Al-0.06 Sc-0.02 Yb and Al-0.06 Sc-0.02 Gd alloys (hereafter abbreviated as Al-Sc-Yb and Al-Sc-Gd, respectively) achieve peak Vickers microhardness values, which are greater by a factor of 1.7 and 1.6, respectively, than the peak hardness of the Al-0.06 Sc alloy at 300ºC (Fig. 7.1). After achieving peak hardness, the hardness begins to decrease upon further aging, providing a first indication of the presence of over aging and the commencement of the growth and coarsening stage.

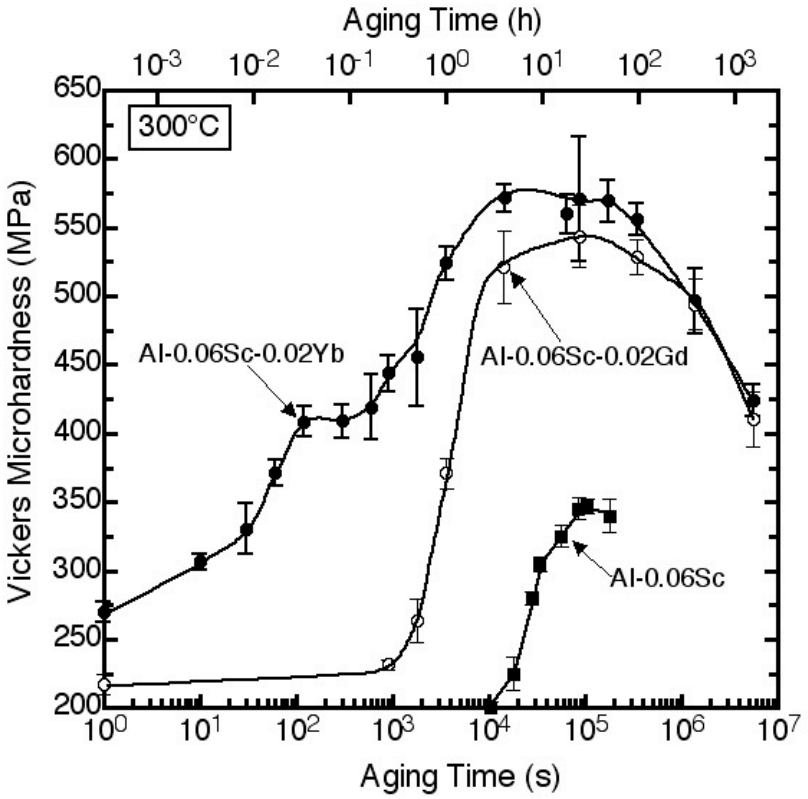

Figure 7.1: Vickers microhardness of Al-0.06 Sc-0.02 Yb and Al-0.06 Sc-0.02 Gd *vs*. aging time at 300°C, compared with a binary Al-0.06 Sc alloy (at.%) [21, 26].

The Al-Sc-Yb alloy exhibits a shorter incubation time than do the Al-0.06 Sc, Al-0.12 Sc and Al-Sc-X alloys with similar volume fractions, ϕ, where X is Mg, Zr, or Ti [26, 28, 100, 102]. Whereas in the other Al-Sc and Al-Sc-X alloys the incubation times range from 0.25 - 2 h, the Al-Sc-Yb alloy exhibits a slightly increased hardness over the other homogenized Al alloys and pure Al upon direct quenching from the homogenization temperature: 270 MPa compared with ~200 MPa for Al-0.06 Sc and Al-0.06 Sc-0.005 Zr alloys [28]. Upon aging, the hardness continues to increase rapidly: after only 5 min and it has increased over the homogenized value by 140 MPa. Before the final peak hardness is achieved, there appears to be an initial rapid rise in hardness followed by a plateau, which is followed by a second rapid rise in hardness. This is due to the disparate precipitation kinetics of Yb and Sc. The nucleation and growth (i.e. the early aging times) in the Al-Sc-Yb system are discussed in detail elsewhere [100, 174].

7.3.2 Microstructure: Volume Fraction, ϕ, Precipitate Radius, <R(t)> and Number Density, $N_v(t)$

For both Al-Sc-RE alloys, the precipitates ($L1_2$ structure) are approximately spheroidal and coherent with the matrix up to the longest aging time analyzed (1536 h), as indicated by the presence of Ashby-Brown or coffee-bean strain contrast, which is typical of coherent precipitates (Fig. 7.2). The average precipitate radius remains small during aging in both alloys (Fig. 7.3). For the Al-Sc-Yb alloy, the average radius, <R(t)>, of the precipitates increases from 2.9 ± 0.5 nm after 24 h to 5.5 ± 1.2 nm after 1536 h of aging, as determined by LEAP tomography (2-3 samples per aging treatment). For the Al-Sc-Gd alloy, <R(t)> increases from 2.4 ± 0.3 nm to 5.1

± 0.4 nm between 24 and 1536 h, respectively (Table 7.1). At a given aging time, the Al-Sc-Gd alloy has a smaller <R(t)> value than the Al-Sc-Yb alloy.

The number density of precipitates, $N_v(t)$, was determined from the LEAP tomographic data (Fig. 7.4 and Table 7.1), by counting the individual precipitates in the 3-D reconstructions from 2-3 different samples. After the nucleation and growth stage, this plot exhibits both the growth and coarsening stages of precipitation. The data for the Al-Sc-Yb alloy reaches a maximum $N_v(t)$ value of (5.25±0.55) x 10^{22} m^{-3} at 24 h. The value of $N_v(t)$ at peak hardness for the Al-Sc-Gd alloy is slightly smaller, (4.1±0.44) x 10^{22} m^{-3} at 96 h. Both the Al-Sc-Yb and the Al-Sc-Gd alloys have larger $N_v(t)$ values than the binary Al-Sc alloys with similar volume fractions of precipitates (ϕ = 0.24% and 0.49%, respectively) [21]. Fig. 7.4 also demonstrates that the onset of coarsening is later in the Al-Sc-Gd alloy than in the Al-Sc-Yb alloy.

Beyond 24 h of aging for Al-Sc-Yb and 96 h for Al-Sc-Gd, when the number density, $N_v(t)$ values are decreasing, the volume fraction, ϕ, achieves ϕ = 0.33±0.01 % for Al-Sc-Yb and ϕ = 0.28±0.01 % for Al-Sc-Gd (as calculated for the longest aging time). These values were calculated from the fraction of solute atoms remaining in the matrix, as measured by LEAP tomography. This fraction was then subtracted from the exact composition of the alloy to obtain the amount in the precipitates. The value of ϕ is slowly increasing between 24 and 1536 h for both alloys (Fig. 7.5), although there is only a small change (0.02% for Al-Sc-Yb and 0.005% for Al-Sc-Gd) indicating that the transformation is nearly complete and ϕ is close to the equilibrium volume fraction, ϕ^{eq}. This small change in ϕ indicates that the system is most likely in a quasi-

stationary-state and in the growth and coarsening regime rather than pure coarsening. There is a 15 % smaller value of ϕ in the Al-Sc-Gd alloy, as compared with the Al-Sc-Yb alloy, due to a smaller Gd concentration in the precipitates compared with Yb in the Al-Sc-Yb alloy and a slightly smaller overall concentration of Sc in the Al-Sc-Gd alloy.

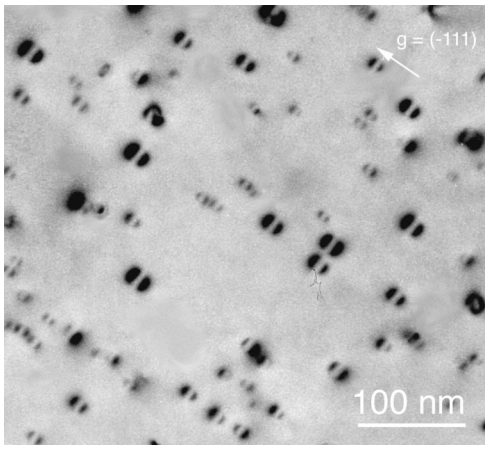

Figure 7.2: Two-beam bright-field TEM image of Al-0.06 Sc-0.02 Yb aged for 1536 h at 300˚C showing Ashby-Brown strain contrast typical of coherent precipitates. [110] orientation.

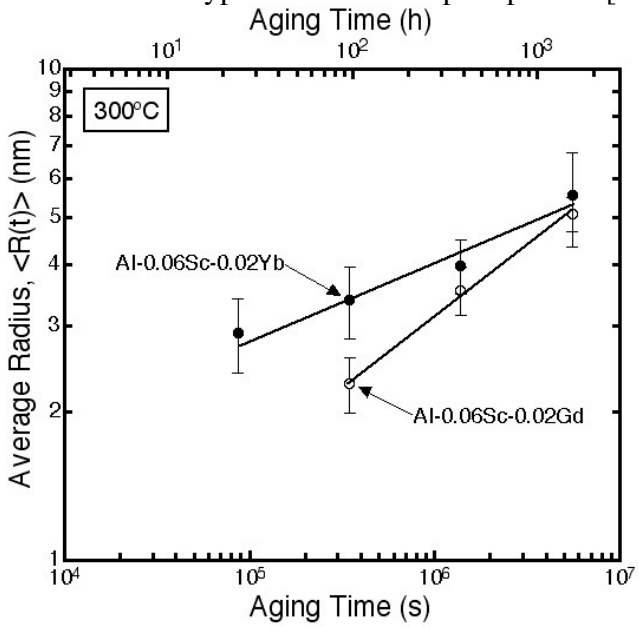

Figure 7.3: Average precipitate radius, <R(t)>, vs. aging time at 300°C for Al-0.06Sc-0.02Yb and Al-0.06Sc-0.02Gd alloys.

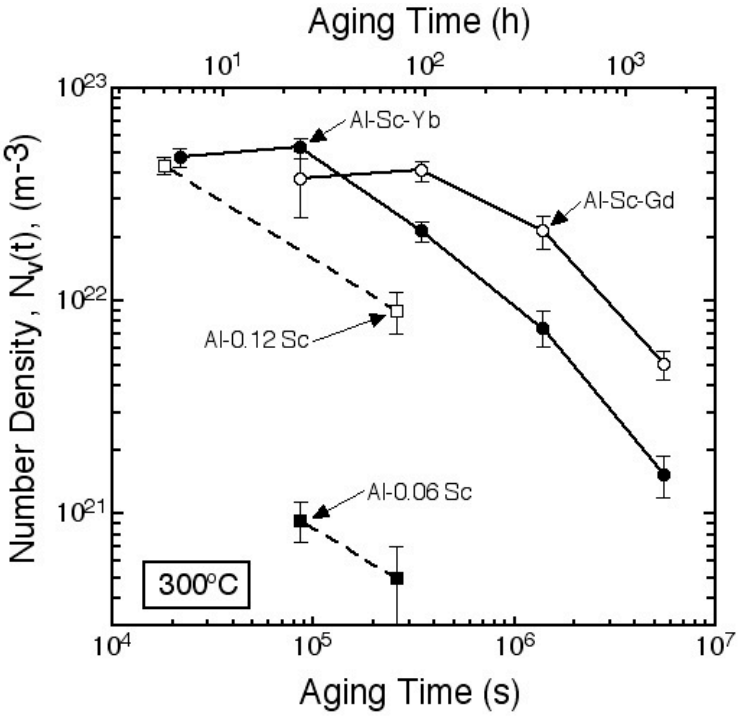

Figure 7.4: Number density of precipitates, $N_v(t)$, vs. aging time at 300°C for Al-Sc-Yb and Al-Sc-Gd. The slopes of the curves represent the time exponents which are smaller than minus one.

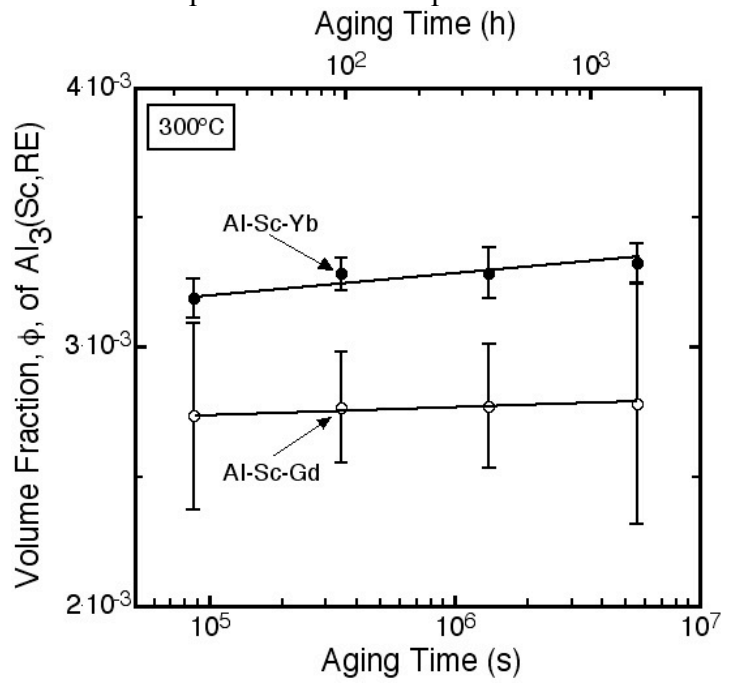

Figure 7.5 Volume fraction (ϕ) of $Al_3(Sc,RE)$ precipitates vs. aging time at 300˚C for Al-Sc-Yb and Al-Sc-Gd alloys.

Table 7.1: Average Precipitate Radii, <R(t)>, and Number Densities, $N_v(t)$, of Al-0.06 Sc-0.02 Yb and Al-0.06 Sc-0.02 Gd.

Alloy – aging treatment	Average Precipitate Radius, <R(t)>, (nm)	Number Density of precipitates, $N_v(t)$, (m^{-3})
Al-Sc-Yb - 6 h	2.38±0.4	$(4.73\pm0.5)\times10^{22}$
Al-Sc-Yb - 24 h	2.9±0.5	$(5.25\pm0.55)\times10^{22}$
Al-Sc-Yb - 96 h	3.4±0.6	$(2.14\pm0.23)\times10^{22}$
Al-Sc-Yb - 16 d	4.0±0.5	$(7.5\pm1.4)\times10^{21}$
Al-Sc-Yb - 64 d	5.5±1.2	$(1.14\pm0.57)\times10^{21}$
Al-Sc-Gd - 24 h	2.4±0.3	$(3.75\pm1.27)\times10^{22}$
Al-Sc-Gd - 96 h	2.3±0.3	$(4.1\pm0.44)\times10^{22}$
Al-Sc-Gd - 16 d	3.6±0.4	$(2.14\pm0.38)\times10^{22}$
Al-Sc-Gd - 64 d	5.1±0.4	$(5.69\pm2.14)\times10^{21}$

7.3.3 Temporal Evolution of Composition of the α-Matrix and the $L1_2$ Precipitates

The concentration of Sc and RE in the α-Al matrix were measured by LEAP tomography. For the Al-Sc-Yb alloy, the Yb and Sc concentrations decrease with increasing aging time even at the longest aging time, which is consistent with an increasing volume fraction (Fig. 7.6). In the Al-Sc-Gd alloy, the Sc matrix concentration decreases up to 1536 h of aging, while the Gd matrix concentration remains constant, within error, (Fig. 7.7) between 24 and 1536 h of aging.

The compositions of the precipitates were also measured by LEAP tomography. In the Al-Sc-Yb alloy, Yb precipitates out faster than does Sc [100], thereby initially forming $Al_3(Yb_{1-x}Sc_x)$ precipitates. With increasing aging time, the concentration of Sc in the precipitates continues to increase, until it is greater than that of Yb, thereby forming $Al_3(Sc_{1-x}Yb_x)$ precipitates (Fig. 7.8). The Yb/Sc concentration ratio (at.%) reaches a constant value of 0.25±0.01 after 96 h of aging.

The distribution of elements within the precipitates in the Al-Sc-Yb alloy changes between 24 and 1536 h of aging. After 24 h of aging, a Sc-rich spherical shell around a Yb-rich core is clearly observed from a slice through a three-dimensional LEAP reconstruction (Fig. 7.9). In Fig. 7.10 another three-dimensional reconstruction is shown which contains isoconcentration surfaces of 8% Yb delineating the cores of the precipitates. The core/shell structure is also observed in the proxigram (Fig. 7.11). The segregation of Sc to the α-Al/$Al_3(Sc_{1-x}Yb_x)$ heterophase interface is pronounced after aging for 24 hrs (Fig. 7.11a). After aging for 1536 h (64 days), the Yb-rich core of atoms is less pronounced as the Sc concentration now exceeds the Yb concentration everywhere within the precipitates (Fig. 7.11b). At 1536 h, however, some segregation of Sc to the heterophase interface is still observed, as evidenced by the positive values of the relative Gibbsian interfacial excess of Sc at the α-Al/$Al_3(Sc_{1-x}Yb_x)$ interface (Fig. 7.12).

In the Al-Sc-Gd alloy, precipitation occurs less rapidly than in the Al-Sc-Yb alloy, as indicated by the hardness measurements, which do not increase above the homogenized hardness value until after 15 minutes of aging at 300°C. After 24 h, the concentration of Gd in the precipitates is only 2.7 at.%. At aging times of 96 h and longer, the Gd concentration decreases somewhat and then remains approximately constant at 2.0 at.%. Furthermore, the onset of coarsening of the precipitates in Al-Sc-Gd alloy occurs after 96 h since $N_v(t)$ remains constant, within error, between 24 and 96 h. Interfacial segregation of Sc is observed for all of the aging times, with the Gd tending toward the center of the precipitate. The relative Gibbsian interfacial excess of Sc at the α-Al/$Al_3(Sc_{1-x}Gd_x)$ interface, as given by Eq. 7.1, increases slightly during the growth and coarsening regime (Fig. 7.10).

$$\Gamma_{Sc}^{Al,Gd} = \Gamma_{Sc} - \Gamma_{Gd}\left(\frac{C_{Al}^{\alpha}C_{Sc}^{\beta} - C_{Al}^{\beta}C_{Sc}^{\alpha}}{C_{Al}^{\alpha}C_{Gd}^{\beta} - C_{Al}^{\beta}C_{Gd}^{\alpha}}\right) - \Gamma_{Al}\left(\frac{C_{Sc}^{\alpha}C_{Gd}^{\beta} - C_{Sc}^{\beta}C_{Gd}^{\alpha}}{C_{Al}^{\alpha}C_{Gd}^{\beta} - C_{Al}^{\beta}C_{Gd}^{\alpha}}\right); \qquad (7.1)$$

where Γ_m is the Gibbsian interfacial excess of element m and C_m^n is the equilibrium concentration of element m in phase n, where α and β are the matrix and precipitate phases, respectively. Both Γ_m and C_m^n were obtained from the 3DAP tomography proxigrams.

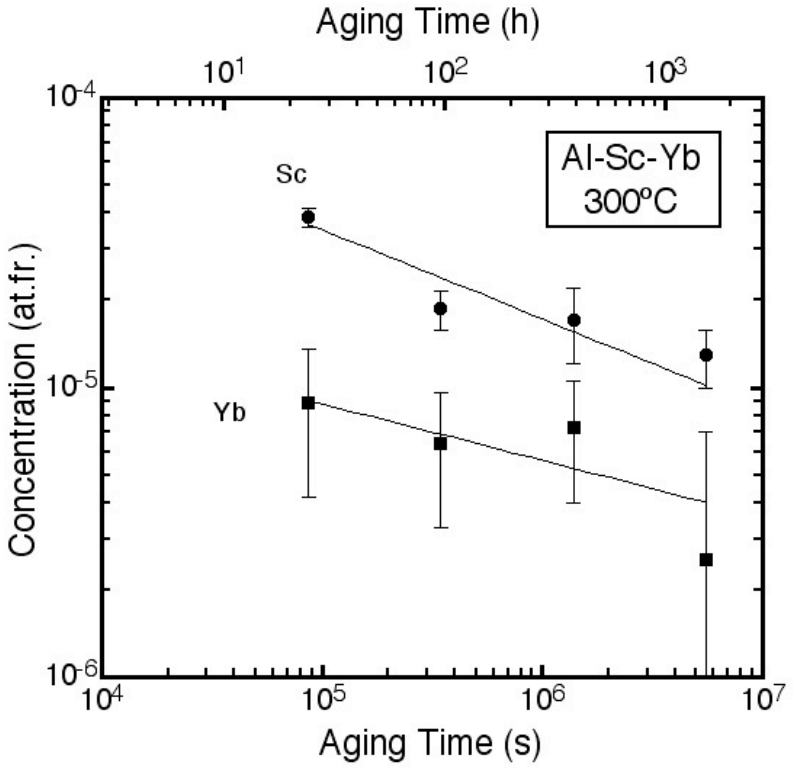

Figure 7.6: Concentrations of Yb and Sc in the matrix vs. aging time at 300°C in the Al-Sc-Yb alloy.

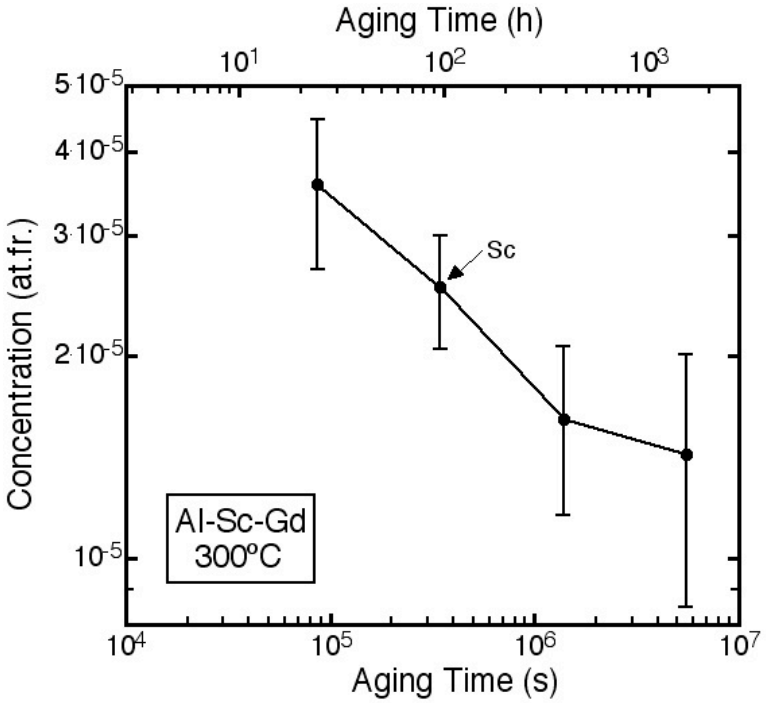

Figure 7.7: Concentration of Sc in the α-Al matrix in the Al-0.06Sc-0.02Gd alloy.

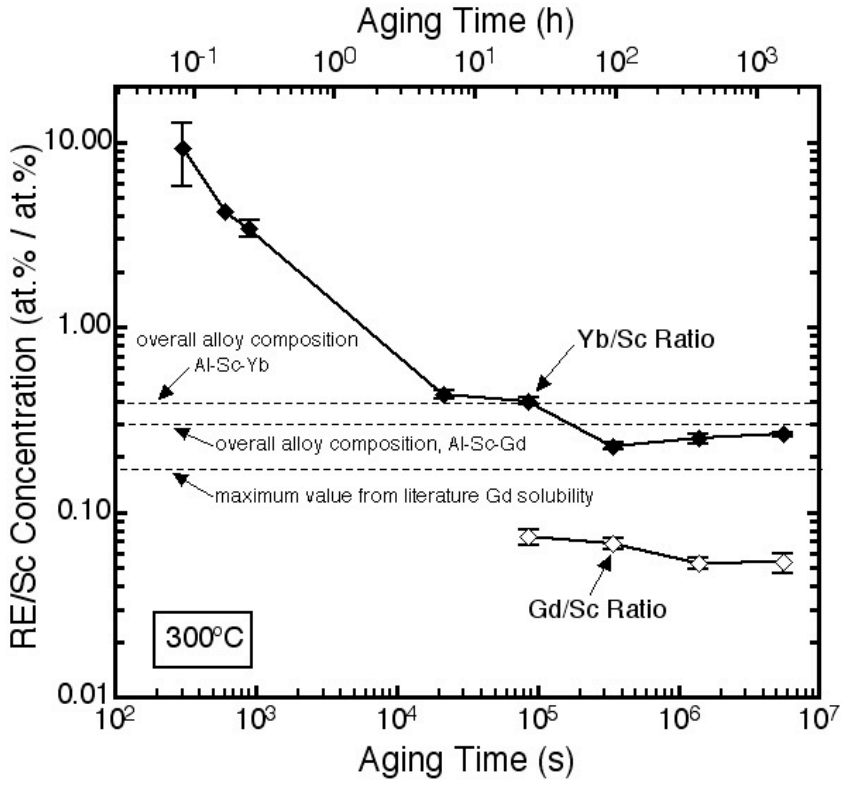

Figure 7.8: Ratio of RE to Sc concentration (at%/at.%)) in the precipitates *vs*. aging time at 300°C for the Al-Sc-Yb and Al-Sc-Gd alloys.

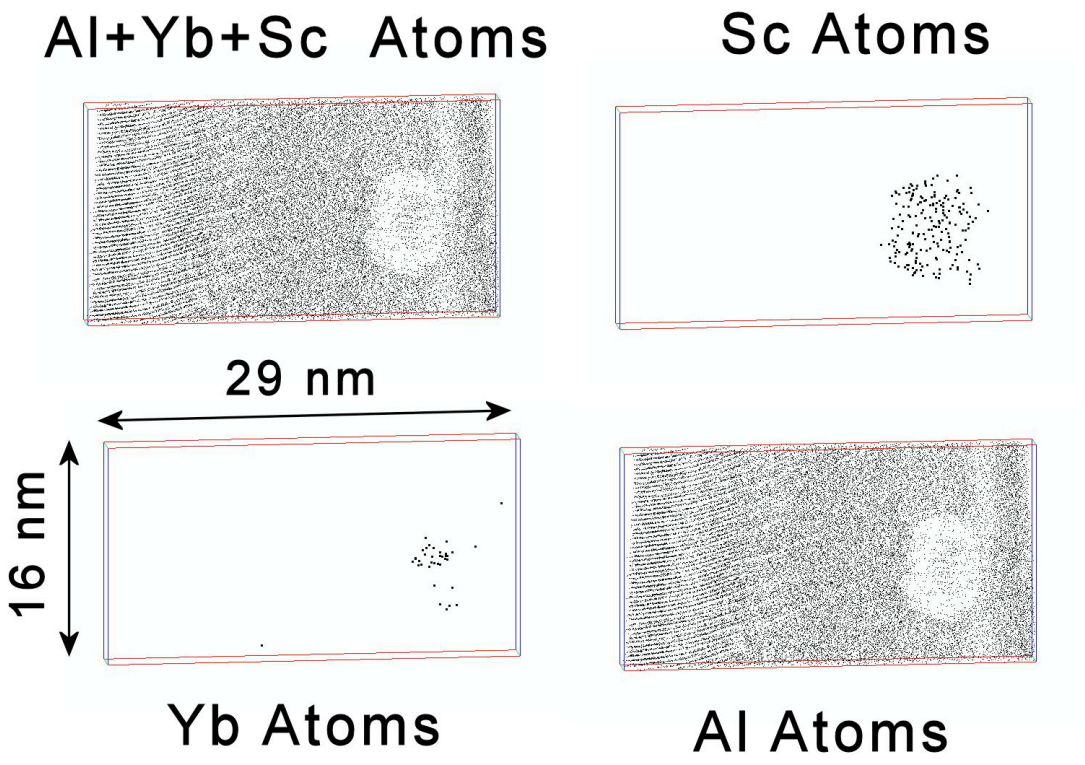

Figure 7.9: LEAP reconstruction of Al-Sc-Yb showing core/shell atomic density. 2 nm thick slice. The differences in evaporation field can be observed in the differences in atomic densities between the core, shell and matrix phases.

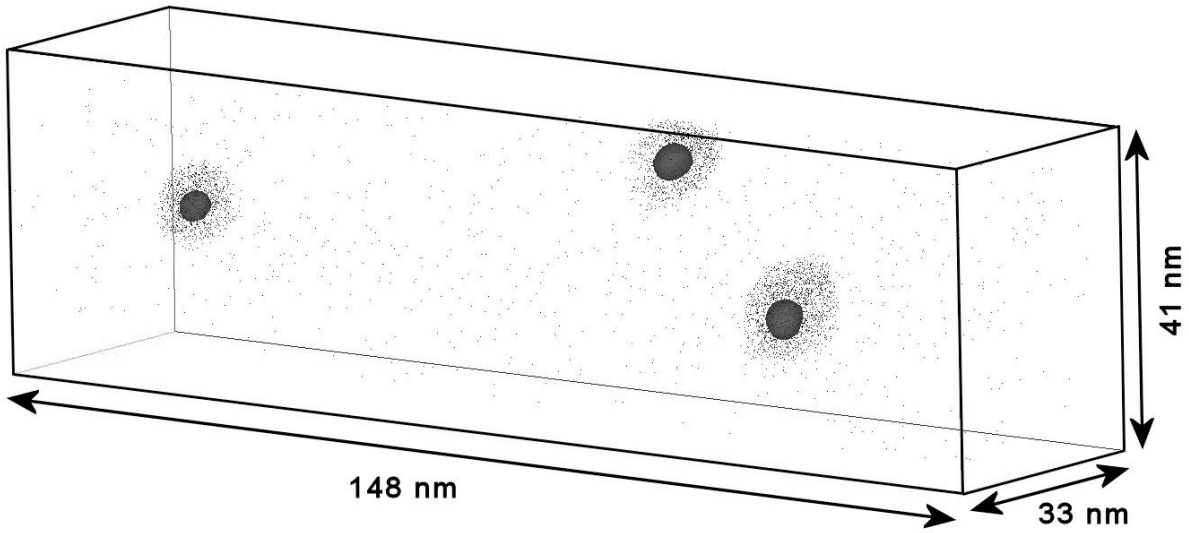

Figure 7.10: Three-dimensional atom-probe tomographic reconstruction exhibiting three $Al_3(Sc_{1-x}Yb_x)$ precipitates in an Al-0.06Sc-0.02Yb alloy for a 24 h aging time at 300°C. The 8 at.% Yb isoconcentration surface within the precipitates delineates the Yb core, with the Sc atoms surrounding the Yb core. The Al atoms are omitted for clarity. Total volume of the parallelepiped is 200,244 nm^3.

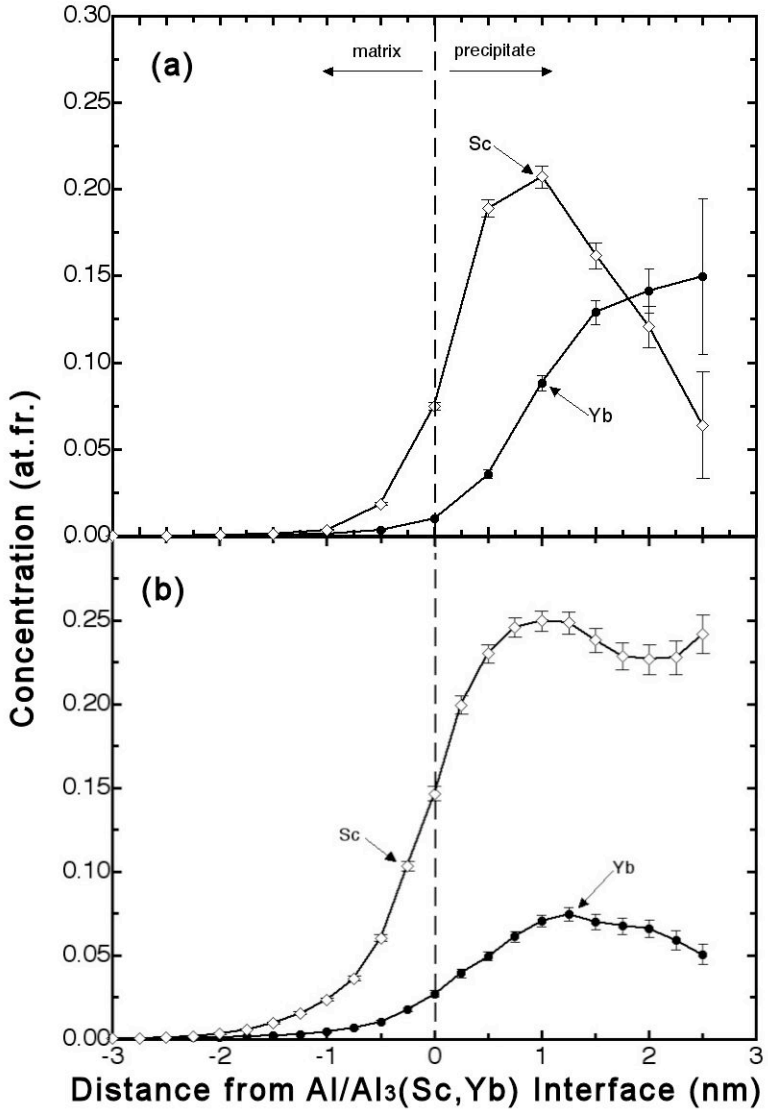

Figure 7.11: Proximity histograms of Al-0.06 Sc-0.02 Yb showing the concentrations of Yb and Sc as a function of radial distance from the heterophase interface: (a) 24 h aging time; (b) 64 h aging time at 300˚C.

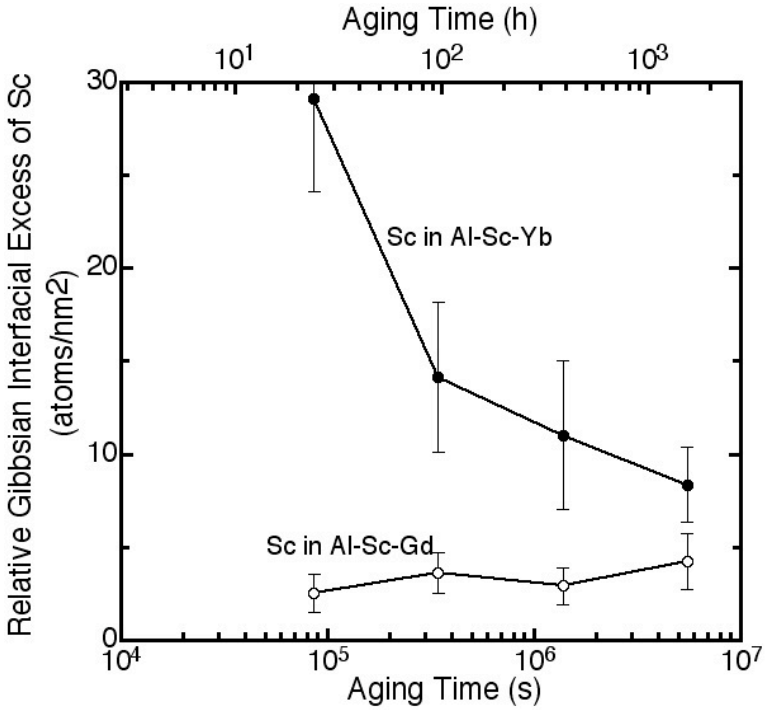

Figure 7.12: Relative Gibbsian interfacial excess of Sc in Al-Sc-Yb at the α-Al/$Al_3(Sc_{1-x}Yb_x)$ heterophase interface and in Al-Sc-Gd at the α-Al/$Al_3(Sc_{1-x}Gd_x)$ heterophase interface vs. aging time at 300ºC.

7.4 Discussion

7.4.1 Microstructure and Volume Fraction

The larger hardness value in the Al-Sc-Yb alloy, compared to the Al-0.06Sc alloy, may be due to the larger volume fraction of precipitates (ϕ = 0.33 % *vs.* 0.24 % [20]). An increase in ϕ of 38% leads to a hardness increase of 65%. Similarly in the Al-Sc-Gd alloy, a 17% increase in the volume fraction (ϕ = 0.28% *vs.* 0.24%) leads to a 57% increase in the peak microhardness. Additionally, when compared with the Al-0.06Sc alloy [20], the Al-Sc-Yb and Al-Sc-Gd alloys have increased $N_v(t)$ of smaller precipitates by more than an order of magnitude. Both the

increased number density and the increased volume fraction, contribute to a larger value of the Orowan stress (where the Orowan stress is approximated by the microhardness increment divided by 3). When compared with an Al-0.08at.%Sc alloy, the microhardness is about the same for Al-Sc-Yb and slightly greater than for Al-Sc-Gd [99].

Binary alloys with similar volume fractions (ϕ = 0.24% for Al-0.06Sc and ϕ = 0.49% for Al-0.12Sc) have smaller or equal N_v values [20, 21] with maximum measured N_v values of 9.3×10^{20} and 4.3×10^{22}, respectively (Fig. 7.4). This increase in the hardness of the alloy and N_v values of precipitates was also observed in Al-Sc-RE alloys with 0.005±0.003% of solute which have ϕ = 0.22 and 0.25 % for the Yb and Gd additions [100]. It appears that even in small quantities, the RE alter significantly the precipitation kinetics.

7.4.2 Precipitate Coarsening

The temporal evolution of growth and coarsening is followed in the Al-Sc-Yb and Al-Sc-Gd alloys. After 24 h of aging for Al-Sc-Yb and 96 h of aging for Al-Sc-Gd, the value of $N_v(t)$ begins to decrease, while <R(t)> is concomitantly increasing. This, combined with the slight increase in volume fraction beyond these aging times (Fig. 7.5), indicates that the system is close to quasi-stationary-state coarsening ($\frac{\partial C_i}{\partial t} \approx 0$), with a small amount of growth occurring in parallel. Similar to the Al-Sc-RE system, in the Ni-Al-Cr system, the stages of precipitation were traced. Concurrent growth and coarsening is also seen in this system [139, 175-178].

The Lifshitz-Slyozov-Wagner (LSW) diffusion limited coarsening model for binary alloys [80, 81, 179] assumes that: (i) the diffusion fields of the precipitates do not overlap; (ii) dilute solid-solution theory is applicable; (iii) coarsening occurs in a stress-free matrix; (iv) the linearized version of the Gibbs–Thomson equation is valid; (v) no elastic interactions occur between precipitates, thereby limiting the precipitate volume fraction to zero; (vi) precipitates have a spherical morphology; and (vii) precipitates coarsen with a fixed chemical composition. This has been extended to concentrated multicomponent alloys by Umantsev and Olson [82], and analyzed in detail for ternary alloys, including capillary effects, by Kuehmann and Voorhees [83]. The time exponent for the evolution of $\langle R(t) \rangle$ of the ternary alloys is predicted to be 1/3, the same as for the binary alloys, albeit with a different rate constant, K_{KV}, than the LSW model. Similarly, the coarsening constants for non-ideal and non-dilute alloys can be significantly different than those of dilute alloys, although the time exponents are the same [180]. Mechanisms other than diffusion-limited coarsening have also been considered, such as precipitate diffusion and coagulation and coalescence [181] vs. evaporation-condensation (the latter is the implicit mechanism of LSW theory), depending on if the vacancy resides mainly in the matrix or precipitate phases [182]. Another possibility is interface limited coarsening [183, 184].

The following equations from the Kuehmann and Voorhees model for coarsening in ternary alloys [83] are used to analyze the data for the longer aging times in the Al-Sc-Yb and Al-Sc-Gd alloys. These equations assume that quasi-stationary coarsening is occurring:

$$< R(t) >^3 - < R(t_o) >^3 = K_{KV}(t - t_o); \tag{7.2}$$

$$N_v(t)^{-1} - N_v(t_o)^{-1} = 4.74 \frac{K_{KV}}{\phi_{eq}}(t - t_o); \tag{7.3}$$

$$\Delta C_i^{\alpha}(t) =< C_i^{\alpha,ff}(t) > - C_i^{\alpha,eq}(\infty) = \kappa_{i,KV}^{\alpha}(t)^{-1/3}; \tag{7.4}$$

where K_{KV} and $\kappa_{i,KV}^{\alpha}$ are the coarsening rate constants for <R(t)> and $\Delta C_i^{\alpha}(t)$, respectively; <$R(t_o)$> is the average precipitate radius at the onset of quasi-stationary coarsening at time t_o and $N_V(t_o)$ is the precipitate number density at the onset of quasi-stationary coarsening at time t_o. The quantity $\Delta C_i^{\alpha}(t)$ is denoted a supersaturation and is the difference between the concentration in the far-field α-matrix, $< C_i^{\alpha,ff}(t) >$, and the equilibrium γ-matrix solute-solubility, $C_i^{\alpha,eq}(\infty)$. The quantity $C_i^{\alpha,eq}(\infty)$ needs to be both determined experimentally and calculated as it is not available for Al-Sc-Yb multicomponent alloys at 573 K. The theoretical expression for K_{KV} for the evolution of the precipitate radius is given by [173]:

$$K_{KV} = \frac{8\sigma^{\alpha/\beta}V_m}{9\left(\frac{\Delta c_{Yb}}{D_{Yb}}\left(\Delta c_{Yb}G''_{YbYb} + \Delta c_{Sc}G''_{YbSc}\right) + \frac{\Delta c_{Sc}}{D_{Sc}}\left(\Delta c_{Yb}G''_{YbSc} + \Delta c_{Sc}G''_{ScSc}\right)\right)} \tag{7.5}$$

where k_i is the distribution coefficient and is given by $C_{precipitate}/C_{matrix}$, the G'' are the second derivatives of the Gibbs free energy (assumed here to be dilute ideal solid-solution), Δc_x is

($c_{precipitate}$ - c_{matrix}) of element x, V_m is the volume of a mole of $Al_3(Sc,Yb)$ atoms (V_m=1.035x10^{-5} m^3 mol^{-1}) and $\sigma^{\alpha/\beta}$ is the interfacial free energy. Additionally, the rate constant for the evolution of the matrix supersaturation, $\kappa_i^{\alpha,KV}$, is given by:

$$\kappa_{KV} = \frac{\left(3\sigma^{\alpha/\beta}V_m\right)^{2/3}\Lambda^{1/3}\Delta c_{Yb}}{\left(\Delta c_{Yb}\left(\Delta c_{Yb}G''_{YbYb} + \Delta c_{Sc}G''_{YbSc}\right) + \Delta c_{Sc}\left(\Delta c_{Yb}G''_{YbSc} + \Delta c_{Sc}G''_{ScSc}\right)\right)} \tag{7.6}$$

$$\text{where: } \Lambda = \left(\frac{\Delta c_{Yb}}{D_{Yb}}\left(\Delta c_{Yb}G''_{YbYb} + \Delta c_{Sc}G''_{YbSc}\right) + \frac{\Delta c_{Sc}}{D_{Sc}}\left(\Delta c_{Yb}G''_{YbSc} + \Delta c_{Sc}G''_{ScSc}\right)\right) \tag{7.7}$$

7.4.2.1 Average Precipitate Radius Evolution

The time exponent for the evolution of <R(t)> (Eq. 2) derived, using a multiple linear regression analysis for the Al-Sc-Yb alloy is 0.18±0.03 and for the Al-Sc-Gd alloy 0.22±0.01 (Table 7.2). These alloys are both coarsening somewhat slower than predicted by the theory and by various prior studies on Al-Sc binary alloys, which all showed a $t^{1/3}$ dependence [11, 13, 19, 21, 22, 185, 186]. The Al-Sc-Zr [2] and Al-Sc-Ti [102] alloys have lower time exponents, in the range of 0.05-0.1, indicating that Yb and Gd are not as effective at slowing the coarsening as are Zr or Ti. It is unclear why the Al-Sc-Gd alloy is coarsening faster than the Al-Sc-Yb.

The coarsening constants, K_{KV}, from Eq. 2 were also determined from the experimental data using a multiple linear regression analysis (which also takes into account the values of t_o and <R(t_o)>). For the Al-Sc-Yb alloy, K_{KV} is equal to (2.87±0.3) x 10^{-32} m^3 s^{-1} (Table 7.2) and for the Al-Sc-Gd alloy K_{KV} is (2.19±0.12) x 10^{-32} m^3 s^{-1}. These are larger K_{KV} values than the ones

obtained for the Al-Sc-Zr alloys at 300°C. For the alloy with the closest composition to the alloys studied here, Al-0.07Sc-0.019Zr, the coarsening constant is (5.13±2.07) x 10^{-33} m^3 s^{-1}, once again confirming that the RE are not as effective as Zr at reducing the coarsening resistance [2]. It is not possible to calculate the theoretical coarsening constants since the interfacial Gibbs free energy and diffusivities of the RE in the ternary alloys are unknown.

Table 7.2: Experimentally Measured Time Exponents and Rate Constants for the Average Precipitate Radius, <R(t)>

Alloy	Radius Rate Constant (m^3 s^{-1})	Radius Time Exponent, n
Al-Sc-Yb	(2.87±0.3)x10^{-32}	0.18±0.03
Al-Sc-Gd	(2.19±0.12)x10^{-32}	0.22±0.01

7.4.2.2 The Temporal Evolution of the Number Density of Precipitates, $N_v(t)$

The experimental time exponents for the evolution of $N_v(t)$ (Eq. 3), calculated using a multiple regression analysis, are -0.84±0.05 for the Al-Sc-Yb alloy and -0.76±0.06 for the Al-Sc-Gd alloy (Table 7.3), which are less than the predicted model value of -1. This implies that a true quasi-stationary state coarsening has not been achieved. While it is assumed, based on the slower diffusivity of the other light rare earth elements (La-Sm), that Gd diffuses slower than Sc, it does not appear that, once coarsening commences, it has a significant effect on decelerating the coarsening rate. These time exponents show that both Yb and Gd are not as effective at retarding the coarsening kinetics as Zr [2], where time exponents for similar aging treatments were found to be greater than -1 (and in some cases positive, although this indicates coarsening has not commenced). The later onset of coarsening in the Al-Sc-Gd alloy is probably due to the differing precipitation kinetics in the two alloys.

Figure 7.13 displays the product of $N_v(t)$ and t *vs*. aging time. This should be a constant if the system is in a stationary state. For both of the Al-Sc-RE alloys, $N_v(t)$*t is still increasing with aging time up to 16 days (384 h) of aging, indicating that the alloys are in a quasi-stationary state, at least up to this point. The system has not yet reached a stationary state since the distribution of the elements within the precipitates is still changing up to the longest aging time, 1536 h, as discussed in section 4.3 and there is still a slight increase in ϕ (Fig. 7.5). It is most likely in a quasi-stationary state.

Table 7.3: Experimentally Determined Values for the time exponent, n, for the evolution of the Number Density, $N_v(t)$, as a Function of Aging Time at 300˚C.

Alloy	Time Exponent, n
Al-Sc-Yb	-0.84±0.05
Al-Sc-Gd	-0.76±0.06

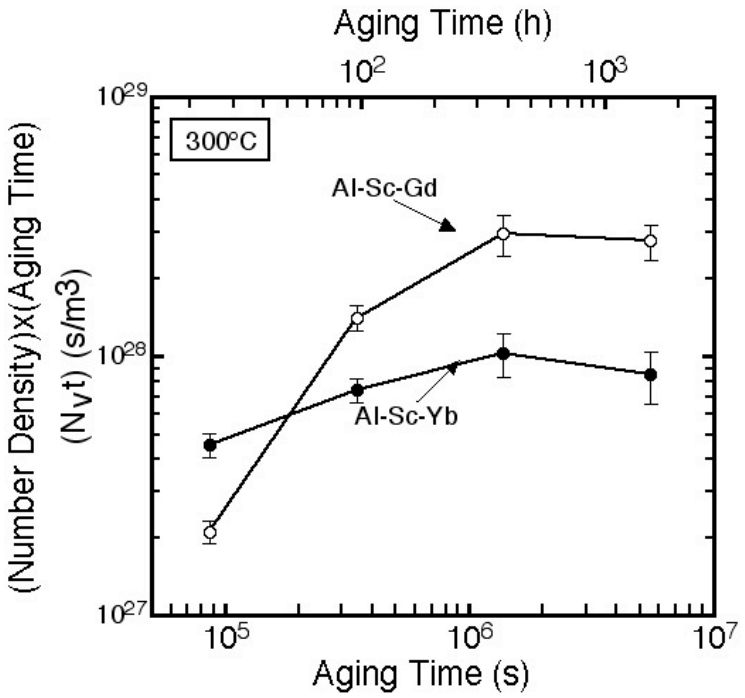

Figure 7.13: Number density, $N_v(t)$ multiplied by aging time vs. aging time at 300˚C.

7.4.2.3 α-Al Matrix Supersaturation, ΔC_i^{α}

The equilibrium solid-solubilities of Yb and Sc in the α-Al matrix of the Al-Sc-Yb alloy at infinite time were determined from Eq. 4 utilizing a multiple linear regression analysis (Fig. 7.6 and Table 7.4). In the Al-Sc-Yb alloy, the equilibrium solubilities in the α–Al matrix are found to be 2.5 ± 1 at. ppm for Yb and 2.7 ± 1 at. ppm for Sc. The equilibrium concentration of Al in the matrix is determined in a similar manner to that of Yb and Sc, and is found to be 99.9995±0.0098at.%. This validates the fitting procedure since the concentrations of the three elements sum to 100%.

For the Al-Sc-Yb alloy, the rate constant for supersaturation of Yb in the α-Al matrix in Eq. 4, $\kappa_{Yb}^{\alpha,KV}$, is (3.0±3.4) x 10^{-4} at.fr. $s^{1/3}$, while for Sc supersaturation the value for $\kappa_{Sc}^{\alpha,KV}$ is (1.5±0.2) x 10^{-3} at.fr. $s^{1/3}$ (Table 7.5). The rate constant for Al supersaturation in the matrix, $\kappa_{Al}^{\alpha,KV}$, is (-1.8±2.8) x 10^{-3} at.fr. $s^{1/3}$. The rate constants sum to zero which validates the fitting procedure for the rate constants. It is not possible to calculate the theoretical coarsening constants since the interfacial Gibbs free energy and diffusivities of the RE in the ternary alloy are unknown. Coarsening constants for the supersaturation of solute in the matrix were not measured for the Al-Sc-Zr system [3], therefore no comparison is possible.

In the Al-Sc-Yb alloy, the measured time exponent for Yb is -0.10 and for Sc is -0.23 (Table 7.5). These values are larger than the value of -0.33 predicted by the coarsening model [83], indicating that the coarsening occurs at a slower rate than predicted. When compared to the Al-

Sc-Zr system, the time exponents for the supersaturation are similar [3]: Sc was found to be -0.33 in this alloy and the Zr supersaturation decreased with a time exponent of -0.11. There have been several studies that monitored the supersaturation of Sc in binary Al-Sc alloys using electrical resistivity measurements (Al-0.15 %Sc in the temperature range of 533-733K [125] and Al-0.17 %Sc in the temperature range of 673-723K [185]) and these have found that the ΔC_{Sc}^{α} decays with a $t^{-1/3}$ dependence. This indicates that, similarly to the <R(t)> evolution, there is some slowing of the coarsening compared to binary alloys when Yb is added.

Using the same procedures as for the Al-Sc-Yb alloy, the equilibrium solubility of Sc in the Al-Sc-Gd alloy is found to be 5.8±2 at. ppm (Fig. 7.7 and Table 7.4). $\kappa_{Sc}^{\alpha,KV}$ in Al-Sc-Gd is (1.4±0.6)x10^{-3} at.fr. $s^{1/3}$ (Table 7.5) and the time exponent for ΔC_{Sc}^{α} is -0.32, which is close to that predicted by the model [83]. The majority of the Gd (91 %) remains in the matrix and does not dissolve in the precipitates. The concentration of Gd in α-Al remains constant at around 150±10 at. ppm. A possible explanation is that Gd has a limited solubility in the precipitate phase, which according to Ref. [5] is 3.75%. ΔC_{Gd}^{α} and the time exponent for Gd supersaturation in the matrix are not calculated because a significant fraction of the Gd atoms are in the matrix, and the change in its concentration in the matrix during coarsening is within the experimental measuring error.

The presence of RE has an effect on the Sc solubility in the matrix. The values of the Sc solubility in α-Al for both Al-Sc-RE alloys are smaller than that measured in an Al-2.2Mg-0.12Sc alloy (89±30 at. ppm) [173], and also smaller than measured in a binary Al-0.15Sc alloy

(50 at. ppm) [125]. A recent study of an Al-0.09Sc-0.047Zr alloy yielded an even higher solid-solubility of Sc, 120±30 at. ppm, although the value from the calculated ternary phase diagram presented in this reference is only 7 at. ppm [3].

Table 7.4: Experimentally measured solid-solubilities of Sc and RE in the α-Al matrix.

Alloy	Sc (at .ppm)	RE (at. ppm)
Al-Sc-Yb	2.7±5	2.5±1
Al-Sc-Gd	5.8±2.0	150±10

Table 7.5: Experimentally Measured Time Exponents and Rate Constants for the Supersaturation in the α-Al matrix

Alloy	Sc time exponent	RE time exponent	Rate Constant (Sc) (at.fr. $s^{1/3}$)	Rate Constant (RE) (at.fr. $s^{1/3}$)
Al-Sc-Yb	-0.23±0.04	-0.10±0.03	$(1.5\pm0.2)\times10^{-3}$	$(2.6\pm3.4)\times10^{-4}$
Al-Sc-Gd	-0.32±0.02	-	$(1.4\pm0.6)\times10^{-3}$	-

7.4.2.4 Interfacial Energy and Diffusivity of Yb in the Matrix

The diffusivity and interfacial free energy for a binary alloy can be calculated from coarsening data from an approach due to Ardell [128]. This has been applied to a binary Al-0.17Sc alloy in the range of 673-723 K [185]. The interfacial free energy has also been calculated in an Al-0.15Sc alloy [125]. This approach has been extended to a ternary alloy in Ref. [173], and additionally to a non-dilute ternary alloy in Ref. [178].

The expression for diffusivity of Yb in this alloy at 300˚C, D_{Yb}, and the interfacial energy, $\sigma^{\alpha/\beta}$, are given by [173]:

$$D_{Yb} = \frac{\Delta c_{Yb}\left(\Delta c_{Yb} G''_{YbYb} + \Delta c_{Sc} G''_{YbSc}\right)}{\frac{4}{9}\frac{\kappa_{KV}}{\Delta c_{Yb} K_{KV}^{2/3}}\chi - \frac{\Delta c_{Sc}}{D_{Sc}}\left(\Delta c_{Yb} G''_{YbSc} + \Delta c_{Sc} G''_{ScSc}\right)} \tag{7.8}$$

$$\sigma^{\alpha/\beta} = \frac{\kappa_{KV} K_{KV}^{1/3}\left(\Delta c_{Yb}\left(\Delta c_{Yb} G''_{YbYb} + \Delta c_{Sc} G''_{YbSc}\right) + \Delta c_{Sc}\left(\Delta c_{Yb} G''_{YbSc} + \Delta c_{Sc} G''_{ScSc}\right)\right)}{2V_m \Delta c_{Yb}} \tag{7.9}$$

where $\chi = \Delta c_{Yb}\left(\Delta c_{Yb} G''_{YbYb} + \Delta c_{Sc} G''_{YbSc}\right) + \Delta c_{Sc}\left(\Delta c_{Yb} G''_{YbSc} + \Delta c_{Sc} G''_{ScSc}\right)$, G'' are the second derivatives of the Gibbs free energy (we assume a dilute ideal solid-solution), Δc_x is ($c_{precipitate}$ - c_{matrix}) of element x, and V_m is the volume of a mole atoms in the $Al_3(Sc,Yb)$ phase (V_m=1.035x10^{-5} m^3 mol^{-1}).

Eqs. 7.8 and 7.9 were utilized along with the experimentally measured coarsening constants to calculate D_{Yb} in the ternary alloy and $\sigma^{\alpha/\beta}$ between the precipitate and α-Al matrix phases in the growth and coarsening regime [173]. The calculated diffusivity of Yb in Al-Sc-Yb is D_{Yb} = (5±4) x 10^{-21} m^2 s^{-1} at 300˚C. We know from experiment, however, that Yb precipitates out of the matrix before the Sc [100, 187]. The value of D_{Yb} calculated for earlier aging times (before the majority of the Sc forms precipitates) ranges from 10^{-19} – 10^{-18} m^2 s^{-1}, depending of the method used to calculate D_{Yb} [187] (See Table 6). During the coarsening stage, however, D_{Yb} a likely reason for the slower D_{Yb} is that Yb may be kinetically trapped in the interior of the precipitates. Since it is known that diffusion is more correlated in ordered precipitates, it hence occurs at a lower rate [92] than in the α-Al matrix.

The value of D_{Yb} calculated for the binary Al-Yb alloy, (5.7±1.9)x10^{-17} m^2 s^{-1} [187], is faster than D_{Yb} measured for the Al-Sc-Yb alloy during either the early aging period or after 24 h of aging. Additionally, beyond 24 h of aging, D_{Yb} is slower than the value of D_{Sc} in binary Al-Sc alloys

which is $9x10^{-20}$ m^2 s^{-1} at 300˚C [97]. Perhaps the presence of Sc lowers the value of D_{Yb}, implying that the off-diagonal terms of the diffusion tensor are not zero.

A value of D_{Sc} is also calculated using the same procedure as in Eq. 5 and 6. A value of D_{Yb} = $(5.7\pm1.9)x10^{-17}$ m^2 s^{-1} [187], which is the value measured for the binary Al-Yb alloy, is input into the calculation. A value of D_{Sc} = $(4.9\pm3.1)x10^{20}$ m^2 s^{-1} is measured. This is within an order of magnitude of the value from the literature of the binary Al-Sc alloy [97]. The Sc is contained mostly in the shell of the precipitates and is hence not kinetically trapped within the intermetallic precipitate.

The interfacial free energy, $\sigma^{\alpha/\beta}$, in the ternary Al-Sc-Yb is calculated to be $\sigma^{\alpha/\beta}$ = 670±150 mJ m^{-2} . This is significantly higher than the values recently calculated similarly for manner binary Al-0.12%Sc alloy [188] and a value of ~25 mJ m^{-2} was obtained for 300˚C. In an Al-2.2%Mg-0.12%Sc alloy, $\sigma^{\alpha/\beta}$ = 158±36 mJ m^{-2} [173] and 225 mJ m^{-2} in a recent study on Al-1.1%Mg-0.16%Sc at 400˚C [189]. It was noted that $\sigma^{\alpha/\beta}$ would be much larger if there was a smaller solid-solubility of Sc in the matrix (2 at. ppm), which is the case here. Thus, the value of $\sigma^{\alpha/\beta}$ we calculate here may be due to the smaller solubility of Sc in the α-Al matrix.

7.4.3 Temporal Evolution of Precipitate Composition

The APT results for the Al-Sc-Yb alloy demonstrate that the initial precipitates have a composition corresponding to $Al_3(Yb_{1-x}Sc_x)$ because they are richer in Yb than Sc. After 5 minutes of aging the Yb/Sc concentration ratio is 9.25 (Fig. 7.8). A possible explanation for the rapid precipitation of Yb is that it is a kinetic effect due to a larger D_{Yb} (at least in the initial

stages even though the diffusivity we calculated for the coarsening regime is much smaller than that of Sc in Al).

In addition to diffusivities controlling the precipitation kinetics, the nucleation current of Al_3Yb could be higher because of the greater driving force. In the previous chapter, the values for ΔF_{ch}, the chemical driving force per unit volume, ΔF_{el} is the elastic free energy have were calculated for the Al-Sc-Yb alloy and compared with the binary Al-0.06at.%Sc alloy. As concluded in the previous chapter, there is not much difference in the calculated driving forces of these two alloys which could be the result of the assumption of ideal solution.

The Sc appears to diffuse to the precipitates at a slower rate because it has a smaller diffusivity in Al-Sc-Yb than does Yb. As the Sc diffuses to the precipitates, it first forms a spherical shell around the precipitates as shown by the three-dimensional reconstructions from LEAP tomography (Fig. 7.9-10). With increasing aging time at 300°C, the Sc diffuses into the center of the precipitates, as the diffusion of Sc in the ordered $L1_2$ precipitates is slower than in the α-Al matrix. Eventually, it exceeds the Yb concentration at all locations within the precipitates.

The shells of Yb and Sc seem to interdiffuse (Fig. 7.11), confirming that Yb and Sc can substitute for one another in the $Al_3(Sc,Yb)$ precipitates, indicating that Yb is replacing some of the more expensive Sc in this alloy, while retaining a constant value of ϕ. The maximum solubility of Yb in α-Al, however, is 248±7 at. ppm, based on LEAP measurements on a Al-0.06Yb binary alloy, which was aged at the eutectic temperature of 625˚C for 72 h. The literature value for the Yb solubility in Al is ca. 2000 [124], although this reference does not show data

points at concentrations of several hundred atomic parts per million and Massalski [136] claims there is no significant solubility of Yb in Al. Despite the limited solid-solubility of Yb in α-Al, Yb is an effective choice for replacing the more expensive Sc in Al-Sc base alloys.

The Yb/Sc concentration ratio (at.% / at.%) in the precipitates achieves a value of 0.23 after 96 h of aging and remains relatively constant at longer times (Fig. 7.8). Although the Yb/Sc ratio remains constant after 96 h, the value of the relative interfacial excess of Sc continues to decrease with increasing aging time up to 64 days, indicating that the system has not achieved a stationary-state. (Fig. 7.12) Since the distribution of the elements within the precipitates continuously evolves up to the longest aging time, the coarsening constants associated with the supersaturation of each of the elements in the precipitates could not be measured. Furthermore, since the interdiffusion of the Yb and Sc core/shell layers is so slow, as expected from the highly correlated diffusion in the $L1_2$ structure, it is estimated that the Sc diffusivity within $Al_3(Yb_{1-x}Sc_x)$ is $3x10^{-26}$ m^2 s^{-1}. This is six orders of magnitude slower than Sc in the Al matrix [97].

In addition to the precipitation kinetics, some of the Sc segregation in Al-Sc-Yb could be due to a local equilibrium effect since Al_3Sc has a smaller lattice parameter than Al_3Yb. It is anticipated that the Sc interfacial segregation will reduce the elastic strain in the matrix. A similar effect of segregation was observed for Ti or Zr ternary additions to Al-Sc alloys [3, 102]. Both Ti and Zr decrease the lattice parameter mismatch and are observed to segregate at the α-Al/$Al_3(Sc_{1-x}Ti_x)$ or α-Al/$Al_3(Sc_{1-x}Zr_x)$ heterophase interfaces. A third potential driving force for interfacial segregation of Sc in Al-Sc-Yb to the α-Al/$Al_3(Yb_{1-x}Sc_x)$ interface is due to a chemical (electronic) effect as is the case for the segregation of Mg segregation at the α-Al/Al_3Sc interface

[73]. A recent study, however, using lattice kinetic Monte Carlo simulations found that the cause for Zr segregation at the α-Al/$Al_3(Sc_{1-x}Zr_x)$ heterophase interface is kinetics and not a chemical effect [32]. By setting the diffusivity of both elements equal in the LKMC simulation, such that the elements diffuse to the precipitates at the same rate, a uniform distribution of elements is observed.

Gadolinium does not form Al_3Gd ($L1_2$) precipitates in binary Al-Gd alloys, instead it forms precipitates with the DO_{19} structure [190]. In the Al-Sc-Gd alloy, Al_3Sc ($L1_2$) precipitates form with <10% of the Gd partitioning to the precipitates. The concentration of Gd in the precipitates is smaller than Yb in the Al-Sc-Yb alloy for a given aging treatment. After 24 h of aging, the Gd concentration in the precipitates is only 2.1 %, while the Yb concentration in the precipitates is 7.4 % in the Al-Sc-Yb alloy, which is thus greater than the Gd concentration by a factor of 2.6. The Gd concentration remains approximately constant at around 2% to the longest aging time (Fig. 7.8), which is somewhat less than the maximum solubility of Gd in Al_3Sc, which is 3.75 % [5]. This makes Gd a less interesting candidate for use in Al-Sc-X alloys as a replacement for Sc. This small Gd concentration may also be the reason for the absence of an increase in peak microhardness in the current Al-Sc-Gd alloy with 200 at. ppm Gd compared with an Al-Sc-Gd alloy with 50 at. ppm of Gd [100]. Both alloys have a similar concentration of Gd in the precipitate and thus the additional Gd in the present alloy does not add to the value of ϕ.

Gd segregates to the center of the precipitates, similar to the effect observed in an Al-0.06Sc-0.005Gd alloy [100]. The relative Gibbsian interfacial excess of Sc at the α-Al/Al_3(Sc,Gd) interface increases slightly in the range of aging times from 24 to 1536 h and hence the Gd is

diffusing to the center of the precipitates. A steady-state distribution of elements in the precipitates is not achieved and hence the coarsening constants associated with the supersaturation in the precipitates is not calculated. When compared to the Al-Sc-Yb alloy, the relative Gibbsian interfacial excess of Sc at the α-Al/$Al_3(Sc_{1-x}Gd_x)$ heterophase interface in the Gd alloy is smaller (Fig. 7.12). One possible explanation is a kinetic effect: in the Al-Sc-Gd alloy, the kinetics could be so slow that only a small change occurs. By contrast, in the Al-Sc-Yb alloy, the Yb forms precipitates before the Sc does, hence eliminating the need for the Yb to diffuse to the center. The lower interfacial excess of Sc in the Al-Sc-Gd alloy may also be attributed to the fact that Gd increases the lattice parameter mismatch to a lesser extent than does Yb. A monotonic decrease in the lattice parameter from the center to the interface may be expected to minimize the elastic strain energy.

7.5 Conclusions

The kinetic pathways for the formation of the nanostructure in Al-0.06at.% Sc-0.02at.% Yb and Al-0.06at.% Sc-0.02at.% Gd alloys are studied at an aging temperatures of 300˚C for aging times up to 1536 h utilizing Vickers microhardness, local-electrode atom-probe tomography and transmission electron microscopy.

- Vickers microhardness measurements demonstrate that additions of 0.02% Yb or Gd to Al-0.06Sc alloys increases the microhardness of these alloys over the peak hardness of the binary Al-0.06Sc. The peak precipitate number densities, $N_v(t)$ of the ternary alloys are greater than that of the binary alloys (5.25±0.55) x 10^{22} and (4.1±0.44) x 10^{22} ppt/m^3 for Al-Sc-Yb and Al-Sc-Gd, respectively, compared with (9.33±2.0) x 10^{20} ppt/m^3 for Al-0.06Sc.

Additionally, there is an increase in the volume fraction of precipitates, ϕ, due to the presence of the RE. The Al-0.08Sc alloy has a peak microhardness equal to that of the Al-Sc-Yb alloy and a slightly larger microhardness value than the Al-Sc-Gd alloy.

- The system is in a quasi stationary-state since ϕ for both alloys is increasing slightly with increasing aging time (Fig. 7.5). Additionally, the slope of the product $N_v(t)*t$ vs. aging time approaches a value of zero at 384 h of aging, indicating that both alloys are not in a stationary state, but rather a quasi-stationary state, before this time.
- The coarsening rate of Al-Sc-RE is decreased slightly by the presence of the Gd or Yb compared to binary Al-Sc alloys, as evidenced by time exponents for the evolution of the radius, $N_v(t)$, and α-Al matrix supersaturation. The RE are not, however, as effective at retarding the coarsening as additions of Zr or Ti to Al-Sc alloys as evidenced by coarsening rate constants and time exponents for coarsening.
- In the Yb containing Al-Sc-Yb alloy, it is found that the majority of the precipitates that form initially have the stoichiometry $Al_3(Yb_{1-x}Sc_x)$ ($L1_2$ structure), with Sc diffusing subsequently to the precipitates resulting in a core/shell precipitate structure (Figs. 7.9-11). Eventually the Yb and Sc inter-diffuse leading to a more uniform concentration throughout the precipitates. The Yb/Sc concentration ratio (at.%/at.%) achieves a value of 0.20 after 96 h of aging, thus making it a good candidate for replacing some of the more expensive Sc.
- The diffusivity of Yb is calculated for the Al-Sc-Yb alloy and is found to be $(5\pm4) \times 10^{-21}$ m^2 s^{-1} at 300˚C, which is smaller than the diffusivity of Sc in the Al-Sc-Yb alloy. It is also slower than D_{Yb} calculated in the Al-Yb alloy and for early aging times in the Al-Sc-Yb alloy. It is suggested that the Yb is kinetically trapped in the center of the precipitate at these

aging times. The interfacial free energy was calculated to be $\sigma^{\alpha/\alpha'} = 670 \pm 150$ mJ m^{-2}. This is greater than values calculated for Al-Sc and Al-Sc-Mg alloys in [173].

- In the Al-Sc-Gd alloy, $Al_3(Sc_{1-x}Gd_x)$ ($L1_2$ structure) precipitates form with a small percentage of Gd (2.9%) in the precipitates on the Sc sublattice. The relative interfacial Gibbsian excess of Sc at α-Al/$Al_3(Sc_{1-x}Gd_x)$ heterophase interface and the ratio of the Sc concentration to Gd concentration in the precipitates remains constant between 24 and 1536 h of aging at 300°C.

8. Creep Properties of Al-Sc-RE (RE = Gd or Yb) Alloys

8.1 Introduction

As indicated from the initial creep experiments on the Al-0.06at.%Sc-0.005at.%RE alloys (Chapter 5), the creep resistance of the alloys with RE additions increases when compared with RE free Al-Sc and Al-Sc-X alloys. In the present chapter, the creep properties are examined in detail for the Al-0.06Sc-0.02RE alloys and also for the Al-0.06Sc-0.005RE alloys with radii larger than 9 nm. An increase in normalized threshold stress with average precipitate radius is observed. Each of the RE containing alloys has a higher normalized threshold stress when compared with RE free alloys. The effects of lattice parameter mismatch are also discussed. At very large radii ~29 nm, the normalized threshold stress has begun to decrease due to the semicoherent nature of the precipitates.

8. 2 Experimental Procedures

Creep experiments were performed on four different Al-Sc-RE alloys: Al-(580±30)Sc-(242±8)Yb, Al-(610±30)Sc-(182±9)Gd, Al-(540±30)Yb-(80±10)Yb and Al-(630±30Sc-(50±10)Gd. These are the same alloys that were examined in previous chapters with chemical compositions verified by ATI Wah Chang (Albany, OR). These alloys will be referred to as Al-Sc-200RE and Al-Sc-50RE for the alloys with concentrations of 200 and 50 ppm RE, respectively. The procedures for the creep experiments and the microstructural analysis are the same as for the Al-Sc-Ti and Al-Sc-RE alloys which were discussed in Chapter 3. The minimum

strain rates were observed at multiple stresses for each sample. For a single sample, the stress is always increased since there is a change in the dislocation density with increases stress.

8.3 Results

8.3.1 Microhardness and Microstructure

Fig. 8.1 shows the average precipitate radius, <R(t)>, as measured by TEM, for the various aging treatments of the Al-Sc-RE alloys (also listed in Table 8.1). The radius increases significantly with increasing temperature and aging time, achieving much higher values than the Al-Sc-Ti alloy for comparable Sc diffusion distance. Fig. 8.2 shows the evolution of Vickers microhardness with aging at 300°C and 350°C. As was discussed in the previous chapters, for aging at 300°C there is a rapid increase after an initial incubation period, followed by a decrease during the growth and coarsening regime. The microhardness values at 350°C are much lower and decrease by 100 MPa for the Al-Sc-200Yb alloy and 35 MPa for the Al-Sc-200Gd alloy between 0.25 and 96 h of aging.

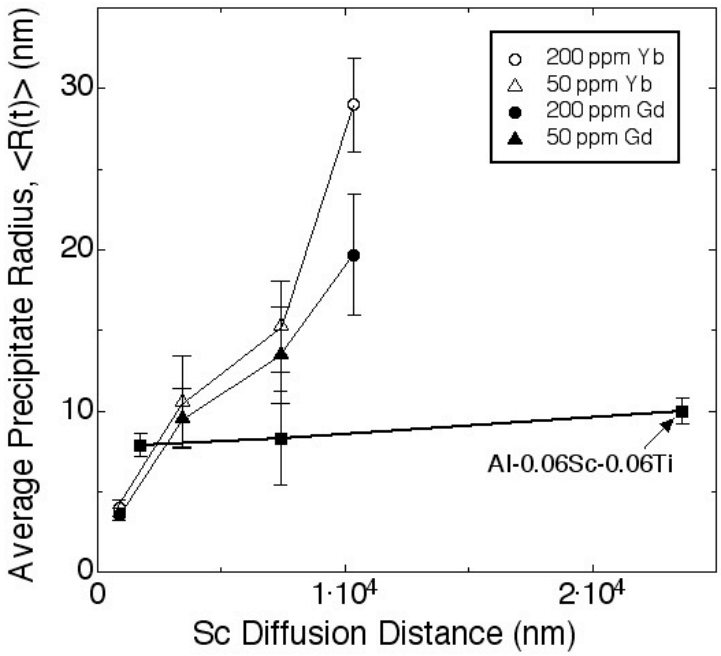

Figure 8.1: Average precipitate radii, <R(t)>, vs. Sc diffusion distance for the Al-0.06Sc-RE alloys with 50 or 200 ppm RE (Yb or Gd). Al-Sc-RE alloys are compared with the <R(t)> for the Al-0.06Sc-0.06Ti (at.%) alloy. The diffusivity of Sc is used [97] since the diffusivities of Yb and Gd in Al are not known.

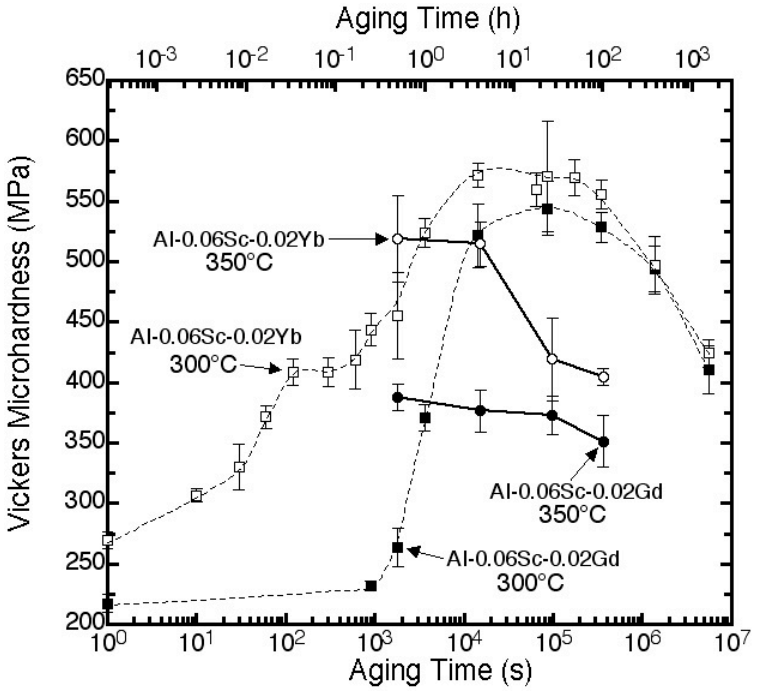

Figure 8.2: Vickers microhardness vs. aging time at 300˚C and 350˚C for Al-0.06Sc-0.02Yb (at.%) and Al-0.06Sc-0.02Gd (at.%).

8.3.2 Threshold Stress Values

Figs. 8.3-6 show that the Al-Sc-RE alloys exhibit creep behavior at 300°C characterized by a high apparent stress exponents of n_{ap} = 29-37, which is indicative of the presence of a threshold stress, σ_{th}, below which the creep rate, $\dot{\varepsilon}$, cannot be experimentally measured [62]. By plotting $\dot{\varepsilon}^{1/n}$ vs. σ [84], threshold stresses are calculated. The relationship between n and n_{ap} is [191]:

$$n_{ap} = \frac{n}{\left(1 - \frac{\sigma_{th}}{\sigma}\right)} \tag{8.2}$$

As discussed in earlier chapters, the Al-Sc-50RE alloys (Yb or Gd) have a much higher creep resistance than Al-Sc [20] or Al-Sc-Zr alloys [28]. As shown in Table 8.1 and Fig. 8.3-4, at larger values of <R(t)>, the threshold stresses of these alloys continues to be higher for the RE containing alloys. As <R(t)> increases from the range of 9-10 nm to 13-15 nm, there is a decrease in the creep resistance and threshold stress.

Similar creep results are observed for the Al-Sc-200RE (Yb or Gd) alloys. Figs. 8.5-6 and Table 8.1 show that the creep resistance and the threshold stress initially increase with increasing radius for both Al-Sc-200RE alloys. The maximum threshold stress is found to be 29±10 MPa (4.0±0.5 nm radius) for Al-Sc-200Yb and 28±6 MPa (2.3±0.3 nm radius) for Al-Sc-200Gd. The threshold stresses decrease for radii in excess of 10 nm, for both alloys. This is similar to the effect observed for an Al-0.06 Sc-0.06 Ti (at.%) alloy where there was initially an increase in the threshold stress with increasing average precipitate radius, but eventually the threshold stress was diminished at even larger <R(t)>, as shown in Chapter 5 [102].

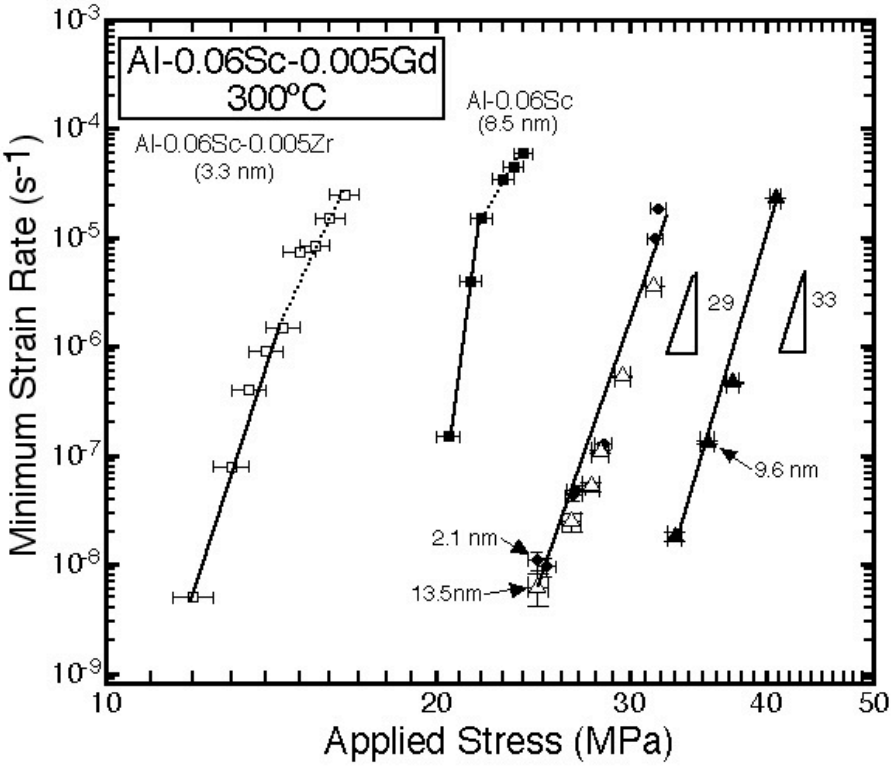

Figure 8.3: Minimum strain rate vs. applied stress for the Al-0.06Sc-0.005Gd (at.%) at 300˚C.

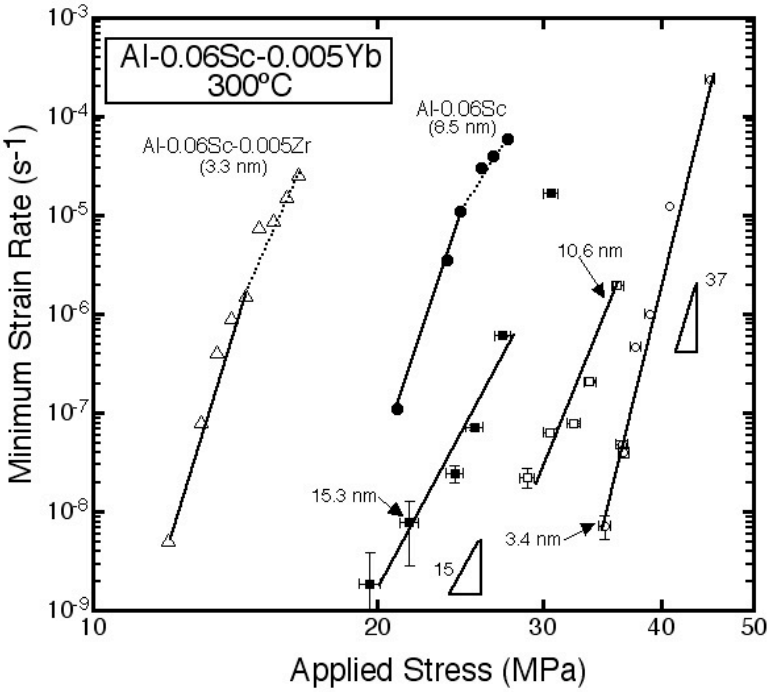

Figure 8.4: Minimum strain rate vs. applied stress for the Al-0.06Sc-0.005Yb (at.%) at 300˚C.

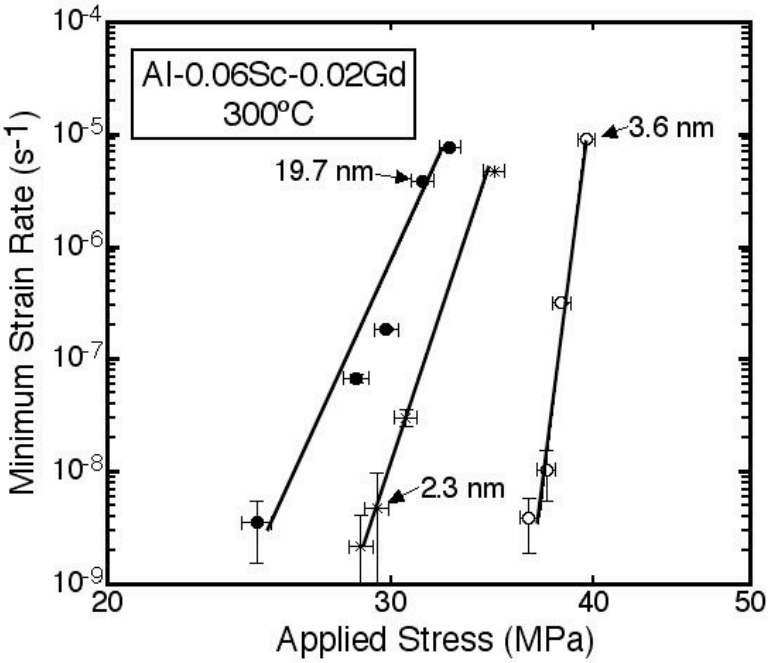

Figure 8.5: Minimum strain rate vs. applied stress for the Al-0.06Sc-0.02Gd (at.%) at 300˚C.

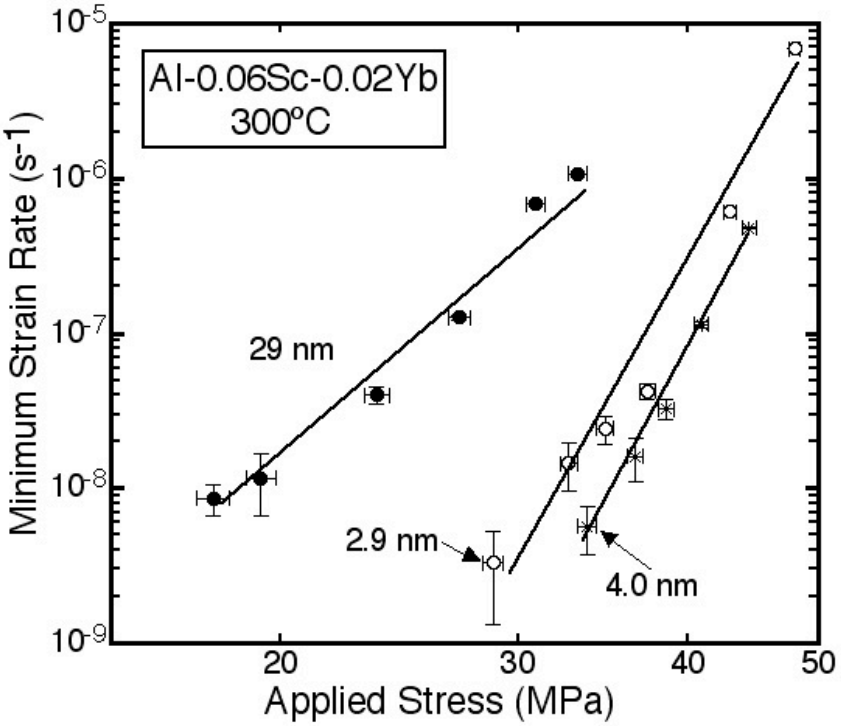

Figure 8.6: Minimum strain rate vs. applied stress for the Al-0.06Sc-0.02Yb (at.%) at 300˚C.

An additional feature observed in Figs. 8.3-6 is that the slope in the minimum strain rate vs. applied stress plot is somewhat lower for the Yb containing alloys than for the Al-Sc [20] and Al-Sc-Zr alloys [28]. This is consistently the case for both of the Yb containing alloys, for all values of <R(t)>. The Al-Sc-Gd alloys, however, have higher n_{ap} values.

Table 8.1: Average precipitate radii, <R(t)> and the threshold stresses σ_{th} for Al-Sc-RE alloys having undergone various heat treatments.

Alloy	Average Precipitate Radius, <R(t)> (nm)	Threshold Stress, σ_{th} (MPa)	Heat Treatment
Al-Sc-200Yb	2.9±0.5	27±11	24 h - 300˚C
	4.0±0.5	29±8	16 d - 300˚C
	29±9.2	12±4	24 h - 300˚C + 10 d - 400˚C
Al-Sc-200Gd	2.3±0.3	28±6	24 h - 300˚C
	3.6±0.4	36±7	16 d - 300˚C
	19.7±3.8	24±6	24 h - 300˚C + 10 d - 400˚C
Al-Sc-50Yb	10.6±2.9	25±6	24 h - 300˚C + 24 h - 400˚C
	15.3±2.8	20±10	24 h - 300˚C + 5 d - 400˚C
Al-Sc-50Gd	9.6±1.8	32±7	24 h - 300˚C + 24 h - 400˚C
	13.5±3.0	24±8	24 h - 300˚C + 5 d - 400˚C

8.3.3 Primary Creep

The Al-Sc-RE alloys displayed a high level of primary creep, likely due to the fact that the RE containing samples are at stresses which are relatively high. An example of the total strain on a single sample is shown in Fig. 8.7 for the Al-Sc-50Yb alloy with <R(t)> = 10.6 nm. The samples had reached the 5% total strain point and yet were still able to obtain minimum strain rates of $8x10^{-8}$ s^{-1}. The dislocation density increases at higher stresses as the structure evolves [192], and the subgrain size decreases [193]. Although some elastic deformation of the sample occurs, most

of the deformation is plastic since the sample measured upon conclusion of the creep experiment is has decreased in length by same amount as the total amount of strain recorded.

8.4 Discussion

8.4.1 Coarsening Resistance

As was shown in Fig. 8.1, <R(t)> increases with increased aging time or temperature. The precipitates attain larger sizes in all of the Al-Sc-RE alloys than in the Al-0.06Sc-0.06Ti alloy discussed in previous chapters. Furthermore, Fig. 8.2 shows that the microhardness decreases after aging at 300°C. There is a much more significant decrease for the Al-Sc-RE alloys in the microhardness than was observed in the Al-0.06Sc-0.06Ti alloy, which is consistent with the growth and coarsening of the precipitates. Together these two figures indicate that the Al-Sc-RE alloys have a lower coarsening resistance, when compared with the Al-Sc-Ti and Al-Sc-Zr alloys. The microstructure post-creep for the Al-Sc-200Gd pre-aged for 16 d at 300°C is shown in Fig. 8.8, and the precipitates are shown to remain spherical and do not coarsen significantly during the creep test (<R(t)> increases to 4.1±0.5 nm from 3.6±0.4 nm).

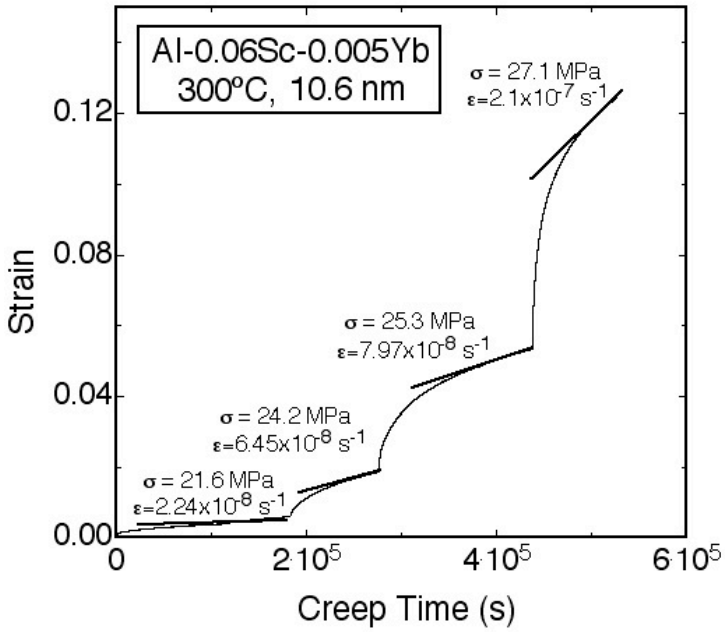

Figure 8.7: Variation of strain with time at 300˚C for several applied stresses for a single sample for the Al-0.06at.%Sc-0.005at.%Yb alloy with <R(t)> = 10.6 nm. Significant primary strain is observed.

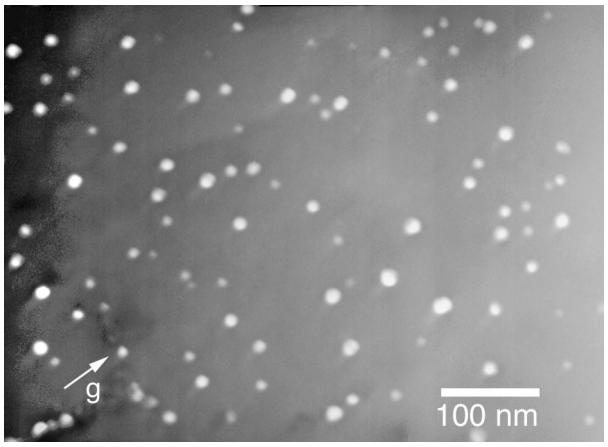

Figure 8.8: Post creep TEM of Al-0.06at.%Sc-0.02at.%Gd aged for 26 days at 300˚C.

8.4.2 Normalized Threshold Stress Increase with <R(t)>

Strains and stresses are introduced into the matrix when a misfitting precipitate is present. This stress field has been described by Mura [194] and Nembach [195]. The stress field around a misfitting precipitate is [195]:

$$\sigma_{obst}(x, y, z - h_z) = \frac{2\mu\varepsilon R^3}{\rho^5}\begin{pmatrix} 3x^2 - \rho^2 & 3xy & 3x(z-h_z) \\ 3xy & 3y^2 - \rho^2 & 3y(z-h_z) \\ 3x(z-h_z) & 3y(z-h_z) & 3(z-h_z)^2 - \rho^2 \end{pmatrix} \quad (8.3)$$

where ε is the constrained precipitate/matrix mismatch, $\rho = (x^2+y^2+(z-h_z)^2)$, μ is the shear modulus of the matrix and R is the precipitate radius. The diagram displaying the x, y, z and h_z coordinates can be found in Fig. 8.9 [195]. A recent work by Xiang and Srolovitz [121] modeled the dislocation motion over misfitting, non-penetrable precipitates and found the resulting paths which the dislocations take in climbing over the precipitate.

Figs. 8.3-6 show that for each of the four Al-Sc-RE alloys examined, the creep resistance is higher than for RE-free alloys with similar ϕ and <R(t)> values. Fig. 8.10 shows the normalized threshold stress vs. <R(t)>. The normalized threshold stress is given by $\sigma_{th}/\Delta\sigma_{or}$ where $\Delta\sigma_{or}$ is calculated from:

$$\Delta\sigma_{or} = M\frac{0.4\mu b}{\pi\lambda}\frac{\ln(2\bar{r}/b)}{\sqrt{1-\nu}} \quad (8.4)$$

The use of the normalized threshold stress removes the dependency on precipitate volume fraction, since the interprecipitate spacing, λ, is dependent on volume fraction. This allows for direct comparison of alloys with different volume fractions of precipitates. The RE containing alloys were plotted along with the Al-Sc[20], Al-Sc-Zr [28], Al-Mg-Sc [26] and Al-Sc-Ti [102] alloys; with all of the Al-Sc-RE alloys displaying higher normalized threshold stress values. All of the alloys show an increase in the normalized threshold stress with an increase in <R(t)>.

Initially the absolute value of the threshold stress increases for the Al-Sc-RE alloys, but eventually σ_{th} will decrease with even larger <R(t)> due to the lower $N_v(t)$. The normalized threshold stress continues to increase even when the absolute value of the threshold stress decreases, since the $\Delta\sigma_{or}$ also decreases with <R(t)>.

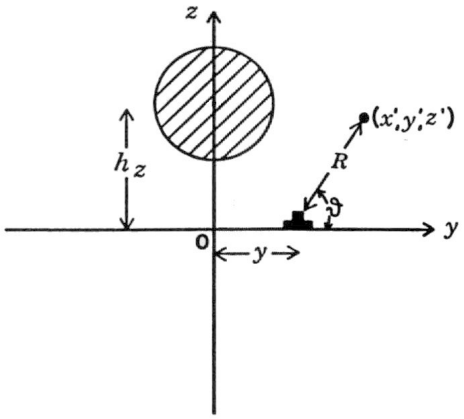

Figure 8.9: Schematic showing the x, y, z and h_z coordinates [195].

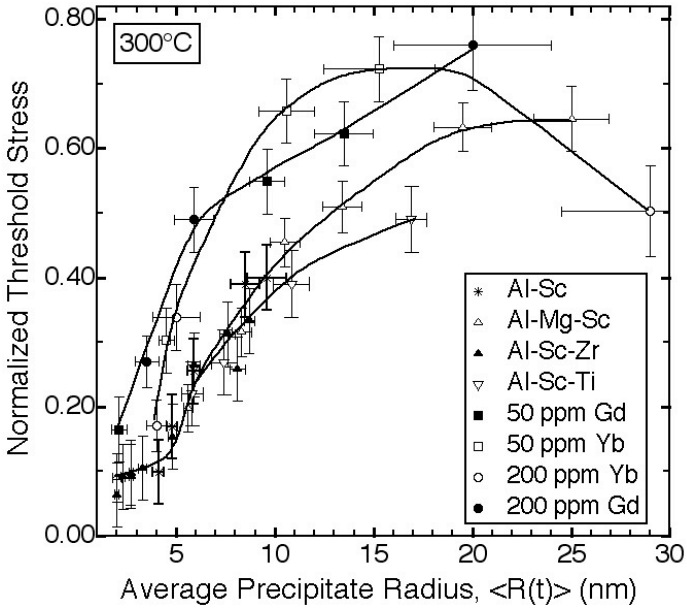

Figure 8.10: Threshold stress, σ_{th}, normalized by the Orowan stress, $\Delta\sigma_{or}$, for all four Al-Sc-RE (50 and 200 ppm Yb or Gd) alloys vs. average precipitate radius, <R(t)>, for creep at 300˚C. Data compared with that of the Al-Sc [20], Al-Sc-Zr [28] Al-Mg-Sc [26] and Al-Sc-Ti systems.

An increase in normalized threshold stress with increasing lattice parameter mismatch was recently predicted by a model which considered the elastic effects on climb of dislocations over precipitates [9]. The elastic strain fields will have an effect on the forces on the dislocation and hence the climb of the dislocation over the precipitate. The model, as well as previous experimental results on the Al-Sc [20], Al-Sc-Zr [28], and Al-Mg-Sc [26] systems and those shown earlier in this thesis, indicate that increasing <R(t)> leads to an increase in $\sigma_{th}/\Delta\sigma_{or}$ due to the fact that the glide and climb forces on a dislocation are dependent on R.

8.4.3 Precipitate Lattice Parameter and its Effect on Creep Resistance

σ_{th} in the Al-Sc-200RE and Al-Sc-50 RE alloys are higher than in the previously studied Al-Sc or Al-Sc-X alloys with similar volume fractions. For an Al-0.06at.%Sc alloy at 300˚C studied by Marquis et al [20], the threshold stresses were 8 and 19 MPa for 4.1 and 8.5 nm radius, respectively. Threshold stresses for an Al-0.07Sc-0.02Zr (at.%) alloy with <R(t)> = 8.7 nm is found to be 20 MPa [28], which is a 25% lower value of σ_{th} than in the Al-Sc-50Yb alloy with similar <R(t)>.

Higher volume fractions, ϕ, are needed in the RE-free alloys to attain similar threshold stresses. Threshold stresses for the Al-0.12at.%Sc alloy were measured to be in the range of 14-22 MPa for precipitate radii of 3.0-5.8 nm [20]. This alloy had much higher volume fractions ranging from 0.46-0.49 % depending on the aging temperature, as compared to ϕ = 0.21-0.33 % for the present alloys. For the Al-0.18at.%Sc alloy with a volume fraction ranging from 0.71 to 0.75, the

threshold stresses were even higher [20], ranging from 17-32 MPa for precipitates ranging in size from 1.4 - 9.6 nm. Thus, the addition of 200 ppm of RE leads to the same increase in normalized threshold stress as 600-1200 ppm of Sc.

The remarkable increase in σ_{th} (Figs. 8.3-6) and the normalized threshold stress (Fig. 8.10) displayed by the Al-Sc-RE alloys may be due to the known increased lattice parameter mismatch between the α-Al matrix and the $Al_3(Sc_{1-x}RE_x)$ precipitates [5, 8] as compared to Al_3Sc, $Al_3(Sc_{1-x}Zr_x)$ [29] or $Al_3(Sc_{1-x}Ti_x)$ [29]. Increased mismatch results in an increase of elastic interactions between lattice dislocations and the precipitates they bypass by climb, resulting in a higher value of σ_{th}.

The lattice parameters at room temperature for the intermetallic $Al_3(Sc_{1-x}RE_x)$ phases are shown in Fig. 8.11. As the RE replaces the Sc in the $Al_3(Sc_{1-x}RE_x)$ phase, the lattice parameter, and thus the mismatch with Al, increases. This is in contrast to Ti which decreases the lattice parameter of the $L1_2$ phase. Vegard's law, which assumes a linear dependence of the lattice parameter on the composition of the phase, is used to determine the intermediate lattice parameters. The lattice parameter mismatches at 300˚C for the precipitate compositions measured via LEAP in the various alloys are listed in Table 8.2. The unconstrained and constrained mismatches are given. These quantities are related through:

$$\varepsilon_s = \frac{\delta}{1 + 4\mu/\left(3B_p\right)} \tag{8.5}$$

where δ is the unconstrained mismatch obtained by Vegard's law, ε_s is the constrained mismatch, μ is the shear modulus of the matrix (25.4 GPa at room temperature [61]) and B_p is the bulk modulus of the precipitate (91.5 GPa at room temperature [172]).

Table 8.2: Mismatches at 300°C at the α-Al/$Al_3(Sc_{1-y}X_y)$ interface assuming the solute is uniformly distributed in the precipitate. Also given is the percentage increase in mismatch with respect to Al_3Sc. Precipitate compositions are based on LEAP measurements. Coefficient of thermal expansion used is that of pure Al_3Sc (16.0×10^{-6} K^{-1} [122]).

Alloy	Matrix/Precipitate Unconstrained Mismatch at 300°C for Uniformly Distributed Solute (%), δ	Matrix/ Precipitate Constrained Mismatch at 300°C (%), ε_s	% Increase in Mismatch Compared with Al_3Sc
Al-Sc-200Yb [8]	1.531	1.11	46
Al-Sc-200Gd [5]	1.196	0.87	14
Al-Sc-50Yb [8]	1.249	0.91	19
Al-Sc-50Gd [5]	1.196	0.87	14
Al-Sc [29]	1.048	0.77	-
Al-Sc-Zr [29]	1.044	0.76	-0.3
Al-Sc-Ti [29]	0.718	0.52	-31

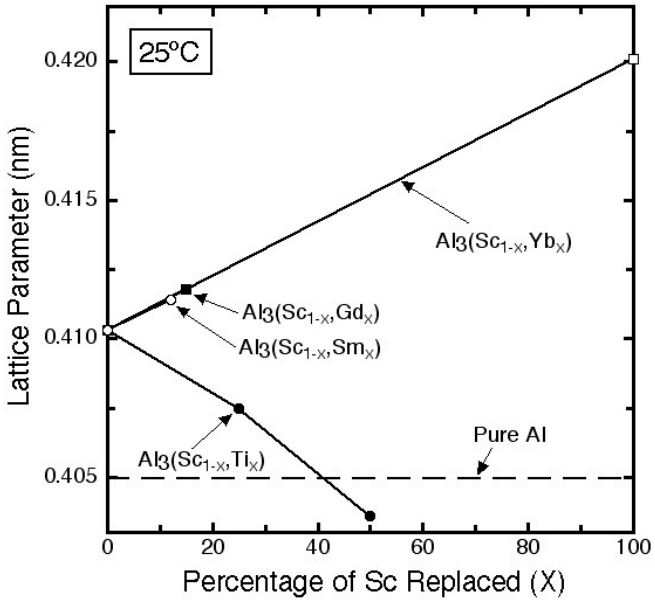

Figure 8.11: Lattice parameters at 25°C with increasing rare earth (RE) element replacing the Sc in the $Al_3(Sc_{1-x}RE_x)$ [4, 5, 8]. Data for Ti is also shown [29].

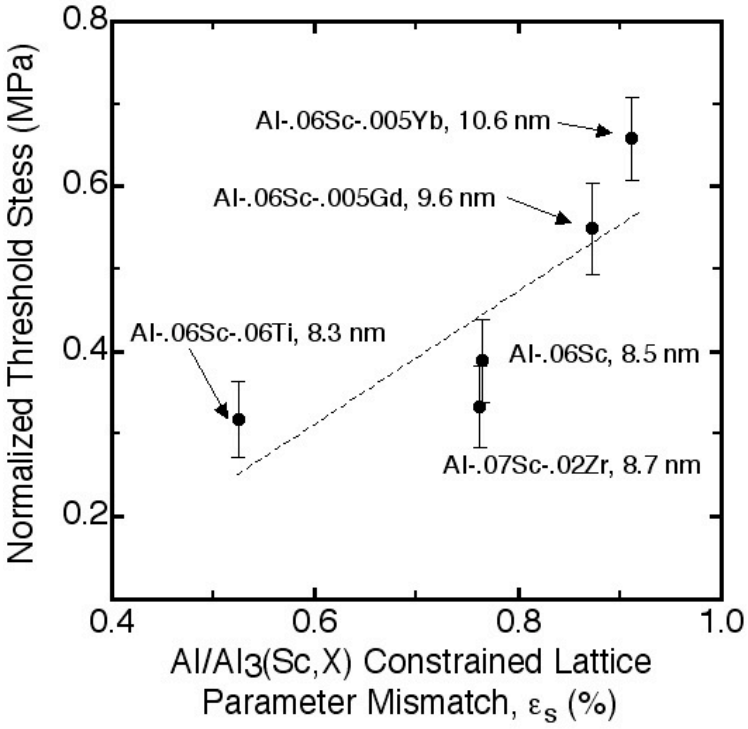

Figure 8.12: Threshold stress, σ_{th}, normalized by the Orowan stress, $\Delta\sigma_{or}$, vs. constrained mismatch, ε_s, at 300˚C for Al-Sc [20], Al-Sc-Zr [28], Al-Sc-Ti and Al-Sc-50RE alloys. <R(t)> ranges from 8.3 to 10.6 nm.

In Fig. 8.10 it is shown that the difference between the binary and the ternary alloys is more apparent at larger radii since the elastic interaction volume of the precipitate scales with R^3. The increase in normalized threshold stress is plotted with respect to the mismatch in Fig. 8.12 for <R(t)> = 8-10 nm. The general trend is that the normalized threshold stress increases with increasing lattice parameter mismatch.

Since the precipitate radii are somewhat different between the different alloys, Fig. 8.13 shows the normalized threshold stress values corrected for radius. The correction in $\sigma_{th}/\Delta\sigma_{or}$ with R was made assuming linear behavior according to:

$$\Delta(\sigma_{th}/\Delta\sigma_{or}) = \left(\frac{\sigma_{th,2}/\Delta\sigma_{or,2} - \sigma_{th,1}/\Delta\sigma_{or,1}}{R_2 - R_1}\right)\Delta R \tag{8.6}$$

where subscripts 1 and 2 refer to the quantities at the two data points closest to the 8-10 nm range, in order to obtain the slope in that region. This correction results in a somewhat diminished normalized threshold stress for Al-Sc-50Gd and Al-Sc-50Yb. These results suggest that even with the small amount of Gd or Yb in the alloy, there is a significant effect on lattice parameter and normalized threshold stress.

Since it is observed that the lattice parameters have an effect on the threshold stresses (Fig. 8.12), the lattice parameters are confirmed by TEM for the Al-Sc-RE alloys. It is anticipated that the lattice parameter in the matrix will be close to that of pure aluminum because there is very little solute left (< 20 ppm for the Al-Sc-Yb alloys) in the matrix. The Al matrix lattice parameter is determined to be 0.405±0.005 nm in the Al-Sc-200Yb alloy after 64 days of aging. The diffraction pattern is shown in Fig. 8.14. The lattice parameter for the $Al_3(Sc_{1-x}Yb_x)$ precipitate phase, is measured from the diffraction pattern to be 0.417±0.006 nm at the temperature of the specimen in the TEM. This is close to the value according to Vegard's law for a precipitate with uniform composition, which gives a lattice parameter of 0.413 nm. A similar procedure was employed for the Al-Sc-200Gd alloy and the lattice parameter of the precipitate phase was found to be 0.411±0.008 nm. This is a smaller lattice parameter than was observed for the Al-Sc-200Yb alloy, as expected due to the lower RE content in the precipitates in the Al-Sc-Gd alloys.

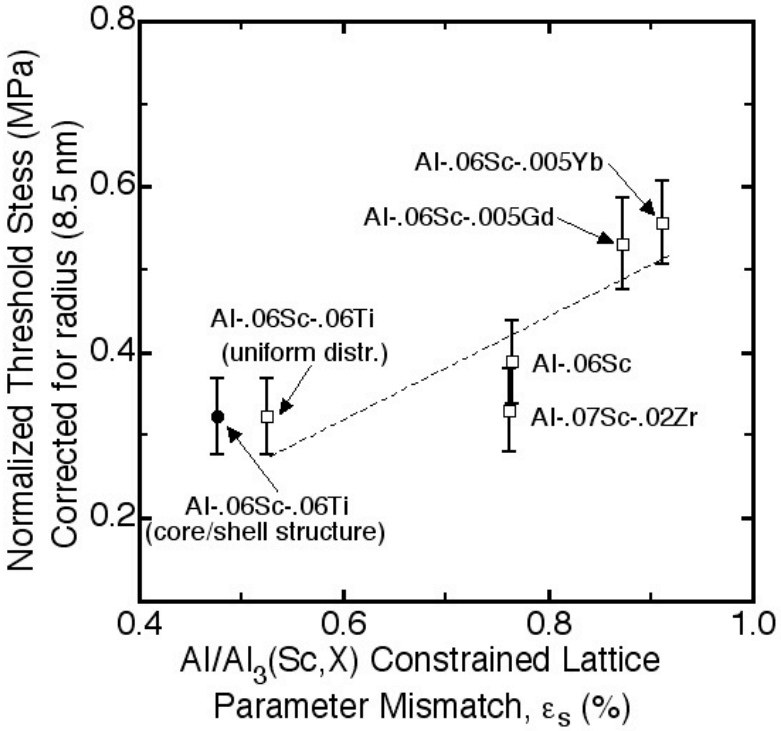

Figure 8.13: Threshold stress, σ_{th}, normalized by the Orowan stress, $\Delta\sigma_{or}$, vs. constrained mismatch, ε_s, at 300˚C for Al-Sc [20], Al-Sc-Zr [28], Al-Sc-Ti and Al-Sc-50RE alloys. Corrected for <R(t)> to 8.5 nm.

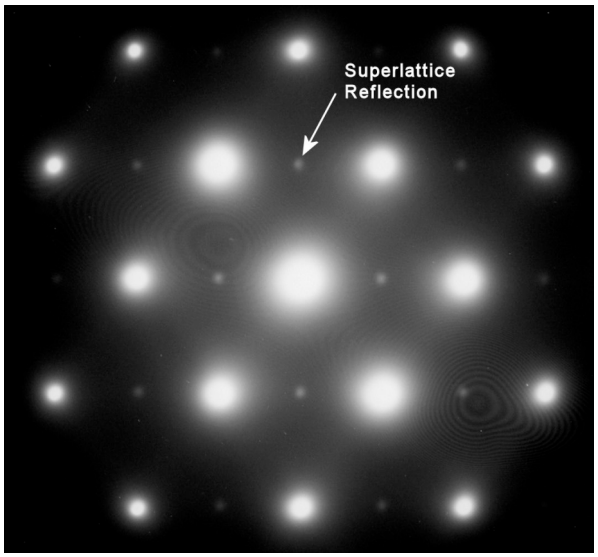

Figure 8.14: TEM diffraction pattern showing superlattice reflections of the $Al_3(Sc_{1-x}Yb_x)$ phase from Al-0.06at.%Sc-0.02at.%Yb aged for 64 hrs at 300˚C. [110] projection.

8.4.4 Effect of Non-Uniform Distribution of Solute in the Precipitates

The lattice parameter mismatches shown in Table 8.2 assume a uniform composition within the precipitates. However, from the LEAP results in the previous chapter, it was demonstrated that the distribution of RE and Sc in the precipitate was not uniform, showing a core/shell structure. It is anticipated that the stresses in the surrounding matrix will be relaxed when the element with the smaller misfit is found at the interface. The topic of a non-uniform composition leading to non-uniform mismatch within the precipitate has been studied by Dunn et al. [196]. Assuming a linear function of the lattice parameter change, they found that the stress field in the matrix will increase as the difference in the lattice parameters increases.

For a core/shell structure with mismatches between the core, shell and matrix phases, the stress field in the matrix has been calculated by Farjami and Voorhees [197]. The stress field was calculated assuming the following displacements, u, in the core, shell and matrix phases:

$$u^{core} = A^{core} r \tag{8.7}$$

$$u^{shell} = A^{shell} r + \frac{B^{shell}}{r^2} \tag{8.8}$$

$$u^{matrix} = \frac{B^{matrix}}{r^2} \tag{8.9}$$

where A and B are constants and r is the distance from the center of the precipitate.

This resulted in:

$$\sigma_{rr}^{matrix} = \frac{-(4r_{sh}^2(3k_{sh}r_{sh}(-3k_{sh}(r_{sh}^3 - r_c^3)\delta_{sh} - 3k_{sh}r_c^3\delta_c)) + 2r_{sh}Y\lambda_{sh})\mu_m)}{3r^3(6k_{sh}^2(r_{sh}^3 - r_c^3) + k_{sh}(3k_{sh}(r_{sh}^3 - 2r_c^3) + 4r_c^3(\lambda_{sh} + \mu_m) + r_{sh}^3(-6\lambda_{sh} + 8\mu_m)) - 4B))}$$

where $B = 2r_{sh}^3\lambda_{sh}\mu_m + k_{sh}(-r_{sh}^3\mu_m + r_c^3(\lambda_{sh} + \mu_m))$ and $Y = (-9k_{sh}r_{sh}^3\delta_{sh} + 2r_c^2(3k_{sh}r_c(\delta_{sh} - \delta_c)))$. The bulk modulus, k_{sh} (91.5 GPa [172]) and Lame constant, λ_{sh}, are assumed to be the same for the core and shell regions. μ_m represents the shear modulus in the matrix (25.4 GPa [61]), r_c and r_{sh} represent the radii of the core and shell regions, and δ_c and δ_{sh} represent the mismatches between the core/shell and shell/matrix, respectively. This assumes that the surface stresses are zero. Finally, it is found that $\sigma_{rr}^{matrix} = -2\sigma_{\theta\theta}^{matrix}$.

For our data, the situation which most closely resembles a core/shell structure is in the Al-Sc-200ppm Yb alloy upon pre-aging for 24 h at 300˚C. This aging treatment gives rise to <R(t)> = 2.9 nm with an Al_3Yb core of 1.8 nm. The ratio of the magnitudes of the stress fields (calculated in the radial direction) between the homogeneously distributed precipitate and the core/shell structure is 1.17. This confirms that the core/shell structure can relax some of the stresses in the surrounding matrix. The Al_3Yb core and Al_3Sc shell in the Al-Sc-Yb alloys interdiffuse at longer aging times leaving more homogeneously distributed concentrations of solute within the precipitates. Thus at longer aging times the assumption of homogeneous distribution is appropriate.

A similar approach can be used for the Al-0.06Sc-0.06Ti alloy, since at longer aging times the Ti segregates to the interface. For <R(t)> = 8.3 nm, the precipitate is assumed to have a core with 2% Ti and a 1 nm thick shell containing 6% Ti. The lattice parameters of these two phases are calculated using Vegard's law. The ratio of the magnitude of the stress field (calculated in the radial direction) between the homogeneously distributed precipitate and the core/shell structure

is 1.1. Once again this shows that some of the stresses in the matrix can be relaxed. When applying this to Figs. 8.12 and 8.13, the ratio of the stress fields is used to calculate a new equivalent mismatch (by assuming that the stress field is directly proportional to the mismatch and thus multiplying the mismatch by the calculated ratio). It can be seen (Fig. 8.13) that for the core/shell approximation the Al-Sc-Ti point is shifted to the left.

8.4.5 Decrease of the Normalized Threshold Stress with Large <R(t)>

In a previous study on an Al-2.2Mg-0.12Sc (at.%) alloy, the normalized threshold stress does not decrease as precipitates become semi-coherent at radii above 11 nm [26], as expected from the relaxation of the misfit stresses as the interface with the introduction of interfacial dislocations. Several mechanisms were suggested by the authors, including the presence of residual modulus and lattice mismatch stresses which are not fully relaxed by the dislocations. Another suggested mechanism is that the misfit dislocations at the matrix-precipitate interface interact elastically with the matrix dislocations, impeding their climb motion.

For the 29±9 nm precipitates in the Al-Sc-Yb sample, the first evidence of a decrease in the normalized threshold stress is observed in Fig. 8.10, due to the semi-coherent nature of the precipitates. The threshold stress, however, is still at $0.5\Delta\sigma_{or}$, which is well above the value of σ_{th} predicted for non-interacting incoherent particles [64]. Thus, there must be some residual interaction between the climbing dislocations and the precipitate. This could either be in the form of residual mismatch stresses which have not been fully relaxed at the interface or there could be elastic field interaction with the interfacial dislocations.

One can estimate the radius, R_{crit}, at which a misfitting precipitate will become semicoherent:

$$R_{crit} = \frac{b}{2\delta} \tag{8.10}$$

For the Al-Sc-200Yb alloy, the critical radius, R_{crit} is calculated to be 8.7 nm. For the Al-Sc-50Yb alloy, R_{crit} is 11.6 nm. For both of the Al-Sc-Gd alloys (50 and 200 ppm), the critical radius is calculated to be 13.6 nm. Thus for the large radii examined, the precipitates would be semi-coherent. From this calculation, for the 13.5±3.0 nm Al-Sc-200Gd sample, there would be ~1 interfacial dislocation expected across the precipitate. Indeed, Fig. 8.15 shows that the precipitates of Al-Sc-200Gd are not coherent after an aging treatment of 24 h at 300˚C followed by 120h at 400˚C (13.5±3.0 nm), due to the lack of symmetrical Ashby-Brown strain contrast.

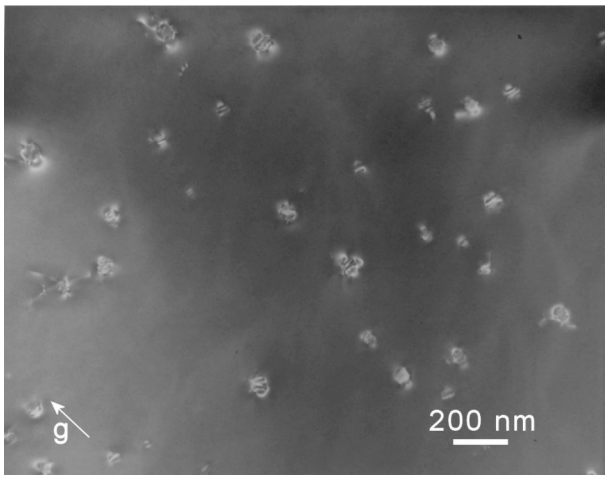

Figure 8.15: Bright-field TEM micrograph of Al-0.06at.%Sc-0.02at.%Gd aged for 24 h at 300˚C followed by 120h at 400˚C. [110] projection.

8.5 Conclusions

The creep properties of Al-0.06 Sc-0.005 RE (at.%) and Al-0.06 Sc-0.02 RE (at.%) (RE = Yb or Gd) are studied.

- The <R(t)> values for the Al-Sc-RE alloys increase significantly during aging at 400˚C, after pre-aging at 300˚C. These alloys attain much higher radii than the Al-Sc-Ti alloy which confirms that these alloys have a lower coarsening resistance.
- Each of the Al-Sc-RE alloys display threshold stresses at each of the radii studied. The creep resistance of these alloys is observed to be higher than for Al-Sc, Al-Sc-Zr, Al-Sc-Ti and Al-Mg-Sc alloys with similar values for <R(t)> and ϕ.
- The normalized threshold stresses increased with increasing values of <R(t)>, similar to other Al-Sc and Al-Sc-X alloys. This is in agreement with a recent model which considered the effects of lattice parameter mismatch.
- The normalized threshold stresses were higher in the <R(t)> = 8-10 nm range for the Al-Sc-RE alloys compared with Al-Sc, Al-Sc-Ti and Al-Sc-Zr alloys. This was attributed to the higher lattice parameter mismatches between the matrix and the precipitate phase with the addition of RE.
- At large <R(t)>, evidence of a decrease in normalized threshold stress was observed since the precipitates are semi-coherent and the mismatch stresses are relaxed.

9. Effects of Zr on the Precipitation of $Al_3(Yb_{1-x}Sc_x)$ and $Al_3(Sc_{1-x}Yb_x)$ in Al-Sc-Yb Alloys: Microstructure and Resulting Creep Properties

9.1 Introduction

Previous chapters have examined the effects of the addition of slow diffusing elements, such as Ti and Zr, to Al. This analysis demonstrated that the addition of these elements decreases the rate of precipitate coarsening. Furthermore, it has been shown that RE, in particular Yb, replace the Sc in the $Al_3(Sc_{1-x}RE_x)$ precipitates and increase the creep resistance. This thesis concludes with a study of quaternary Al-Sc-Yb-Zr alloys which contain additions of both of types of elements. The interactions among the alloying elements will be examined.

It is well known that the addition of small amounts micro-alloying elements or impurity atoms can greatly affect the precipitation kinetics of the other solute elements in Al alloys. For example, when 0.1at.% Si is added to an Al-0.18t.%Zr alloy, there is a 60% increase in the hardness and a decrease in the incubation time, since the hardness already increases in the as-quenched state. This occurs since the Si is incorporated into the precipitates on the Al sublattice [198]. Additions of 0.1% Si to Al-Hf alloys and Ag additions to Al-Cu-Mg alloys [150] can also lead to an increase in hardening. In a recent study on a 6111 aluminum alloy, the increase in strength upon aging at 175˚C for 30 min following a pre-aging at 79-107˚C is 60-85 MPa, while the strength increase is only 20-25 MPa in a sample which has not undergone the pre-aging treatment [152]. This is attributed to the change in the clustering of atoms during the pre-aging treatment.

There is experimental evidence in various alloy systems for the existence of cross-diffusion, which implies that one element has an effect on the diffusivity of another element. This gives rise to the so-called "off-diagonal" terms in the diffusion tensor. Systems where the off-diagonal diffusion terms are not zero include Fe-, Cu- and Ni-based alloys [199-202]. The diffusivity in the presence of solute atoms has also been modeled, with a summary of the various methods given by Nastar [203].

In addition to the overall changes in the diffusion rate, the specific interactions between atoms and their effects on diffusion have been examined. For example, Mg and O form dimers in Ag alloys [204] and it has been proposed that these dimers trap vacancies since the complex dilates the Ag lattice [204], and hence slow down diffusion. Furthermore, Mao et. al. demonstrated that clusters of Al (Al n-mers) and Cr (Cr n-mers) diffuse faster in the Ni matrix than an individual Al or Cr atom [181], with Al-Al and Cr-Cr dimers diffusing at the fastest rate. They attributed this behavior to attractive vacancy-solute interactions at distances greater than the first nearest-neighbor distance.

The following sections of this chapter detail the results of a study on Al-Sc-Yb-Zr alloys. The interactions among the alloying elements and the resulting mechanical properties will be examined.

9.2 Experimental Procedures

The compositions of the alloys are Al-0.07Sc-0.02Yb-0.02Zr and Al-0.06Sc-0.02Yb-0.004Zr (at. ppm) (verified by Wah Chang (Albany, OR)). Henceforth, these alloys will be referred to as the

200 ppm Zr and 50 ppm Zr alloys. The microstructural analyses and creep experiments were performed in a similar manner to those discussed for ternary alloys in Chapter 3.

9.3 Results

9.3.1 Microhardness upon Aging at 300˚C

For aging at 300˚C, the Vickers microhardness exhibits a much longer incubation time for both the 50 and 200 ppm Zr alloys, as compared to the Al-0.06Sc-0.02Yb (at.%) alloy containing *no* Zr (hereafter referred to as Al-Sc-Yb) (Fig. 9.1) [99]. The alloy with 50 ppm of Zr has a shorter incubation time compared with the 200 ppm Zr alloy (5 min vs. 15 min). For the 200 ppm Zr alloy, the hardness only increases by 20 MPa after 15 min of aging. For the 50 ppm Zr alloy, the hardness increases by 40 MPa after 5 minutes of aging. Both of the Al-Sc-Yb-Zr alloys have an incubation time shorter than an Al-0.06Sc-0.005Zr (at.%) alloy, which exhibits its first significant hardening between 30 and 60 min.

For both Al-Sc-Yb-Zr alloys, there is only one rapid increase in the microhardness, between 15 and 60 min. By contrast, the Al-Sc-Yb discussed in prior chapters has a distinct plateau between the first and second rapid increases in microhardness, which is attributed to the initial precipitation of $Al_3(Yb_{1-x}Sc_x)$ followed by a second precipitation stage as Sc diffuses to the Yb-rich precipitates. Additionally, both the Zr containing alloys retain their hardness up to 64 days of aging at 300˚C.

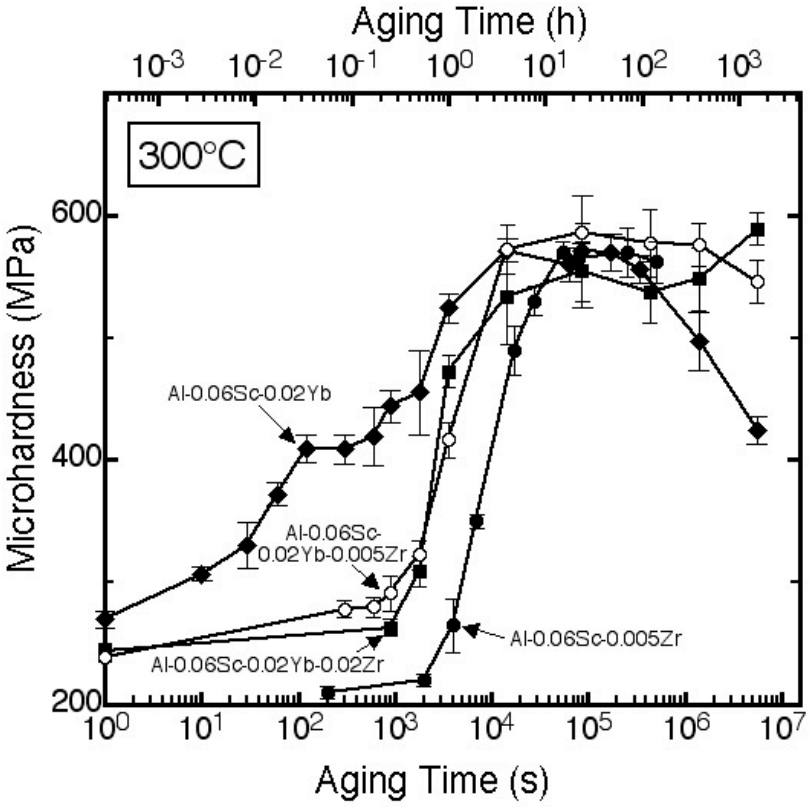

Figure 9.1: Vickers Microhardness of the 50 and 200 ppm Zr alloys compared with Al-0.06Sc-0.02Yb and Al-0.06Sc-0.005Zr [28] alloys.

9.3.2 Microstructure Upon Aging at 300˚C

In the unaged state, there are no precipitates visible in the three-dimensional LEAP reconstruction (Fig. 9.2). After 15 min of aging, there is evidence that precipitation is occurring in both Al-Sc-Yb-Zr alloys (Figs. 9.3-4), since some clustering of the atoms is observed. The 50 ppm Zr alloy (Fig. 9.3) appears to have somewhat larger precipitates, with an average radius, <R(t)>, equal to 0.67±0.19 nm. The largest precipitate in the data set has R = 1.32 nm. In the 200 ppm Zr alloy (Fig. 9.4), <R(t)> = 0.56±0.08 nm, and the largest value of R is 0.82 nm. These quantities are determined using the envelope method, as discussed in the Appendix A.

The ratio of Yb to Sc concentration in the precipitates, $C_{Yb}^{\beta}/C_{Sc}^{\beta}$ (at. %/at. %), after 15 min is displayed in Fig. 9.5 (a and b). There is a wide range of Yb/Sc concentrations in the precipitates. The average of $C_{Yb}^{\beta}/C_{Sc}^{\beta}$ for the 50 ppm Zr alloy is 0.99 and for the 200 ppm Zr alloy $C_{Yb}^{\beta}/C_{Sc}^{\beta}$ = 1.17. For comparison, the Yb/Sc ratio in the precipitates is shown for the Al-Sc-Yb alloy (Fig. 9.5c). The average Yb/Sc ratio in the precipitates has a larger value in this alloy, with $C_{Yb}^{\beta}/C_{Sc}^{\beta}$ = 2.12. In the Al-Sc-Yb alloy the majority of the clusters, including the smaller ones, have Yb/Sc ratios greater than unity. The precipitate size distributions can also be observed from Fig. 9.5. The Al-Sc-Yb alloy has much larger precipitates than either of the two Zr containing alloys.

After 1 h of aging, <R(t)> = 0.81±0.38nm for the 50 ppm alloy and <R(t)> = 0.92±0.61 nm for the 200 ppm alloy. Figs. 9.6 (a and b) show that $C_{Yb}^{\beta}/C_{Sc}^{\beta}$ decreases with increasing values of R, although there is significant scatter in the R values for precipitates with R < 0.75 nm. The larger precipitates have a smaller Yb/Sc ratio which reach 0.05 at large R. This is much lower than the overall ratio of Yb to Sc in the alloy, indicating that more Sc than Yb has precipitated. In contrast to the 15 min aging time, the 200 ppm alloy now has a larger <R(t)>, perhaps due to slight differences in the overall alloy compositions.

For even longer aging times, up to 1536 h, <R(t)> and the number density, $N_v(t)$, are similar for both alloys (Figs. 9.7 and 9.8), within experimental error. We showed that these Zr containing alloys coarsen slowly at longer aging times at 300˚C [205], as evidenced by the retention of microhardness and the temporal evolution of <R(t)> and $N_v(t)$.

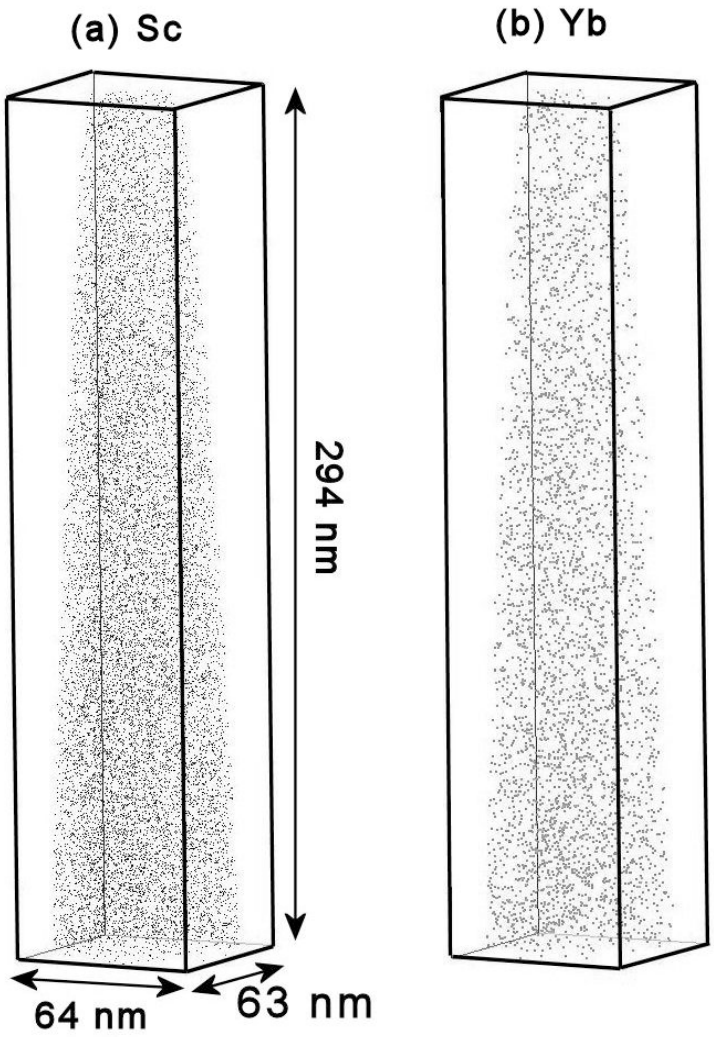

Figure 9.2: 3-dimensional reconstruction of a data set from LEAP tomography for the unaged condition of the 200 ppm Zr alloy, showing a fairly uniform distribution of solute atoms: (a) Sc atoms and (b) Yb atoms.

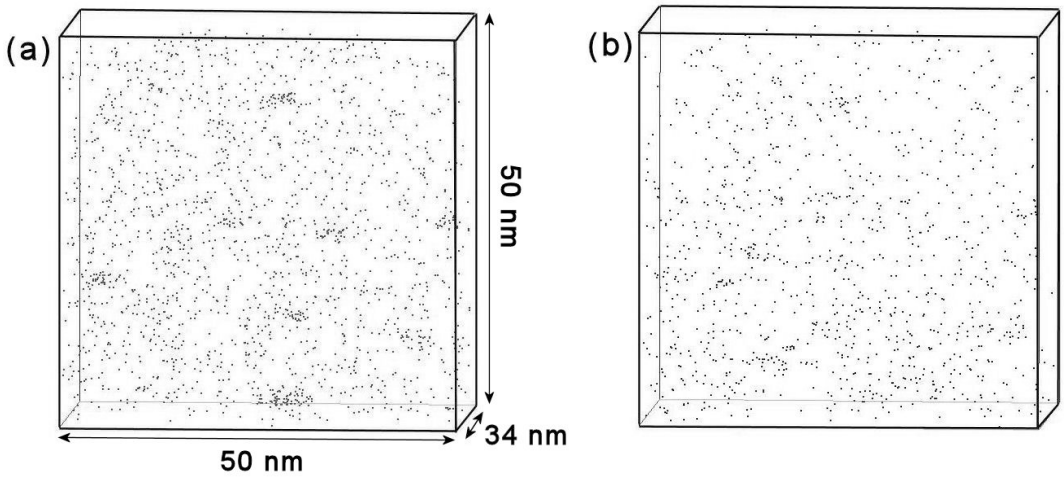

Figure 9.3: (a) Sc and (b) Yb atoms of the 50 ppm Zr alloy for 15 minutes of aging. Data set contains 2.6 million atoms.

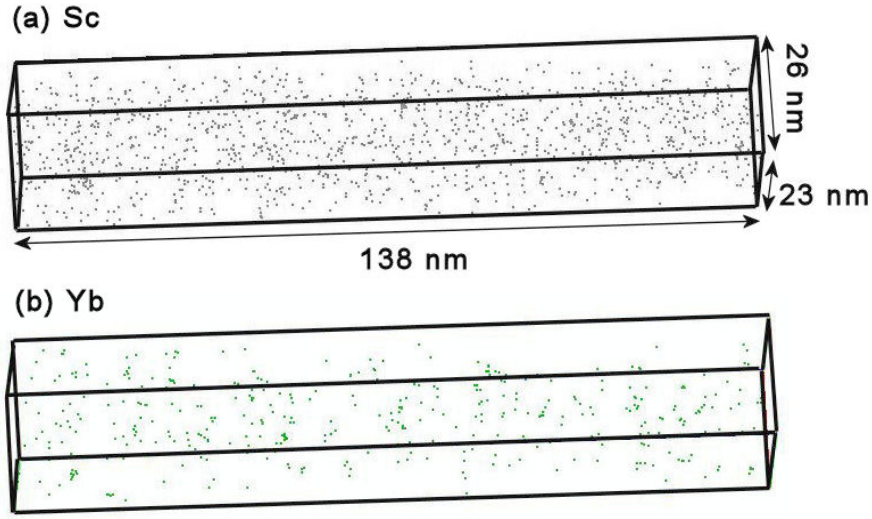

Figure 9.4: (a) Sc and (b) Yb atoms for the 200 ppm Zr alloy at 15 min of aging. Data set contains 2.4 million atoms.

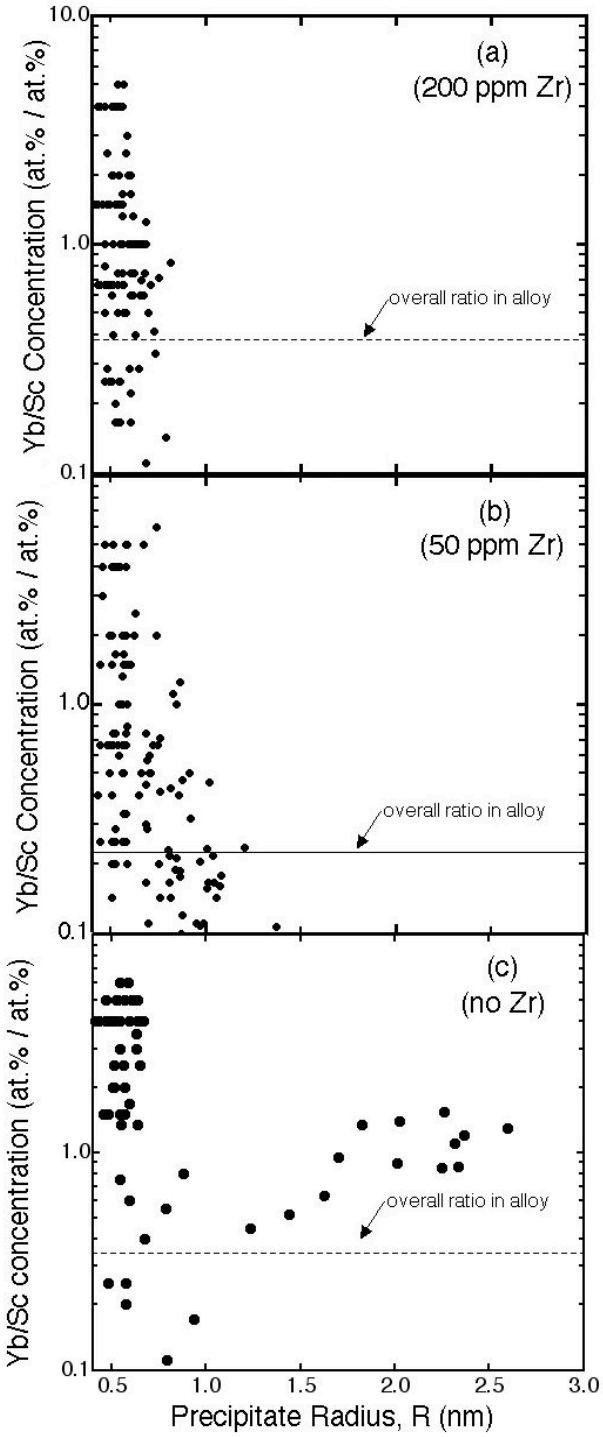

Figure 9.5: Yb/Sc concentration ratios vs. precipitate radius <R(t)> within the individual precipitates for aging for 15 minutes: (a) 200 ppm Zr alloy and (b) 50 ppm Zr alloy and (c) Al-Sc-Yb (no Zr).

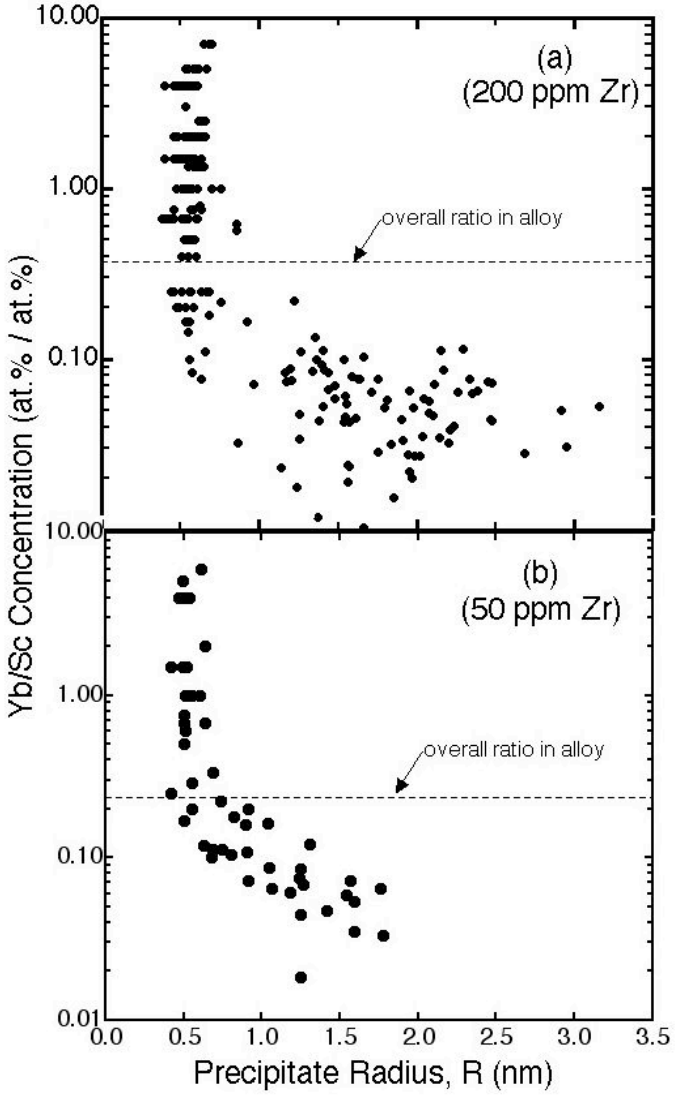

Figure 9.6: Yb/Sc concentrations within individual precipitates for 1 h of aging at 300˚C (a) 200 ppm Zr alloy and (b) 50 ppm Zr alloy.

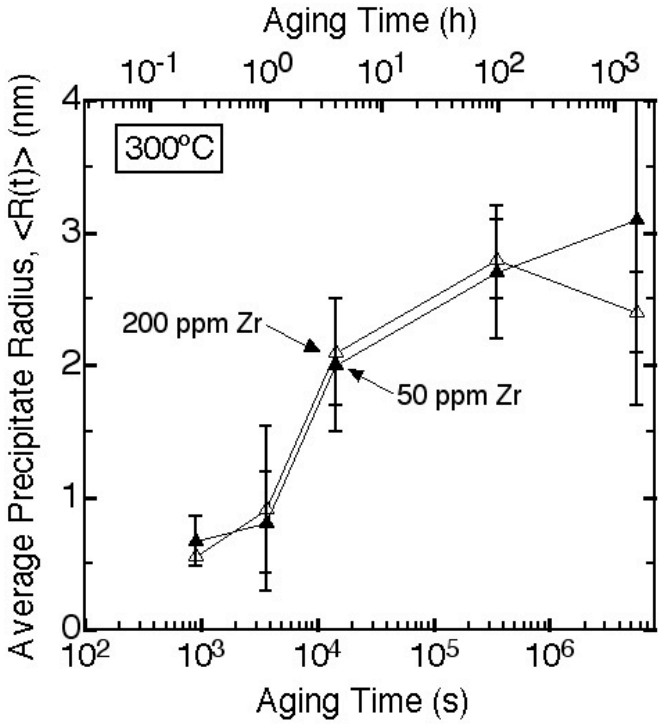

Figure 9.7: Average Precipitate Radius, <R(t)>, vs. aging time at 300˚C 50 ppm Zr and 200 ppm Zr alloys.

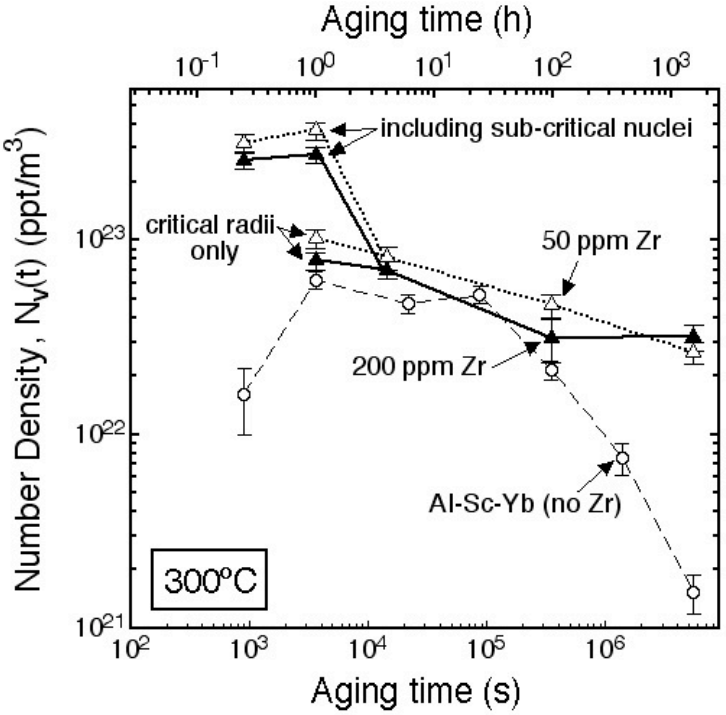

Figure 9.8: Number density of precipitates, $N_v(t)$, vs. aging time at 300˚C for 50 ppm Zr alloy and 200 ppm Zr alloy compared with the Al-Sc-Yb alloy containing no Zr.

9.3.3 Radial Distribution Functions (RDFs)

The partial RDFs for interactions between each of the elements are measured to shed light on the mechanism causing the longer incubation time with the addition of Zr. For the 200 ppm Zr alloy, values greater than unity are observed for the partial Yb-Zr and Zr-Yb RDFs for distances of less than one nanometer (Fig. 9.9a). The Yb-Zr (and Zr-Yb) interactions increase slightly at 15 min for the 200 ppm alloy. After 15 min the maximum value, which is at the first nearest-neighbor distance, has increased to 2.25. In the 50 ppm Zr alloy in the homogenized state (Fig. 9.10a) there are peaks between the 2^{nd} and 3^{rd} nearest neighbor distance. The interaction between Yb and Zr is, however, less obvious than in the alloy with 200 ppm Zr.

The partial Yb-Yb RDF shows that after 15 minutes, there is a greater Yb-Yb interaction, compared with the homogenized state for the 200 ppm Zr alloy (Fig. 9.9b). At 15 min the Yb is forming $Al_3(Yb_{1-x}Sc_x)$ precipitates, which is reflected in values of greater than 10 in the partial RDF. There are also large values for the Yb-Yb partial RDF of the 50 ppm Zr alloy in the homogenized state (Fig. 9.10b), with a peak value of 17, which signifies that the concentration is 17 times the average concentration at that particular distance. This indicates an interaction between the Yb atoms in the unaged state.

The Zr-Zr partial RDF for the 200 ppm Zr alloy in the unaged state has values that remain close to unity, ranging from 0.9 to 1.4 (Fig. 9.9c). There is no significant change after aging for 15 min, with the maximum value being 1.7 times the average concentration in the alloy. The reason for the lack of clustering of Zr atoms is its small diffusivity in Al [97]. The 50 ppm Zr alloy,

exhibits similar results for the unaged state (Fig. 9.10c). The peaks fluctuate as there are fewer Zr atoms. The error and the significance of the peaks in the partial RDFs is discussed in Appendix B.

In the unaged state for the 200 ppm Zr alloy (Fig. 9.9d), there is a slight attractive interaction between Sc and Yb. The partial Sc-Zr RDF does not show any interaction between these two elements. While the Sc-Sc partial RDF does not increase much above unity, there is, however, a strong repulsive interaction at the first nearest-neighbor

distance and a attractive interaction at the second nearest-neighbor distance indicating some possible short range order. For comparison, at 15 min of aging (Fig. 9.9e), there is a greater Sc-Sc and Sc-Yb interaction, with the maximum values of the peaks achieving 2.7 and 4, respectively. This is anticipated because at longer aging times there are both $Al_3(Yb_{1-x}Sc_x)$ and $Al_3(Sc_{1-x}Yb_x)$ precipitates. The Sc-Zr partial RDF after 15 minutes, however, remains close to unity.

The 50 ppm alloy in the unaged state exhibits the same repulsive interaction between Sc atoms in the Sc-Sc partial RDF (Fig 9.10d). Similar to the 200 ppm Zr alloy, little interaction is observed between the Zr and Sc atoms in the unaged state. There is, however, a considerable interaction between the Sc and Yb atoms, even higher than in the richer Zr-alloy.

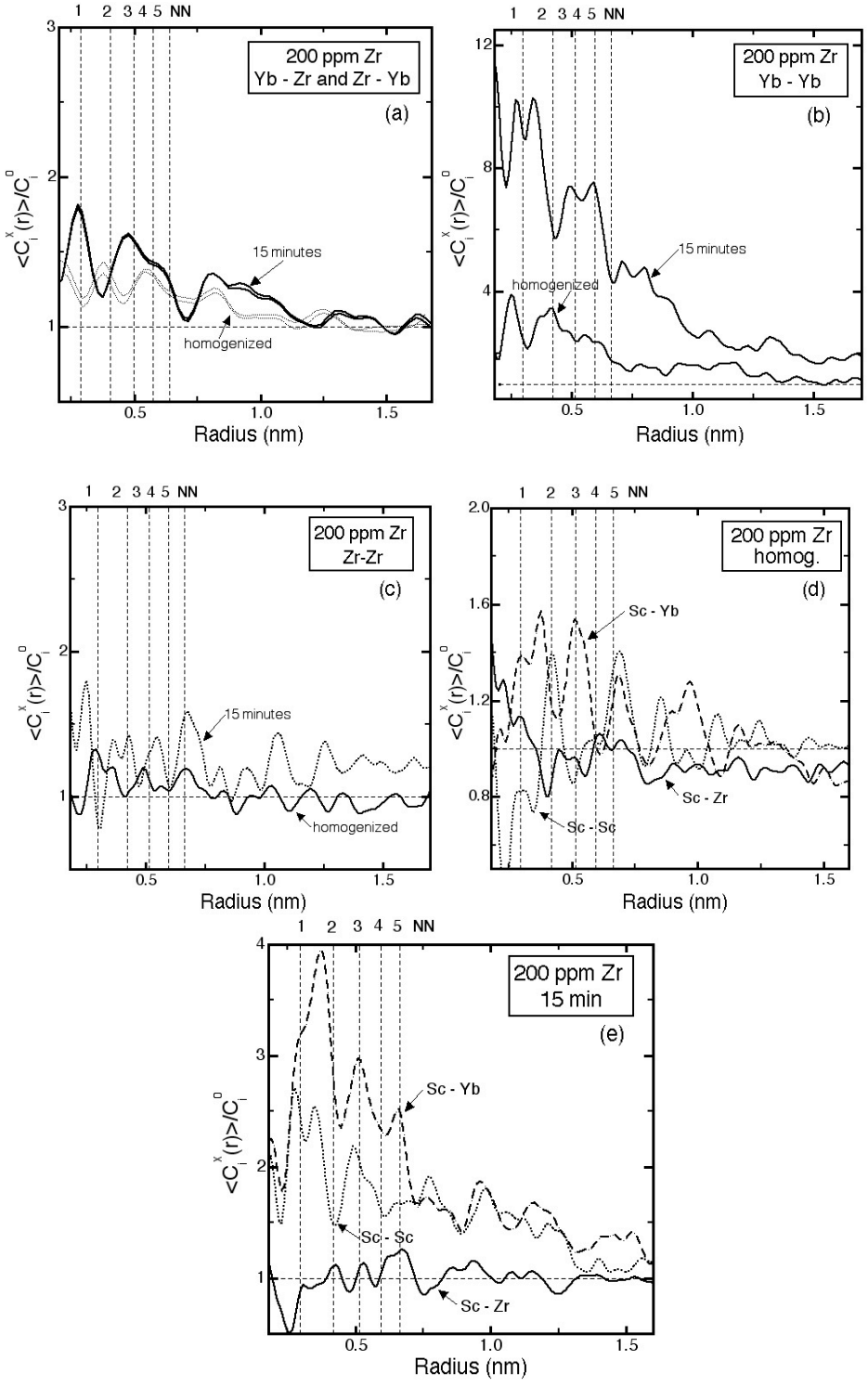

Figure 9.9: Partial radial distribution functions (RDFs) for 200 ppm Zr alloy: (a) Zr-Yb; (b) Yb-Yb; (c)Zr-Zr; (d) Sc partial RDFs for the homogenized state; (e) Sc partial RDFs for 15 minutes of aging.

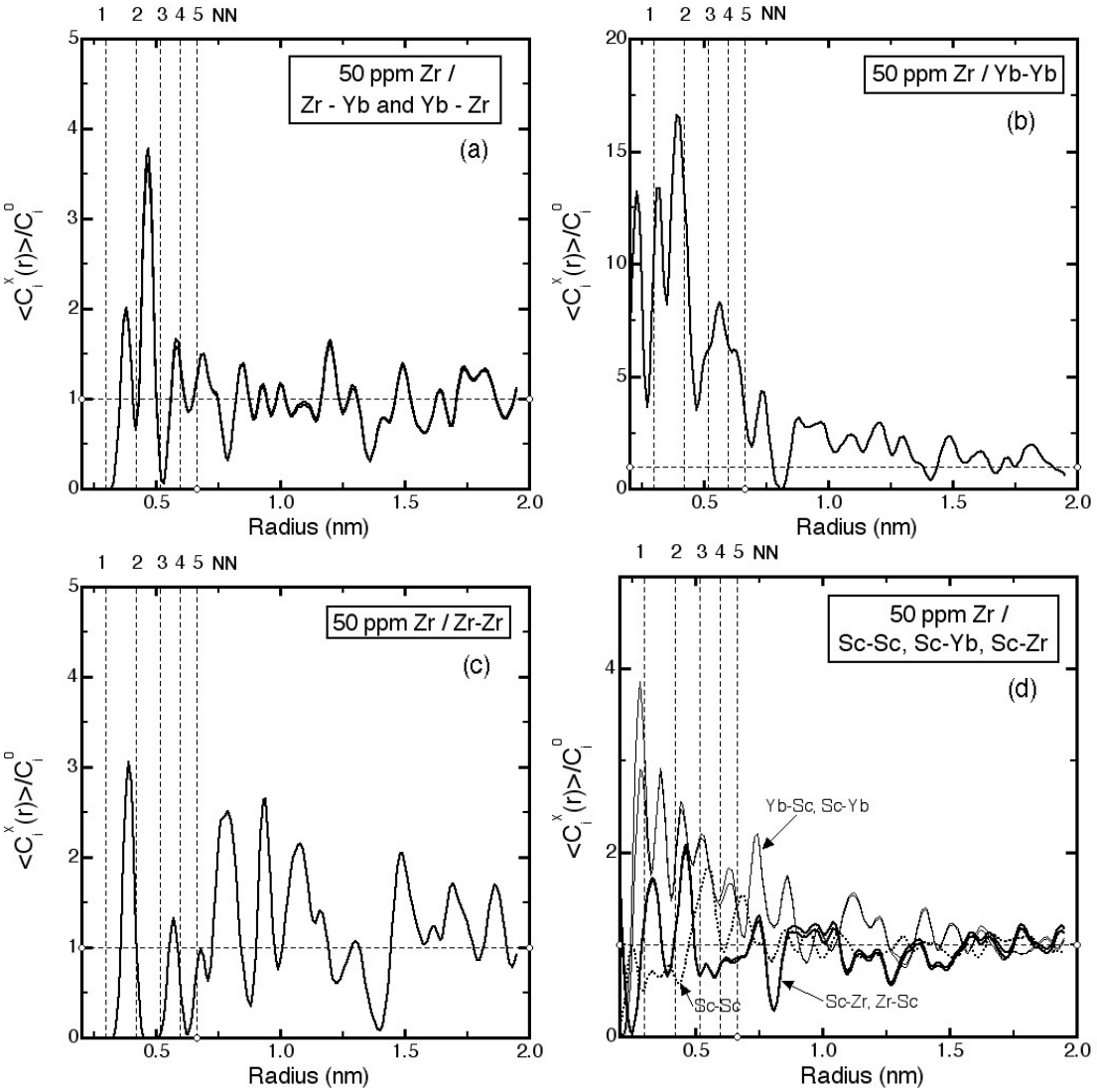

Figure 9.10: Partial radial distribution functions (RDFs) for the 50 ppm Zr alloy in the homogenized state: (a) Zr-Yb; (b) Yb-Yb; (c) Zr-Zr; (d) all Sc partial RDFs.

9.3.4 Properties at Temperatures in the Range of 350-375˚C

Since the Zr containing alloys retain their hardness during aging at 300˚C to 1536 h, the microhardness was measured for specimens aged at the higher temperatures of 350 and 375˚C (Fig. 9.11). The peak microhardness values decrease with increasing aging temperature. Once a

hardness value is attained, however, it remains constant with aging time to 96 h of aging at 350˚C and 375˚C and for up to 1536 h at 300˚C. A similar trend is observed for an Al-0.07Sc-0.02Zr alloy [28]. In contrast, for the ternary Al-Sc-RE (with additions of 50 or 200 ppm Yb or Gd), the microhardness decreases upon aging to 96 h at 350˚C, as shown in previous chapters.

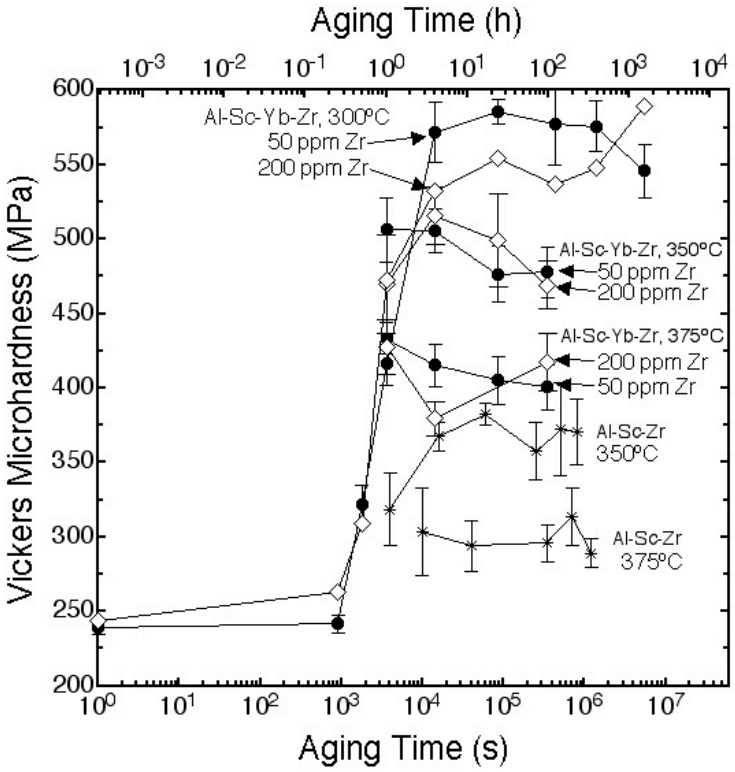

Figure 9.11: Vickers microhardness vs. aging time at 300˚C, 350˚C and 375˚C for the 200 ppm Zr alloy and the 50 ppm Zr alloy compared with Al-0.07Sc-0.02Zr (at.%) [28, 206].

9.3.5 Creep Properties

A high level of creep resistance is observed in the Al-Sc-Yb-Zr alloys (Fig. 9.12). When comparing the results to those of an Al-Sc-Yb alloy with similar <R(t)> values, the data for the minimum strain rate vs. stress plot fall in the same region. There is a large apparent stress exponent, which is indicative of a threshold stress, as given by:

$$\dot{\varepsilon} = A(\sigma - \sigma_{th})^n \exp\left(-\frac{Q}{R_g T}\right) \tag{9.1}$$

The threshold stress of the 200 ppm Zr alloy is 23±9 MPa, Table 9.1. For the 50 ppm Zr alloy, the threshold stress is smaller at 16±3 MPa, with the smaller threshold stress resulting from the smaller slope in the stress vs. minimum strain rate plot. The Yb-containing alloys, whether or not they contain Zr, have much higher creep resistance than an Al-Sc-Zr alloy [28] with a similar <R(t)> value.

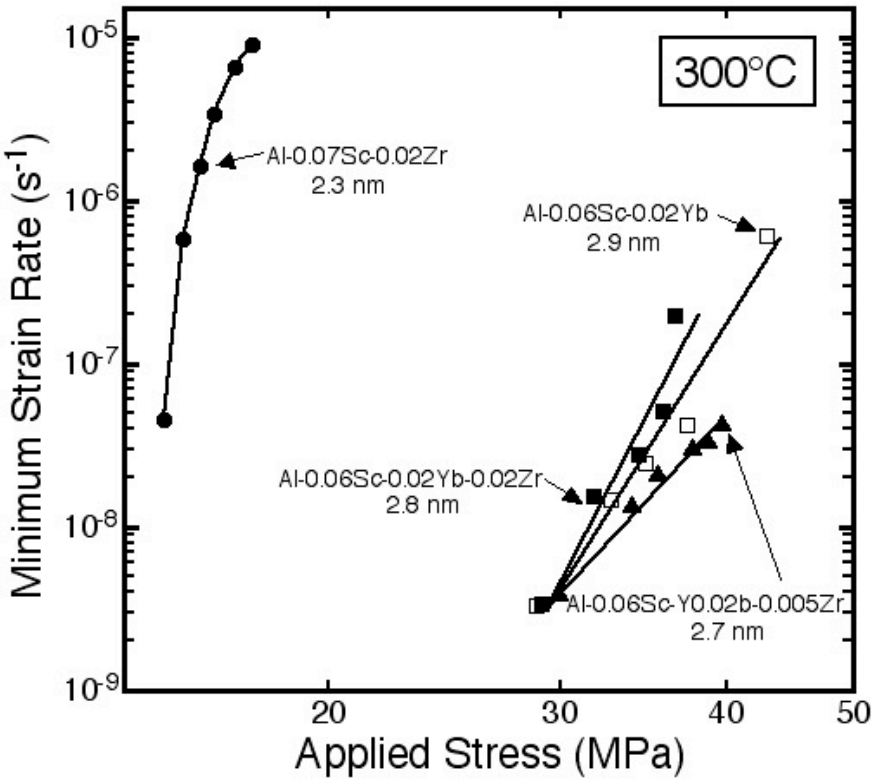

Figure 9.12: Double logarithmic plot showing minimum strain rate vs. applied stress. Values of <R(t)> are given for each alloy.

Table 9.1: Creep threshold stresses and corresponding average precipitate radii, <R(t)>, for Al-Sc-Yb, Al-Sc-Yb-Zr and Al-Sc-Zr alloys [28].

Alloy (at.%)	Threshold Stress, σ_{th}, (MPa)	Average Precipitate Radius, <R(t)> (nm)
Al-0.06Sc-0.02Yb	25±5	2.9±0.5
Al-0.06Sc-0.02Yb-0.005Zr	16±3	2.7±0.5
Al-0.06Sc-0.02Yb-0.02Zr	23±9	2.8±0.3
Al-0.07Sc-0.02Zr	14±1	2.3±0.1

9.4 Discussion

9.4.1 Precipitate Nucleation

9.4.1.1 Radial Distribution Functions

The Zr has an effect on the diffusivity of Yb, since the precipitation kinetics are slowed with the addition of Zr to the Al-Sc-Yb alloy. In a recent study on Al-Li-Sc alloys, it was shown that the coarsening of $L1_2$ $Al_3(Li_{1-x}Sc_x)$ precipitates occurs at a slower rate with the addition of Sc [131]. There was a higher $N_v(t)$ of precipitates with a smaller <R(t)> than in Al-Li alloys without Sc. Additionally, Soisson and Martin employed lattice kinetic Monte Carlo (LKMC) simulations to study the effects of small concentrations, down to 10 ppm, of a ternary impurity element on the formation of clusters [207]. Depending on the parameters assigned to this simulated impurity element, even at these concentrations, the formation of clusters can either be enhanced or suppressed depending on the interactions among the elements and vacancies.

The RDF results shed light on the interactions among the elements. The partial Yb-Zr and Zr-Yb RDFs (Fig. 9.9a) show that there are interactions between the Yb and Zr atoms in the unaged state. The Yb-Zr (and Zr-Yb) interaction increases after 15 minutes for the 200 ppm Zr alloy. In

the 50 ppm Zr alloy, there is a smaller interaction of Yb with Zr (Fig. 9.10a). This interaction with Zr, even in the unaged condition, could be one reason why the Yb precipitation is slowed with the addition of Zr to the alloy. As discussed in the introduction to this chapter, there is much evidence of one element having an effect on the diffusivity of another. The likelihood that Zr is affecting the Yb diffusivity increases if they are in close proximity to each other.

The integral of the partial RDF for Zr-Yb is calculated to determine the area under the curve with respect to the radius (Fig. 9.13) according to [208]:

$$c(r_2) - c(r_1) = \int_{r_1}^{r_2} g(r) 4\pi r^2 dr \tag{9.2}$$

where g(r) is the radial distribution function and $c(r_2)$ - $c(r_1)$ represents the area under the curve for radial distances out to r_2; i.e. the area between the partial RDF curve and the horizontal line at unity. A positive value indicates that there is a correlation between Yb and Zr. The partial Zr-Yb RDF for the 200 ppm Zr alloy shows that there is an increased interaction after aging for 15 min – the maximum value of the integral increases from 0.03 to 0.045. One can see a distinct difference between the two aging times. Hence, there must be some interaction in the 200 ppm Zr alloy.

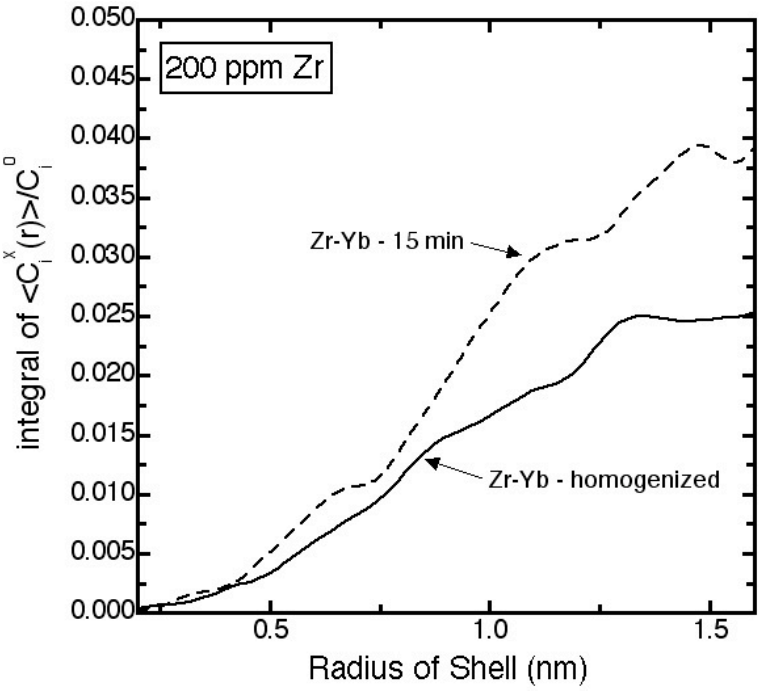

Figure 9.13: Integrals of the partial Zr-Yb RDF for the 200 ppm Zr in the homogenized state and 15 min of aging at 300°C.

9.4.1.2 Clustering – Zr in Precipitates

The partial RDF results demonstrate that the Zr has an interaction with Yb in the unaged state implying that Zr is involved in the nucleation process. Deschamps et al. suggest that the nucleation of Al_3Sc precipitates is catalyzed by the relatively immobile Zr atoms [31]. Additionally, Fuller et al. suggest that the precipitates in dilute Al-Sc-Zr alloys are nucleating on Sc-Sc, Zr-Zr or Sc-Zr dimers or larger clusters [2]. Kinetic Monte Carlo (KMC) simulations of Al-Zr-Sc alloys also show that there is a higher concentration of Zr at the very center of the precipitate, which was attributed to a thermodynamic effect [32], unlike the Zr shell around the edge of the precipitates which was attributed to kinetics. Thus, if the Zr has the same effect on the formation of $Al_3(Sc_{1-x}Yb_x)$ it should be present in the precipitates.

The LEAP tomographic results show that after 15 min of aging there are very few precipitates, as captured by the envelope method, which contain a Zr atom (Table 9.2). Hence, it is not possible that the main mechanism of precipitation involves nucleation on Zr atoms or Zr-containing clusters. The main effect the Zr is having is to slow down the diffusivity of the Yb, or reducing the thermodynamic chemical driving force for precipitation. Due to the small diffusivity of Zr in Al, the root-mean-squared diffusion distance of Zr is not large enough for the Zr atoms to reach the precipitates after 1 h. The small Zr concentration is consistent with the proxigrams for these alloys aged for 1 h [205].

Table 9.2: Zr concentration in the precipitates and the percentage of clusters and precipitates containing Zr atoms for early aging times at 300˚C.

Alloy – Aging Treatment	Percentage of clusters and precipitates with Zr atoms (%)
200 ppm Zr – 15 min	0
50 ppm Zr – 15 min	2.1
200 ppm Zr – 1 h	8.5
50 ppm Zr – 1 h	0

9.4.2 Growth and Coarsening

9.4.2.1 Ratio of Yb and Sc in Precipitates

For both Al-Sc-Yb-Zr alloys, there is a wide range of precipitate concentrations after 15 min of aging, as shown in Fig. 9.5 (a and b). This indicates that Yb and Sc atoms precipitate simultaneously. Although there is a difference between the average $C_{Yb}^{\beta}/C_{Sc}^{\beta}$ in the two Zr containing alloys, they are more similar to each other than to the Al-Sc-Yb alloy, which contains more Yb in the precipitates (Fig. 9.5c). The value for $C_{Yb}^{\beta}/C_{Sc}^{\beta}$ is twice as high in the Al-Sc-Yb alloy after 15 min as for the Zr containing alloys. The value for the Al-Sc-Yb alloy is high since,

after 15 minutes, 91% of the Yb has precipitated. The slower precipitation kinetics can still be observed after 1 h of aging: the percentage of total solute precipitated (Yb + Sc) is 20% smaller for the Zr containing alloys than for the Al-Sc-Yb alloy (Fig. 9.15). The volume fraction of precipitates is also correspondingly smaller for the Zr containing alloys (Fig. 9.14).

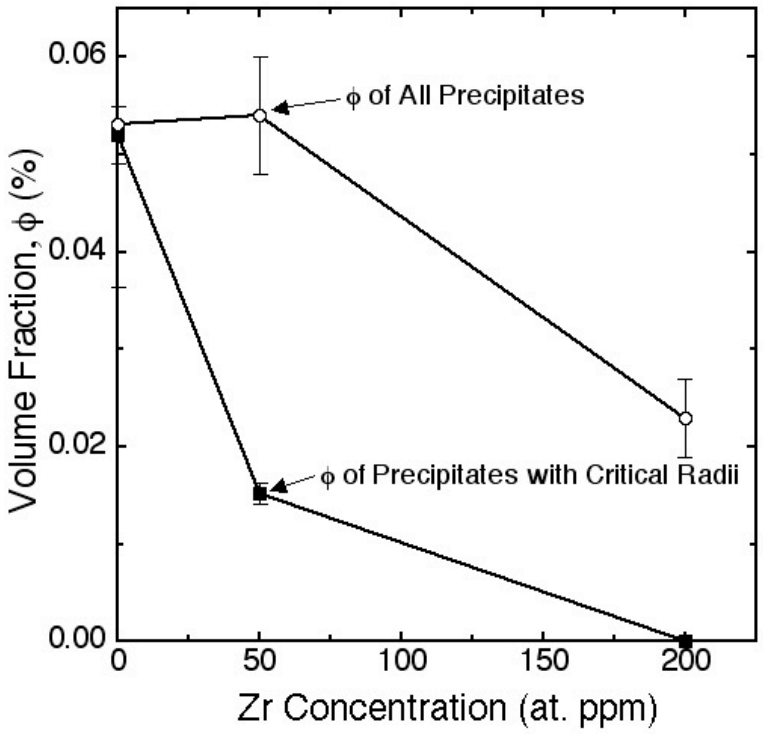

Figure 9.14: Volume fractions, ϕ, at 15 minutes of aging for Al-Sc-Yb as a function of Zr concentration.

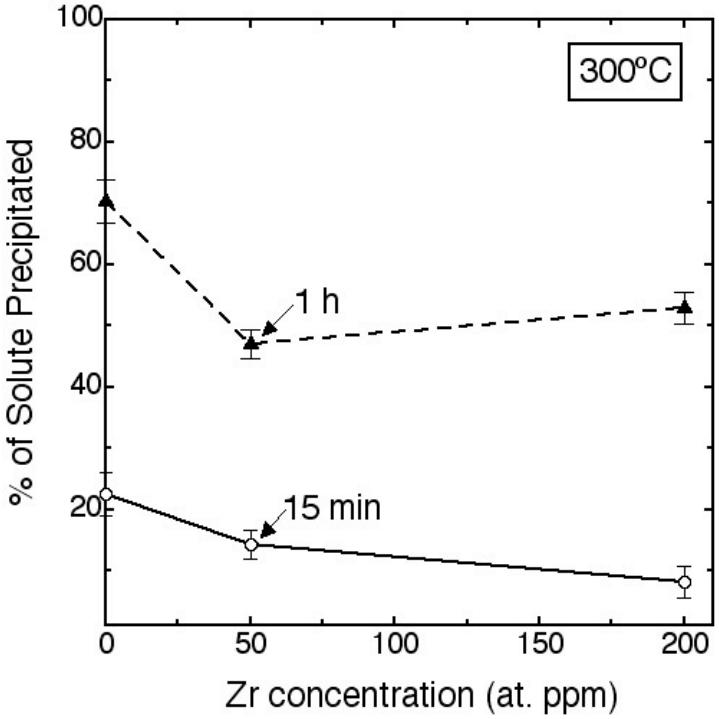

Figure 9.15: Percentage of solute (Yb + Sc) precipitated after 15 minutes and 1 h of aging.

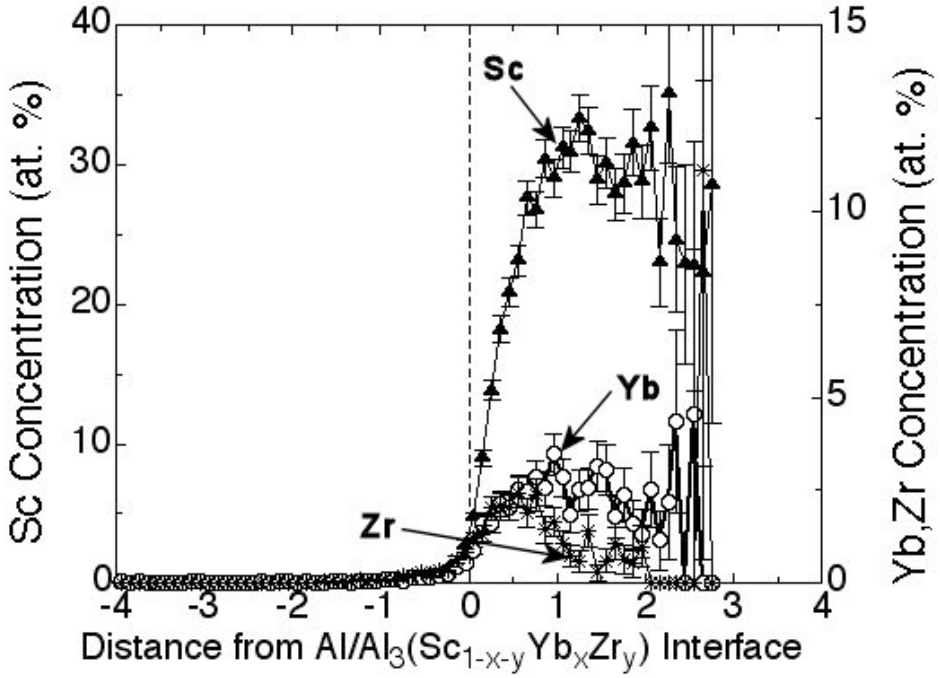

Figure 9.16: Proxigram of 200 ppm Zr alloy showing concentration as a function of distance from the Sc isoconcentration surface for 1 h of aging [205]. Based on a 9at.% Sc isoconcentration surface.

Simultaneous precipitation of Yb and Sc leads to a uniform distribution of Yb and Sc in the precipitates (Fig. 9.16). The core/shell structure, which is visible in the ternary Al-Sc-Yb alloy, is no longer observable in the quaternary alloys. Furthermore, the two stage precipitation process apparent in the Al-Sc-Yb alloy is not apparent in the Zr containing alloys as there is only one region of rapid increase in microhardness (Fig. 9.1). Finally, it is of interest to note that Zr does segregate to the interface at longer aging times (Fig. 9.16). This is similar to that found in Al-Sc-Zr, where the slow-diffusing Zr diffuses to the interface at later aging times [3].

9.4.2.2 Precipitate Size Distributions and Nucleation Rate

At 1 h of aging, it is seen from the precipitate size distribution (PSD) (Fig. 9.17c) for the 200 ppm Zr alloy that there is a bi-modal distribution of precipitates: the sub-critical precipitates and those with radii above R*, the critical radius. It is estimated that R* lies at the minimum of 1 nm, similar to the value found in Ni-Al alloys by Xiao and Haasen [169]. For the 50 ppm Zr alloy, the bi-modal distribution of precipitates is not really evident since there are few precipitates with R > 1 nm (Fig. 9.17d). $N_v(t)$ (Fig. 9.8) is calculated using the value of R* = 1 nm for both alloys. $N_v(t)$ is similar for the two Zr containing alloys as well as the Al-Sc-Yb alloy. Additionally, $N_v(t)$ is calculated including the sub-critical nuclei. These values are also similar between the two Zr containing alloys.

After 15 minutes, there are only small precipitates in the 200 ppm alloy (Fig. 9.17a). The 50 ppm Zr alloy has only a few more precipitates with larger R values (Fig. 9.17b). The number of total precipitates, including sub-critical nuclei, remains constant for both alloys between 15 min.

Since there are only small precipitates, a bi-modal distribution is not observed and R* value cannot be estimated for the 15 min aging time.

Using the $N_v(t)$ data ranging from the unaged condition through the 1 h aging time, the nucleation rates are estimated to be $2.8x10^{19}$ m^{-3} s^{-1} and $2.4x10^{19}$ m^{-3} s^{-1} for the 50 and 200 ppm Zr alloys, respectively. The nucleation rate is calculated from the increase in $N_v(t)$ with aging time. These are smaller than the value of $1.9x10^{20}$ m^{-3} s^{-1} found for the Al-Sc-Yb alloy. Compared to Hyland's work on Al-Sc alloys [18], the nucleation currents for the quaternary Al-Sc-Yb-Zr alloys are greater than in an Al-0.11at.%Sc alloy, where the nucleation current is $9x10^{18}$ m^{-3} s^{-1} at 288°C and $1.01x10^{19}$ m^{-3} s^{-1} at 343°C.

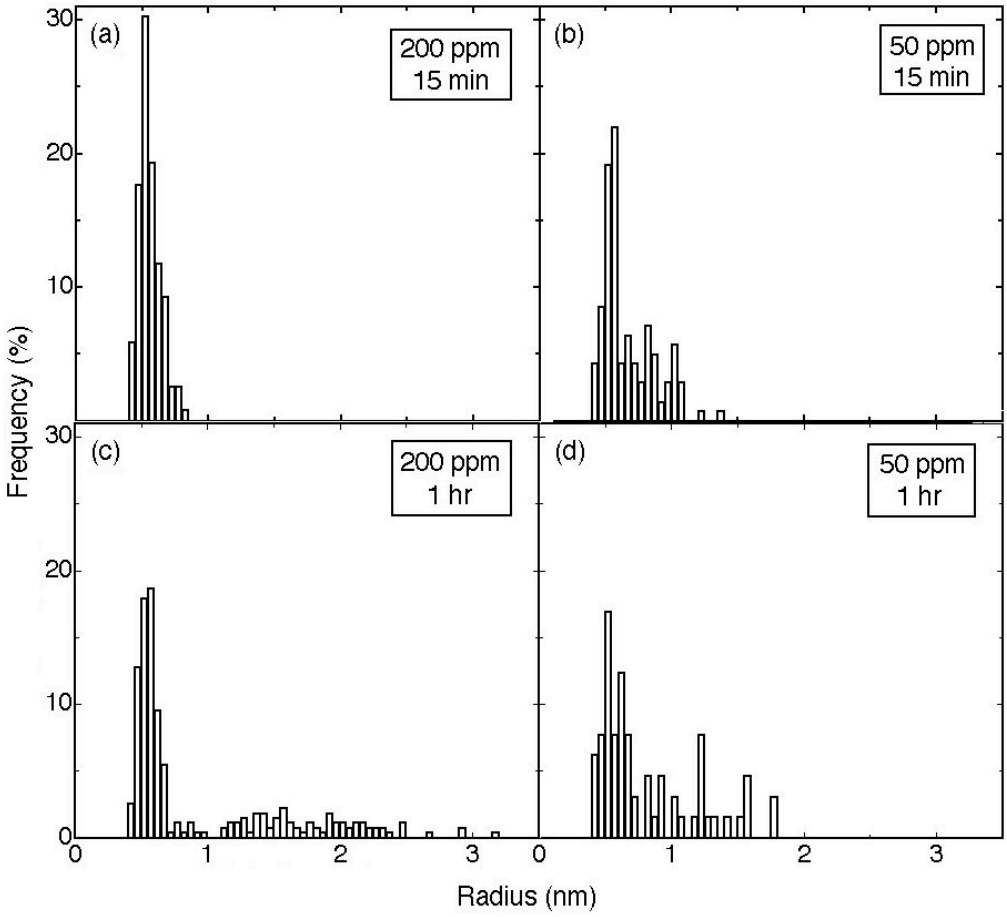

Figure 9.17: Precipitate size distribution (PSD) for early aging times: (a) 200 ppm Zr – 15 minutes; (b) 50 ppm Zr – 15 minutes; (c) 200 ppm Zr – 1 h; (d) 50 ppm Zr – 1h.

9.4.2.3 High Temperature Aging

In recent research performed in the Materials Science Department at Northwestern University [205], it was found that the Al-Sc-Yb-Zr alloys (with the same composition as those studied herein) have slow coarsening kinetics at 300˚C with time exponents and coarsening constants smaller than predicted by the model for coarsening in a ternary alloy [83]. Since these alloys are coarsening-resistant at 300˚C, the 50 and 200 ppm Zr alloys are aged at higher temperatures. The alloys exhibit fairly constant values of the Vickers microhardness upon aging at 350˚C and

375˚C (Fig. 9.11), indicating that once the precipitates form, they grow and coarsen slowly. The 50 and 200 ppm Zr alloys have very similar microhardness values for the same aging treatment. This confirms, once again, that only a small amount of Zr is necessary to retard the coarsening resistance. A future study, utilizing LEAP tomography and TEM to determine <R(t)>, $N_v(t)$ and $\Delta C_i^{\alpha}(t)$, would shed more light on the coarsening resistance of the precipitates in these alloys as a function of temperature.

The Al-Sc-Yb-Zr alloys are similar to Al-Sc-Zr alloys at higher temperatures, in that once a microhardness value is achieved, this value is retained up to aging times of several hundred hours [28, 206]. Additions of 200 ppm of Zr to Al-0.07Sc are found to have a large effect on the coarsening resistance in the Al-Sc-Zr system [2]. The quaternary alloys do have somewhat larger hardness values at a given temperature, which could be the result of differences in the precipitation kinetics among the alloys. Finally, the Al-Sc-Yb-Zr alloys maintain their microhardness up to 96 h of aging, whereas, the Al-0.06Sc-0.02Yb alloy displays a microhardness decrease of 100 MPa between 24 and 96 h of aging at 350˚C.

9.4.3 Creep Properties

As shown in Figure 9.12, the 50 and 200 ppm Zr alloys have creep resistance that is significantly greater than the Al-Sc-Zr alloy, which contains no Yb [28]. When comparing to the ternary Al-0.06Sc-0.02Yb alloy with a similar <R(t)> value, it appears that the addition of Zr does not reduce significantly the creep resistance. The lattice parameter mismatch is known to have an effect on the threshold stress [9] and the creep results for the 50 and 200 ppm Zr alloys are consistent with this model. The lattice parameter mismatch for an $Al_3(Sc_{0.75}Yb_{0.25})$ precipitate

with the α-Al matrix is 1.65 % at 300˚C, assuming a uniform distribution of Yb and Sc in the precipitate phase. Zirconium only reduces the lattice parameter of the $Al_3(Sc_{1-x}Zr_x)$ phase by 0.02%. In contrast, the lattice parameter mismatch for the Al-Sc alloys is 1.05 % [122]. Hence, the Al-Sc and Al-Sc-Zr alloys have a lower creep resistance than the Yb containing alloys.

Fig. 9.18 displays the normalized threshold stress vs. <R(t)>. The normalized threshold stress is the threshold stress divided by the calculated Orowan stress, which takes into account the difference in volume fractions among the different alloys. The Orowan stress is calculated from:

$$\Delta\sigma_{or} = M\frac{0.4Gb}{\pi\lambda}\frac{\ln\left(2\bar{r}/b\right)}{\sqrt{1-\nu}}; \tag{9.3}$$

where M = 3.06 is the orientation factor for aluminum [86], G = 25.4 GPa is the shear modulus of aluminum [61], ν = 0.345 is Poisson's ratio for aluminum, b = 0.286 is the magnitude of the Burgers vector [61], λ is the interprecipitate spacing, and $\bar{r} = \pi/4 < R >$ is the mean planar radius [106]. This plot demonstrates that the 200 ppm Zr alloy has larger normalized threshold stress than does the Al-Sc [20], Al-Sc-Ti [102], and Al-Sc-Zr [28] alloys. This is a result of the larger mismatch between the matrix and precipitate phase in the Al-Sc-Yb-Zr alloy compared with Al-Sc alloys containing no Yb.

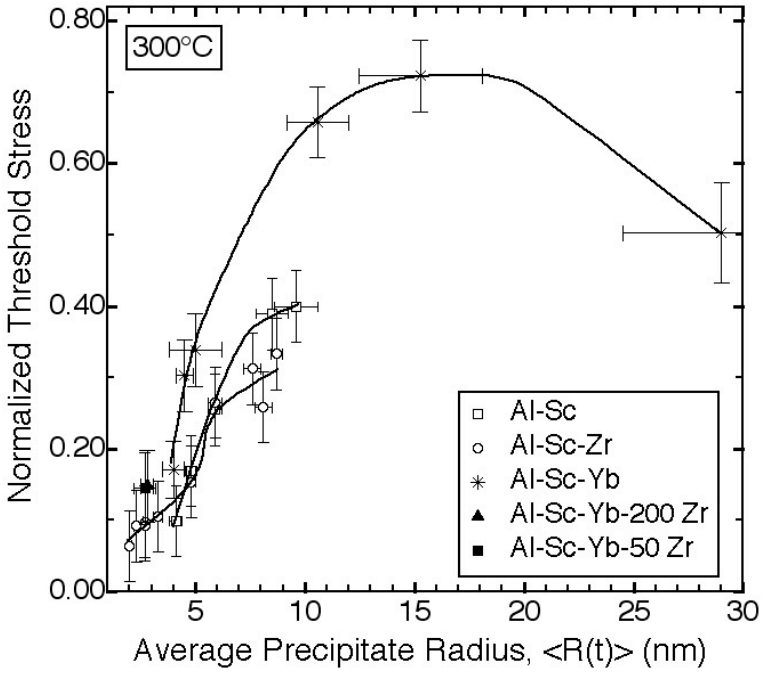

Figure 9.18: Normalized threshold stress vs. average precipitate radius, <R(t)> for various Al-Sc [20], Al-Sc-Zr [28] and Al-Sc-Yb alloys for creep at 300˚C. The data point for the two alloys fall in almost exactly the same location.

9.5 Conclusions

The microstructure and creep properties of an Al-0.06Sc-0.02Yb-0.02Zr (at.%) alloy and an Al-0.06Sc-0.02Yb-0.005Zr (at.%) alloy were studied. It was determined that:

- There is a single rapid increase in the microhardness after an initial incubation period of 5 - 15 minutes, in contrast to the Al-0.06Sc-0.02Yb (at.%) alloy that exhibits a distinct two-stage precipitation sequence.
- The Yb and Sc precipitate from solid-solution simultaneously, and the average Yb/Sc (at.%/at.%) ratio in the precipitates is close to unity (0.99 and 1.17 after 15 minutes aging for the 50 and 200 ppm Zr alloys, respectively). These ratios are smaller than that of the Al-Sc-Yb alloy, where most of the Yb precipitates before the Sc.

- The precipitation kinetics are diminished in the Zr containing alloys, as evidenced by the ~20% less solute precipitated after 1 h of aging, as compared with the Al-Sc-Yb alloy.
- The RDF results show an interaction between the Zr and the Yb for the 200 ppm Zr alloy, since the partial Zr-Yb and Yb-Zr RDF achieve values of 1.7 and are consistently above the horizontal line of unity in the unaged state.
- It is determined that the majority of precipitates do not nucleate on Zr atoms, as there are no detectable Zr atoms in more than 90% of the precipitates.
- The creep resistance of the Al-Sc-Yb-Zr alloys (50 and 200 ppm Zr) are similar to that of an Al-Sc-Yb alloy. The mismatch between the matrix and the precipitate phase is determined to affect the creep resistance. The presence of Yb in the precipitates increases the lattice parameter mismatch between the matrix and precipitate phase to 1.65%, while Zr only diminishes the lattice parameter mismatch by 0.2%. The normalized threshold stress values for the two Zr containing alloys lies above that of Al-Sc [20] and Al-Sc-Zr [28] alloys for precipitates with similar radii.

.

10. Final Remarks and Conclusions

The ultimate goal of this research program is to produce castable, high-temperature Al alloys since these are lighter weight than other metal alloys typically used in high-temperature creep-resistant applications. The addition of the slow diffusing elements combined with the RE provides some improvement in the properties of Al-Sc alloys.

This thesis has demonstrated that additions of Ti, Zr and RE (Yb or Gd) to Al-Sc alloys offer tremendous potential for developing high-temperature creep-resistant Al alloys. The addition of Ti, a slow diffusing transition metal element, has led to an improvement in the coarsening resistance over Al-Sc alloys. Additions of rare earth elements have led to significant improvements in the creep resistance over binary Al-Sc alloys. Combination of slow diffusing transition metal elements (Ti or Zr) and rare earth elements (Yb or Gd) leads to alloys which display coarsening resistant precipitates along with an improvement of creep resistance. Yb additions in particular have proven to be interesting additions in the Al-Yb, Al-Sc-Yb and Al-Sc-Yb-Zr alloys, since they are fully soluble in the precipitate phase. A further benefit of alloying additions to Al-Sc alloys is that all of the additions studied in this thesis have a lower cost than Sc and thus the successful replacement of Sc in the precipitates could lower the cost of the Al-Sc alloys.

11. Suggestions for Future Work

This thesis has shown that ternary and quaternary alloying additions have a significant effect on the microstructure and creep properties of Al-Sc alloys. Many questions remain as to the exact mechanisms by which these elements interact. Additional understanding of the alloys could lead to further improvements in the properties. Several directions for future study are proposed:

11.1 Mechanisms for Interaction Among Solute Elements

It would be intriguing to determine more closely what the mechanisms of interactions are among the solute elements. Interaction energies between the various solute elements could be studied in more detail. Kinetic Monte Carlo simulations could be used to model the precipitation in these alloys. If these mechanisms for interaction are known, they could be exploited and help determine the direction of future research.

11.2 Scalability

The alloys produced in this thesis were all cast on a laboratory scale, meaning that each cast consisted of a few hundred grams. It is of interest to see how these alloys react upon casting on a larger scale. This is especially important given the rapid diffusion of Yb. The samples that were homogenized were all smaller pieces (~1gm) cut from the initial casting. Thus, the cooling rate is thought to be reasonably high. In a larger casting, however, the center of the piece could cool at a significantly slower rate, leading to considerable differences in the precipitation of Yb. Perhaps the addition of the slower diffusing Zr will be able to retard the precipitation kinetics of the Yb in larger pieces as well.

11.3 Improvements in the Volume Fraction of Precipitates

The elements studied in this thesis are known to have low solubilities in Al. Since increased volume fraction improves the mechanical properties, it would be interesting to find elements which would have a higher volume fraction. For example, Ta and Hf have been shown to the higher solid solubility in Al [123]. Although it is known that the combination of elements in the matrix reduces the solubility, perhaps a combination of elements can be found which leads to an increased volume fraction.

11.4 Sm and the Lighter Rare Earth Elements

As was shown in this thesis, the creep of the Al-Sc-Yb and Al-Sc-Gd alloys is significantly improved over that of Al-Sc binary alloys. This remarkable increase in the creep properties was maintained with the addition of only 50 ppm of RE to the alloy, which led to only ~2% RE concentration in the precipitate. Since the solubility of samarium (Sm) in the precipitate is similar to that of Gd [4, 5, 209], it is anticipated that despite its limited solubility in not only the precipitate phase but also the α-Al matrix, it may still have a significant effect on the creep resistance. The lighter RE (La-Nd) are known to have an even more limited solubility in the $Al_3(Sc_{1-x}RE_x)$ phase (<1at.% [209]), but perhaps this small amount is enough to make a substantial improvement in the creep resistance of Al-Sc alloys.

References

[1] Bergner, D. and N.V. Chi, "Untersuchungen zur Diffusion von 3 d-Metallen in Al" Wissenschaftliche Zeitschrift der Padagogischen Hochschule “N.K. Krupskaja”, **Halle XV, Heft 3,** (1977).

[2] Fuller, C.B. and D.N. Seidman, "Temporal Evolution of Al(Sc,Zr) Alloys: Part II – Coarsening of $Al_3(Sc_{1-x},Zr_x)$ Precipitates" Acta Mater., **53,** 5415-5428 (2005).

[3] Fuller, C.B., J.L. Murray, and D.N. Seidman, "Temporal Evolution of the Nanostructure of Al(Sc,Zr) Alloys, Part I – Chemical Compositions of $Al_3(Sc_{1-x}Zr_x)$ Precipitates" Acta Mater., **53,** 5401-5413 (2005).

[4] Petzow, G. and G. Effenberg, *Ternary Alloys*. (ASM International.

[5] Zalutskaya, O.I., V.G. Kontseyoy, N.I. Karamishev, V.R. Ryabov, and I.I. Zalutskii, "Ternary Systems Gd-Y-Al, Gd-Tb-Al, Gd-Dy-Al, Gd-Ho-Al, Gd-Er-Al, Gd-Sc-Al, to 25at.% rare-earth metals" Dopovidi Akademii Nauk Ukr. RSR, 751-753 (1970).

[6] Horovotz, C.T., K.A. Gschneider, G.A. Melson, D.H. Youngblood, and H.H. Schock, *Scandium: Its Occurence, Chemistry, Physics, Metallurgy, Biology and Technology*. (Academic Press, London, 1975).

[7] Zalutskaya, O.I., V.G. Ryabov, and I.I. Zalutskii, Dopovidi Akademii Nauk Ukr. RSR, 255-259 (1969).

[8] Palenzona, A.J., J. of the Less-Common Metals, **29,** 289-292 (1972).

[9] Marquis, E.A. and D.C. Dunand, "Model for Creep Threshold Stress in Precipitation-Strengthened Alloys with Coherent Particles" Scripta Mater., **47,** 503-508 (2002).

[10] Polmear, I.J., *Light Alloys: Metallurgy of the Light Metals*. (Edward Arnold, 1981).

[11] Drits, M.Y., L.B. Ber, Y.G. Bykov, L.S. Toropova, and G.K. Anastas'eva, "Ageing of alloy Al-0.3at.%Sc" Phys. Met. Metall., **57,** (6), 118-126 (1984).

[12] Costello, F.A., J.D. Robson, and P.B. Prangnell, "The Effect of Small Scandium Additions to AA7050 on the As-cast and Homogenized Microstructure" Mater. Sci. For., **396-402,** 757-762 (2002).

[13] Riddle, Y.W. and T.H. Sanders, "A Study of Coarsening, Recrystallization, and Morphology of Microstructure in Al-Sc-(Zr)-(Mg) Alloys" Metall. Mater. Trans. A, **35,** 341-350 (2004).

[14] Jones, M.J. and F.J. Humphreys, "Interaction of recrystallization and precipitation: The effect of Al_3Sc on the recrystallizaion behaviour of deformed aluminum" Acta Mater., **51,** 2149-2159 (2003).

[15] Norman, A.F., S.S. Birley, and P.B. Prangnell, "Development of new high strength Al-Sc filler wires for fusion welding 7000 series aluminum aerospace alloys" Sci. and Tech. of Welding and Joining, **8,** 235-245 (2003).

[16] Neubert, V., B. Smola, I. Stulikova, A. Bakkar, and J. Reuter, "Microstructure, Mechanical Properties and Corrosion Behaviour of Dilute Al-Sc-Zr Alloy Prepared by Powder Metallurgy" Mater. Sci. and Eng. A, **Accepted for Publication,** (2007).

[17] Venkateswarlu, K., L.C. Pathak, A.K. Ray, G. Das, P.K. Verma, M. Kumar, and R.N. Ghosh, "Microstructure, Tensile Strength and Wear Behaviour of Al-Sc- Alloy" Mater. Sci. and Eng. A, **383,** 374-380 (2004).

[18] Hyland, R.W., "Homogeneous Nucleation Kinetics of Al_3Sc in a Dilute Al-Sc Alloy" Metall. Trans. A, **23A,** 1947-1955 (1992).

[19] Novotny, G.M. and A.J. Ardell, "Precipitation of Al_3Sc in binary Al-Sc alloys" Mater. Sci. and Eng. A, **A318,** 144-154 (2001).

[20] Marquis, E.A., D.N. Seidman, and D.C. Dunand, "Precipitation Strengthening at Ambient and Elevated Temperatures of Heat-Treatable Al(Sc) Alloys" Acta Mater., **50,** 4021-4035 (2002).

[21] Marquis, E.A. and D.N. Seidman, "Nanoscale Structural Evolution in Al_3Sc Precipitates in Al(Sc) Alloys" Acta Mater., **49,** 1909-1919 (2001).

[22] Iwamura, S. and Y. Miura, "Loss in Coherency and coarsening behavior in Al_3Sc precipitates" Acta Mater., **52,** 591-600 (2004).

[23] Kendig, K. and D. Miracle, "Strengthening Mechanisms of an Al-Mg-Sc-Zr Alloy" Acta Mater., **50,** 4165-4175 (2002).

[24] Toropova, L.S., D.G. Eskin, M.L. Kharakterova, and T.V. Dobatkina, *Advanced Aluminum Alloys Containing Scandium*. (Gordon & Breach, 1998).

[25] Sawtell, R.R. and C.J. Jensen, "Mechanical Properties and Microstructures of Al-Mg-Sc Alloys" Metall. Trans. A, **21A,** 421-430 (1990).

[26] Marquis, E.A., D.N. Seidman, and D.C. Dunand, "Effect of Mg addition on the creep and yield behavior of an Al-Sc alloy" Acta Mater., **51,** 4751-4760 (2003).

[27] Fuller, C.B., D.N. Seidman, and D.C. Dunand, "Creep Properties of Coarse-Grained Al(Sc) alloys at 300C" Scripta Mater., **40,** 691-696 (1999).

[28] Fuller, C.B., D.N. Seidman, and D.C. Dunand, "Mechanical Properties of Al(Sc,Zr) Alloys at Ambient and Elevated Temperatures" Acta Mater., **51,** 4803-4814 (2003).

[29] Harada, Y. and D.C. Dunand, "Microstructure of Al_3Sc with ternary transition-metal additions" Mater. Sci. and Eng. A, **329-331,** 686-695 (2002).

[30] Forbord, B., W. Lefebvre, F. Danoix, H. Hallem, and K. Marthinsen, "Three-Dimensional Atom Probe Investigation on the Formation of Al_3(Sc,Zr)-dispersoids in Aluminium Alloys" Scripta Mater., **51,** 333-337 (2004).

[31] Deschamps, A., L. Lae, and P. Guyot, "In Situ Small-angle Scattering Study of the Precipitation Kinetics in an Al-Zr-Sc Alloy" Acta Mater., **55,** 2775-2783 (2007).

[32] Clouet, E., L. Lae, T. Epicier, W. Lefebvre, M. Nastar, and A. Deschamps, "Complex Precipitation Pathways in Multi-Component Alloys" Nature of Materials, **5,** 482-488 (2006).

[33] Hallem, H., W. Lefebvre, B. Forbord, F. Danoix, and K. Merthinsen, "Formation of $Al_3(Sc_xZr_yHf_{1-x-y})$-dispersoids in aluminum alloys" Mater. Sci. and Eng. A, **421,** (1-2), 154-160 (2006).

[34] Tolley, A., V. Radmilovic, and U. Dahmen, "Segregation in Al_3(Sc,Zr) precipitates in Al-Sc-Zr alloys" Scripta Mater., **52,** 621-625 (2005).

[35] Clouet, E., M. Nastar, A. Barbu, C. Sigli, and G. Martin, "Precipitation in Al-Zr-Sc alloys: a comparison between kinetic Monte Carlo, cluster dynamics and classical nucleation theory" Solid-Solid Phase Transformations in Inorganic Materials, TMS, 1-21 (2005).

[36] Schmidt, U., A.L. Beresina, K.V. Chuistov, T.A. Monastyrskaja, and A.D. Rud. *Decomposition of Rapidly Quenched Supersaturated Al-Sc-X (X:Li,Ta,Ti) Alloys.* in *Advanced Light Alloys and Composites*. 1998: Kluwer Academic Publishers.

[37] Hyde, K.B., A.F. Norman, and P.B. Prangnell, "The effect of Ti on grain refinement in Al-Sc alloys" Mater. Sci. For., **396,** (4), 39-44 (2002).

[38] *Cambridge Engineering Selector*. Version 4.1 2003.

[39] Buschow, K.H.J. and Vanvucht, Philips Research Reports, **22,** 233 (1967).

[40] Cannon, J.F. and H.T. Hall, J. Less-Common Metals, **40,** 313 (1975).

[41] Quan, M.X., P. Haldar, J. Werth, and B.C. Giessen, in *Rapidly Solidified Alloys and Their Mechanical and Magnetic Properties*, B.C. Giessen, D.E. Polk, and A.I. Taub, Editors. 1986, MRS: Pittsburgh. p. 299.

[42] Sawtell, R.R. and J.W. Morris, "Exploratory Alloy Development in the System Al-Sc-X" Proc. of Dispersion Strengthened Aluminum Alloys, 409-420 (1988).

[43] Ruder, A. and D. Eliezer, "Microstructure and the Thermal Stability of Rapidly Solidified Aluminum -- Rare Earth Alloys" Isr. J. Technology, **24,** (1-2), 149-156 (1988).

[44] Fu, G., F. Sun, L. Ren, W. Chen, and K. Qian, "Modification behavior of trace rare earth on impurity phases in commercial purity aluminum" J. Rare Earth, **20,** 61-66 (2002).

[45] Nie, Z., T. Jin, J. Fu, G. Xu, J. Yang, J. Zhou, and T. Zuo, "Research on Rare earth in Aluminum" Mater. Sci. For., **396-402,** 1731-1736 (2002).

[46] Nie, Z., T. Jin, J. Zou, J. Fu, J. Yang, and T. Zuo, "Development on research of advanced rare-earth aluminum alloy" Trans. Nonferrous Met. Soc. China, **13,** 509-514 (2003).

[47] Nie, Z.R., J.B. Fu, J.X. Zou, T.N. Jin, J.J. Yang, G.F. Xu, H.Q. Ruan, and T.Y. Zuo, "Advanced Aluminum Alloys Containing Rare-earth Erbium" Mater. Sci. For., **28,** (2004).

[48] Yuan, G.S., Z.Y. Zhao, X.D. Zhu, J.P. Kuang, Y. Liu, and Z.J. Xing, "Structure and Mechanical-Properties of Rapidly Solidified Al-Li-Cu-Mg Alloys Containing Minor Zirconium And Rare-Earths" Mat. Sci. and Eng. A, **134,** 1179-1181 (1991).

[49] Borbe, P.C., F. Erdmann-Jesnitzer, and W. Schoebel, "Investigations of Aluminum - Rare-Earth Metal Alloys" Aluminum, **59,** (8), 213-218 (1983).

[50] Fass, M. and D. Eliezer, "Oxidation Behavior of Rapidly Solidified Aluminum Rare-Earth Alloys" J. Mater. Sci. Lett., **8,** 178-182 (1989).

[51] Kloc, L. and J. Fiala, "Harper-Dorn creep in metals at intermediate temperatures revisited: Constant structure test of pure Al" Mater. Sci. and Eng. A, **410-411,** 38-41 (2005).

[52] Park, K., E.J. Lavernia, and F.A. Mohamed, "Creep Behavior and Substructure in an Al-Li Alloy" Acta Metall. Mater., **38,** (10), 1837-1848 (1990).

[53] Spigarelli, S., M. Cabibbo, E. Evangelista, and S. Cucchieri, "Evaluation of the creep properties of an Al-17Si-1Mg-0.7Cu alloy" Mater. Lett., **56,** 1059-1063 (2002).

[54] Sherby, O.D. and O.A. Ruano, "Rate-controlling processes in creep of subgrain containing aluminum materials" Mater. Sci. and Eng. A, **410-411,** 8-11 (2005).

[55] Zhu, S.J., K. Kucharova, and J. Cadek, "High-Temperature Creep in an Al-8.5Fe-1.3V-1.7Si Alloy Processed by Rapid Solidification" Met. Mat. Trans. A, **31A,** 2229-2237 (2000).

[56] Deshmukh, S.P., R.S. Mishra, and K. Kendig, "Creep behavior and threshold stress of an extruded Al-6Mg-2Sc-1Zr alloy" Mater. Sci. and Eng. A, **381,** 381-385 (2004).

[57] Kaibyshev, R., O. Sitdikov, I. Mazurina, and D.R. Lesuer, "Deformation behavior of a 2219 Al alloy" Mater. Sci. and Eng. A, **A334,** 104-113 (2002).

[58] Deshmukh, S.P., R.S. Mishra, and K.L. Kendig, "Creep behavior of extruded Al-6Mg-1Sc-1Zr-10vol.%SiCp composite" Mater. Sci. and Eng. A, **410-411,** 53-57 (2005).

[59] Li, Y. and F.A. Mohamed, "An investigation of creep behavior in an SiC-2124 Al composite" Acta Mater., **45,** (11), 4775-4785 (1997).

[60] Karnesky, R.A., L. Meng, and D.C. Dunand, "Strengthening Mechanisms in Aluminum Containing Coherent Al_3Sc precipitates and Incoherent Al_2O_3 Dispersoids" Acta Mater., **55,** 1299-1308 (2007).

[61] Frost, H.J. and M.F. Ashby, *Deformation-Mechanism Maps: The Plasticity and Creep of Metals and Ceramics*. (Pergamon, Oxford, 1982).

[62] Cadek, J., *Creep in Metallic Materials*. (Elsevier, New York, 1988).

[63] Arzt, E. and J. Rosler, "The Kinetics of Diclocation Climb over Hard Particles - II. Effects of an Attractive Particle-Dislocation Interaction" Acta Metall., **36,** (4), 1053-1060 (1988).

[64] Rosler, J. and E. Arzt, "The Kinetics of Dislocation Climb Over Hard Particles - I. Climb Without Attractive Particle-Dislocation Interaction" Acta Metall., **36,** (4), 1043-1051 (1988).

[65] Rosler, J. and E. Arzt, "A New Model-Based Creep Equation for Dispersion Strengthened Materials" Acta Metall., **38,** (4), 671-683 (1990).

[66] Rosler, J., "Back-stress Calculation for Dislocation Climb Past Non-interacting Particles" Mater. Sci. and Eng. A, **339,** 334-339 (2003).

[67] Chen, Y.C., M.E. Fine, and J.R. Weertman, "Microstructural Evolution and Mechanical Properties of Rapidly Solidified Al-Zr-V alloys at High Temperatures" Acta Metall. Mater., **38,** (5), 771-780 (1990).

[68] Shewfelt, R.S. and L.M. Brown, "High-temperature strength of dispersion-hardened single crystals" Phil. Mag., **30,** 1135 (1974).

[69] Lagneborg, R., "Bypassing of dislocations past particles by a climb mechanism" Scripta Metall., **7,** 605 (1973).

[70] McLean, M., "On the threshold stress for dislocation creep in particle strengthened alloys" Acta Metall., **33,** 545-556 (1985).

[71] Pichler, A. and E. Arzt, "Creep of dispersion strengthened alloys controlled by jog nucleation" Acta Mater., **44,** (7), 2751-2758 (1996).

[72] Mishra, R.S., H. Jones, and G.W. Greenwood, "On the threshold stress for diffusional creep in pure metals" Phil. Mag. A, **60,** (6), 581-590 (1989).

[73] Marquis, E.A., D.N. Seidman, M. Asta, C. Woodward, and V. Ozolins, "Mg Segregation at Al/Al_3Sc Heterophase Interfaces on an Atomic Scale: Experiments and Computations" Phys. Rev. Lett., **91,** 36101-36101-36101-36103 (2003).

[74] Murray, J.L., "Al-Sc-Ti Phase Diagram" personal communication, (2003).

[75] Hellman, O.C., J.A. Vandenbroucke, J. Rüsing, D. Isheim, and D.N. Seidman, "Analysis of Three-Dimensional Atom-Probe Data by the Proximity Histogram" Micros Microanal, **6,** 437-444 (2000).

[76] Hellman, O.C., J. Vandenbroucke, J. Blatz du Rivage, and D.N. Seidman, "Application software for data analysis for three-dimensional atom probe microscopy" Mater. Sci. and Eng. A, **327,** (1), 29-33 (2002).

[77] Ashby, M. and L. Brown, "Diffraction Contrast from Spherically Symmetrical Coherency Strains" Phil. Mag., **8,** 1083-1102 (1963).

[78] Fuller, C.B., *Ph.D. thesis*. 2003, Northwestern University; http://arc.nucapt.northwestern.edu/refbase/show.php?record=147.

[79] Doherty, R.D., "Role of interfaces in kinetics of internal shape changes" Metal Science, **16,** 1-13 (1982).

[80] Lifshitz, I.M. and V.V. Slyozov, J. Phys. Chem. Solids, **19,** 35-50 (1961).

[81] Wagner, C., Z. Elektrochem, **65,** 581-591 (1961).

[82] Umantsev, A. and G.B. Olson, "Ostwald Ripening in Multicomponent Alloys" Scripta Metall. Mater., **29,** 1135-1140 (1993).

[83] Kuehmann, C.J. and P.W. Voorhees, "Ostwald Ripening in Ternary Alloys" Metall Mater Trans A, **27A,** 937-943 (1996).

[84] Lagneborg, R. and B. Bergman, "The Stress/Creep Rate Behaviour of Precipitation-Hardened Alloys" Metal Sci, **10,** 20-28 (1976).

[85] Hirsch, P.B. and F.J. Humphreys, in *The Physics and Strength of Plasticity*, A. Argon, Editor. 1969 p. 189, MIT Press: Cambridge, MA.

[86] Martin, P.W., *Precipitation Hardening*. (Butterworth-Heinemann, 1998, p. 81).

[87] Brown, L.M. and R.K. Ham, *Dislocation-Particle Interactions*, in *Strengthening Methods in Crystals*. 1971, App. Sci. Pub.

[88] Tabor, D., Br. J. of App. Phys., **7,** 159-165 (1956).

[89] Miura, Y., M. Nakayama, and A. Furuta. in *JIMIS-7*. 1993.

[90] Baumann, S.F. and D.B. Williams, "Experimental Observations in the Nucleation and Growth of δ'(Al_3Li) in Dilute Al-Li Alloys" Met. Trans. A, **16A,** 1203-1211 (1985).

[91] Mullins, W.W. and R.F. Sekerka, "Morphological Stability of a Particle Growing by Diffusion or Heat Flow" J. App. Phys., **34,** (2), 323-331 (1963).

[92] Shewmon, P.G., *Diffusion in Solids*. (McGraw-Hill, New York, 1963).

[93] Asta, M., S.M. Foiles, and A.A. Quong, "First-Principles calculations of bulk and interfacial thermodynamic properties for fcc-based Al-Sc alloys" Phys. Rev. B, **57,** 11265-11275 (1998).

[94] Thompson, M.E., C.S. Su, and P.W. Voorhees, "The Equilibrium Shape of a Misfitting Precipitate" Acta Metall. Mater., **42,** 2107-2122 (1994).

[95] Thornton, K., N. Akaiwa, and P.W. Voorhees, "Large-scale Simulations of Ostwald Ripening in Elastically Stressed Solids. II. Coarsening Kinetics and Particle Size Distribution" Acta Mater., **52,** 1365-1378 (2004).

[96] Dregia, S.A. and P. Wynblatt, "Equilibrium Segregation and Interfacial Energy in Multicomponent Systems" Acta Metall. Mater., **39,** (5), 771-778 (1991).

[97] Fujikawa, S.I., "Impurity Diffusion of Scandium in Aluminum" Defect and Diffusion For., **143-147,** 115-120 (1997).

[98] Touloukian, Y.S., R.K. Kirby, R.E. Taylor, and P.D. Desai, *Thermophysical Properties of High Temperature Solid Materials*. (Macmillan, New York, 1967).

[99] Karnesky, R.A., M.E. Van Dalen, D.C. Dunand, and D.N. Seidman, "Effects of substituting rare-earth elements for scandium in a precipitation-strengthened Al-0.08at.%Sc alloy" Scripta Mater., **55,** 437-440 (2006).

[100] Van Dalen, M.E., D.C. Dunand, and D.N. Seidman, "Nanoscale Precipitation and Mechanical Properties of Al-0.06 at.% Sc Alloys Micro-Alloyed with Yb or Gd" J. Mater. Sci., **41,** 7814-7823 (2006).

[101] Karnesky, R.A., D.N. Seidman, and D.C. Dunand, "Creep of Al-Sc Microalloys with Rare-earth Element Additions" Mater. Sci. For., **519-521,** 1035-1040 (2006).

[102] Van Dalen, M.E., D.C. Dunand, and D.N. Seidman, "Effects of Ti additions on the nanostructure and creep properties of precipitation-strengthened Al-Sc alloys" Acta Mater., **53,** 4225-4235 (2005).

[103] Kelly, T.F., T.T. Gribb, J.D. Olson, R.L. Martens, J.D. Shepard, S.A. Wiener, T.C. Kunicki, R.M. Ulfig, D.R. Lenz, E.M. Strennen, E. Oltman, J.H. Bunton, and D.R. Strait, "First Data from a Commercial Local Electrode Atom Probe (LEAP)" Micros. Microanal., **10,** 373-383 (2004).

[104] Kelly, T.F. and M.K. Miller, "Atom Probe Tomography" Rev. of Sci. Instr., **78,** (3), 031101-031101-031120 (2007).

[105] Seidman, D.N., "Perspective: From Field-ion microscopy of Single Atoms to Atom-probe Tomography: A journey: "Atom-probe Tomography"" Rev. of Sci. Instr., **78,** 031101-031101-031103 (2007).

[106] Ardell, A.J., "Precipitation Hardening" Metall. Trans. A, **16A,** 2131 (1985).

[107] Murken, J., O. Girard, R. Hohner, B. Skrotzki, and G. Eggeler, "On the Influence of Stress and Strain on the Coarsening of Precipitates in Al-alloys under Creep Conditions" Mater. Sci. For., **331-337,** 1507-1512 (2000).

[108] Nakajima, T., M. Takeda, and T. Endo, "Strain Enhanced Precipitate Coarsening during Creep of a Commercial Magnesium Alloy AZ80" Mater. Trans., **47,** (4), 1098-1104 (2006).

[109] Liu, Z. and M. Asta, In preparation, (2007).

[110] Liu, Z., *Thermodynamics of Nano-scale Precipitate-strengthened Fe-Cu and Al-transition-metal Systems from First-principles Calculations*. 2006, Ph. D. Thesis, Northwestern University.

[111] Morris, M.A., "Creep deformation of an aluminum alloy with intermetallic precipitates" Phil. Mag. A, **65,** (4), 943-960 (1992).

[112] Kaibyshev, R., F. Musin, E. Avtokratova, and Y. Motohashi, "Deformation behevior of a modified 5083 aluminum alloy" Mater. Sci. and Eng. A, **392,** 373-379 (2005).

[113] Cadek, J., K. Kucharova, and S.J. Zhu, "Creep behaviour of an oxide dispersion strengthened Al-5Mg alloy reinforced by silicon carbide particulates - an oxide dispersion strengthened Al-5Mg-30SiCp composite" Mater. Sci. and Eng. A, **272,** (45-56), (1999).

[114] Li, Y., R. Nutt, and F.A. Mohamed, "An Investigation of Creep and Substructure Formation in 2124 Al" Acta Mater., **45,** (6), 2607-2620 (1997).

[115] Knipling, K.E., Ph.D. Thesis, Northwestern University, http://arc.nucapt.northwestern.edu/refbase/files/Knipling-2006_1785.pdf, (2006).

[116] Kucharova, K., S. Zhu, and J. Cadek, "High Temperature Creep of an Al-8.5Fe-1.3V-1.7Si Alloy" Kovove Meterialy, **40,** 69-84 (2002).

[117] Mohamed, F.A., K. Park, and E.J. Lavernia, "Creep behavior of discontinuous SiC-Al composites" Mater. Sci. and Eng. A, **150,** 21-35 (1992).

[118] Mishra, R.S., T.K. Nandy, and G.W. Greenwood, "The threshold stress for creep controlled by dislocation-particle interaction" Phil. Mag. A, **69,** (6), 1097-1109 (1994).

[119] Takesue, H., K. Oh-ishi, Z. Horita, and M. Nemoto, "Effect of fine precipitation of coherent disordered phase on creep strength of L12-ordered Co3Ti" Mater. Sci. and Eng. A, **239-240,** 479-484 (1997).

[120] Hausselt, J.H. and W.D. Nix, Acta Metall., **25,** 1491 (1977).

[121] Xiang, Y. and D.J. Srolovitz, "Dislocation climb effects on particle bypass mechanisms" Phil. Mag., **86,** (25-26), 3937-3957 (2006).

[122] Harada, Y. and D.C. Dunand, "Thermal Expansion of Al_3Sc and $Al_3(Sc_{0.75}X_{0.25})$" Scripta Mater., **48,** 219-222 (2003).

[123] Knipling, K.E., D.C. Dunand, and D.N. Seidman, "Criteria for Developing Castable, Creep-Resistant Aluminum-Based Alloys - A Review" Zeitschrift fur Metallkunde, **97,** (3), 246-265 (2006).

[124] Kononenko, V.I. and S.V. Golubev, "Phase Diagrams of Binary Systems of Aluminum with La, Ce, Pr, Nd, Sm, Eu, Yb, Sc, and Y" Russian Metall., **2,** 197-199 (1990).

[125] Jo, H.H. and S.I. Fujikawa, "Kinetics of precipitation in Al-Sc alloys and low temperature solid solubility of scandium in aluminum studied by electrical resistivity measurements" Mater. Sci. and Eng. A, **171,** 151-161 (1993).

[126] Royset, J. and N. Ryum, "Scandium in Aluminum Alloys" Int. Mater. Rev., **50,** (2), 1-26 (2005).

[127] Tsivoulas, D. and J.D. Robson, "Coherency loss of Al_3Sc precipitates during ageing of dilute Al-Sc alloys" Mater. Sci. For., **519-521,** 473-478 (2006).

[128] Ardell, A.J., "Interfacial Free Energies and Solute Diffusivities from Data on Ostwald Ripening" Interface Sci., **3,** 119-125 (1995).

[129] Ardell, A.J. *Precipitate Coarsening in Solids: Modern Theories, Chronic Disagreement with Experiment*. in *Phase Transformations '87*. 1988. London: The Institute of Metals.

[130] Akaiwa, N. and P.W. Voorhees, "Late-stage Phase Separation: Dynamics, Spatial Correlations, and Structure Functions" Phys. Rev. E, **49,** 3860-3880 (1994).

[131] Joh, C.H., K. Yamada, and Y. Miura, "Effect of Sc-Addition on the Coarsening Behavior of Al_3Li Precipitates in Al-Li Alloys" Materials Transactions, JIM, **40,** (5), 439-442 (1999).

[132] van Dalen, M.E., D.C. Dunand, and D.N. Seidman, *Precipitation Strengthening in Al(Sc,Ti) Alloys*, in *Affordable Metal-Matrix Composites*, A.B. Pandey, et al., Editors. 2003, TMS. p. 195-201.

[133] Lefebvre, W., F. Danoix, G. Da Costa, F. De Geuser, H. Hallem, A. Deschamps, and M. Dumont, "3DAP Measurements of Al content in Different Types of Precipitates in Aluminum Alloys" Surf. Interface Anal., **39,** 206-212 (2007).

[134] Mondolfo, L.F., *Aluminum Alloys: structure and properties*. (Butterworths, London, 1976).

[135] Murray, J.L., "The Al-Sc (Aluminum-Scandium) System" J. of Phase Equil., **19,** (4), 380-384 (1998).

[136] Massalski, *Binary Alloy Phase Diagrams*. (ASM Int., 1990).

[137] Sha, G. and A. Cerezo, "Field ion microscopy and 3-D atom probe analysis of Al_3Zr particles in 7050 Al alloy" Ultramicroscopy, **102,** 151-159 (2005).

[138] Marquis, E.A., D.N. Seidman, M. Asta, and C. Woodward, "Composition evolution of nanoscale Al_3Sc precipitates in an Al-Mg-Sc alloy: Experiments and computations" Acta Mater., **54,** 119-130 (2006).

[139] Schmuck, C., P. Caron, A. Hauet, and D. Blavette, "Ordering and precipitation in gamma' phase in low supersaturated Ni-Cr-Al model alloy: an atomic scale investigation" Phil. Mag. A, **76,** (3), 527-542 (1997).

[140] Schmuck, C., Ph.D. Thesis, Univeristy of Rouen, (1997).

[141] Sudbrack, C., *Decomposition behavior in model Ni-Al-Cr-X superalloys : temporal evolution and compositional pathways on a nanoscale*. 2004, Ph.D. thesis, Northwestern University: http://arc.nucapt.northwestern.edu/refbase/show.php?record=16.

[142] Sudbrack, C.K., R.D. Noebe, and D.N. Seidman, "Direct observations of nucleation in a nondilute multicomponent alloy" Phys. Rev. B, **73,** 212101 (2006).

[143] De Geuser, F., W. Lefebvre, and D. Blavette, "3D atom probe study of solute atoms clustering during natural ageing and pre-ageing of an Al-Mg-Si alloy" Phil. Mag. Lett., **86,** (4), 227-234 (2006).

[144] Ziman, J.M., *Models of disorder: the theoretical physics of homogeneously disordered systems*. (Cambridge University Press, Cambridge, 1979).

[145] Miura, Y., K. Horikawa, K. Yamada, and M. Nakayama, "Precipitation Hardening in an Al-2.4Li-0.19Sc Alloy" Aluminum Alloys: Their Physical and Mechanical Properties, **2,** 161-168 (1994).

[146] Di, Z., S. Saji, W. Fujitani, and S. Hori, "Composite Precipitates in Al-Li-Ti Alloys" Transactions of the Japan Institute of Metals, **28,** (10), 827-828 (1987).

[147] Gayle, F.W. and J.B. Vander Sande, ""Composite" Precipitates in an Al-Li-Zr Alloy" Scripta Met., **18,** 473-478 (1984).

[148] Norman, A.F. and P. Tsakiropoulos, "The microstructure and properties of high pressure gas-atomized Al-Li-Hf alloy powders" Mat. Sci. and Eng. A, **134,** 1144-1147 (1991).

[149] Ringer, S.P., K. Hono, T. Sakurai, and I.J. Polmear, "Cluster hardening in an aged Al-Cu-Mg alloy" Scripta Mater., **36,** (5), 517-521 (1997).

[150] Ringer, S.P., T. Sakurai, and I.J. Polmear, "Origins of Hardening in Aged Al-Cu-Mg-(Ag) Alloys" Acta Mater., **45,** (9), 3731-3744 (1997).

[151] Sofyan, B.T., I.J. Polmear, and S.P. Ringer, "Precipitation Processes in Al-4Cu-(Mg,Cd) (wt.%) Alloys" Mater. Sci. For., **396-402,** 613-618 (2002).

[152] Bryant, J.D., "the Effects of Preaging Treatments on Aging Kinetics and Mechanical Properties in AA6111 Aluminum Autobody Sheet" Metall. Mater. Trans. A, **30A,** 1999-2006 (1999).

[153] Radmilovic, V., M.K. Miller, D. Mitllin, and U. Dahmen, "Strain-compensated Nano-clusters in Al-Si-Ge Alloys" Scripta Mater., **54,** 1973-1978 (2006).

[154] Murayama, M. and K. Hono, "Pre-precipitate Clusters and Precipitation Processes in Al-Mg-Si Alloys" Acta Mater., **47,** (5), 1537-1548 (1999).

[155] Ringer, S.P., S.K. Caraher, and I.J. Polmear, "Response to Comments on Cluster Hardening in an Aged Al-Cu-Mg Alloy" Scripta Mater., **39,** (11), 1559-1567 (1998).

[156] Brechet, Y. and G. Martin, "Nucleation problems in metallurgy of the solid state: recent developments and open questions" C.R. Physique, **7,** 959-976 (2006).

[157] Schneider, M., G. Gottstein, L. Lochte, and J. Hirsch, "A Statistical Model for Precipitation - Applications to Commercial Al-Mn-Mg-Fe-Si Alloys" Mater. Sci. For., **396-402,** 637-642 (2002).

[158] Chen, Z., Z. Zheng, and S.P. Ringer, "Effect of Small Addition of Sc on the Microstructural Evolution in Al-15Ag Alloy" J. Mater. Sci. Technol., **21,** (5), 630-634 (2005).

[159] Miller, M.K., *Atom Probe Tomography: Analysis at the Atomic Level*. (Kluwer Academic, New York, 2000).

[160] Hyde, J.M. and C.A. English, "An Analysis of the Structure of Irradiation Cu-enriched Clusters in Low and High Nickel Welds" Proc. of MRS Fall 2000 Meeting, **650,** 1-12 (2001).

[161] Stoloff, N.S., *Intermetallic Compounds and Ordered Phases*, in *Strengthening Methods in Crystals*, A. Kelly and R.B. Nicholson, Editors. 1971, Applied Science Publishers: London.

[162] Ringer, S.P., "Advanced Nanostructural Analysis of Aluminium Alloys Using Atom Probe Tomography" Mater. Sci. For., **519-521,** 25-34 (2006).

[163] Wendt, H. and P. Haasen, "Nucleation and Growth of Gamma'-precipitates in Ni-14at.%Al" Acta Metall., **31,** (10), 1649-1659 (1983).

[164] De Geuser, F., W. Lefebvre, P. Auger, F. Danoix, A. Bigot, and D. Blavette, "Atom Probe Tomography II: The Precipitation in Al Base Alloys" Adv. Eng. Mater., **8,** (12), 1206-1209 (2006).

[165] Murarka, S.P. and R.P. Agarwala, "Diffusion of Rare Earth Elements in Aluminum" Govt. of India Atomic Energy Comm., (1968).

[166] Pasturel, A. and C. Chatillon-Colinet, "Thermodynamic study of the valence state of ytterbium in $YbAl_2$ and $YbAl_3$ compounds" J. of the Less-Common Metals, **90,** 21-27 (1983).

[167] Colinet, C., A. Pasturel, and K.H.J. Buschow, "Molar enthalpies of formation of LnAl2 compounds" J. Chem. Thermodynamics, **17,** 1133-1139 (1985).

[168] Borzone, G., A.M. Cardinale, N. Parodi, and G. Cacciamani, "Aluminum compounds of the rare earths: enthalpies of formation of Yb-Al and La-Al alloys" J. Alloys and Compounds, **247,** (141-147), (1997).

[169] Xiao, S.Q. and P. Haasen, "HREM Investigation of Homogeneous Decomposition in a Ni-12 at%Al Alloy" Acta Metall. Mater., **39,** (4), 651-659 (1991).

[170] Schmitz, G. and P. Haasen, "Decomposition of an Al-Li Alloy - The Early Stages Observed by HREM" Acta Metall. Mater., **40,** (9), 2209-2217 (1992).

[171] Doherty, R.D., *Ch. 14: Diffusive Phase Transformations in the Solid State*, in *Physical Metallurgy*, R.W. Cahn and P. Haasen, Editors. 1983, Elsevier: Amsterdam.

[172] Hyland, R.W. and R.C. Stiffler, "Determination of the elastic constants of polycrystalline Al_3Sc" Scripta Metall. Mater., **25,** 202 (1991).

[173] Marquis, E.A. and D.N. Seidman, "Coarsening kinetics of nanoscale Al_3Sc precipitates in an Al-Mg-Sc Alloy" Acta Mater., **53,** 4259-4268 (2005).

[174] Van Dalen, M.E., D.C. Dunand, and D.N. Seidman, "Precipitation of Al-Sc-RE alloys" to be submitted for publication, (2006).

[175] Pareige-Schmuck, C., F. Soisson, and D. Blavette, "Ordering and phase separation in low supersaturated Ni-Cr-Al alloys: 3D atom probe and Monte Carlo simulation" Mater. Sci. and Eng. A, **250,** (1), 99-103 (1998).

[176] Pareige, C., F. Soisson, G. Martin, and D. Blavette, "Ordering and phase separation in Ni-Cr-Al: monte carlo simulations vs three-dimensional atom probe" Acta Mater., **47,** (6), 1889-1899 (1999).

[177] Sudbrack, C.K., K.E. Yoon, R.D. Noebe, and D.N. Seidman, "Temporal evolution of the nanostructure and phase compositions in a model Ni-Al-Cr alloy" Acta Mater., **54,** (12), 3199-3210 (2006).

[178] Sudbrack, C.K., R.D. Noebe, and D.N. Seidman, "Compositional pathways and capillary effects during isothermal precipitation in a nondilute Ni–Al–Cr alloy" Acta Mater., **55,** (1), 119-130 (2007).

[179] Ratke, L. and P.W. Voorhees, *Growth and Coarsening*. (Springer, Berlin, 2002).

[180] Calderon, H.A., P.W. Voorhees, J.L. Murray, and G. Kostorz, "Ostwald Ripening in Concentrated Alloys" Acta Metall. Mater., **42,** (3), 991-1000 (1994).

[181] Mao, Z., C.K. Sudbrack, K.E. Yoon, G. Martin, and D.N. Seidman, "The mechanism of morphogenesis in a phase-separating concentrated multicomponent alloy" Nature Materials, **6,** 210-216 (2007).

[182] Roussel, J. and P. Bellon, "Vacancy-assisted phase separation with asymmetric atomic mobility: Coarsening rates, precipitate composition and morphology" Phys. Rev. B, **63,** 184114-184111-184115 (2001).

[183] Ardell, A.J.O., V., "Trans-interface Diffusion-controlled Coarsening" Nature Materials, **4,** (4), 309-316 (2005).

[184] Ardell, A.J., D. Kim, and V. Ozolins, "Ripening of L12 Ni_3Ti Precipitates in the Framework of the Trans-interface Diffusion-controlled Theory of Particle Coarsening" Z. Metallkd., **97,** (3), 295-302 (2006).

[185] Watanabe, C., T. Kondo, and R. Monzen, "Coarsening of Al_3Sc Precipitates in an Al-0.28 Wt Pct Sc Alloy" Metall. Mater. Trans. A, **35,** 3003-3008 (2004).

[186] Nakayama, M., A. Furuta, and Y. Miura, "Precipitation of Al_3Sc in Al-0.23mass%Sc Alloy" Materials Transactions, JIM, **38,** (10), 852-857 (1997).

[187] van Dalen, M.E., "Microstructure and Creep Properties of Al-Sc Alloys Micro-alloyed with Lanthanides (Yb or Gd) and Transition Metals (Ti or Zr)" Ph.D. Thesis, Northwestern University, (2007).

[188] Royset, J. and N. Ryum, "Kinetics and mechanisms of precipitation in an Al-0.2wt.%Sc alloy" Mater. Sci. and Eng. A, **396,** 409-422 (2005).

[189] Watanabe, C., D. Watanabe, and R. Monzen, "Coarsening Behavior of Al_3Sc Precipitates in an Al-Mg-Sc Alloy" Mater. Trans., **47,** (9), 2285-2291 (2006).

[190] Buschow, K.H.J., "Phase Relations and Intermetallic Compounds in the Systems Neodymium-Aluminum and Gadolinium-Aluminum" J. Less-Common Metals, **9,** 452-456 (1965).

[191] Chaudhury, P.K. and F.A. Mohamed, "Effect of Impurity Content on Superplastic Flow in the Zn-22% Al Alloy" Acta Metall., **36,** (4), 1099-1110 (1988).

[192] Courtney, T.H., *Mechanical Behavior of Materials*. (McGraw-Hill, Boston, 2000).

[193] Mukherjee, A.K., J.E. Bird, and J.E. Dorn, "Experimental Correlations for High-Temperature" Trans. ASM, **62,** 155-179 (1969).

[194] Mura, T., *Micromechanics of Defects in Solids*. (Martinus Nijhoff Publishers, Dordrecht, 1987).

[195] Nembach, E., *Particle Strengthening of Metals and Alloys*. (John Wiley & Sons, New York, 1997).

[196] Dunn, H.L., B.L. Karihaloo, J. Wang, and X. Yi, "Strain Distributions in Nano-onions with Uniform and Non-uniform Compositions" Nanotechnology, **17,** 3380-3387 (2006).

[197] Farjami, S. and P.W. Voorhees, Personal Communication, (2007).

[198] Sato, T., A. Kamio, and G. Lorimer, "Effects of Si and Ti additions on the nucleation and phase stability of the $L1_2$-type Al_3Zr phase in Al-Zr alloys" Mater. Sci. For., **217-222,** 895-900 (1996).

[199] Kirkaldy, J.S. and Y. D.J., *Diffusion in the Condensed State*. (The Institute of Metals, London, 1987).

[200] Barros, J., B. Malengier, R. Van Keer, and Y. Houbaert, "Modeling Silicon and Aluminum Diffusion in Electrical Steel" J. Phase Equilibria and Diffusion, **26,** (5), 417-422 (2005).

[201] Divinski, S.V., F. Hisker, C. Herzig, R. Filipek, and M. Danielewski, "Self- and Interdiffusion in Ternary Cu-Fe-Ni Alloys" Defect and Diffusion For., **237-240,** 50-61 (2005).

[202] Hayashi, S., W. Wang, J. Sordelet, and B. Gleeson, "Interdiffusion Behavior of Pt-Modified gamma-Ni + gamma'-Ni3Al Alloys Coupled to Ni-Al-Based Alloys" Metall Mater Trans A, **36A,** 1769-1775 (2005).

[203] Nastar, M., "A Mean Field Theory for Diffusion in a Dilute Multi-component Alloy: A New Modelfor the Effect of Solutes of Self-Diffusion" Phil. Mag., **85,** (32), 3767-3794 (2005).

[204] Kluthe, C., T. Al-Kassab, and R. Kirchheim, "Early stages of oxide precipitation in Ag-0.42at.%-Mg - examined with the tomographic atom probe" Mater. Sci. and Eng. A, **353,** 112-118 (2003).

[205] Gyger, T., "Evolution of Nanoscale Precipitates in Al-Sc-Yb-Zr at Elevated Temperatures" Senior Independent Work Northwestern University, (2006).

[206] Fuller, C.B., Personal Communication, (2002).

[207] Soisson, F. and G. Martin, "Monte Carlo simulations of the decomposition of metastable solidsolutions: transient and steady-state nucleation kinetics" Phys. Rev. B, **62,** (1), 203-214 (2000).

[208] Al-Raoush, R., "Microstructure Characterization of Granular Materials" Physica A, **377,** 545-558 (2007).

[209] Harada, Y. and D.C. Dunand, "Microstructure and Hardness of Scandium Trialuminide with Ternary Rare-Earth Additions" Mater. Sci. For., **539-543,** 1565-1570 (2007).

[210] Hyde, J.M., *Computer Modeling Analysis of Microscale Phase Transformations, Ph.D. Thesis*. 1993, Oxford University.

[211] Van Dalen, M.E., D.C. Dunand, and D.N. Seidman, "Precipitation of Al-Sc-RE alloys" to be submitted for publication, (2007).

[212] Vaumousse, D., A. Cerezo, and P.J. Warren, "A Procedure for Quantification of Precipitate Microstructures from Three-dimensional Atom Probe Data" Ultramicros., **95,** 215-221 (2003).

[213] Heinrich, A., T. Al-Kassab, and R. Kirchheim, "Investigation of the early stages of decomposition of Cu-0.7at.% Fe with the tomographic atom probe" Mater. Sci. and Eng. A, **353,** 92-98 (2003).

[214] Miller, M.K. and E.A. Kenik, "Atom Probe Tomography: A Technique for Nanoscale Characterization" Micros. Microanal., **10,** 336-341 (2004).

[215] Al-Kassab, T. and R. Kirchheim, "Investigation of the phase decomposition in alloys with the tomographic atom probe" Mater. Sci. and Eng. A, **324,** 168-173 (2002).

[216] Wolde-Giorgis, D., T. Al-Kassab, and R. Kirchheim, "Nucleation and growth in Cu-0.7at.% Ti as studied with the tomographic atom probe" Mater. Sci. and Eng. A, **353,** 152-157 (2003).

[217] Kolli, R.P. and D.N. Seidman, "Comparison of Compositional and Morphological Atom-probe Tomography Analysis for a Multicomponent Fe-Cu Steel" Micros. & Microanal., accepted for publication (2007).

[218] Maruyama, K., H. Endo, and H. Hoshino, "Short- and Intermediate-Range Order in Liquid Bi-$BiBr_3$ Mixtures: Importance of Voids" J. Phys. Soc. Japan, **76,** (2), 024601 (2007).

[219] Hung, P.K. and L.T. Vinh, "Local Microstructure of Liquid and Amorphous Al_2O_3" J. of Non-Cryst. Sol., **352,** 5531-5540 (2006).

[220] Goharshadi, E.K., A. Morsali, and G.A. Mansoori, "A Molecular Dynamics Study on the Role of Attractive and Repulsive Forces in Internal Energy, Internal Pressure and Structure of Dense Fluids" Chem. Phys., **331,** (2-3), 332-338 (2007).

[221] Louzguine-Luzgin, D.V. and A. Inoue, "Thermal Expansion of an Amorphous Alloy. Reciprocal-space vs. Real-space Distribution Function" Physica B, **388,** 290-293 (2007).

[222] Liu, H., F.J. Ke, H. Pan, and M. Zhou, "Molecular Dynamics Simulation of the Diffusion Bonding and Tensile Behavior of a Cu-Al Interface" Acta Phys. Sinica, **56,** (1), 407-412 (2007).

[223] Cheng, S., W. Wang, X. Bian, and X. Qin, "Structure Evolution of Cu-Cu type Clusters in Cu-In Alloy Melts" Phys. Lett. A, **331,** 387-392 (2004).

[224] Kato, H., E. Matsubara, A. Inoue, N. Nishiyama, and H.S. Chen, "Heat of Evolution and Structural Analysis on the Non-Newtonian Viscous Flow of $Pd_{40}Ni_{40}P_{20}$ Glassy Alloy" Mater. Sci. and Eng. A, **375-377,** 444-448 (2004).

[225] Moody, M.P., L.T. Stephenson, P.V. Liddicoat, and S.P. Ringer, "Contingency Table Techniques for Three Dimensional Atom Probe Tomography" Micros. Res. & Tech., **70,** 258-268 (2007).

Appendix A: Searching for Clusters in an Al-0.06Sc-0.02Yb Alloy: The Envelope Method and the Density of Clusters

A.1 Introduction

The maximum separation distance or envelope methods [159, 160, 210] are used to determine the level of clustering and precipitation in an Al-0.06at.%Sc-0.02at.%Yb alloy [100, 211]. The principal behind this is that atoms in a precipitate or cluster will have a smaller distance between them than solute atoms distributed randomly in the matrix. As inputs to the algorithm, a maximum separation distance, d_{max}, and the type of atoms for which to search are set by the user. In the case of the Al-Sc-Yb alloys, we search for clusters of Yb. The term "cluster" is used in this section to describe groups of atoms which are detected by algorithm. These clusters can be either precipitates with a well-defined ordered structure, or pre-precipitate clusters which do not have a defined structure.

For each Yb atom, the program searches within a radius equivalent to d_{max}. If there is another Yb atom within this distance, it is included in the cluster. The volume within a radius of d_{max} from this new Yb atom is then examined to see if there are other Yb atoms. This procedure is repeated until no more Yb atoms are found within d_{max} of any of the Yb atoms. Next, a minimum number of atoms which constitutes a cluster, N_{min}, is entered by the user. Any clusters found with less than this many Yb atoms will be discarded. Finally, this method extends an "envelope" within which the atoms of other types are also included in the cluster. All of the atoms (of all types) which are found in a grid cell containing a Yb atom in the cluster will be denoted as part of the cluster.

This method of defining an envelope has been refined. Methods to remove the excess shell of matrix atoms around the precipitate have been examined. One method is to erode the shell by removing the atoms furthest from the Yb atom until a change in slope in the plot of the number of atoms in the cluster vs. composition is reached, which indicates that the interface has been reached [212].

The envelope method can be used to determine the number of clusters and precipitates and also the radius of the precipitates, based on the number of atoms in the precipitate. The minimum number of atoms which constitutes a cluster, N_{min}, and the maximum separation distance d_{max} values are chosen by the user and both of these parameters can greatly affect the results obtained. Past studies have used this method to study the microstructure of the material [204, 213-215]. In a paper describing Cu-0.7at.% Ti [216], the critical distance for the cluster search method is such that the number of clusters does not change significantly with small change in the critical distance. They specify that they use a value of $N_{min} = 5$ atoms.

The envelope method is used in the study of the Al-0.06at.%Sc-0.02at.%Yb alloy since in the early stages of precipitation $Al_3(Yb_{1-x}Sc_x)$ precipitates form, before the Sc atoms cluster or precipitate. As was shown in the previous chapters, the nucleation of precipitates occurs much faster in Yb containing alloys than in other Al-Sc [21] and Al-Sc-X [2, 100, 102] alloys studied previously. An attempt is made to determine the parameters of the envelope method which most accurately describe the clustering and nucleation of Yb in the Al-Sc-Yb alloy.

A.2 Results and Discussion

A.2.1 Effect of Varying Parameters

In the Al-0.06Sc-0.02Yb alloy, we search for clusters of Yb, since Yb-rich $Al_3(Yb_{1-x}Sc_x)$ precipitates are the first to form [99, 100, 211]. This system is an instructive system on which to show the effects of the changes in the parameters since the solute atoms are dilute, with a concentration of only 200 atomic ppm for Yb and 600 ppm for Sc in the overall alloy. Due to the dilute concentration, other issues encountered when using this method will be minimized, including the problem of solute atoms in the matrix being counted as part of the precipitate and a low partitioning ratio of the solute between the matrix and precipitate phases.

In the random solid solution, the Yb atoms would be expected to be ~6 nm apart, if the atoms were evenly distributed on a square array. As seen in Fig. A.1, there are clusters with as few as 5 atoms which are clearly distinguishable in the matrix. In this particular cluster, the atoms are all within 1 nm, which is much closer than the average distance between atoms in the random solid solution. It should be noted that in the LEAP the exact crystallographic positions are not retained during evaporation of the atoms from the tip. It has been widely estimated that the resolution in the x-y plane is on the order of 0.2 nm [104].

The parameter d_{max} of the envelope method affects the size and number of clusters detected. The reconstructions for the different d_{max} values for a 120 s aging time at 300˚C can be seen in Fig. A.2. The number and size of clusters clearly increases with increasing d_{max} from 0.6-1.2 nm. When comparing the number of detected clusters in a data set for a short (30 s) and a longer (10

min) aging time, Fig A.3 and A.4 show that at both aging times the detection of small clusters varies especially greatly with d_{max}. When comparing the clusters which contain 8 or more Yb atoms, there is a much smaller increase in the number of clusters detected for d_{max} = 0.8 to 1.6 nm (27% for 30 s and 28% for 10 min between 0.8 – 1.6 nm) than with the clusters containing 5 or more Yb atoms (158 % increase for 30 s and 175% increase for 10 min). Thus, it is the clusters with 5-8 atoms which are most sensitive to the parameters used.

Also shown in Figs. A.3 and A.4 is that for both aging times there is a continuous increase in the number of clusters detected beyond 0.8 nm, and there does not appear to be a plateau at any reasonable value of d_{max}. A reasonable value for d_{max} would be on the same order of magnitude as the theoretical atom separation distance (the second nearest neighbor distance for the Yb atoms in an $L1_2$ structure is 0.4201 nm). Since the detection efficiency is significantly less than one (60%) in the LEAP, the value of d_{max} might be expected to be greater than the 2^{nd} nearest neighbor distance.

Fig. A.5 gives an indication as to why there is a decrease in Fig. A.3 in the number of clusters detected when increasing d_{max} from 0.6 to 0.8 nm. At 0.6 nm, there are some larger clusters which get split into two pieces, thus artificially raising the number of detected clusters. Fig. A.6 shows the precipitate size distribution, which shows many precipitates with less than 10 Yb atoms at 30 s, while there are also a significant number of precipitates which are between 10-100 Yb atoms and some even larger. The number of clusters detected in turn affects the number density of precipitates detected (Fig. A.7). As can be seen, the number density of precipitates

which have achieved a critical radius is much lower. These are the larger clusters, and hence they are less sensitive to the envelope algorithm.

As pointed out by Kolli et. al. [217], who studied a multi-component Fe alloy with Cu precipitates, initially the number of clusters detected decreases as parts of larger precipitates are no longer being counted separately. As d_{max} is further increased, the number of clusters then increases as less dense precipitates are included, and finally decreases to one for really large d_{max} as the precipitates are all lumped into one large precipitate. For the Al-Sc-Yb alloy the initial decrease followed by an increase is seen. However, since the solute concentration is so low, the number of detected clusters does not decrease within 5 nm.

A.2.2 Density of Clusters Algorithm

Figs. A.3 and A.4 highlight the differences in the microstructure at different aging times of 30 s and 10 min at 300˚C. At 30 s there is a high number of small clusters which will have a great effect on the number of detected clusters as d_{max} is changed. The solute content in the matrix is lower at 10 min, which makes the partitioning ratio greater between the two phases, making it easier for the algorithm to detect precipitates.

In order to ascertain what the most accurate value of d_{max} is, and to determine when clusters become precipitates with an ordered structure, I wrote a program which measures the density of atoms in the clusters, after they have been determined by the envelope method, with a large d_{max} of 1.4 nm (Fig. A.8). This program calculates the distance between all of the atoms in the cluster

and for each atom determines the distance to the nearest atom. The average of all of the minimum distances is then taken for all of the atoms in the cluster.

There is a wide range of densities for the small clusters, even at longer aging times of 10 min (Fig. A.9). The larger clusters, which are most definitely precipitates, have a more dense atomic structure ~0.4 nm for the average distance between nearest neighbor Yb atoms. There are some smaller clusters which are this dense, but there are also many smaller clusters which are less dense. This spread in densities could be a significant result and not a side effect of the way the clusters are calculated. As seen in Fig. A.1, the atoms are all within one nm but they still appear to be much closer than for a random solid solution (6 nm). This could point to how these clusters form, although, it is difficult to tell in the LEAP what the crystal structure is of the Yb atoms (Fig. A.1), and at which point they stop interacting significantly with each other, since it have been observed that the interactions beyond the 1^{st} nearest neighbor are significant [181]. A suggested mechanism is that some precipitates form earlier than others, especially since the wide range of densities persists up to 10 min of aging when 89 % of the Yb has precipitated out of the solid solution. Thus, the value of d_{max} used should be 1 nm to capture the less dense clusters.

Figures:

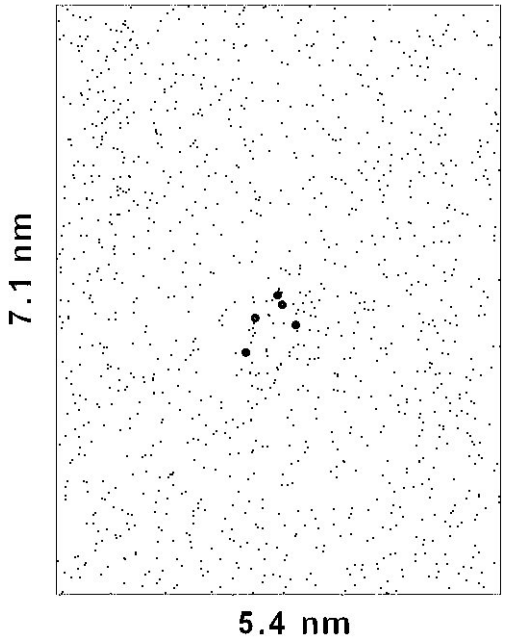

Figure A.1: Reconstruction of Yb cluster from 10 min aging time at 300°C for Al-0.06Sc-0.02Yb (at.%). The data is a 1 nm thick slice from the data set, which is the width of the furthest atoms in the cluster. The large atoms are Yb and the small atoms are Al and Sc.

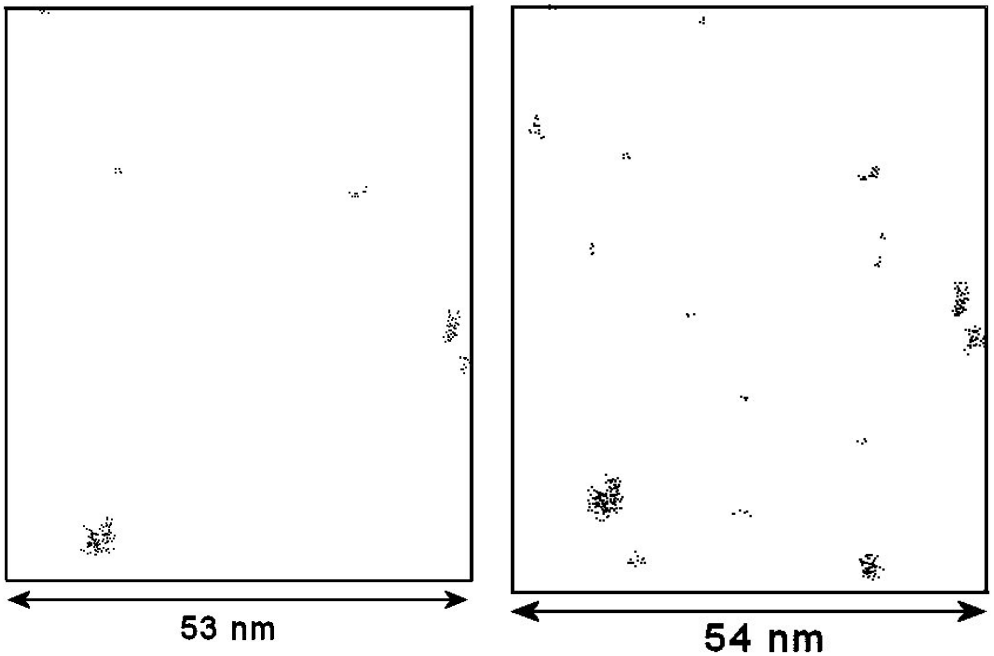

(a) (b)

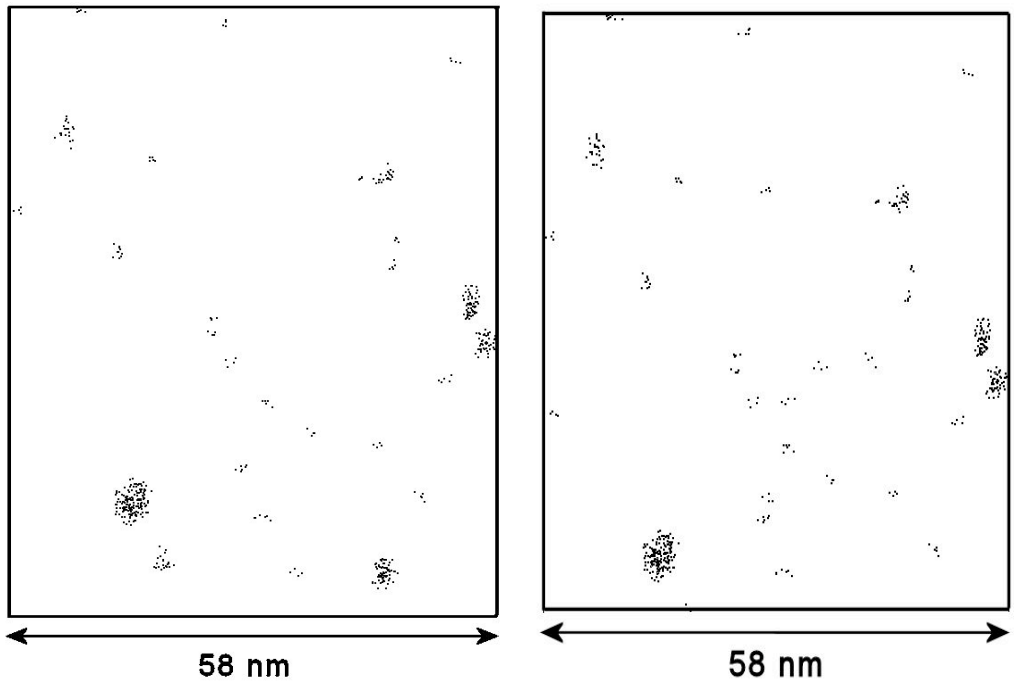

(c) (d)

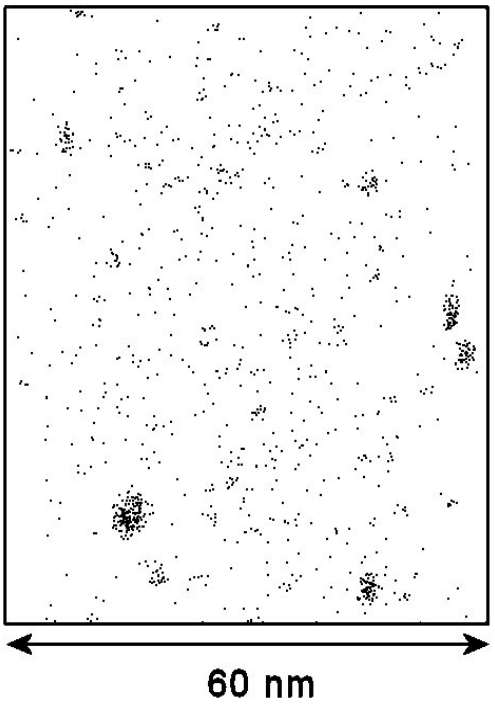

(e)

Figure A.2: Reconstructions for Al-0.06Sc-0.02Yb (at.%) aged for 120 sec at 300°C. Variation with dmax (a) 0.6 nm (b) 0.8 nm (c) 1.0 nm (d) 1.2 nm (e) all Yb atoms. Al and Sc atoms omitted from all reconstructions for clarity. Dimensions: x-direction increases from 52.7 to 60.0 nm, as the number of clusters increase since the box is drawn around the outermost atoms.

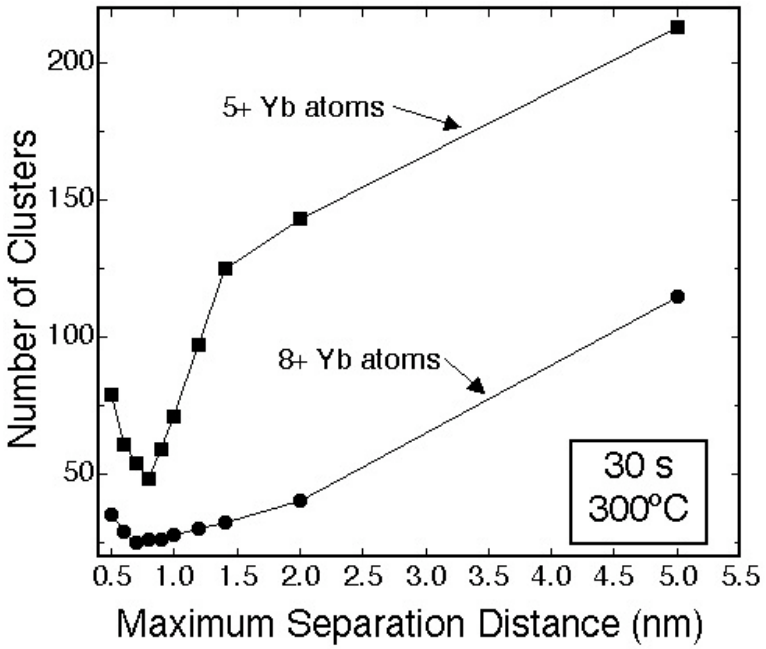

Figure A.3: Number of clusters detected vs. d_{max} and with a change in N_{min} for 30 s of aging at300°C for Al-0.06Sc-0.02Yb (at.%).

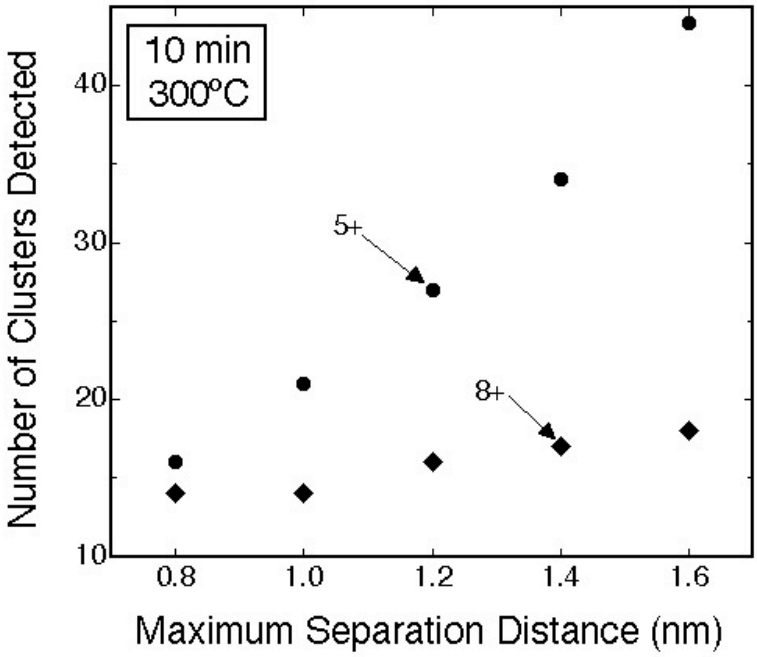

Figure A.4: Number of clusters detected vs. d_{max} and with a change in N_{min} for 10 min of aging at 300°C for Al-0.06Sc-0.02Yb (at.%).

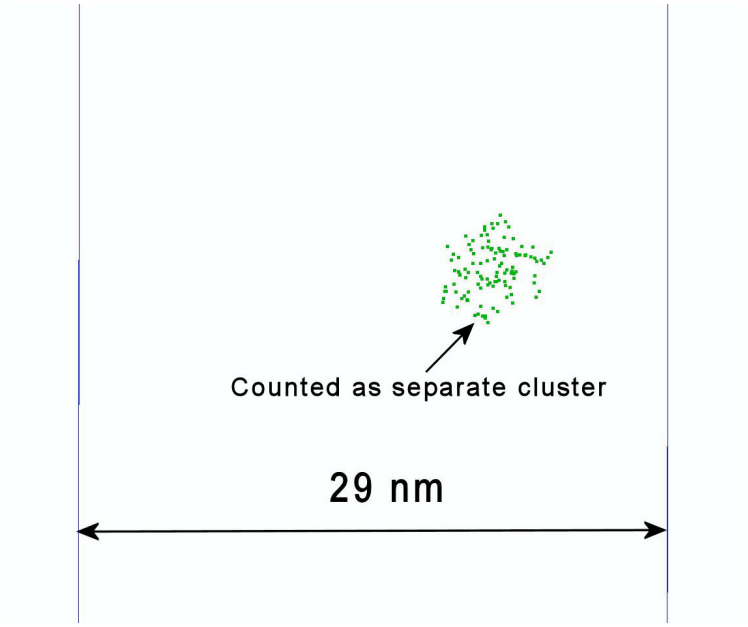

Figure A.5: Portion of a reconstruction of 30 s aging time at 300°C for Al-0.06Sc-0.02Yb (at.%) with d_{max} = 0.6 nm showing the bottom portion of a larger precipitate counted as a separate small cluster.

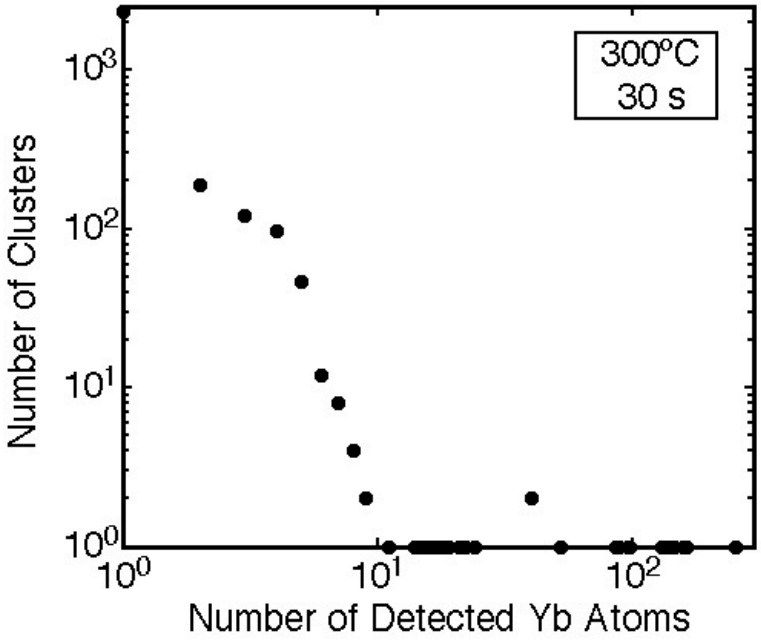

Figure A.6: Number of clusters vs. number of detected Yb atoms (uncorrected for detector efficiency) in the cluster for the 30 s aging time at 300°C for Al-0.06Sc-0.02Yb (at.%).

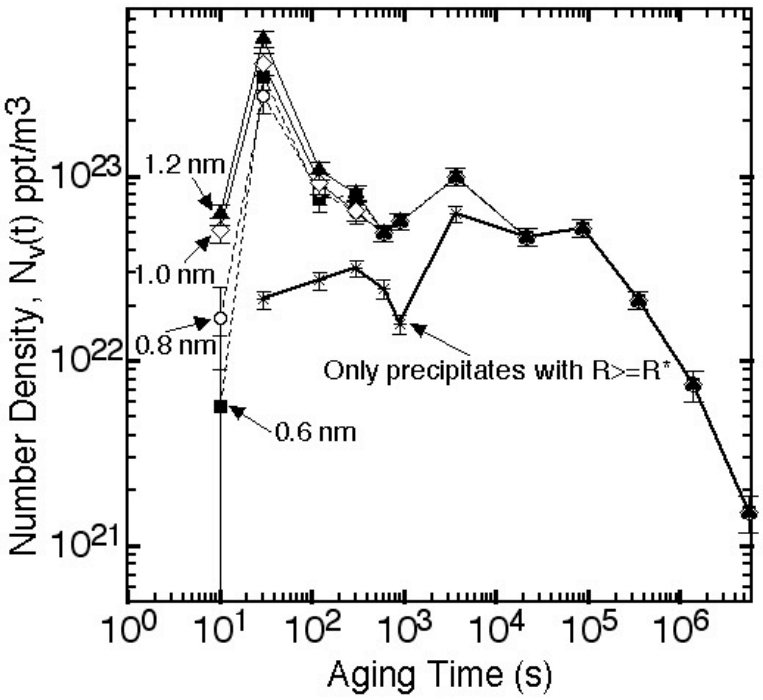

Figure A.7: Number density of precipitates, $N_v(t)$, vs. aging time at 300˚C for various values of d_{max} and for the precipitates with R≥R* for Al-0.06Sc-0.02Yb (at.%).

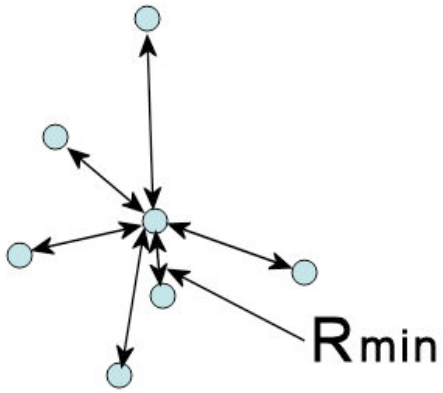

Figure A.8: Schematic showing the density of clusters method. The method calculates R_{min} for each atom and then takes the average R_{min} value for all of the atoms in the cluster.

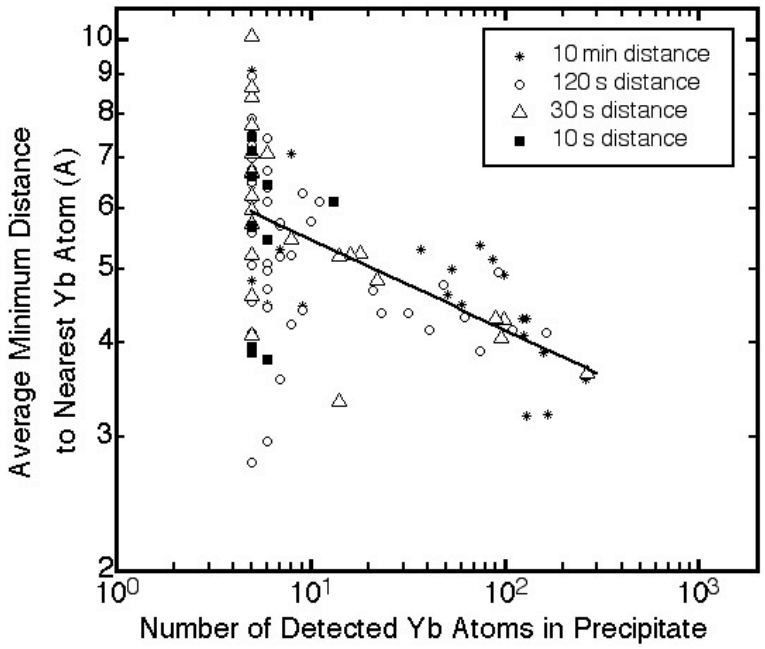

Figure A.9: The average distance to the nearest Yb atom in the cluster vs. the number of Yb atoms detected in the precipitate for aging times ranging from 10 s to 10 min at 300˚C for Al-0.06Sc-0.02Yb (at.%).

Appendix B: Details of the Radial Distribution Function

B.1 Introduction

In this section, the details of the RDFs are studied in more detail. The radial distribution function technique is of significance not only in this thesis, but it has wide-ranging applications. In addition to the RDFs which are measured for crystalline materials, which are discussed in this thesis, RDFs have been used for studying liquids, both experimentally [218, 219] and simulated [220]. They have also been used in an amorphous alloy to compare the average distance between atoms [221]. The transition from amorphous to crystalline at an interface has been simulated using the RDF technique [222]. RDFs have also been calculated from x-ray diffraction measurements to examine the cluster formation in melts [223]. Non-metallic applications in solids include: characterization of irregularly shaped granular materials [208] and amorphous alloys [224].

The partial RDFs for the Al-Sc-Yb-Zr system showed some interactions among the solute elements. This conclusion was reached since there are values in the partial RDFs which were greater than unity. There were also peaks observed in the partial RDFs. The error associated with these measurements must be determined. Furthermore, the partial RDFs of the most dilute solute elements are compared with a random distributions of atoms. The effects of data set size are also addressed.

B.2 Results/Discussion

B.2.1 Error Bars

The initial bin sizes are 0.02 nm. Thus, in 2 nm there are 100 bins. The error bars are large with this bin size, especially when a dilute solute is examined. The partial Zr-Yb RDF for the Al-0.06Sc-0.02Yb-0.005Zr (at.%) alloy is shown in (Fig. B.1) with error bars calculated from counting statistics. The errors are so large since there are so few solute atoms in the experimental data set of 7 million atoms. The bin size can be increased to increase the number of atoms in the bin (Fig. B.2). The error bars are reduced, however, resolution is also reduced. The values of the experimental partial RDFs in this case are reduced to closer to one. Even when the bin size is increased, for the 50 ppm Zr alloy, the error bars go through the horizontal line through one. This indicates that the fluctuations are not significant.

B.2.2 Random Distribution of Atoms

The experimental partial RDFs were compared with a random distribution of atom types. This was performed using the existing experimental data set, but randomly assigning atom types to the atoms, using a uniform random distribution. Hence, the spatial coordinates of the atoms was retained. The same concentrations of atoms are used as in the experimental alloy. The randomization of atom types was also mentioned by Moody et. al. [225] as a way to construe greater meaning from the atom probe tomography data. These authors were evaluating the effectiveness of the contingency table technique in detecting atomic clustering.

It can be seen in Fig. B.3 that for a partial Zr-Yb RDF of the alloy with 50 ppm Zr and 200 ppm Yb, there are fluctuations ranging from 0-2.8. When compared to the experimental data, for Zr-Yb (also with 50 and 200 ppm concentrations of Zr and Yb, respectively) there are peaks ranging from 0.1-3.4 in the data before the bins are combined. Hence, it is not possible to conclude from the experimental data if there is an interaction between Zr and Yb from the direct RDF plot. The Yb-Yb interactions are also examined (Fig. B.4). Even for the higher concentration of Yb (200 ppm), peaks can still be seen for the data set with randomized atoms.

B.3 RDF from Simulated Data Set

Partial RDFs were also calculated from a simulated data set. All of the atoms in the simulated data set sit exactly on the FCC lattice sites. The atom types are randomly generated as in the previous section, using a uniform random distribution with the same concentrations as in the experimental alloy. The simulated data set is set to contain the same number of atoms as the previous data set for the 50 ppm Zr alloy, 7 million atoms.

Figs. B.5 and B.6 show the partial Zr-Yb and Zr-Zr RDFs. It can be seen that only certain bins contain atoms since the atoms only sit at specific locations – corresponding to the nearest neighbor distances. There is still scatter in the data, similar to the scatter observed for the experimental data set with randomly assigned atom types.

Fig. B.7 and B.8 show the Zr-Yb and Yb-Yb partial RDFs for a larger simulated data set with 24 million atoms. The maximum peak height has been reduced. Since the shells contain more

atoms, fluctuations in the number of atoms within a shell will have a smaller effect on the shell composition.

B.4 Conclusions

The error associated with the partial RDFs for the interactions between solute elements with concentrations of 50 ppm and 200 ppm is large. Even for interactions between solute elements of 200 ppm and 200 ppm, such as in the case of Yb-Yb, there is significant error. These variations in the peak heights is also observed when the atoms are randomized for the experimental data set and for the simulated FCC lattice. Hence, significantly larger data sets are required to extract truly meaningful conclusions from the RDF analysis, although with the current data it is possible to draw conclusions about the differences between aging times and alloys.

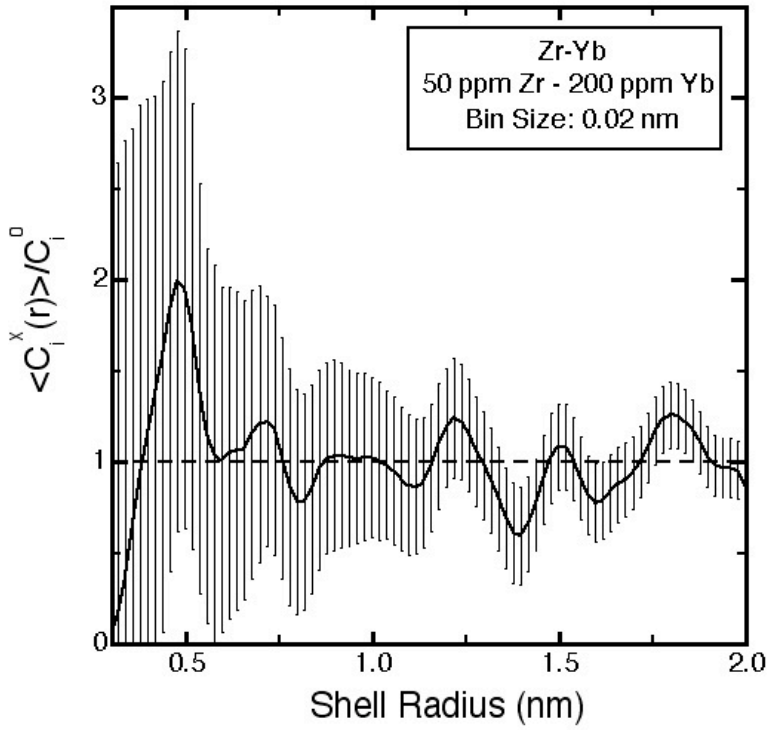

Figure B.1: Experimental Zr-Yb partial RDF in the unaged state for the Al-0.06Sc-0.02Yb-0.005Zr (at.%) alloy. The bin size is 0.02 nm.

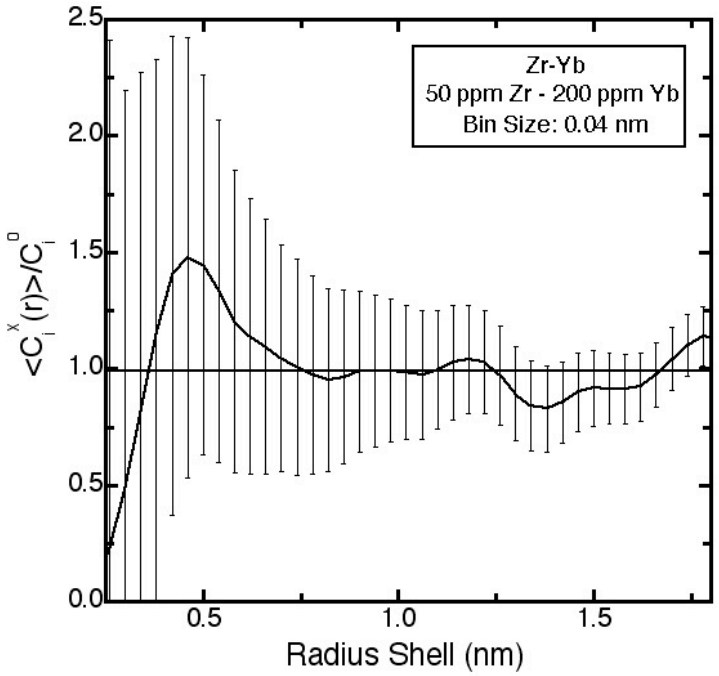

Figure B.2: Experimental Zr-Yb partial RDF in the unaged state of the Al-0.06Sc-0.02Yb-0.005Zr (at.%) alloy with a larger bin size of 0.04 nm.

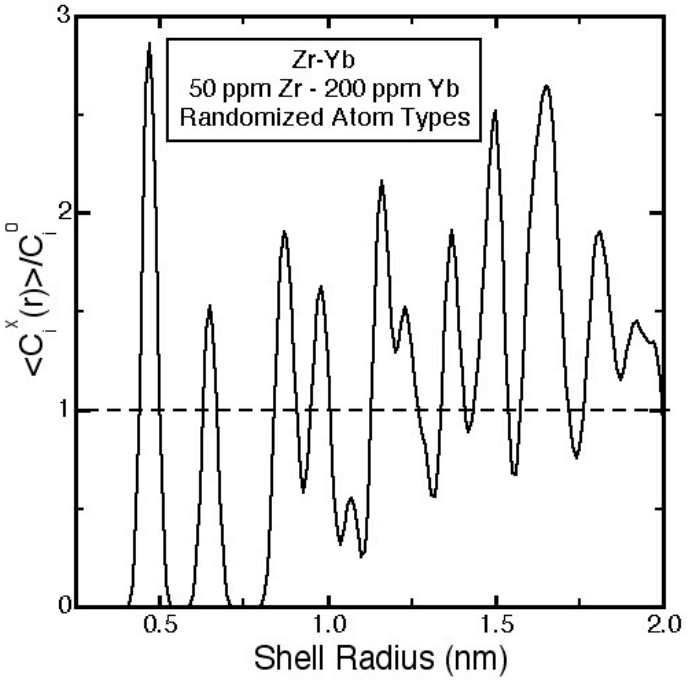

Figure B.3: Zr-Yb partial RDF from the Al-0.06Sc-0.02Yb-0.005Zr (at.%) alloy. The atom types are randomized within the experimental data set, thus retaining the spatial coordinates of the atoms.

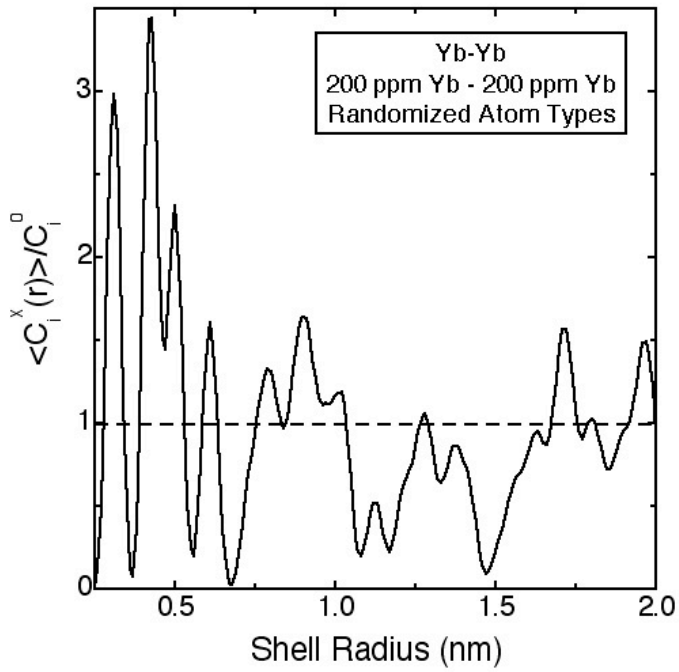

Figure B.4: Yb-Yb partial RDF from the Al-0.06Sc-0.02Yb-0.005Zr (at.%) alloy. The atom types are randomized within the experimental data set, thus retaining the spatial coordinates of the atoms.

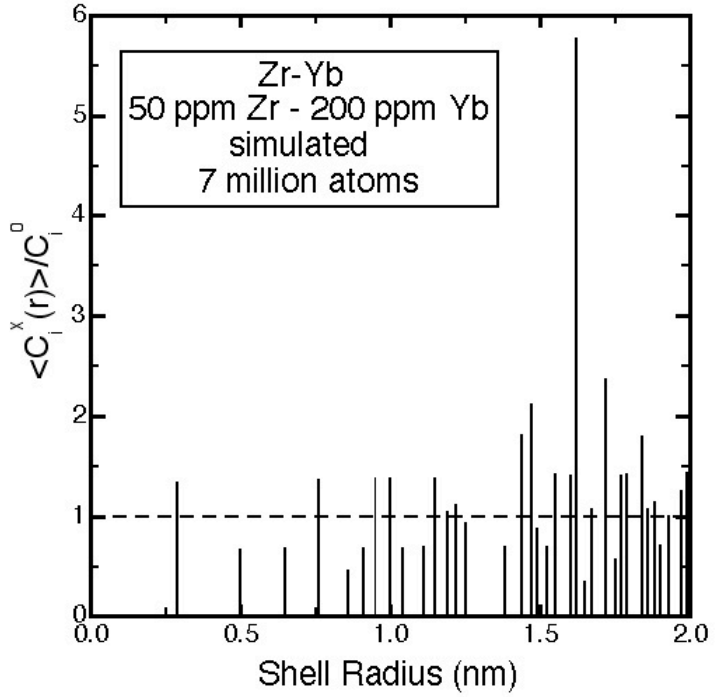

Figure B.5: Zr-Yb partial RDF of simulated FCC lattice containing 7 million atoms for the Al-0.06Sc-0.02Yb-0.005Zr (at.%) alloy.

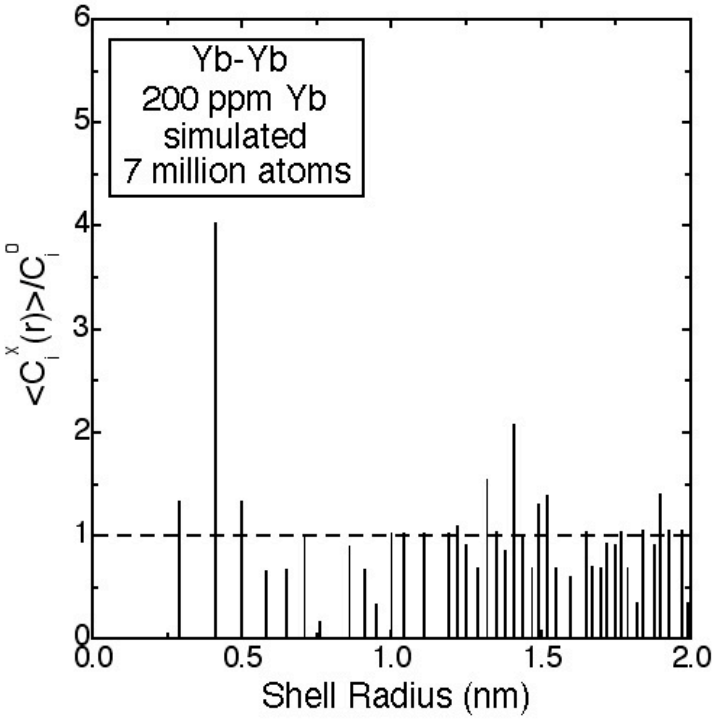

Figure B.6: Yb-Yb partial RDF of simulated FCC lattice containing 7 million atoms Zr-Yb for the Al-0.06Sc-0.02Yb-0.005Zr (at.%) alloy.

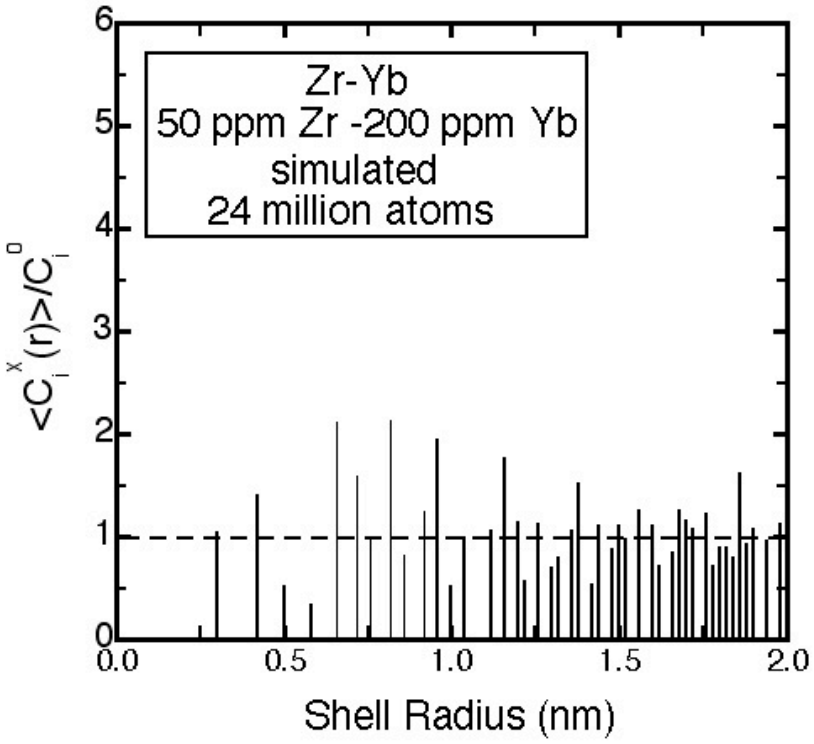

Figure B.7: Zr-Yb partial RDF of simulated FCC lattice containing 24 million atoms for the Al-0.06Sc-0.02Yb-0.005Zr (at.%) alloy.

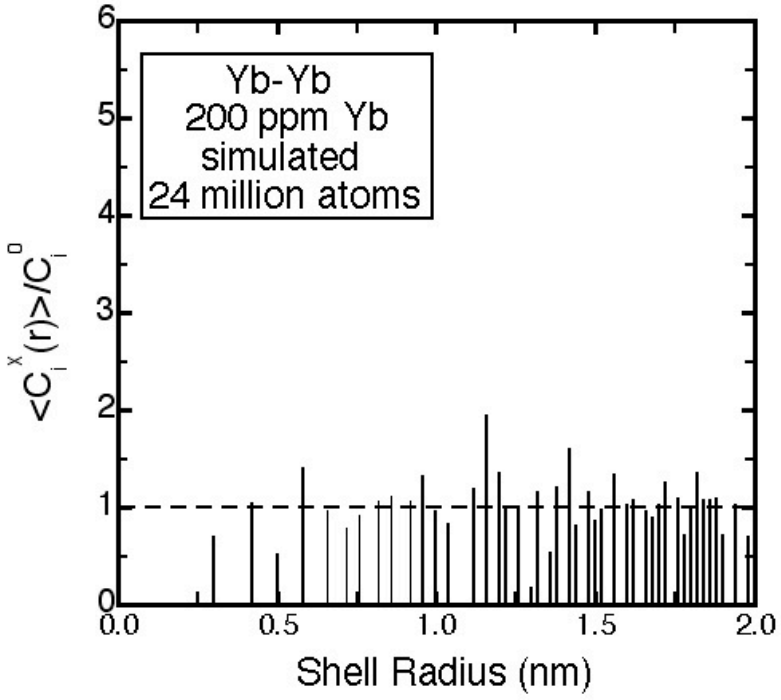

Figure B.8: Yb-Yb partial RDF of simulated FCC lattice containing 24 million atoms for the Al-0.06Sc-0.02Yb-0.005Zr (at.%) alloy.

Appendix C: Variation in Precipitate Concentration with Radius

The variation in concentration in the precipitates with precipitate radius, R, is examined. Various factors could be affecting the concentration of the precipitates, including that precipitates of different sizes could have formed at different times (when there were different amounts of solute in the matrix) and that the coarsening process will redistribute the solute from the small precipitates to the large ones (which will disproportionally affect the atoms in the shells of the precipitates).

For the Al-0.06Sc-0.02Yb-0.02Zr (at.%) alloy, the precipitate concentration was examined as a function of R. Figs. C1-C3 show the concentration of Zr, Yb and Sc as a function of radial distance from the α-Al/$Al_3(Sc_{1-x-y}Yb_xZr_y)$ heterophase interface for precipitates with different radii ranging from 2.4-4.1 nm. It is found that Zr segregates to the interface for each of the radii shown in the figure. C_{Zr} is only slightly higher for the larger radii (Fig. C1). The C_{Yb} does increase with an increase in R (Fig. C2). Conversely, C_{Sc} decreases with increasing R (Fig. C3). There are various mechanisms which could be the origin of this effect, including that the precipitates formed at different times when there were different amounts of solute in the matrix or that precipitates with different amounts of solute coarsen at different rates.

For the Al-0.06Sc-0.02Yb-0.005Zr (at.%) alloy, there are some precipitates which are considerably larger than any of the other precipitates in the data sets (greater than 8.6 nm vs. smaller than 4.5 nm) (Fig. C4). These large precipitates are not found in the alloy containing

more Zr (0.02%). For the precipitates which are considerably larger than the rest of the precipitates, there is a lower concentration of Zr at the interface (~0.2% compared with a maximum of 1.1% for the precipitates smaller than 4.5 nm). It thus appears that Zr at the interface has the effect of slowing down the growth and coarsening.

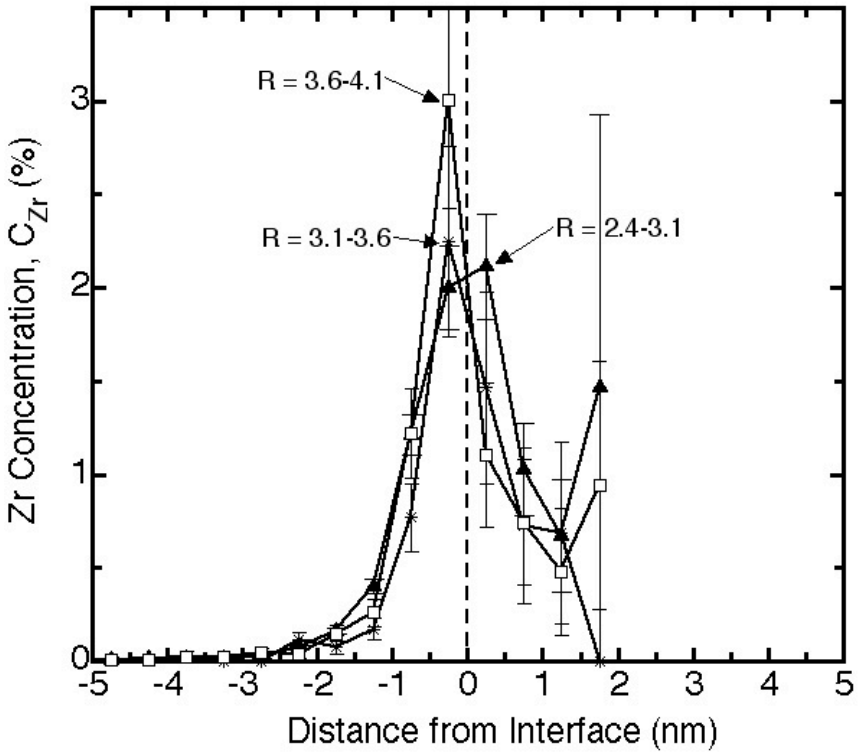

Figure C1: Proximity histogram showing the concentration of Zr as a function of radial distance from the matrix/precipitate interface. The composition of the alloy examined is Al-0.06Sc-0.02Yb-0.02Zr (at.%). Each line represents the summation of the concentration in each of the precipitates with R values in the range given.

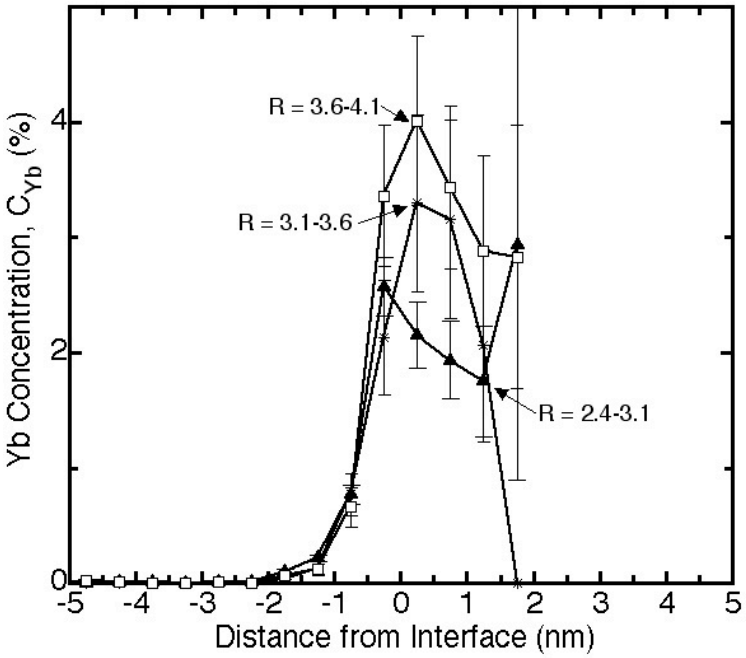

Figure C2: Proximity histogram showing the concentration of Yb as a function of radial distance from the matrix/precipitate interface. The composition of the alloy examined is Al-0.06Sc-0.02Yb-0.02Zr (at.%). Each line represents the summation of the concentration in each of the precipitates with R values in the range given.

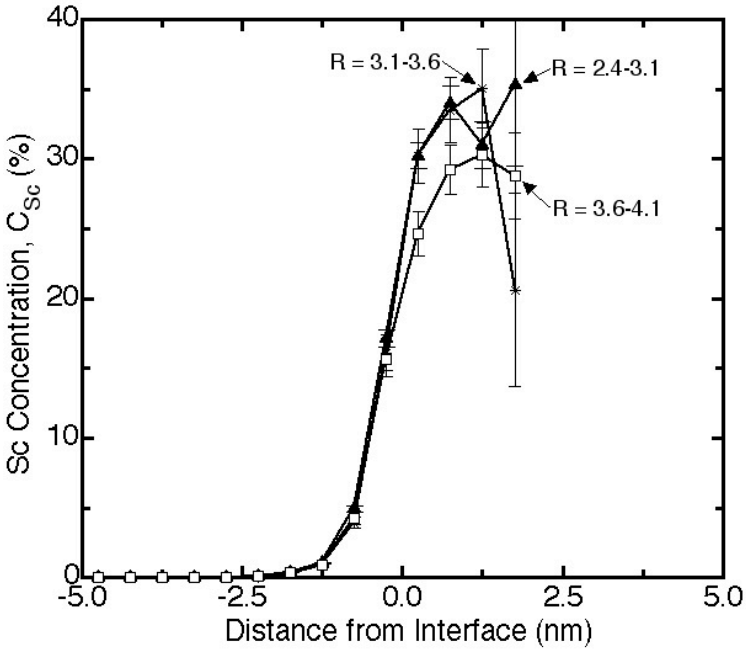

Figure C3: Proximity histogram showing the concentration of Sc as a function of radial distance from the matrix/precipitate interface. The composition of the alloy examined is Al-0.06Sc-0.02Yb-0.02Zr (at.%). Each line represents the summation of the concentration in each of the precipitates with R values in the range given.

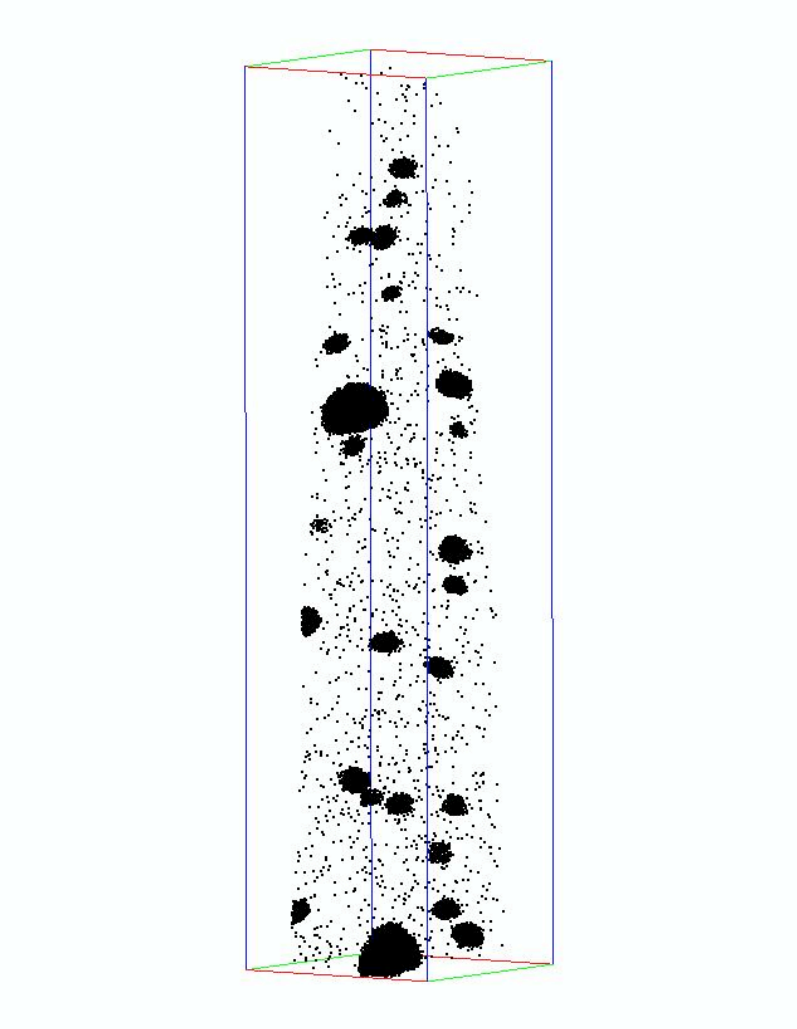

Figure C4: 3-dimensional reconstruction of Al-0.06Sc-0.02Yb-0.005Zr (at.%) aged for 64 days at 300˚C. (Dimensions: 72x72x297 nm^3)

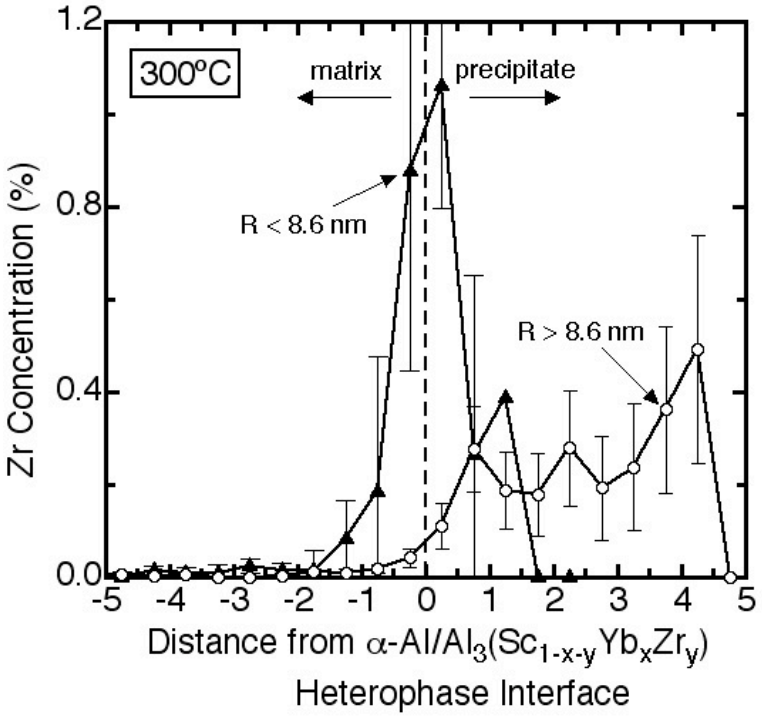

Figure C5: Proximity histogram showing the concentration of Zr as a function of radial distance from the matrix/precipitate interface. The composition of the alloy examined is Al-0.06Sc-0.02Yb-0.005Zr (at.%). Each line represents the summation of the concentration in each of the precipitates. The open circles represents the concentration for the two large precipitates and the solid symbols represents the summation of the small precipitates.

Appendix D: Comparison of Average Precipitate Radii as calculated by Transmission Electron Microscopy and Local-Electrode Atom-Probe Tomography

D.1 Introduction

The calculation of <R(t)> is critical to the results presented in this thesis. <R(t)> gives an indication of the coarsening and it also is used to predict the mechanical properties, both room temperature strength and creep properties. A comparison of the average precipitate radius, <R(t)>, as calculated by different experimental techniques is made. This is done to ensure that the techniques are not systematically producing an error.

One potential source of error is that the interface is not necessarily abrupt. Although according to high resolution TEM, in Al-Sc [21] and Al-Sc-Zr [2] alloys the interface is abrupt. Another potential source for bias in the measured values of <R(t)> is how the interface between the matrix and the precipitate is defined. The interface can be defined in different ways within a particular method. For the LEAP results, the interface does not appear abrupt since there are differences in the evaporation of the two phases. Since the evaporation field of the intermetallic precipitate is higher, it evaporates with a smaller radius of curvature than the surrounding matrix. The lack of uniformity on the surface leads to an overlap in the trajectories of the atoms originating from near the interface region. In this study, the interface is defined as the inflection point in the concentration on the proximity histogram plot. For TEM, error in the measured <R(t)> can come from several sources, including the alignment of the microscope. Error could

also be introduced during the measurement procedure, where the precipitates' size is determined from the contrast on the micrograph.

D.2 Results/Discussion

Table D.1 Experimentally determined average precipitate radii, <R(t)>, for Al-0.06Sc-0.06Ti aged for 24 h at 300˚C followed by 120 h at 400˚C.

Experimental Method	Measured <R(t)>
TEM	8.3±2.9
LEAP	7.8±2.3

Table D.2 Experimentally determined average precipitate radii, <R(t)>, for Al-0.06Sc-0.02Yb aged for 16 d at 300˚C.

Experimental Method	Measured <R(t)>
TEM	4.0±0.5
LEAP	3.9±0.6

The radii are calculated for the Al-0.06Sc-0.06Ti alloy and the Al-0.06Sc-0.02Yb alloys for the same aging condition, utilizing both TEM and LEAP. The radii calculated by LEAP are slightly smaller than those calculated by TEM (2.5–6% smaller). The measured values are within experimental error. Since both methods give similar results, it lends credibility to the measurements of <R(t)> found in this thesis.

Appendix E: Additions of Sm to Al-Sc Alloys

Concentrations 0.02at.% of Sm were also added to an Al-0.06at.%Sc alloy. Figure E.1 shows the microhardness vs. aging time at 300˚C. The Sm containing alloy has a lower microhardness when compared with the other Al-Sc alloys with RE additions (Yb or Gd). Fig. E.2 shows an optical micrograph which shows Sm-rich precipitates after a homogenization treatment at 640˚C for 72 h. This indicates that in the homogenized state the Sm is not in the matrix and thus has a limited solid-solubility in the matrix.

One possible explanation for the lower microhardness compared with the Al-Sc-Yb alloy is that in the Al-Sc-Sm alloy there is a lower volume fraction (0.25% for Al-Sc-Sm compared with 0.33% for Al-Sc-Yb) since most of the Sm does not form precipitates upon aging. Instead, the Sm forms eutectic precipitates during casting. The Al-Sc-Gd alloy also has a lower volume fraction of precipitates when compared to Al-Sc-Yb, since the Gd also has a limited solubility in the precipitates.

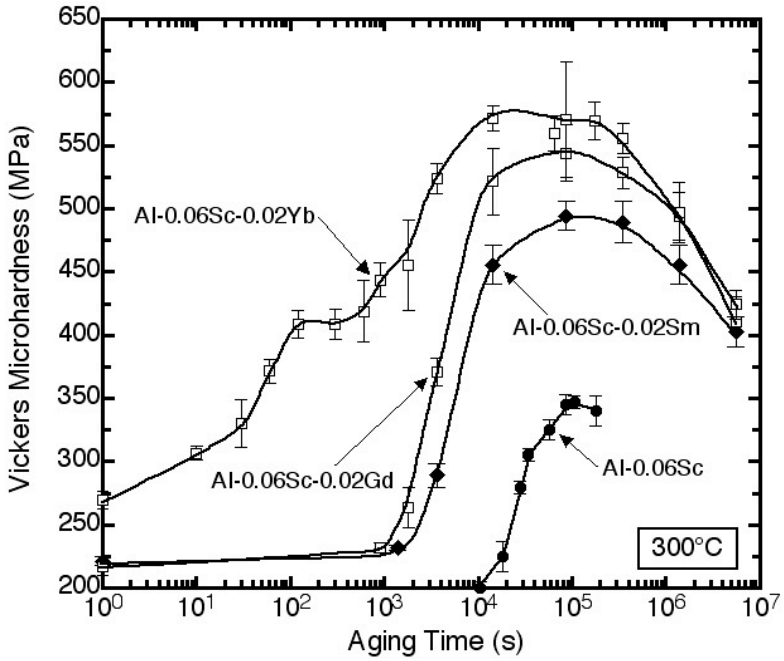

Figure E.1: Vickers microhardness vs. aging time at 300˚C for Al-0.06Sc-0.02RE alloys. Ternary alloys compared with Al-0.06Sc [20].

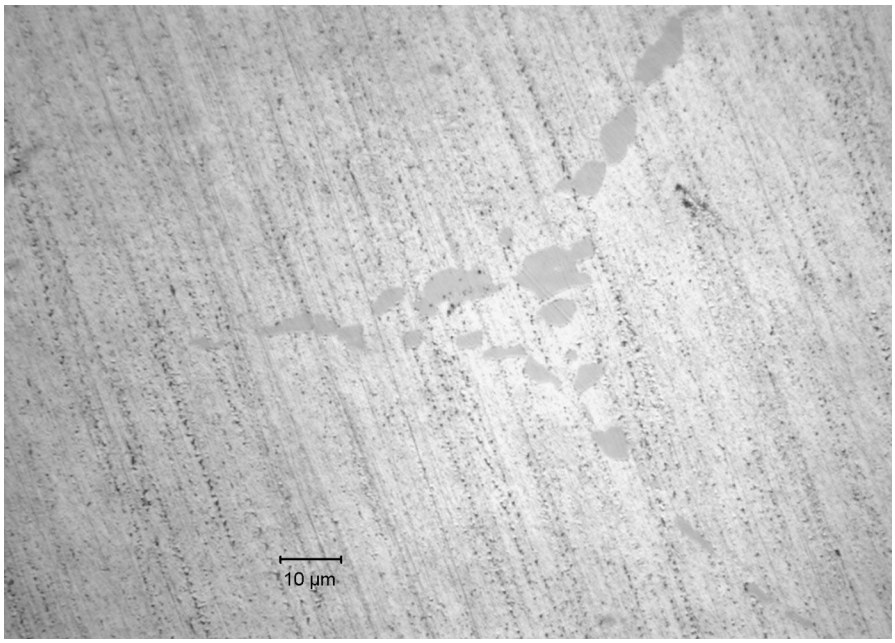

Figure E.2: Optical micrograph of Al-0.06Sc-0.02Sm in the homogenized state showing Sm-rich precipitates.